



**AFRL-RQ-WP-TR-2013-0189**

**APPLICATION OF ADVANCED LASER DIAGNOSTICS  
TO HIGH-IMPACT TECHNOLOGIES**

**Task Order 0002: Science and Applications of Ultrafast, Ultraintense  
Lasers**

**Larry P. Goss**

**Innovative Scientific Solutions, Inc.**

**NOVEMBER 2013**

**Final Report**

**Approved for public release; distribution unlimited.**

*See additional restrictions described on inside pages*

**STINFO COPY**

**AIR FORCE RESEARCH LABORATORY  
AEROSPACE SYSTEMS DIRECTORATE  
WRIGHT-PATTERSON AIR FORCE BASE, OH 45433-7542  
AIR FORCE MATERIEL COMMAND  
UNITED STATES AIR FORCE**

## NOTICE AND SIGNATURE PAGE

Using Government drawings, specifications, or other data included in this document for any purpose other than Government procurement does not in any way obligate the U.S. Government. The fact that the Government formulated or supplied the drawings, specifications, or other data does not license the holder or any other person or corporation; or convey any rights or permission to manufacture, use, or sell any patented invention that may relate to them.

This report was cleared for public release by the USAF 88th Air Base Wing (88 ABW) Public Affairs Office (PAO) and is available to the general public, including foreign nationals.

Copies may be obtained from the Defense Technical Information Center (DTIC)  
(<http://www.dtic.mil>).

AFRL-RQ-WP-TR-2013-0189 HAS BEEN REVIEWED AND IS APPROVED FOR  
PUBLICATION IN ACCORDANCE WITH ASSIGNED DISTRIBUTION STATEMENT.

\*//Signature//

---

AMY C. LYNCH  
Project Engineer  
Combustion Branch  
Turbine Engine Division

//Signature//

---

ANDREW J. WESTMAN  
Branch Chief  
Combustion Branch  
Turbine Engine Division

//Signature//

---

ROBERT D. HANCOCK  
Principal Scientist  
Turbine Engine Division  
Aerospace Systems Directorate

This report is published in the interest of scientific and technical information exchange, and its publication does not constitute the Government's approval or disapproval of its ideas or findings.

\*Disseminated copies will show “//Signature//” stamped or typed above the signature blocks.

REPORT DOCUMENTATION PAGE				Form Approved OMB No. 0704-0188	
<p>The public reporting burden for this collection of information is estimated to average 1 hour per response, including the time for reviewing instructions, searching existing data sources, gathering and maintaining the data needed, and completing and reviewing the collection of information. Send comments regarding this burden estimate or any other aspect of this collection of information, including suggestions for reducing this burden, to Department of Defense, Washington Headquarters Services, Directorate for Information Operations and Reports (0704-0188), 1215 Jefferson Davis Highway, Suite 1204, Arlington, VA 22202-4302. Respondents should be aware that notwithstanding any other provision of law, no person shall be subject to any penalty for failing to comply with a collection of information if it does not display a currently valid OMB control number. <b>PLEASE DO NOT RETURN YOUR FORM TO THE ABOVE ADDRESS.</b></p>					
1. REPORT DATE (DD-MM-YY) November 2013		2. REPORT TYPE Final		3. DATES COVERED (From - To) 01 February 2005 – 10 April 2013	
4. TITLE AND SUBTITLE APPLICATION OF ADVANCED LASER DIAGNOSTICS TO HIGH-IMPACT TECHNOLOGIES Task Order 0002: Science and Applications of Ultrafast, Ultraintense Lasers				5a. CONTRACT NUMBER F33615-03-D-2329-0002	
				5b. GRANT NUMBER	
				5c. PROGRAM ELEMENT NUMBER 62203F	
6. AUTHOR(S) Larry P. Goss				5d. PROJECT NUMBER 3048	
				5e. TASK NUMBER	
				5f. WORK UNIT NUMBER QOHE	
7. PERFORMING ORGANIZATION NAME(S) AND ADDRESS(ES) Innovative Scientific Solutions, Inc. 2766 Indian Ripple Road Dayton, OH 45440-3638				8. PERFORMING ORGANIZATION REPORT NUMBER 2829, DO 0002 Final	
9. SPONSORING/MONITORING AGENCY NAME(S) AND ADDRESS(ES) Air Force Research Laboratory Aerospace Systems Directorate Wright-Patterson Air Force Base, OH 45433-7542 Air Force Materiel Command United States Air Force				10. SPONSORING/MONITORING AGENCY ACRONYM(S) AFRL/RQTC	
				11. SPONSORING/MONITORING AGENCY REPORT NUMBER(S) AFRL-RQ-WP-TR-2013-0189	
12. DISTRIBUTION/AVAILABILITY STATEMENT Approved for public release; distribution unlimited.					
13. SUPPLEMENTARY NOTES Report contains color. PA Case Number: 88ABW-2013-5333; Clearance Date: 17 Dec 2013. On many of the papers, the U.S. Government is joint author and has the right to use, modify, reproduce, release, perform, display, or disclose the work.					
14. ABSTRACT <p>This report describes the results of experimental and numerical investigations on the development of extreme-light diagnostics. The purpose of this program was to develop extreme-light diagnostic tools that could be utilized in the future for exploring new frontiers of aerospace science and performing in-place nondestructive evaluation and inspections of newly manufactured and fielded weapons-systems components. The objectives of this research program were realized through an extensive experimental campaign that utilized ultrafast and ultraintense laser systems for the development of advanced sources of secondary emission for nondestructive evaluation. The secondary sources were to include X-rays, energetic electrons, neutrons, and protons. At the crux of the work was the fundamental interaction between an incident, ultrafast, ultraintense laser pulse and a material target. A variety of target materials was explored in this work, and much of the effort was spent on fundamental studies. The results of these studies will serve to guide engineering efforts in establishing these sources for future Air Force applications. Most of the effort was directed toward the development of hard X-ray sources using both metal and liquid targets.</p> <p>The following titles, which have been published in professional journals and conference proceedings or are unpublished reports/presentations, are provided in this report:</p> <ul style="list-style-type: none"> <li>• “Efficiency and scaling of an ultrashort-pulse high-repetition-rate laser-driven X-ray source”</li> <li>• “An Evaluation of fs/ns-LIBS for Measuring Total Particulate Emissions”</li> <li>• “Picosecond Laser Machining of Shaped Holes In Thermal Barrier Coated Turbine Blades”</li> <li>• “Double-pulse and single-pulse laser-induced breakdown spectroscopy for distinguishing between gaseous and particulate phase analytes”</li> <li>• “Hot electron dominated rapid transverse ionization growth in liquid water”</li> </ul>					
15. SUBJECT TERMS Extreme-Light Diagnostics, Ultrafast Lasers, UltraIntense Lasers, Femtosecond Lasers, X-rays, Nondestructive Evaluation					
16. SECURITY CLASSIFICATION OF:			17. LIMITATION OF ABSTRACT: SAR	18. NUMBER OF PAGES 182	19a. NAME OF RESPONSIBLE PERSON (Monitor) Amy C. Lynch 19b. TELEPHONE NUMBER (Include Area Code) N/A
a. REPORT Unclassified	b. ABSTRACT Unclassified	c. THIS PAGE Unclassified			

## TABLE OF CONTENTS

Section	Page
List of Figures .....	iii
List of Tables .....	v
Executive Summary .....	vi
1.0 INTRODUCTION .....	1
2.0 MOTIVATION AND LONG-TERM VISION OF THE PROGRAM.....	2
3.0 EXTREME-LIGHT DIAGOSTICS.....	8
3.1 Extreme-Light Generation of X-rays .....	9
3.2 Laser System and Facility Development.....	12
3.3 X-ray Generation from Laser/Metal-Target Interactions .....	17
3.4 X-ray Generation from Laser/Dielectric-Target Interactions.....	22
3.5 The Impact of Chirp on X-ray Generation for Metals and Dielectrics .....	27
3.5.1 Chirp .....	27
3.5.2 Chirp Impact on X-ray Yield for Metal and Dielectrics .....	29
3.6 Impact of Prepulse on X-ray Yield for Cu and Water Targets.....	34
3.6.1 Impact of Natural Amplified Spontaneous Emission (ASE) on Cu and Water Targets.....	34
3.6.2 Impact of Artificial Prepulse on X-ray Yield from Cu Target.....	38
3.6.3 Impact of Artificial Prepulse on Water-Jet Target.....	44
3.7 Impact of Artificial Prepulse and Chirp on X-ray Yield from a Water-Jet Target .....	46
3.8 Discussions of the Impact of Chirp on X-ray Generation in a Water-Jet Target.....	52
3.9 X-ray Emissions at Relativistic Conditions .....	55
3.9.1 Literature Search for Papers about Electron and X-ray Emissions Generated at Relativistic Conditions.....	56
3.9.2 Measurements of X-rays Generated at Relativistic Conditions.....	58
3.10 Visualizations of Laser/Water-Jet Interactions.....	63
3.10.1 X-ray Visualization.....	63
3.10.2 Shadowgraph Visualization .....	65
4.0 SUMMARY OF PUBLICATIONS AND PRESENTATIOIS .....	71
4.1 Development of Laser-Based X-Ray Source for Dense Spray and Soot Diagnostics.....	71
4.2 Laser-Target Generation of Soft X-Rays .....	71
4.3 Laser Generation of X-Rays for Air-Force Applications .....	72
4.4 Imaging of Laser-Generated Micro-plasmas .....	72
4.5 Development of Laser-Generated X-Ray Source for Air-Force Applications .....	73
4.6 Laser-Induced Breakdown Spectroscopy for Detection of Volatile Aerosols .....	74
4.7 Efficiency and Scaling of Ultrashort-Pulse, High-Repetition-Rate, Laser-Driven X-Ray Source.....	74
4.8 An Evaluation of Femtosecond/Nanosecond-LIBS for Measuring Total Particulate Emissions .....	75
4.9 Picosecond Laser Machining of Shaped Holes in Thermal-Barrier-Coated Turbine Blades.....	75
4.10 Double-Pulse and Single-Pulse Laser-Induced Breakdown Spectroscopy for Distinguishing between Gaseous and Particulate Phase Analysis .....	76
4.11 Hot-Electron-Dominated Rapid Transverse-Ionization Growth in Liquid Water ....	76





## LIST OF FIGURES

Figure	Page
Figure 1. Potential applications from radiation and particles generated by extreme-light/matter interaction.....	3
Figure 2: Gas generator positioned near a nuclear reactor .....	4
Figure 3. Photon flux and energy of the white synchrotron source at BNL .....	6
Figure 4. Schematic of the laser system developed for studies of extreme-light/target-interaction studies .....	13
Figure 5. Layout of developed laser system and test chambers.....	14
Figure 6. Target-chamber schematic for studying laser/liquid-target interactions at relativistic laser intensities.....	15
Figure 7. Rotational devices (a) and three-axis translator (b) used to move the metal targets so that no two laser shots would hit the same spot on the target.....	15
Figure 8. X-ray spectra obtained from laser/metal interactions.....	19
Figure 9. The impact of a prepulse delay time on the conversion efficiency of the bremsstrahlung X-ray emission from a Ti target .....	20
Figure 10. X-ray image of a circuit board made with the 3.4-keV $K\alpha$ radiation from tin.....	21
Figure 11. Comparison of CE for bremsstrahlung emission from Cu using the Legend and the Red Dragon .....	22
Figure 12. Metal-target chamber.....	23
Figure 13. X-ray yield and laser intensity vs. pulse width (positive chirp) .....	24
Figure 14. X-ray yield and laser intensity vs. pulse width (positive chirp) for a glass target.....	24
Figure 15. Schematic of experimental setup for investigating X-ray yield and laser intensity vs. pulse width (positive chirp) for liquid targets using the Red Dragon laser .....	25
Figure 16. X-ray yield and laser intensity vs. pulse width (positive chirp) for a 50- $\mu$ m-diameter menthol-jet target for energy fixed at 2.5 mJ.....	25
Figure 17. X-ray yield and laser intensity vs. pulse width for a 50- $\mu$ m-diameter water-jet target .....	26
Figure 18. Magnitudes of X-ray yields of methanol and water .....	27
Figure 19. Positive and negative linear chirp and quadratic chirp.....	28
Figure 20. Calculated GDD and laser pulse width for the Red Dragon laser .....	29
Figure 21. Impact of chirp on X-ray yield for Cu target for energy fixed at 3.0 mJ .....	31
Figure 22. Impact of chirp on X-ray yield for a glass target for energy fixed at 3.0 mJ .....	32
Figure 23. Impact of chirp on X-ray yield for a 50- $\mu$ m-diameter water-jet target for a laser energy fixed at 3.0 mJ .....	33
Figure 24. Typical temporal structure of ASE from a laser pulse from a CPA system.....	34
Figure 25. Third-order autocorrelator built on this program .....	35
Figure 26. Contrast of the Red Dragon laser .....	36
Figure 27. Two normalized third-order autocorrelations for the Red Dragon laser taken about 1 month apart .....	37
Figure 28. Normalized third-order autocorrelation for the Red Dragon laser .....	38
Figure 29. Artificial prepulse optical system.....	39
Figure 30. Third-order-autocorrelation trace .....	40
Figure 31. Dependence of total and $K\alpha$ X-ray yields on the delay time.....	42
Figure 32. Estimate of X-ray yield .....	42

Figure 33. Dependence of total X-ray yield on water jet distance.....	45
Figure 34. Dependence of total X-ray on prepulse delay time for p-polarization for a 75- μm-diameter water-jet target .....	45
Figure 35. Experimental setup for investigating the impact of prepulse and chirp on X-ray yield from a 75-μm-diameter water jet .....	47
Figure 36. Dependence of X-ray yields on laser linear chirps and pulse widths.....	47
Figure 37. Dependence of electron temperature on linear chirp and pulse width .....	48
Figure 38. X-ray and reflectance spectra for different pulse widths/chirp with a 60-ps prepulse .....	50
Figure 39. Dependence of reflected laser spectra on chirp without prepulse .....	51
Figure 40. Motion of critical-density surface .....	54
Figure 41. Target-chamber schematic for the preliminary results presented in this document.....	58
Figure 42. Best-focus image taken by the focal-spot monitoring system.....	59
Figure 43. Angular distribution of human-dose equivalent (in mRem/hr) recorded by a survey meter.....	60
Figure 44. Dose as a function of distance from the TCC.....	61
Figure 45. Preliminary X-ray spectra along the laser axis.....	62
Figure 46. Typical uncorrected raw X-ray spectrum observed from experiments .....	62
Figure 47. Experimental setup for visualizing laser/water-jet interactions .....	64
Figure 48. Top View of dual-water-jet setup.....	64
Figure 49. Images taken without and with a 10.5-ns object-stream prepulse and the difference .....	65
Figure 50. Illustration of pump-probe shadowgraph experiment of a laser interacting with a water jet.....	66
Figure 51. Pump-probe images of the ionization of air by a probe beam approaching a water-jet target .....	66
Figure 52. Shadowgraph images of a 10-ns-pulse-width YAG laser interacting with a 53- μm-diameter water jet in air.....	67
Figure 53. Random selection of three of the single-shot images at 6 ns, 30 ns and 130 ns...	68
Figure 54. Simultaneous low- and high-resolution shadowgraph images of a tightly focused 30-fs laser .....	69

## LIST OF TABLES

Table	Page
Table 1. Characteristics of the coupled three lasers.....	13
Table 2. Calculated laser parameters for Red Dragon Laser using Eqs. (1) – (7) .....	16
Table 3. The X-ray yields and conversion efficiencies (CE) for bremsstrahlung (broad band BB) and $K\alpha$ X-ray emissions for twelve metals .....	20

## **PREFACE**

This report was prepared by Dr. Larry P. Goss of Innovative Scientific Solutions, Inc., and covers work performed during the period 1 February 2005 through 12 April 2013 under Air Force Contract F33615-03-D-2329, Delivery Order 0002. The contract was administered under the direction of the Air Force Research Laboratory, Wright-Patterson Air Force Base, OH, with Amy Lynch as Government Project Monitor.

## EXECUTIVE SUMMARY

This report describes the results of experimental and numerical investigations on the development of extreme-light diagnostics. The purpose of this effort was to develop extreme-light diagnostic tools that employ radiation and particles generated by extreme-light/target interactions for studying, characterizing, analyzing, and evaluating matter and processes. Realization of these applications could provide a revolutionary capability that would significantly impact Department of Defense (DoD) research, development, and sustainment programs. Such an extreme-light system could be used in a laboratory environment for weapons-systems development, materials development, chemical analysis, and model development/evaluation. It could also be employed for real-time inspection and evaluation of newly fabricated gas-turbine or aircraft components as well as in-place inspections of weapons systems.

The objective of this research program was realized through an extensive experimental campaign that utilized ultrafast and ultraintense laser systems for the development of advanced sources of secondary emission for nondestructive evaluation. The secondary sources were to include X-rays, energetic electrons, neutrons, and protons. The main goal of this research was to gain an understanding of the fundamental interaction between an incident, ultrafast, ultraintense laser pulse and a material target.

This program began with an empty laboratory, no equipment, and no capability to conduct femtosecond/laser interaction studies as related to x-ray emissions. During the course of the program, the capabilities of this laboratory have expanded to the point that it has become a world-class facility for conducting this type of research. To extend the range of our experiments and to provide greater experimental flexibility, a unique coupled laser system has been developed. This system electronically and optically couples three lasers so that the main and prepulse parameters can be independently varied. The coupled laser system can also be used to visualize the pre-/main-pulse interactions during the time when X-ray measurements are made.

Much of the research effort was concentrated on the production of hard X-rays from metal and water targets. In particular, the presence of a laser prepulse in addition to the main laser pulse, the temporal location of the prepulse, and the chirp of the laser were discovered to be important factors for increasing the amplitude of the generated X-rays. Modeling efforts are currently underway in an effort to understand and explain the experimental X-ray yields.

This research on this program could not have been accomplished without the help of many talented scientists and technicians, including Dr. M. Brown, Dr. C. Rettig, Dr. T. Erickson, Mr. K. Frische, Dr. P. Zhang, Dr. V. Ovchinnikov, Dr. J. Morrison, Dr. E. Chowdhury, Dr. J. Nees, Dr. B. Torralva, Dr. D. Hahn, Dr. L. Dosser, Dr. C. Druffner, and Dr. S. Gogineni. Also the guidance and support of Dr. Melvyn Roquemore are gratefully acknowledged.

## 1.0 INTRODUCTION

This report describes the results of experimental and numerical investigations on the development of extreme-light diagnostics. The purpose of this program was to develop extreme-light diagnostic tools that could be utilized in the future for exploring new frontiers of aerospace science and performing in-place nondestructive evaluation (NDE) and inspections of newly manufactured and fielded weapons-systems components.

The objectives of this research program were realized through an extensive experimental campaign that utilized ultrafast and ultraintense laser systems for the development of advanced sources of secondary emission for NDE. The secondary sources were to include X-rays, energetic electrons, neutrons, and protons. At the crux of the work was the fundamental interaction between an incident ultrafast, ultraintense laser pulse and a material target. A variety of target materials was explored in this work, and much of the effort was expended on fundamental studies. The results of these studies will serve to guide engineering efforts in establishing these sources for future Air Force applications. The work was directed mainly toward the development of hard X-ray sources using both metal and liquid targets.

The research conducted during the program resulted in eleven publications and presentations, a list of which can be found in Section 5. Complete copies of five of the publications are included in the Appendix. In this report the motivation for the Air Force to conduct this research is discussed in Section 2. The research efforts are summarized in Section 3, while the publications and presentations are summarized in Section 4.

## 2.0 MOTIVATION AND LONG-TERM VISION OF THE PROGRAM

Maiman demonstrated the first laser in 1960, which started a technology revolution that has resulted in the pervasive application of lasers in such areas as research, electronics, manufacturing, medicine, and warfare. However, very few of these applications were foreseen in the early years of the development of the laser. Charles Townes, in the excellent book entitled, *How the Laser Happened*, points out that when the laser was invented people said, "That's a great idea, but it's a solution looking for a problem." His answer was, "The truth is, none of us who worked on the first lasers imagined how many uses there might eventually be." He attributed the lack of a clear vision for the laser's future to the fact that the laser was really new and people could not use their experience to grasp its importance. By 1975 the vision of the future of the laser had become clear. Major Walter Breen wrote an excellent article describing his vision for the laser as a military and commercial tool. Most of the military applications he foretold have come to pass (<http://www.airpower.maxwell.af.mil/airchronicles/aureview/1975/may-jun/breen.html>). It has now been 28 years since Strickland and Mourou [1985] broke an intensity barrier that had existed for almost 40 years. Their demonstration of chirped-pulse amplification (CPA) initiated a laser-technology revolution that has the potential to become more important than that originated by Maiman.

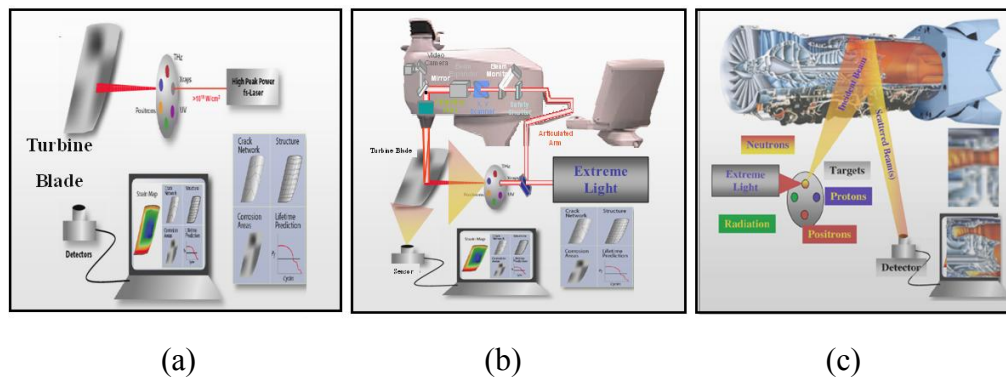
Almost every science and engineering field has benefited from the use of radiation and particles to probe, analyze, inspect, and study atoms, molecules, materials, components, and systems. New sources of high-brightness, ultrashort-pulse sources of radiation and particles have resulted because of the invention of CPA and the subsequent development of extremely intense and extremely short laser pulses [Strickland and Mourou, 1985]. Because of the extreme characteristics of these lasers, they are often referred to as extreme light [Mourou and Umstader, 2002]. The technical publication *Science* has referred to extreme-light research as the "The Next Frontier" [Yamanouchi, 2002]. Extreme light can interact with matter to produce conditions never before realized: peak powers of  $10^{15}$  W, focused intensities of  $10^{22}$  W/cm<sup>2</sup>, electric fields greater than  $10^{11}$  V/cm, magnetic fields of  $10^9$  G, temperatures and pressure greater than  $10^{10}$  K and  $10^9$  bar, respectively, and particle accelerations  $10^{23}$  times that of the earth's gravity [Mourou and Umstader, 2002]. Studies of extreme light/matter interactions are driving new discoveries and insight into fundamental phenomena in physics, chemistry, medicine, and materials science. Some of these discoveries and insight have the potential to stimulate new, pervasive, and revolutionary applications. One capability that is of interest to the Air Force and the subject of this program involves extreme-light diagnostics.

Extreme-light diagnostics is a tool that employs radiation and particles generated by extreme-light/target interactions to study, characterize, analyze, and evaluate matter and processes. Specifically, the interaction of extreme light with clusters, gases, liquids, and solid targets has been used to produce secondary emissions of radiation and elementary particles [Mourou and Umstader, 2002; Ditmire, 2002]. The secondary radiation ranges from soft X-rays to gamma rays. Fundamental particles, including electrons, protons, neutrons, and positrons, have also been generated. Typically, the temporal characteristics of these secondary emissions mirror those of the lasers that generated them, i.e., they are femtosecond-pulsed emissions. Thus, extreme light offers the potential to have an



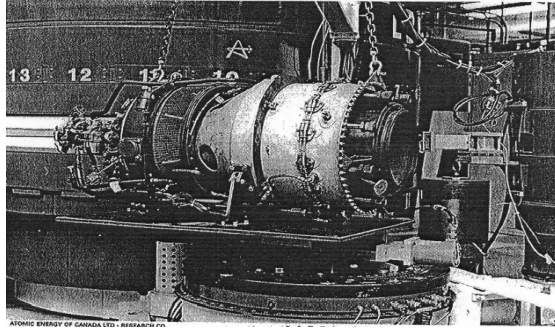
intense, high-brightness, ultrashort-pulse, point source of penetrating radiation [XUV (X-ray ultraviolet) to gamma rays] and particles (electrons, positrons, protons, neutrons).

Figure 1 illustrates a long-term vision of potential applications that could result from the use of radiation and particles generated by extreme-light/matter interactions. Realization of these applications could provide a revolutionary capability that would significantly impact DoD (Department of Defense) research, development, and sustainment programs. Figure 1(a) illustrates an extreme-light diagnostic system that could be set up in a typical laboratory and have the capability to produce a wide range of radiation and particles for research and development. Today each different source of radiation and particles would require a separate system, and many laboratories would be required to house these systems. It appears to be possible to integrate both radiation and particle sources into one system because all of the sources result from the laser interacting with different targets. By switching out the targets and sensors, one could possibly achieve a tunable source of radiation and particles. Such an extreme-light system could be used in a laboratory environment for a wide range of applications, including weapons systems and materials development, chemical analysis, and model development and evaluation. It could also be used for real-time inspection and evaluation of newly fabricated gas-turbine or aircraft components in a shop environment, as in Figure 1(b), or for in-place inspection of weapons systems, as depicted in Figure 1(c).



**Figure 1. Potential applications from radiation and particles generated by extreme-light/matter interaction**

*((a) Illustration of an extreme-light diagnostic system that utilizes a wide range of radiation and particle sources, (b) integration of extreme-light-machining and diagnostic systems, and (c) in-place inspection and analysis of a gas turbine using extreme-light diagnostics.)*



**Figure 2: Gas generator positioned near a nuclear reactor**  
*(where successful neutron-diffraction measurements were made on a rotating disk in the generator [Leggett, 1994])*

The depictions in Figure 1 represent a long-term vision of extreme-light diagnostics. This vision, however, is a reflection of capabilities that have, to a large extent, been demonstrated at the national laboratories; however, one important difference is that extreme-light diagnostics can be located in a laboratory of reasonable size or in the field. The concept of a common source of radiation and particles Figure 1(a) already exists at synchrotron and nuclear-reactor facilities. Indeed, these facilities have been used for many military applications that one would prefer to achieve with extreme-light diagnostics. For example, in-place inspection, illustrated in Figure 1(c), has been accomplished using neutron radiography to detect cracks and corrosion in actual aircraft [Froom, 1998]; however, the use of a radioactive source or a nuclear reactor is required. Thus, practical field or depot use is limited.

A more direct example of the Figure 1(c) concept is shown in Figure 2. In 1994 Leggett demonstrated on an Air Force program that neutron diffraction could be used to measure strain and temperature of a rotating disk in a gas generator. This was accomplished by shooting the neutrons from a nuclear reactor through the walls of a gas generator. The initial intent was to demonstrate this capability in an operating gas-turbine engine. The problem was that the operation of an engine near a nuclear reactor was prohibited because of safety concerns. These examples--and there are many more--illustrate that many revolutionary diagnostic capabilities already exist that could greatly benefit the DoD if they could be routinely used in laboratories of reasonable size. Unfortunately, the requirement for a mega facility means that the capabilities cannot be routinely used. However, the characteristics of the radiation and particle sources used by the national laboratories in experiments of importance to the DoD can aid in addressing the current capabilities of extreme-light diagnostics. To accomplish this, several applications that are of interest to the Air Force and that have been demonstrated at the national laboratories will be discussed.

Argonne National Laboratory (ANL) made a major advance when it was demonstrated that X-rays could be used to study dense sprays in more detail than had been possible previously [Poola et al., 2000]. The problem has been that conventional laser diagnostics could not penetrate the near-nozzle opaque region of turbulent dense spray flames. The near-nozzle region is where the fuel breaks up into droplets that begin to evaporate, mix,

and burn. It is also the region where soot inception begins. Thus, the near-nozzle region establishes the initial conditions for the processes that determine the performance and emissions of combustors. Even though this is a critically important region of the combustor, it is the least understood. This lack of understanding is reflected by the inaccuracies in the spray models that are used to design combustors for aerospace propulsion systems.

ANL demonstrated that X-ray images of fuel density, shock waves, and spray structure could be obtained near the dense spray region of a fuel nozzle that is used in diesel engines [Powell et al., 2003]. Several years ago we made an unsuccessful attempt to investigate a dense-laser-generated spray using extreme-light-generated  $K\alpha$  X-rays. Since that time we have increased our X-ray yields by two orders of magnitude. In this program we are moving into the relativistic optics regime with laser intensities that are two orders of magnitude higher. We will not be able to match the 5.1- $\mu$ s time resolution of the ANL measurements, but we expect to be able to conduct pump-probe measurements by averaging for about  $\times$  min/per timestep. This is sufficient to obtain useful information concerning dense, sooting spray flames.

The compressor and turbine are the two most expensive components of a gas-turbine engine. Depending on the engine, the cost of a turbine or compressor disk with blades can range from  $\sim$  \$30K to as much as \$150K. A large engine may require more than twenty of these rotating components. Shot peening is used to extend the life of these rotating components. Basically, shot peening compresses the surface. The compression creates a large residual stress that extends a fraction of a millimeter into the surface. During the cyclic operation of the engine, the residual stress is relieved. The residual stress remaining in a component is an indicator of its remaining life. Currently, these components have a design life. When its life is reached, the component is replaced. Although the design life may be several years, replacement of these rotating components in a large fleet of engines is very expensive.

Research indicates that many of the replaced components have considerable remaining life. Models are being developed to predict the remaining life of components, based on the remaining residual stress [John et al., 2010]. Ideally, a direct measurement of the residual stress coupled with the model predictions would be an ideal way to estimate the remaining life. Unfortunately, the only method of making residual-stress measurements is destructive because X-rays from conventional laboratory systems do not have sufficient energy and flux to penetrate to the depth needed to make a complete residual-stress map. Recently, Brookhaven National Laboratory (BNL) demonstrated that nondestructive measurements of residual stress could be made in a turbine-blade material, Ti-6Al-4V, using energy-dispersive X-ray diffraction [Croft et al., 2008]. This represents a major advance; however, a synchrotron was required to generate the broad continuum of X-rays used in the experiment. The photon flux for the white source is shown in Figure 3. A band of X-rays around 30 keV with a  $50 \times 700$ - $\mu$ m beam was used. For the X-ray flux at 30 keV and the beam size, it is estimated that  $\sim 10^{11}$  photons/s were delivered to the sample. Our research to date has been focused on the 1 - 20 keV X-ray region.

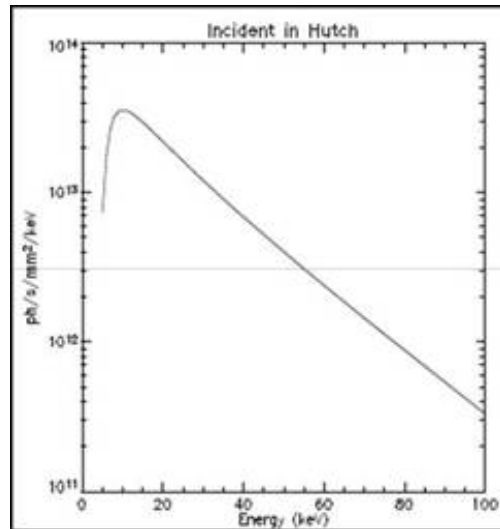


**Figure 3. Photon flux and energy of the white synchrotron source at BNL**

Recently, a major advance was made in generating a peak brightness on the order of  $1 \times 10^{19}$  photons/(s mm<sup>2</sup> mrad<sup>2</sup>) (per 0.1% bandwidth) of 1-MeV X-rays [Chen et al., 2013]. The output was a 5- $\mu$ m beam with a divergence of  $\sim 10$  mrad. Also, the X-ray energy could be scanned over a significant range using a 100-TW, 35-fs-pulse-width, 10-Hz-repetition-rate laser operating at relativistic optics conditions. This laser may be capable of performing nondestructive inspection on engine and aircraft components. However, it is a one-of-a-kind research laser, and considerable laser development will be required before it becomes a practical engineering tool. However, the capabilities are very encouraging with regard to the long-term vision of extreme-light nondestructive inspection (NDI) on weapons systems being realizable. In the near future Umstadter and his team at the University of Nebraska will be attempting to repeat the residual-stress measurements employing the same Ti-6Al-4V sample used in the BNL experiments.

Perhaps the most far-reaching idea of the long-term vision is the use of extreme-light diagnostics to inspect an engine in place. The Defense Advanced Research Projects Agency (DARPA) is expected to launch a new program that could lead to the development of a portable laser-driven system of high-flux neutrons. The neutron-flux goal is  $10^{12}$  neutrons/s/cm<sup>2</sup>. This flux is sufficient to allow diffraction measurements of stress and temperature to be made on the rotating components in an operating gas generator [Leggett, 1994]. Even if this program is not successful, it will provide important information that will be useful in future programs of this type.

Encouraging results have also been obtained using low-energy, high-repetition-rate extreme-light lasers. For example, [Silies et al., 2009] demonstrated that extreme-light diagnostics could be used to make time-resolved, pump-probe X-ray-diffraction measurements at the surface of a GaAs sample. The X-rays were generated with a 4-mJ, 30-fs, 1-kHz laser interacting with a Cu target, and the yield was  $\sim 2 \times 10^9$  X-ray

photons/s/sr. This demonstration indicates that extreme-light diagnostics have potential for studying lattice dynamics and the impact of defects, strain, and contaminants in semiconductors. Such studies can be important in improving the life, quality, and manufacture of semiconductors.

### 3.0 EXTREME-LIGHT DIAGNOSTICS

Advancements in almost every scientific and engineering field have resulted from the use of diagnostics that employ radiation and particles to probe, analyze, inspect, and study atoms, molecules, materials, components, and systems. New sources of high-brightness, ultrashort-pulse sources of radiation and particles have resulted because of the invention of CPA and the subsequent development of extremely intense and extremely short laser pulses [Strickland and Mourou, 1985]. Because of their extreme characteristics, these lasers are often referred to as extreme light or extreme-light lasers [Mourou and Umstadter, 2002]. Extreme light can interact with matter to create conditions that have never been observed in laboratories. Many scientists around the world have recognized the science and technology advancements that could result from research using extreme light. *Science* referred to extreme light as “The Next Frontier” [Yamanouchi, 2002]. An International forum [Organisation for Economic Co-operation and Development (OECD), 2002] and a national workshop [The Science and Applications of Ultrafast, Ultraintense Lasers (SAUUL), 2002] were convened to encourage international collaboration and funding for research and applications using extreme light. The OECD forum helped stimulate European interest in extreme light. Recently, it was announced that the European Union is investing more than a billion dollars in extreme-light laser facilities and research because it is convinced that significant breakthroughs in science and new applications will result from extreme-light research [Frontiers in Extreme Relativistic Optics (FIERO), 2013]. Unfortunately, the investments of the United States in extreme light have been much less significant.

About ten years ago, the Propulsion Directorate of the Air Force Research Laboratory (AFRL) realized that extreme light was capable of producing high-brightness, ultrashort pulses of radiation and particles that could result in a new generation of diagnostics with potential for exploring new frontiers of science and engineering of interest to the DoD and conducting NDE and NDI of materials and weapons-systems components. This recognition resulted in the formulation of the long-term vision (presented in Section 2) for identifying the type of capabilities that, if realized, would have a revolutionary impact on DoD research, development, and sustainment programs as well on a broad range of science and engineering fields that employ radiation and particles in their endeavors. The realization of this long-term vision will require major advancements in (1) energy, repetition rate, size, operability, and maintainability of extreme-light laser, (2) sensitivity, resolution, and extended energy ranges of X-ray and particle detectors, (3) optical materials that can sustain long-term operation of optical and laser components at high-light-intensity and high-temperature conditions, and (4) fundamental understanding required to make the science breakthroughs that can drive revolutionary applications. As part of the natural evolution of extreme-light research, the scientific community has made great progress toward achieving the long-term goal. Indeed, this community has progressed to the point where some of the most far-reaching ideas in the vision, such as laser-generated radiation and particle inspection of gas turbines and their components, do not seem so far-fetched today. Our research group at AFRL has also made some contributions toward achieving this goal.

The Propulsion Directorate (now the Aerospace Systems Directorate) initiated an extreme-light diagnostics program with the goal of conducting research that would contribute to the long-term vision. The program was initiated without a laboratory, lasers, instrumentation, or experience; we had to build a new laboratory and gain the experience and capabilities necessary to conduct the research that is important to the development of extreme-light sources of radiation and particles. This program has been successful in several ways. It has provided us with the experience and opportunities to follow and gain a better understanding of the state-of-the-art of extreme-light research and be an advocate for the type of research that would support the long-term vision of the Air Force.

We have also made technical contributions to the field of laser/plasma interactions (LPI). Much of the literature involving LPI-generated X-rays reported only relative values of X-ray yields. In our first studies we quantified the bremsstrahlung and  $K\alpha$  yields for twelve metals [Rettig et al., 2008], which provided an extensive database for X-ray emissions from metals. We changed our studies from metals to liquid targets. Metal targets create considerable debris that can damage optical elements near the target. Because of the debris problem, we focused our research mainly on the study of water targets. We conducted pump-probe experiments to study the spatial and temporal evolution of plasma generated by a prepulse interacting with a water jet [Brown et al., 2011]. These measurements indicated rapid ionization in the transverse direction, presumably by hot electrons with initial velocities of 0.55 times the speed of light. In many ways this is an ideal target because it is readily available, benign, and can be mixed with many materials that have  $K\alpha$  emissions. However, a major problem is that its X-ray yield is about three orders of magnitude smaller than that for metals. We recently completed a unique study in which we were able to obtain a factor of 100 $\times$  increase in X-ray yield from a water jet using a combination of prepulse and chirp at a laser intensity of  $10^{16}$  W/cm<sup>2</sup> [Zhang et al., 2013]. We obtained a sufficient number of X-ray photons/s to perform various tasks; however, these photons were emitted in all directions.

An attractive aspect of bremsstrahlung emissions is the fact that the angular distribution becomes very peaked, typically in the forward direction (with respect to the motion of the electrons), if the electrons are initially at relativistic energies. Very recently, we conducted some preliminary experiments at relativistic conditions ( $I \approx 10^{18}$  W/cm<sup>2</sup>) to determine whether these conditions would impact the yield and directionality of the X-rays. We obtained very exciting results, observing an abundance of X-rays with energies that ranged from 2 to 800 keV--our maximum detection limit. The X-ray emissions were highly directional; but, to our surprise, the X-rays were emitted mainly in the direction opposite that of the incident light.

### **3.1 Extreme-Light Generation of X-rays**

X-ray generation can be placed in three broad categories, based on the interaction of electron with field: (1) acceleration by fields (Larmor/Thomson-type radiation), (2) broadband emission identified as bremsstrahlung radiation, where electrons inelastically scatter and decelerate by interacting with nuclear and atomic electric fields, and (3) line emission, usually  $\alpha_\alpha$  or  $K_\beta$  radiation, where the electron knocks off an inner-shell

electron. All of the accelerator and free-electron laser-based sources utilize field-accelerated electrons for coherent and incoherent X-ray emission, which--depending on the setup--can be broad or narrowband. Depending on the energy of the incident electrons into a dense material, bremsstrahlung can cover a range from a few electron-volts to tens of mega-electron-volts. Some of the incident electrons undergo elastic scattering in which the K-shell electrons are ejected from an atom. This results in a cascade process where L-shell and M-shell electrons transition to fill the vacancies left by the ionized K-shell electrons. The L-to-K and the M-to-K transitions give rise to K- $\alpha$  and K- $\beta$  lines, respectively. These lines are unique for each atomic species. The transition probability—and, thus, the intensity--of the K- $\alpha$  line is usually much higher than that of the K- $\beta$  line. The percentage of the electron energy converted to X-ray energy is called the X-ray conversion efficiency and can be as large as 15% [Petwal et al., 2007] in X-ray tubes.

Extremely intense laser pulses can also be used to produce bremsstrahlung and K $\alpha$  X-rays [Gibbon, 2005]. However, the processes for generating and accelerating free electrons are different from those in the X-ray tube but are similar for generating bremsstrahlung and K- $\alpha$  emissions. As the laser hits the target, electrons are ionized by multiple processes, depending on the laser intensity and target characteristics. The ionized or free electrons are accelerated by the electric field of the light pulse by processes such as resonance absorption,  $J \times B$ , inverse bremsstrahlung, Brunel heating, and wake-field acceleration and can achieve energies from a few kilo-electron volts to giga-electron volts, depending on the acceleration mechanism, intensity, and target density. The electrons are driven into the cold target and produce bremsstrahlung and K- $\alpha$  X-rays as they lose energy to the material. The initiation of the plasma by ionization of the target atoms and the subsequent acceleration of the electrons occurs during the laser pulse. The pulse width of the laser plus the stopping time of the electrons in the cold target determines the pulse width of the X-rays. LPI-generated X-ray pulse widths of a few hundred femtoseconds have been observed [Reich et al., 2000].

The conversion efficiencies for extreme-light-generated X-rays from solid targets can range from  $10^{-3}$  to  $10^{-7}$  for UV and XUV emissions and from  $10^{-5}$  to  $10^{-9}$  for hard X-rays [Hagedorn et al., 2003]. Extreme-light-generated X-rays have been used in different types of research, including studies of phase transitions [Siders et al., 1999; Rousse et al., 2001; Sokolowski et al., 2001], lattice dynamics [Silies et al., 2009], acoustic waves [Rose-Petruck et al., 1999; Bargheer et al., 2004], and optical phonons, [Sokolowski et al., 2003]. However, their practical and research utility is limited by the small conversion efficiencies and the resulting low yields (number of photons/s/sr/keV) that can be delivered to a specimen. It is the low yield that is the crux of the problem that was addressed in this program. Basically, the program goal was to determine the laser, target, and target environmental conditions that result in optimum X-ray yields for bremsstrahlung and K- $\alpha$  emissions.

The degree of ionization and the acceleration of the electrons are determined by the intensity of the laser. Assuming that the incident light is not tuned to a resonant electronic frequency of the target material, ionization can occur by several mechanisms: (1) multiphoton ionization (MPI), including above-threshold ionization (ATI), (2) semi-



classical tunneling ionization, and (3) impact or avalanche ionization. The particular path followed is determined by the cycle-averaged “ponderomotive” energy that is acquired by the electrons in the presence of the pulse. The ponderomotive potential,  $\Phi$  (or quiver energy), of an electron oscillating in the presence of the applied electric field of the light is directly proportional to the intensity of the light  $I$  and is expressed as

$$\Phi(\text{eV}) = 9.33 \times 10^{-14} \times I(\text{W/cm}^2) \times \lambda^2 (\mu\text{m}^2) = 1.23 \times 10^{-16} \times E^2 (\text{V/cm}) \times \lambda^2 (\mu\text{m}^2) \quad (1)$$

where  $\lambda$  denotes the central wavelength expressed in micrometers [Perry and Mourou, 1994]. During MPI, which can occur at intensities as low as  $10^{10} \text{ W/cm}^2$ , a bound electron receives sufficient energy from interactions with multiple photons to be ionized. The probability of MPI is highest with ultrashort-pulse lasers because of the very large photon density. As the intensity increases, the electric field of the light can modify the Coulomb potential of the electron in a way that increases the probability of the electron being able to tunnel through the potential barrier. This process is called tunneling ionization [Popov et al., 1968]. How electrons are ionized in a strong light field may be determined by the [Keldysh, 1965] parameter  $Y = \text{laser frequency/tunneling frequency}$ , where tunneling frequency is denoted by  $F/\sqrt{2I_p}$ , with  $I_p$  being the ionization potential of the bound electron. A  $Y \geq 1$  points to MPI, whereas,  $Y \ll 1$  corresponds to tunneling ionization. Once ionization occurs, the electrons driven by the oscillating large electric field of the light collide with and knock out bound electrons. This can cause an avalanche effect that leads to a rapid increase in free electrons. Regardless of the nature of the ionization event, once the electron is ionized, it remains under the influence of the laser pulse and is accelerated by its electric field. The laser energy is damped since the coupled free-electron energy can be converted into thermal energy by colliding with ions via inverse bremsstrahlung (collision heating) and other mechanisms [Brunel, 1987]. As laser-driven electrons collide with ions, secondary radiation emission--most notably X-ray emission--is produced from bremsstrahlung and shell transitions.

K $\alpha$  emission results from a two-step process that begins with a hot free electron colliding with an atom and knocking out an inner K-shell electron. An L-shell electron quickly fills the vacancy, emitting the species-characteristic K- $\alpha$  X-ray line. The cross sections for K-shell ionization of elemental materials typically peak at an energy which is three times that of the minimum ionization energy [Hombourger, 1998]. Hence, maximizing the K- $\alpha$  X-ray yield relies, in part, on tailoring the energy of the hot free electrons that are produced during plasma initiation. To date most of the research performed on K $\alpha$  radiation from laser-generated plasmas has employed solid targets--especially metal foils. Liquid droplets and streams have also been examined--particularly for soft X-ray and EUV (extreme-ultraviolet) energies that are appropriate for biomedical imaging and lithography. Stable elemental materials have characteristic K- $\alpha$  lines ranging from 54.3 eV for Li to 98.4 keV for U.

X-ray yields depend strongly on the laser, target, environmental characteristics, and methodology used to optimize the yield. Important laser parameters are energy, peak intensity, pulse width, chirp, angle of incidence, polarization, focus quality, focus location, focal-spot size, and prepulse characteristics. The yield also depends on target

characteristics such as composition, physical state, size, geometry, and surface structure. The environment of the target--vacuum pressure, wall confinement, buffer gas, and temperature--is also important. In [Uryupina et al., 2012] many studies are identified where the impact of these parameters on X-ray yield has been investigated. The methodology for optimizing the yield is also very important, as demonstrated by Lu, et al. [2009]. Thus, many parameters and procedures can impact X-ray yields, which creates several experimental and computational challenges. For example, sufficient control of a large number of parameters is necessary if repeatable experimental results are to be obtained. Also, the optimization process can be complicated because accounting for all of the parameters of the large parameter space becomes a near-impossible task.

While all laser-based X-ray generation begins with ionization, the subsequent electron dynamics are dictated by the above parameters. The details of these temporally and spatially evolving dynamic processes are responsible for the X-ray yield. The technical challenge is to address the large parameter space in such a way that critical laser-matter interaction processes can be identified and understood in sufficient detail to permit laser and target parameters to be optimized for maximum X-ray yield.

### **3.2 Laser System and Facility Development**

This program began with an empty laboratory, no equipment, and no capability to conduct femtosecond/laser interaction studies as related to X-ray emissions. During the course of the program, the capabilities have expanded to the point where the laboratory has become a world-class facility for conducting this type of research. This is illustrated by the following comment made by a recent technical reviewer of this program. "Their laboratory is one of the few laboratory facilities in existence today in which this type of research can be conducted." The following is an overview of the laser system and its capabilities.

To extend the range of our experiments and to provide greater experimental flexibility, a unique coupled laser system has been developed. This system electronically and optically couples three lasers so that the main and prepulse parameters can be independently varied. The coupled laser system can also be used to visualize the prepulse/main-pulse interactions during the time when x-ray measurements are being made. The main pulse and prepulse energies can be increase up to 12 mJ and 1 mJ, respectively. The electronic delay times can be continuously varied from 30 fs to 900 fs and with a 30-fs resolution up to a 10-ns delay and with a 4-ps resolution up to a 900- $\mu$ s delay. Also, the pulse widths and chirp can be independently controlled from 30 fs to more than 300 fs. Moreover, we can use one laser as a probe in a pump-probe experiment while still utilizing the other two as the main pulse and the prepulse lasers.

**Table 1. Characteristics of the coupled three lasers**

Laser 1.	Laser 2.	Laser 3.
KMLabs, Red Dragon (Ti:Sapphire)	Coherent, Legend (Ti:Sapphire)	Spectra Physics, Quanta-Ray GCR4 (YAG)
Wavelength: 800 nm	Wavelength: 800nm	Wavelength: 1064, 532, or 355nm
Repetition Rate: 1 kHz	Repetition Rate Range: 1 kHz	Repetition Rate Range: 1-10 Hz
Output Pulsewidth: 30-310 fs	Output Pulsewidth Range: 40-300 fs	Output Pulsewidth Range: 10 ns
Output Energy: up to 12 mJ	Output Energy: up to 1.25 mJ @ 355 nm	Output Energy: 700mJ @ 1064 nm, 300 mJ @ 532 nm, 200 mJ @ 355 nm

Detailed characteristics of the three coupled lasers used in the laser/target studies are given in Table 1. They consist of a kilohertz repetition rate, 12-mJ/pulse, and 30-fs pulse-width Red Dragon laser system (KM Labs) operating at 800-nm center wavelength. A Coherent Legend, operating at 1 kHz with 1-mJ energy/pulse and a pulse width of 40 fs, is electronically coupled by a lock-to-clock with the Red Dragon. The timing between the pulses of the two lasers can be controlled electronically within  $\pm 1$  ps from 2 ps to  $\approx 1$  ms. The two lasers can also be coupled by an optical delay line. In this case the uncertainty in timing between the pulses from the two lasers is about 30 fs, covering a range from 30 fs to about 3 ns. Thus, this coupled system allows prepulse-main pulse or pump-probe measurements with independent control of the energy, intensity, polarization, wavelength, chirp/pulse width, and timing of the two lasers. There is also a nanosecond Nd:YAG laser synchronized with the two short-pulse laser systems. The schematic of the laser system is shown in Figure 4.

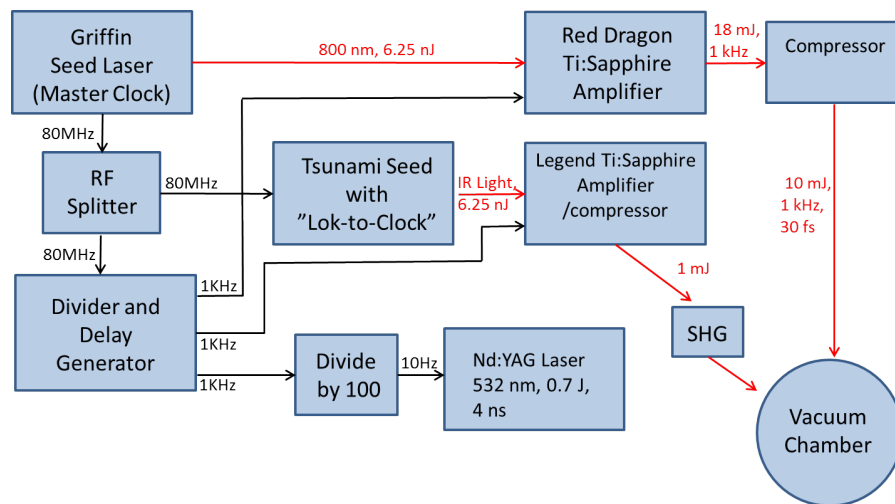
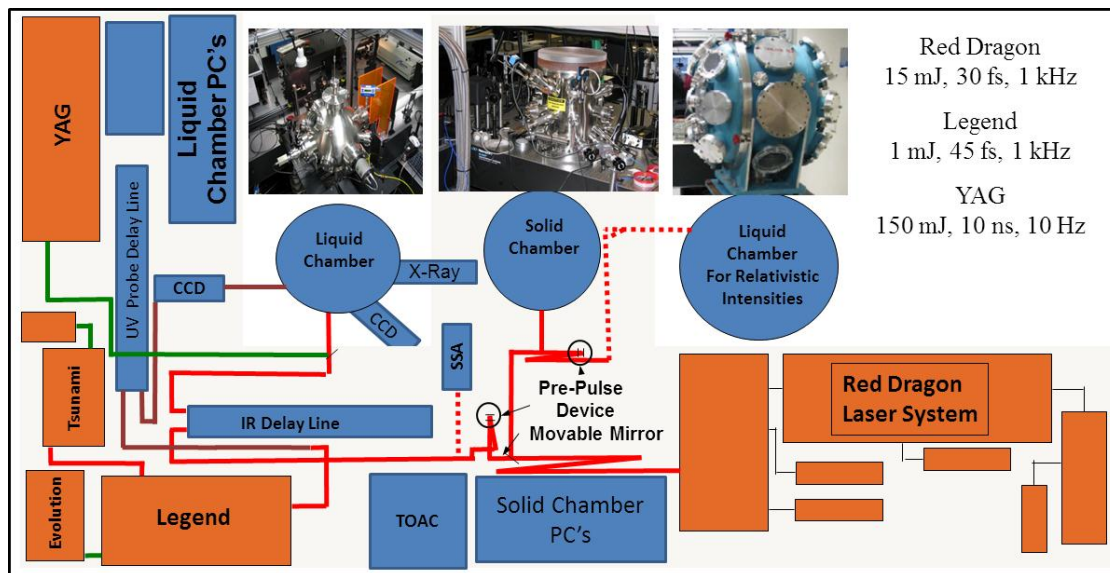


**Figure 4. Schematic of the laser system developed for studies of extreme-light/target-interaction studies**

The laboratory is equipped with three large high-vacuum chambers, two of which are spherical/spheroidal in shape. The larger chamber is about 60 cm in diameter, and the

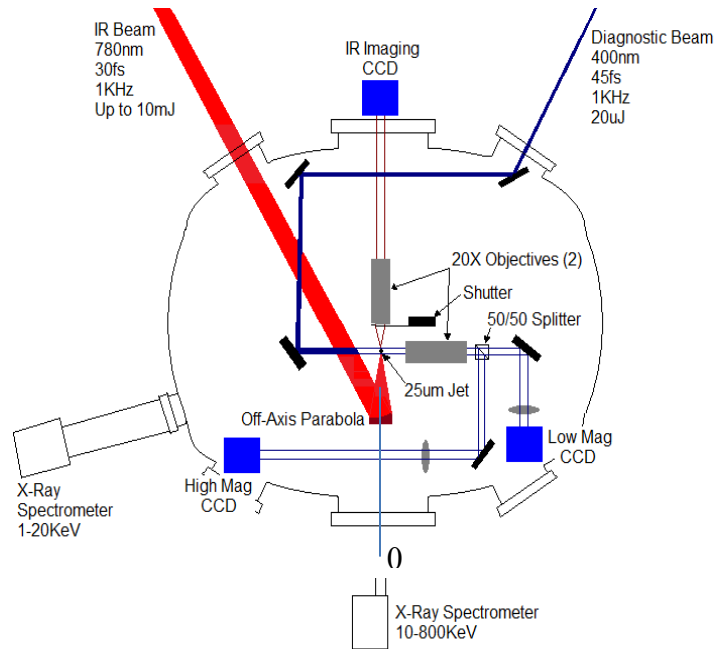
smaller chamber is 30 cm in diameter. These two chambers are set up with a state-of-the-art liquid-target delivery system involving a sophisticated syringe pump that can be operated in a constant-pressure or a constant-flow-rate mode. This system allows the use of off-the-shelf capillaries to produce stable liquid-jet targets down to about 20  $\mu\text{m}$  in diameter. Efforts are underway to reduce the diameter of the target and also change it to a sheet-like target for studying the polarization dependence of LPI with a liquid target. This capability along with the laser system makes the extreme-light laboratory unique among intense-laser laboratories in the U.S.

Figure 5 shows the layout of the coupled laser system along with the three target chambers used to study laser/target interactions. The spherical-shaped chamber shown on the left in Figure 5 was used to study liquid targets at laser intensities below  $10^{18} \text{ W/cm}^2$ . The large spheroidal vacuum chamber on the right in Figure 5 was used to study laser/liquid target interactions at relativistic laser intensities with intensities of  $10^{18} \text{ W/cm}^2$  and higher. Such studies required a large chamber to accommodate a sophisticated optical system, as illustrated in Fig. 6. The optical system installed in this chamber permitted focusing of the beam to an  $\sim 2.6\text{-}\mu\text{m}$ -diameter spot with focal-spot diagnostics. The optical system utilizes the coupled laser system and has an orthogonal imaging system during target alignment that allows location of the focus position on the target within  $< 2\mu\text{m}$ . The tight focus allowed intensities of  $10^{18} \text{ W/cm}^2$  and higher to be achieved.

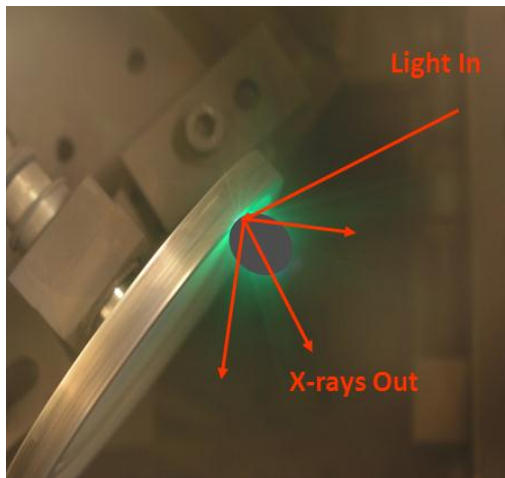


**Figure 5. Layout of developed laser system and test chambers**

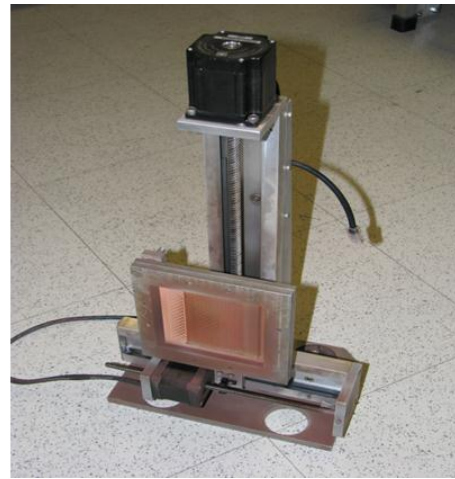
The cylindrical chamber shown in Figure 5 was used for studying solid targets. The solid targets had to be moved so that adjacent laser pulses would hit a new target location during each laser shot. The two different types of devices used to move the solid targets are shown in Figure 7. The first device rotated the target, and the second had a three-axis stage for moving precision metal targets rapidly.



**Figure 6. Target-chamber schematic for studying laser/liquid-target interactions at relativistic laser intensities**



(a)



(b)

**Figure 7. Rotational devices (a) and three-axis translator (b) used to move the metal targets so that no two laser shots would hit the same spot on the target**

Some of the important equations for laser parameters used in this report are given below. Table 2 displays a range of calculated laser parameters for the Red Dragon laser using Eqs. (1) – (7) for variation in laser energy and focal-spot diameter.

Quantity	Symbol	Unit
Pulse energy	$E_{pulse}$	J
Pulse width	$\tau$	s
Repetition rate	$f$	Hz
Wavelength	$\lambda$	cm
Spot size	$D$	cm
Planck's constant ( $6.626 \times 10^{-34}$ )	$h$	J*s
Speed of light ( $3.0 \times 10^{10}$ )	$c$	cm/s

$$P_{peak}(W) = \text{laser peak power} = \frac{E_{pulse}}{\tau} \quad (2)$$

$$P_{avg}(W) = \text{laser average power} = E_{pulse} \times f \quad (3)$$

$$I(W/cm^2) = \text{laser intensity} = \frac{E_{pulse}}{\tau \pi \left(\frac{D}{2}\right)^2} \quad (4)$$

$$\mathcal{E}(V/cm) = \text{laser electric field} = 27.5 \sqrt{I} \quad (5)$$

$$N_{pulse} = \text{number of photons per pulse} = \frac{E_{pulse}}{h \frac{c}{\lambda}} \quad (6)$$

$$N = \text{number of photons per second} = N_{pulse} \times f \quad (7)$$

**Table 2. Calculated laser parameters for Red Dragon Laser using Eqs. (1) – (7)**

Laser	pulse energy mJ	pulse width fs	rep rate Hz	wavelength microns	spot size microns	peak power Watts	avg power Watts	Intensity W/cm <sup>2</sup>	E-field V/cm	# photons/pulse
KMLabs, Red Dragon	12.0	30	1000	0.8	35.0	4.00E+11	12.0	4.16E+16	5.60E+09	4.85E+16
KMLabs, Red Dragon	3.0	30	1000	0.8	35.0	1.00E+11	3.0	1.04E+16	2.80E+09	1.21E+16
KMLabs, Red Dragon	1.0	30	1000	0.8	35.0	3.33E+10	1.0	3.46E+15	1.62E+09	4.04E+15
KMLabs, Red Dragon	12.0	30	1000	0.8	2.5	4.00E+11	12.0	8.15E+18	7.84E+10	4.85E+16
KMLabs, Red Dragon	3.0	30	1000	0.8	2.5	1.00E+11	3.0	2.04E+18	3.92E+10	1.21E+16
KMLabs, Red Dragon	1.0	30	1000	0.8	2.5	3.33E+10	1.0	6.79E+17	2.26E+10	4.04E+15
KMLabs, Red Dragon	12.0	30	1000	0.8	1.0	4.00E+11	12.0	5.09E+19	1.96E+11	4.85E+16
KMLabs, Red Dragon	3.0	30	1000	0.8	1.0	1.00E+11	3.0	1.27E+19	9.80E+10	1.21E+16
KMLabs, Red Dragon	1.0	30	1000	0.8	1.0	3.33E+10	1.0	4.24E+18	5.66E+10	4.04E+15

Note in Table 2 that the Red Dragon with a tight focus can reach relativistic intensities of  $10^{18}$  W/cm<sup>2</sup> and greater. Most of the experiments conducted during this program were for intensities below  $10^{17}$  W/cm<sup>2</sup>; but near the end of the program, some experiments were at an intensity of about  $10^{18}$  W/cm<sup>2</sup>. The results from all of these experiments are presented in this report.

### 3.3 X-ray Generation from Laser/Metal-Target Interactions

Metal targets tend to have the highest X-ray yields because of their high density. Considerable data have been collected on the relative X-ray emissions observed for different laser conditions. However, when this contract began, very few studies had been performed where quantitative data on X-ray yields and efficiencies were obtained. Thus, the first study performed on this program involved obtaining quantitative data on X-ray emissions. The study employed the Legend shown in Figure 5, whose characteristics are given in Table 1. Thin metal foils were mounted on the rotating device shown in Figure 7(a). The rotating device was mounted in the metal-target chamber shown in Figure 5. The laser was focused to a spot size of 35  $\mu$ m full width half maximum (FWHM), and the calculated laser intensity was  $4.2 \times 10^{15}$  W/cm<sup>2</sup>. The X-ray emissions were measured with an AMP TEK XR100 photon-counting spectrometer. Details of this study can be found in Rettig, et al. [2008]; note that the spot width and laser intensity are as given in this report. A copy of this paper is included in the Appendix of this report. The following contains background on what occurs when a femtosecond laser interacts with a metal target to generate X-rays.

An outline of the method for obtaining quantitative results for the X-ray yield and conversion efficiency is given below.

$\Sigma$  means summation over energy:

E = X-ray energy in keV

N(E) = raw number of X-rays detected at energy E over total temporal integration period

$\eta(E)$  = detector efficiency at energy E

NC(E) = N(E)/ $\eta(E)$ ; corrected number of detected X-rays at energy E

$A_{\text{hemi}}$  = area of hemisphere with radius equal to the target-to-detector distance (cm<sup>2</sup>)

$A_{\text{det}}$  = collection area of detector defined by aperture (cm<sup>2</sup>)

T = integration time (s)

Y(E) = X-ray yield at energy E (X-rays/s/4 $\pi$  sr at energy E)

$Y(E) = [NC(E)/T] \times [A_{\text{hemi}}/A_{\text{det}}]$

$Y_{\text{tot}}$  = total X-ray yield summed over all energies (X-rays/s/4 $\pi$  sr)

$$Y_{\text{tot}} = \Sigma (Y(E))$$

CE = conversion efficiency = total energy of emitted X-rays/total input laser energy

P = input laser power (W)

$$CE = \Sigma [Y(E) \times E \times 1000 \text{ (eV/keV)} \times 1.60 \times 10^{-19} \text{ (J/eV)}] / [P(W) \times T(s)]$$

The values for  $A_{\text{hemi}}$  and  $A_{\text{det}}$  were measured for the given experimental setup. The detector efficiency at energy E,  $\eta(E)$ , was supplied by the manufacturer of the detector.  $N(E)$  and T were determined from the experiment; and  $NC(E)$ ,  $Y(E)$ , and  $Y_{\text{tot}}$  were calculated using the formulas above and the measured results.

When a laser pulse is focused to sufficiently high intensity on a metallic target, X-rays are generated through a multi-step process. First, incident radiation ionizes the surface into a near-solid-density plasma. The absorption mechanism of the laser energy into the plasma varies somewhat with intensity but always proceeds through the electron channel. Since typical target surfaces are initially highly conductive, absorption occurs within a skin depth, with the skin depth shrinking rapidly within the first several cycles of the laser light. The partition of the laser energy into the hot thermal and/or nonthermal electrons determines the efficiency with which the laser energy is converted into hot electron energy and especially how efficiently the electron energy is subsequently converted into X-rays. At a modest laser intensity ( $< 10^{15} \text{ W/cm}^2$ ), almost all of the absorbed laser energy transfers through collisional processes such as inverse bremsstrahlung; at higher intensity absorption occurs through collisionless processes, including resonance absorption and the anomalous skin effect [Rozmus and Tikhonchuk, 1990]. A hot-electron distribution is created with effective temperature in the range 1-5 keV, possibly including a nonthermal component at higher energy [Rozmus and Tikhonchuk, 1996]. Finally, energetic electrons, incident on the metallic target, lose energy via collisions within the substrate, slowing down within a mean-free path of the surface. High-energy thermal and nonthermal electrons generate both continuum (bremsstrahlung) radiation through scattering events and characteristic (line) radiation by ionizing inner-shell electrons of target atoms. Both processes are analogous to X-ray generation in conventional X-ray tubes.

Emission originates from a spot size characterized by the laser focus convolved with the electron mean free path in the solid. The temporal pulse length is characterized by the slowing-down time in the substrate and the dynamics of re-absorption [Feurer et al., 2001]. Thus, at least three unique characteristics of the radiation from such an X-ray source are possible: (1) very short pulse length,  $< 1 \text{ ps}$  [Feurer et al., 2001], (2) very small spot size, on the order of  $10 \text{ }\mu\text{m}$  or less (which translates to high spatial coherence), and (3) very high instantaneous brightness, due to the high incident energy density. A short X-ray pulse length has enabled studies of phase transitions [Rousse et al., 2001] and chemical-reaction dynamics [Jiang et al., 2001], while a small source size allowed high-



spatial-resolution imaging and phase-contrast imaging to be utilized to achieve enhanced image fidelity for a given X-ray yield [Boschetto et al., 2007]. Efforts to improve efficiency for the overall conversion to X-rays concentrate on the absorption of the laser energy since conversion from electron energy to X-rays leaves very little to chance.

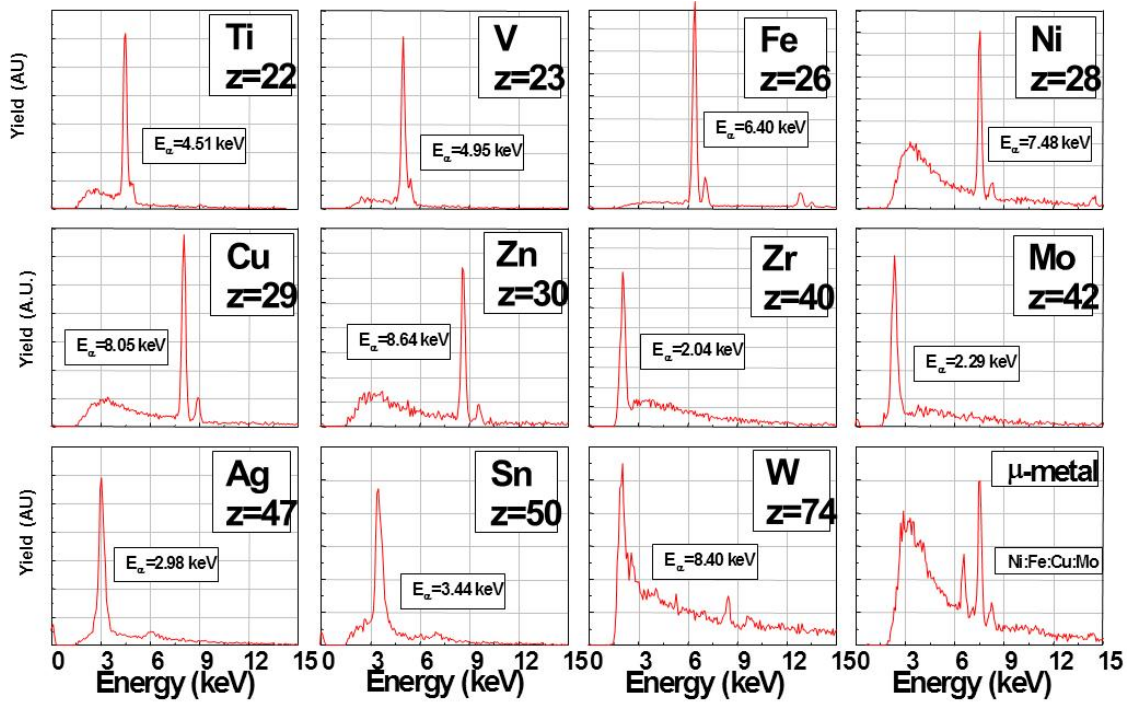


**Figure 8. X-ray spectra obtained from laser/metal interactions**

The spectra for 12 different metal targets are given in Figure 8. The sharp  $K\alpha$  lines characteristic of each of the metals are evident in these spectra. The spectra were analyzed to obtain the X-ray yields and the efficiencies given in Table 2. These data are thought to be from the most comprehensive quantitative study conducted on metals to date.

It is evident that the variations in X-ray yield for the different metals are not large. The average bremsstrahlung yields varied from  $4.8 \times 10^{10}$  for Ti to  $1.3 \times 10^{10}$  photons/s/2 $\pi$  sr for Ni. Thus, the maximum and minimum yields varied by less than a factor of four. The  $K\alpha$  varied from  $2.7 \times 10^{10}$  for Ti to  $3.6 \times 10^9$  photons/s/2 $\pi$  sr for Ni, which is a variation of 7.5. Electron temperatures varied between 3 and 6 keV.

The impact of a prepulse on X-ray emissions for a Ti target is shown in Figure 9. The prepulse was formed by splitting the main laser beam into two beams, with an 80/20% difference in intensity. The 20% beam was passed through an optical delay line and then focused along with the 80% beam on the Ti target. The X-ray conversion efficiency was determined for different delay times, as shown in Figure 9. As noted, the prepulse increased the conversion efficiency by a factor of three compared to the efficiency without a prepulse. The impact of prepulse on the X-ray yield will be important part of this program, as will be described later in this report.

**Table 3. The X-ray yields and conversion efficiencies (CE) for bremsstrahlung (broad band BB) and  $K\alpha$  X-ray emissions for twelve metals**

element	Z	BB Yield (Ph/sec/2p Sr)	BB CE	Eph	Ka (La) Yield (ph/sec/2p Sr)	Ka (La) CE	Peak $T_e$ (keV)	data set
Ti	22	$4.8 \times 10^{10}$	$2.4 \times 10^{-5}$	4.5	$2.7 \times 10^{10}$	$1.1 \times 10^{-5}$		84
V	23	$2.3 \times 10^{10}$	$1.3 \times 10^{-5}$	4.95	$1.1 \times 10^{10}$	$4.9 \times 10^{-6}$	4.9	68
Fe	26	$4.7 \times 10^{10}$	$2.3 \times 10^{-5}$	6.41	$1.5 \times 10^{10}$	$8.6 \times 10^{-6}$		114, 88
Ni	28	$1.3 \times 10^{10}$	$4.3 \times 10^{-6}$	7.48	$3.6 \times 10^9$	$2.4 \times 10^{-6}$	3.1	108, 106
Cu	29	$1.9 \times 10^{10}$	$1.4 \times 10^{-5}$	8.05	$6.5 \times 10^9$	$4.6 \times 10^{-6}$	4.4	99
Zn	30	$1.8 \times 10^{10}$	$1.3 \times 10^{-5}$	8.64	$4.1 \times 10^9$	$3.1 \times 10^{-6}$	5.9	37
Zr	40	$2.5 \times 10^{10}$	$1.4 \times 10^{-5}$	2.01 ( $L_a$ )	$5.2 \times 10^9$	$9.5 \times 10^{-7}$		30
Mo	42	$3.3 \times 10^{10}$	$1.5 \times 10^{-5}$	2.29 ( $L_a$ )	$9.8 \times 10^9$	$2.0 \times 10^{-6}$		93
Ag	47	$9.6 \times 10^9$	$3.7 \times 10^{-6}$	3.0 ( $L_a$ )	$3.0 \times 10^9$	$8.2 \times 10^{-7}$		56
Sn	50	$2.2 \times 10^{10}$	$1.1 \times 10^{-5}$	3.44 ( $L_a$ )	$4.1 \times 10^9$	$1.3 \times 10^{-6}$	4.9	111, 78
W	74	$2.6 \times 10^{10}$	$1.4 \times 10^{-5}$	8.4 ( $L_a$ )	$1.5 \times 10^9$	$1.1 \times 10^{-6}$	4.1	41

(An estimate of the electron temperatures using the decay of the bremsstrahlung emission spectra is also presented)

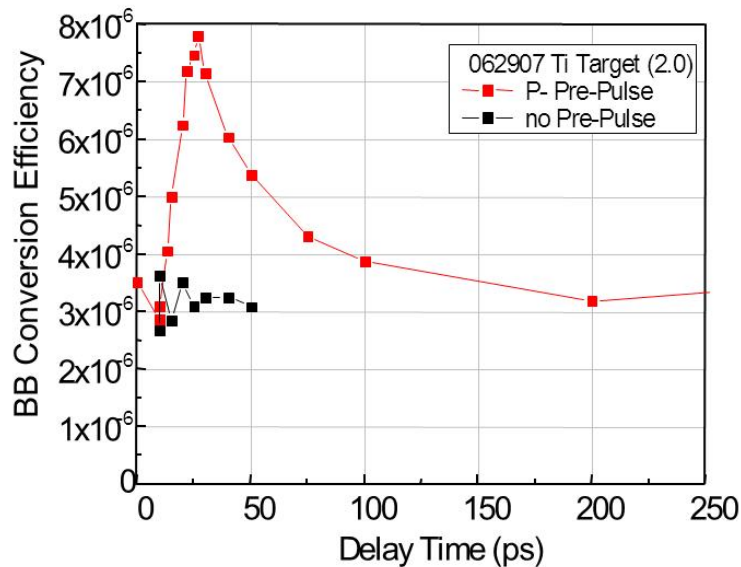


**Figure 9. The impact of a prepulse delay time on the conversion efficiency of the bremsstrahlung X-ray emission from a Ti target**

It is evident that the variations in X-ray yield for the different metals are not large. The average bremsstrahlung yields varied from  $4.8 \times 10^{10}$  for Ti to  $1.3 \times 10^{10}$  photons/s/2 $\pi$  sr

for Ni. Thus, the maximum and minimum yields varied by less than a factor of four. The  $K\alpha$  varied from  $2.7 \times 10^{10}$  for Ti to  $3.6 \times 10^9$  photons/s/ $2\pi$  sr for Ni, which is a variation of 7.5. Electron temperatures varied between 3 and 6 keV. As noted in Figure 10, the X-ray emissions from tin are sufficient to obtain an X-ray image of a circuit board.

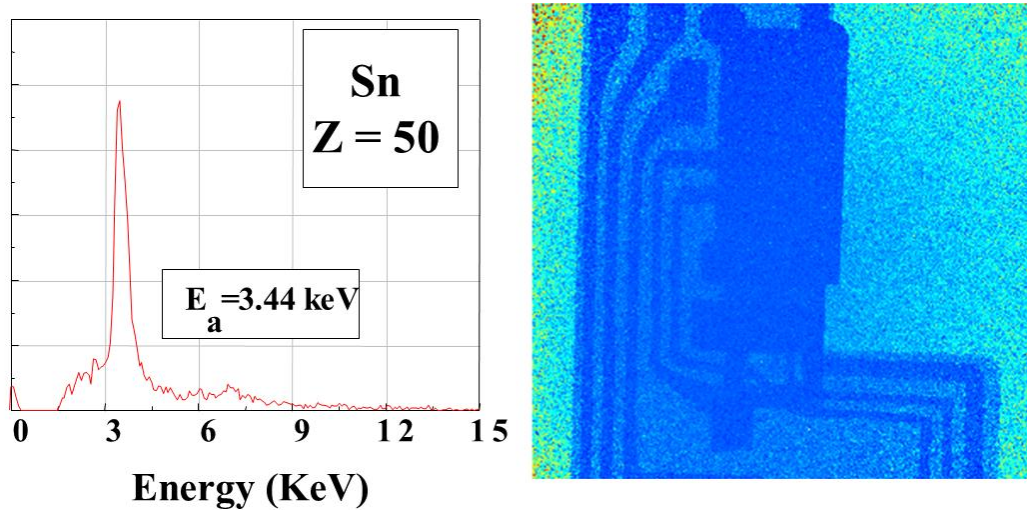


**Figure 10. X-ray image of a circuit board made with the 3.4-keV  $K\alpha$  radiation from tin**

*(The exposure time was about 2 s.)*

The Red Dragon laser was purchased with the expectation that we could achieve much higher X-ray yields and conversion efficiencies from metal targets than those shown in Table 3 because the energy of this laser was more than 12 times that of the Legend. However, the first experiments with the Red Dragon demonstrated this was not the case.

Figure 11 compares the conversion efficiency of the Legend and the Red Dragon for a Cu target. Note that the X-ray conversion efficiency for both the Legend and the Red Dragon increased with laser intensity; however, the efficiency for the Legend was about a factor of 10 larger than that for the Red Dragon. It took a considerable amount of time to understand why the absolute X-ray yields for the Red Dragon were so much smaller than those for the Legend. The cause of the problem and the solution are presented in Section 3.6. As this problem was being addressed, studies were conducted to investigate the impact of laser intensity and energy on X-ray yield. These studies are described in the next section.

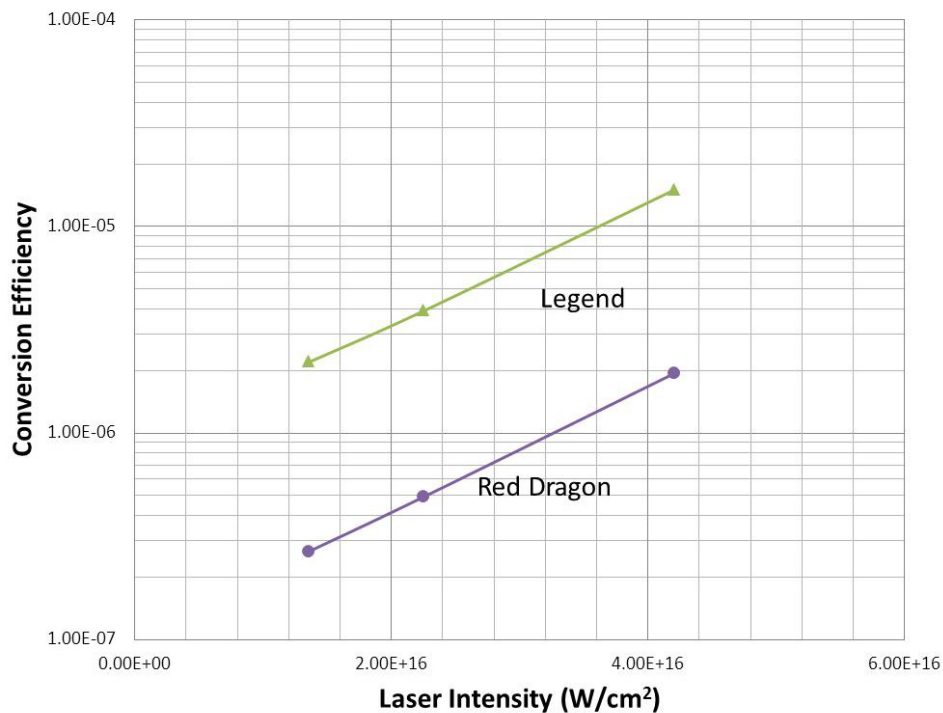


**Figure 11. Comparison of CE for bremsstrahlung emission from Cu using the Legend and the Red Dragon**

### 3.4 X-ray Generation from Laser/Dielectric-Target Interactions

Studies were undertaken to investigate laser interactions with both solid and liquid dielectric targets. The Red Dragon laser was used in these studies. The laser parameters varied were laser intensity and pulse width. P-polarization and an angle of incidence of 45° were fixed for the solid targets. Also, a Cu target was included in the study to permit metal and dielectric results to be compared. The solid targets were mounted on the three-axis translator shown in Figure 7(b). This translator was located inside the metal-target chamber, as shown in Figure 12. The target was moved in such a way that each laser firing hit a new target area. Also, the direction of travel was such that it almost eliminated the fall of debris from laser ablation, preventing it from covering the target area that would receive the next laser pulse. Also shown in Figure 12 is the X-ray spectrometer and cameras for monitoring the target during the experiments.

The experiment with the Cu and dielectric targets was conducted to investigate the sensitivity of the bremsstrahlung X-ray yield to pulse width, with laser intensity and laser energy being varied systematically. Changes in laser pulse width also changed the chirp of the laser, but this was taken into account by fixing the direction of the chirp. Later in the report, the impact of chirp will be explored in detail. The experiments were first conducted with the laser energy fixed at 2.5 mJ, and the laser intensity changed as the pulse width was changed. In the second experiment, the calculated laser intensity was fixed at a calculated value of  $3.6 \times 10^{14} \text{ W/cm}^2$ , and the laser energy changed as the pulse width changed.

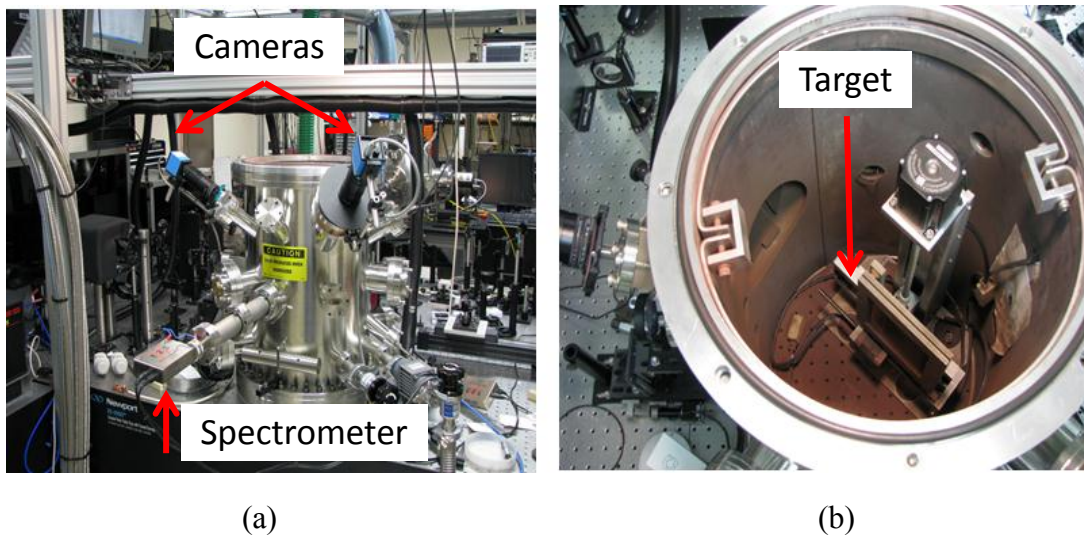


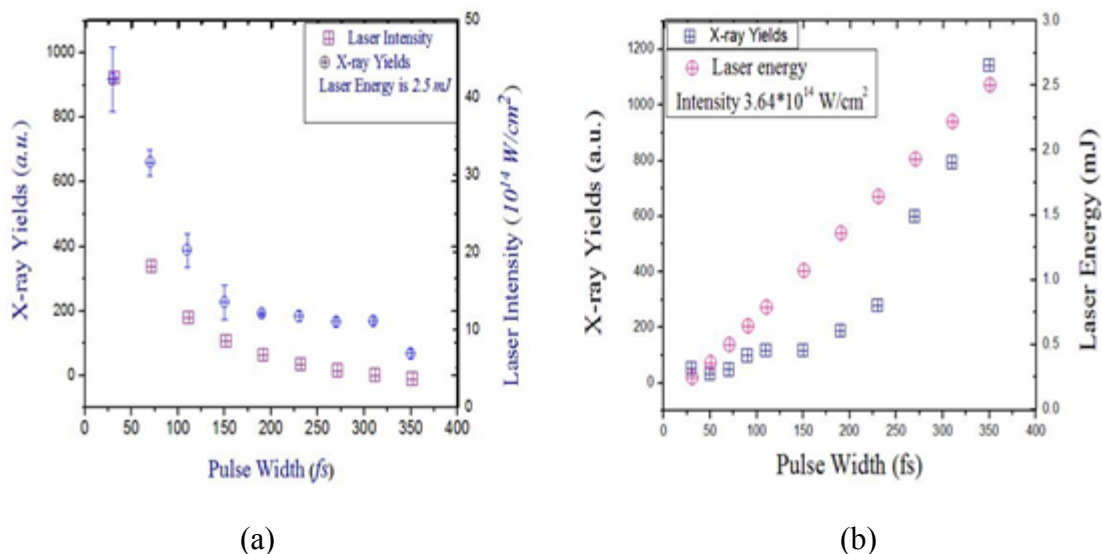
**Figure 12. Metal-target chamber**

*(Photos show the X-ray spectrometer and cameras for monitoring the target during operation (a) and the three-axis translation stage mounted in the chamber (b))*

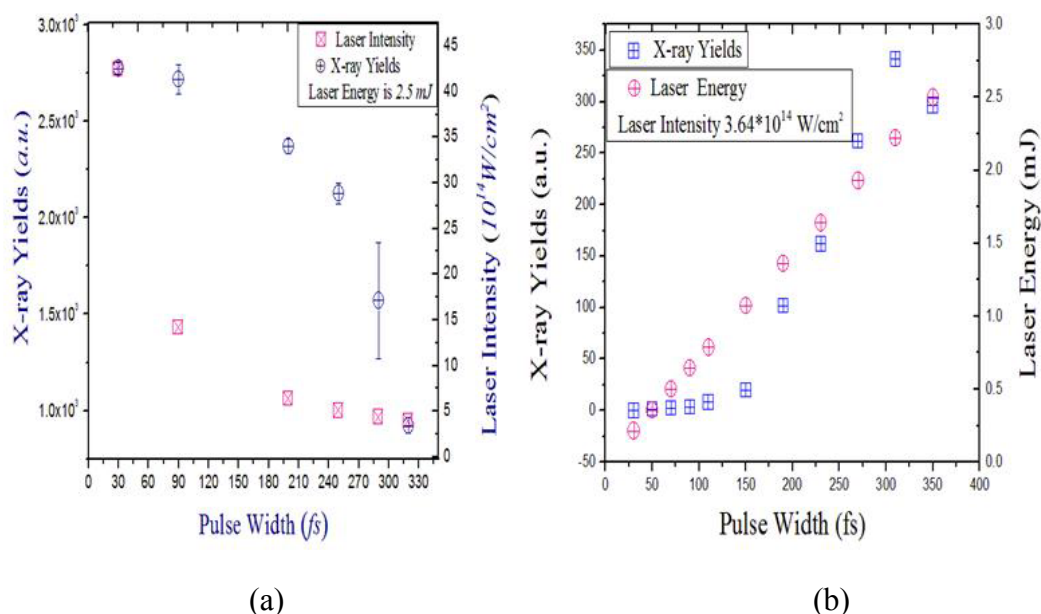
Figure 13 shows how the X-ray yield changed for a Cu target when the pulse width was changed. In Figure 13(a) the laser energy is fixed such that the intensity decreases with pulse width, as expected from Eq. (4). The laser is p-polarized. As the pulse width increases and the intensity decreases, the X-ray yield decreases. This type of behavior is expected from the Figure 10 results. In Figure 13(b), the intensity ( $I$ ) is fixed and the energy ( $E$ ) must increase in accordance with Eq. (4) with the pulse rate. In this case the X-ray yield increases with laser energy. Thus, the X-ray yield depends not only on the intensity but also on the laser energy. The results in Figure 13 are what one would expect for laser interaction with a metal target.

Figure 14(a) shows the impact of laser pulse width, at constant  $E$  and constant  $I$  [Figure 14(b)], on X-ray yield for a glass target. A comparison of Figure 13 for metal and Figure 14 for glass shows that the X-ray yield decreases relatively slowly for glass as the pulse width is increased, whereas the decrease in laser intensity is very rapid for pulse widths between 30 and 200 fs. The X-ray yield for constant laser intensity for glass and metal is also different. At a pulse width of about 150 fs, the X-ray yield at constant  $E$  for the glass target begins to increase dramatically. These results are different from what one would expect. The results become even more interesting for liquid targets.





**Figure 13. X-ray yield and laser intensity vs. pulse width (positive chirp)**  
(for a Cu target (a) for energy fixed at 2.5 mJ and (b) intensity fixed at  $3.6 \times 10^{14} \text{ W/cm}^2$ . The laser energy in (b) has been multiplied by 10; therefore, a reading of 10 on the right y-axis is 1.0 mJ. The laser is p-polarized.)

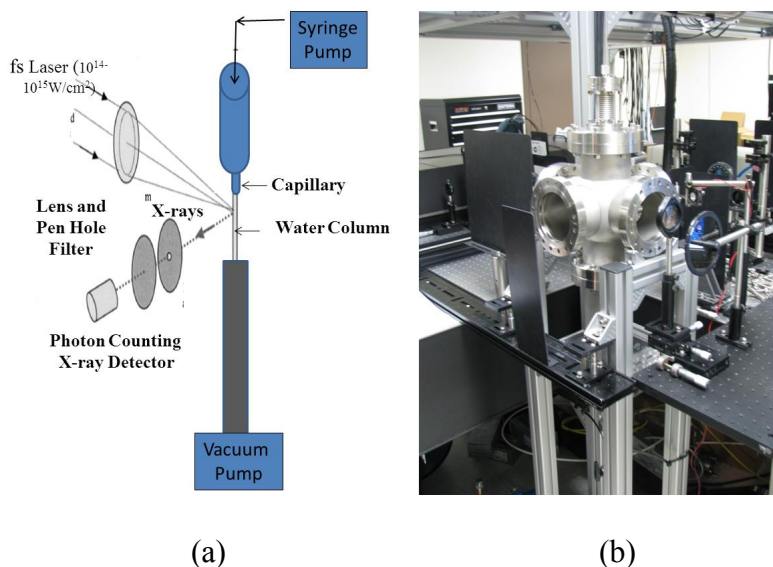


**Figure 14. X-ray yield and laser intensity vs. pulse width (positive chirp) for a glass target**

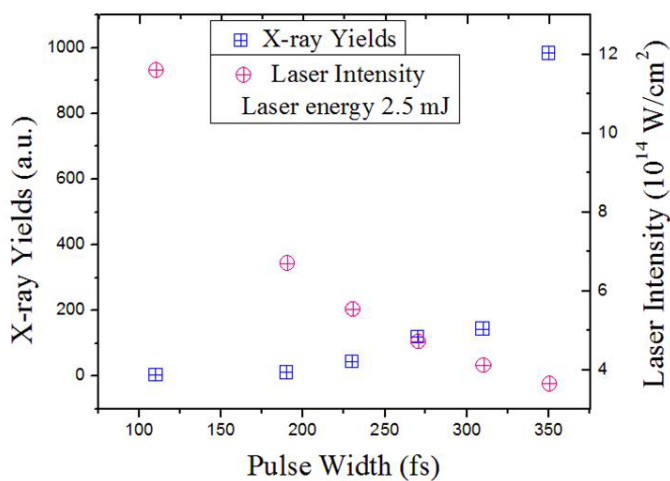
((a) for energy fixed at 2.5 mJ and (b) intensity fixed at  $3.6 \times 10^{14} \text{ W/cm}^2$ . The laser energy in (b) has been multiplied by 10; therefore, a reading of 10 on the right y-axis is 1.0 mJ. The laser is p-polarized.)

Figure 15(a) illustrates the experimental setup for generating a 50- $\mu\text{m}$ -diameter liquid jet, and Figure 15(b) is a photograph of a small liquid-target chamber used in these

experiments. A capillary with a 50- $\mu\text{m}$  inside diameter was used to create the liquid jet. The liquid was forced through the capillary using a syringe pump operated in the constant pressure mode. The X-ray spectrometer was located 90° from the incoming laser. The small liquid-target chamber, which was about 15 cm in diameter, was used to obtain the results for the menthol and water-jet targets shown in Figures 16 and 17. All other liquid-target experiments employed the liquid-target chamber shown in Figure 5.



**Figure 15. Schematic of experimental setup for investigating X-ray yield and laser intensity vs. pulse width (positive chirp) for liquid targets using the Red Dragon laser**



**Figure 16. X-ray yield and laser intensity vs. pulse width (positive chirp) for a 50- $\mu\text{m}$ -diameter menthol-jet target for energy fixed at 2.5 mJ**  
(The laser is *p*-polarized.)

Figure 16 shows the dependence of X-ray yield and laser intensity on pulse width for a 50- $\mu\text{m}$ -diameter liquid-menthol-jet target. Note that the X-ray yield increases slowly until the pulse width reaches about 300 fs; then a very large increase occurs. This increase in

yield is occurring as the laser intensity is decreasing. Again, the inverse relationship between X-ray yield and laser intensity is completely opposite from what would be expected, based on X-ray emissions from metal targets. This same trend is also reflected in the water-target results.

Because the X-ray yields in Figures 16 and 17(a) are relative yields, one cannot judge the difference in magnitudes of the X-ray yields of the methanol and water targets. Experiments were performed to determine the magnitudes of the X-ray yields of methanol and water. The results are shown in Figure 18. It should be noted that the X-ray yield from the water-jet target is about an order of magnitude larger than that from the methanol target, as shown in Figure 18(a). This difference in X-ray yield is also shown by the relative magnitudes of the X-ray spectra in Figure 18(b).

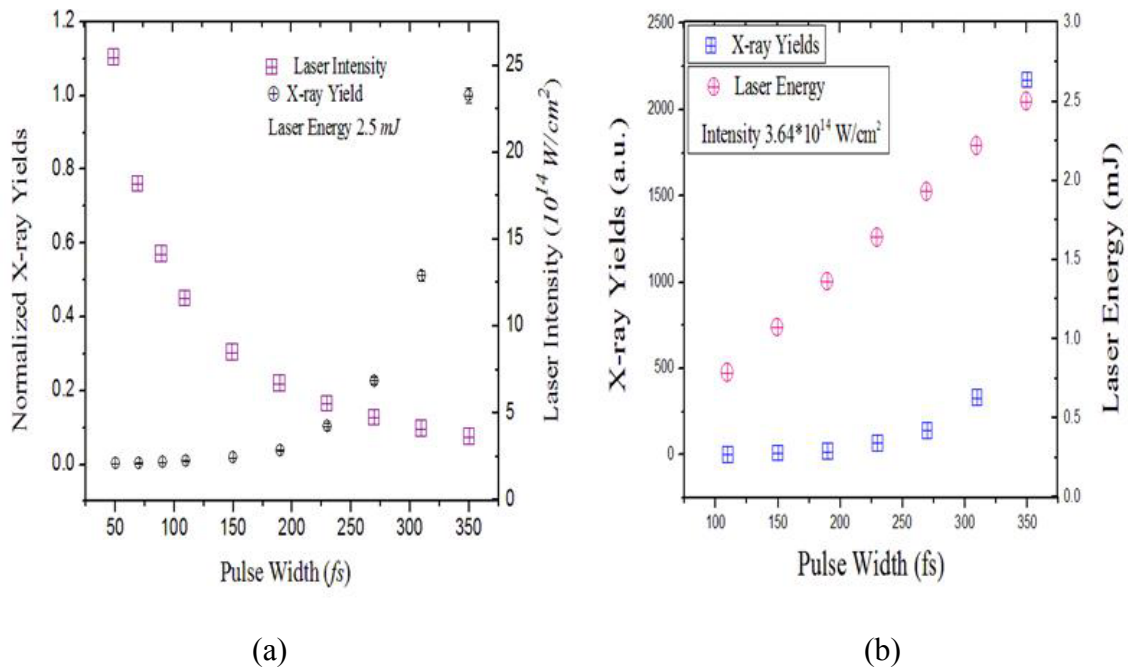


**Figure 17. X-ray yield and laser intensity vs. pulse width for a 50-μm-diameter water-jet target**

((a) for energy of 2.5 mJ and (b) intensity fixed at  $3.6 \times 10^{14} \text{ W/cm}^2$ . The laser energy in (b) has been multiplied by 10; therefore, a reading of 10 on the right y-axis is 1.0 mJ. The laser is p-polarized.)



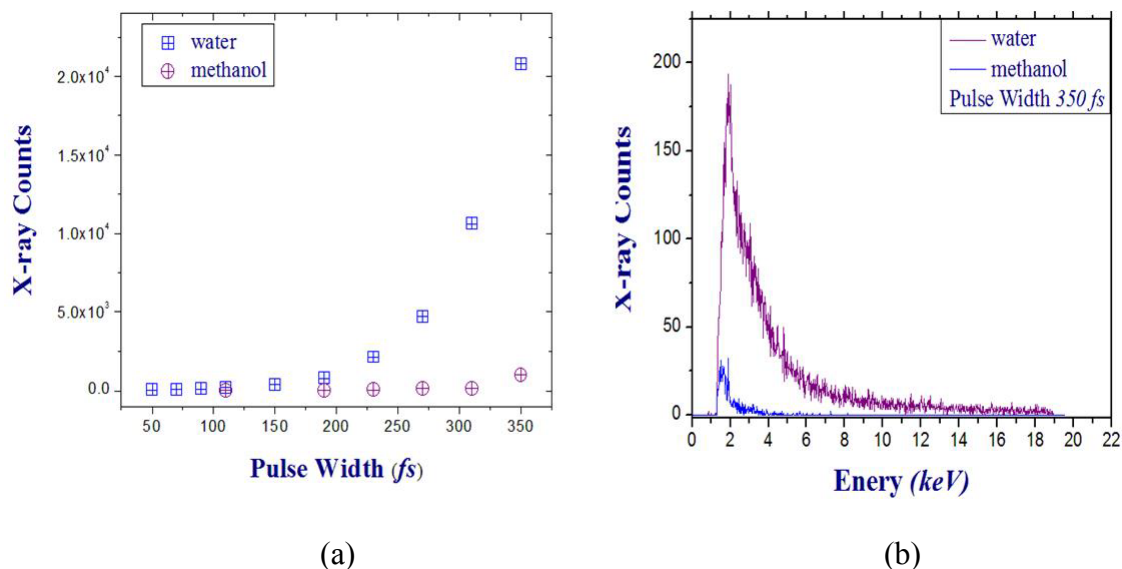


**Figure 18. Magnitudes of X-ray yields of methanol and water**

*((a) Comparison of the X-ray yields from water and methanol jets for a constant laser energy of 2.5 mJ, and (b) the relative magnitudes of the X-ray spectra of water and methanol targets. The laser is p-polarized.)*

The investigation of X-ray yields vs. pulse widths for dielectric targets as compared to metal targets yielded unusual results. The experiments conducted at constant energy showed that for a Cu target, as the pulse width increased, the laser intensity and the X-ray yield decreased. For a solid dielectric such as glass, the X-ray yield decreased with pulse width—but not so fast as for Cu (compare Figures 13 and 14). For the liquid dielectric targets methanol and water, the X-ray yields actually increased as the laser intensity was decreasing and the pulse widths were increasing (Figure 18). The explanation for this unusual behavior prompted an extensive study that became complicated by changes in laser characteristics that were not readily apparent.

It should be noted that as the pulse width is changed, the chirp of the laser also changes. The chirp is the ordering of the colors in the pulse. Chirp for the Red Dragon laser results in such a small broadening of the laser bandwidth that it was not considered important for generation of X-rays. However, our investigation of chirp showed that it was very important to X-ray generation. This investigation is noted in the next section.

### 3.5 The Impact of Chirp on X-ray Generation for Metals and Dielectrics

#### 3.5.1 Chirp

Chirp is basically the time ordering of the colors that make up an ultrashort laser pulse. If the long wavelength (referred to as red) leads the short wavelengths (blue), the pulse has a positive chirp. If the blue leads the red, the pulse has a negative chirp. The temporal description of the real part of the electric field  $E(t)$  of a Gaussian-chirped laser pulse can be written as

$$E(t) = \text{Re } E_0 \exp [-(t/\Delta t)^2] \exp[i(\omega_0 t + \beta t^2 + \gamma t^3 + \dots)] \quad (8)$$

where  $E_0$  is the amplitude of the wave,  $t$  is time,  $\Delta t$  is the time width of the Gaussian pulse,  $\omega_0$  is the annular fundamental frequency of the laser,  $\beta$  is a coefficient that is related to linear chirp, and  $\gamma$  is a parameter related to the quadratic chirp.

A cartoon illustrating the chirp characteristics associated with Eq. (3) is shown in Figure 19. The frequency-domain quantity that is analogous to the instantaneous frequency vs.  $t$  is the group delay vs.  $\omega$ .

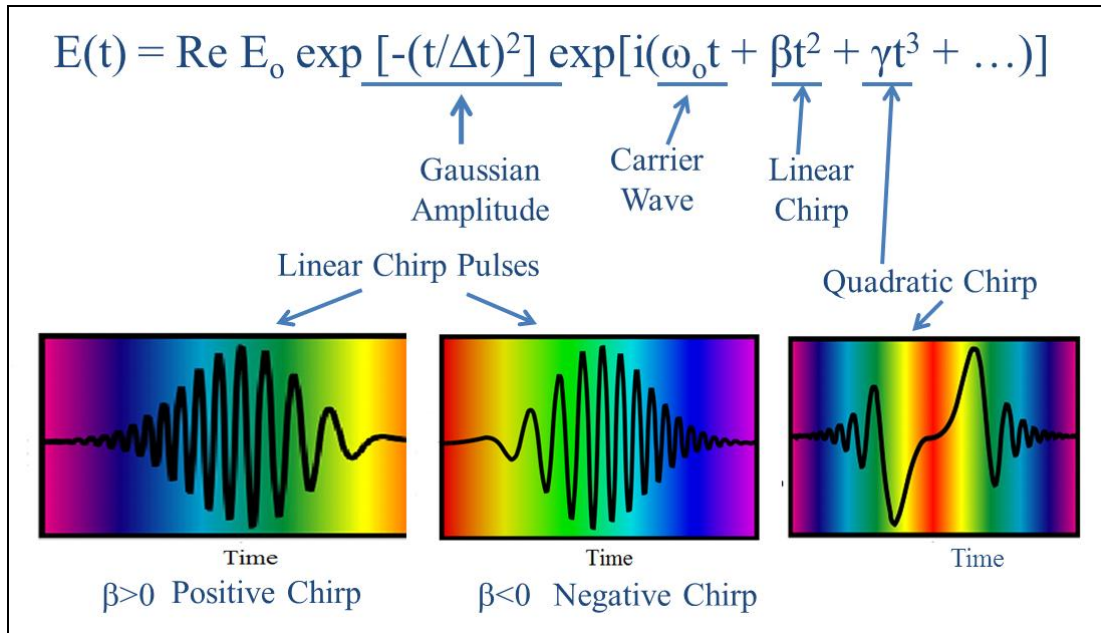


**Figure 19. Positive and negative linear chirp and quadratic chirp**  
(as described by the equation for the temporal evolution of the real part of a Gaussian pulse)

The parameter that describes chirp is called the group-delay dispersion (GDD). To gain an understanding of the GDD, consider the electric field of the light wave in the frequency domain,  $E(\omega)$ , as given by Eq. (4), where  $S(\omega)$  is the amplitude of the wave in the frequency domain and  $\phi(\omega)$  is the spectral phase.

$$E(\omega) = [S(\omega)]^{1/2} \exp[i\phi(\omega)] \quad (9)$$

The group delay is the derivative of the spectral phase and is given by

$$\tau_g(\omega) \equiv d\phi/d\omega \quad (10)$$

The GDD is the derivative of the group delay, as expressed by

$$d\tau_g(\omega)/d\omega = d^2\phi/d\omega^2 \quad (11)$$

The relationship between the pulse width and the GDD for our laser, as provided by the laser manufacturer, is given in Fig. 20. This curve was used to determine the GDD from the pulse width. The pulse width was changed by changing the separation of the compressor gratings. For a typical extreme-light laser, the compressor gratings are adjusted to yield the shortest pulse width. This pulse is referred to as the fully compressed pulse and has near-zero chirp. Negative or positive chirped pulses can be created by increasing or decreasing the separation of the compressor gratings, which also changes the pulse width such that there will be positive or negative chirped pulse for each pulse width. The GDD is a measure of linear chirp or, more specifically, a measure of the chromatic dispersion of the pulse, as noted in Fig. 19 and described by Trebino [[www.physics.gatech.edu/frog](http://www.physics.gatech.edu/frog)].

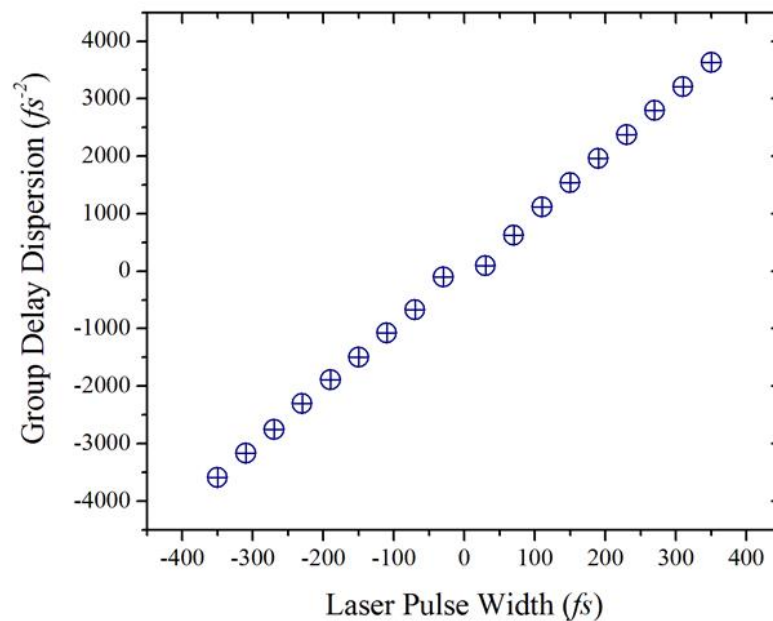


**Figure 20. Calculated GDD and laser pulse width for the Red Dragon laser**  
(as provided by the manufacturer)

### 3.5.2 Chirp Impact on X-ray Yield for Metal and Dielectrics

The plots in Figures 13-18 show that the X-ray yield can change significantly with pulsed width. As noted in the last section, a change in pulse width from the fully compressed pulse also results in a change in chirp, which can be either positive or negative, depending on whether the red or the blue light is leading, respectively. This raises the question of whether chirp (the ordering of the colors in the laser pulse) has an impact on X-ray yield or is it primarily the result of the changing pulse width. A literature search resulted in three papers where the impact of chirp on X-ray yield was investigated.

Several studies demonstrated that chirp can increase X-ray yield. The impact of positive and negative chirp on X-ray yields resulting from the interaction of a  $10^{15}$  W/cm<sup>2</sup>-fs laser with a 40-μm-thick sheet of aqueous solution was investigated by Hatanaka, et al.

[2008b]. A peak in X-ray yield was observed for both positive and negative chirp with an angle of incidence of  $58^\circ$  and with p-polarization. The yield from a negatively chirped 240-fs pulse chirp was about 1.5 times larger than that for the maximum positive chirped pulse and about 10 times larger than that for the transform-limited pulse. These researchers observed that the temperatures obtained from X-ray spectra were about the same for both positive and negative chirp and concluded that temperature did not contribute to the observed differences in bremsstrahlung X-ray yield due to chirp. A model was used to estimate the rate of ionization and bremsstrahlung X-ray emissions due to chirp [Hatanaka et al., 2008b]. They concluded that the increase in X-ray yield with chirp is due to the increased rate of ionization associated with the negative chirp.

The bremsstrahlung X-ray yield, resulting from the interaction of a  $10^{17}$  W/cm<sup>2</sup>-fs laser with a 200- $\mu$ m-diameter water jet, was studied by Fullagar, et al. [2007]. The optimum X-ray yield was obtained when the laser just grazed the edge of the jet. Nearly symmetric peaks in X-ray yield occurred for positive and negative chirp and a pulse width of about 240 fs. They concluded that hot-electron generation, resulting from vacuum heating, was responsible for the observed X-ray yields.

Silies examined the impact of chirp on the  $K_\alpha$  X-ray yield from a 4- $\mu$ m-thick Fe target and a laser intensity of  $5 \times 10^{14}$  W/cm<sup>2</sup> [Silies et al., 2007]. The peak  $K_\alpha$  yield for positive chirp was about 1.7 times the peak for negative chirp. When the laser intensity was reduced by approximately 50%, only a  $K_\alpha$  peak for the positive chirp was observed. Also, the temperatures from the X-ray spectra were higher for positive chirp than for negative chirp. They attributed the higher  $K_\alpha$  yields at positive chirp to the higher measured electron temperatures.

The results of Hatanaka, et al. [2008b], Fullagar, et al. [2007], and Silies, et al. [2007] on the impact of positive and negative chirp on X-ray yield are somewhat confusing. One might anticipate that any increase in X-ray yield would consistently depend on either positive chirp or on negative chirp, independent of the experiment. It is evident that this is not the case. Hatanaka, et al. obtained larger yields for negative chirped pulses than for positive ones for a CsCl water-sheet target. In the case of Fullagar et al., with a cylindrical water target, the yield was the same for both the positive and the negative chirp; whereas Silies, et al. showed that the  $K_\alpha$  yield from an Fe target was larger for a positive chirp than for a negative one. The different results noted in the three papers indicate that the impact of positive and negative chirp on X-ray yield depends, in some unknown way, on the specific characteristics of the experiments. However, the three research groups generally agreed that chirp (either positive or negative) can significantly increase the X-ray yield. Also, they showed that the yields peaked at a pulse width of roughly 230 fs.

Experiments were performed to investigate the impact of chirp on the total bremsstrahlung X-ray yield for Cu, glass, and water targets. The results are shown in Figures 21-23. The GDD was determined from the pulse-width measurements, following the procedure described in the previous section. As noted in Figure 21, the chirp did not result in an increase in the X-ray yield for a Cu target. Indeed, the yield decreased as the

pulse width increased for both positive and negative chirp. The same trend is noted in Figure 13 for the positive chirp.

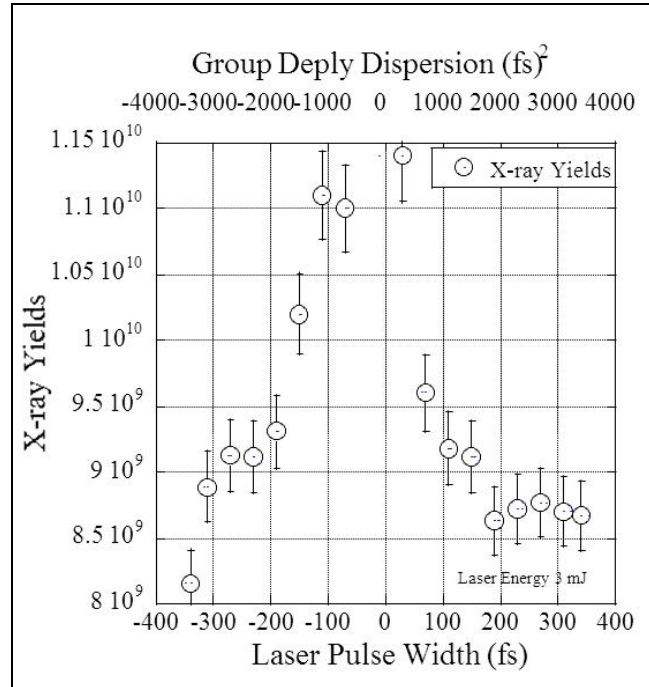


**Figure 21. Impact of chirp on X-ray yield for Cu target for energy fixed at 3.0 mJ**  
(The laser is p-polarized.)

A significant difference was observed in the X-ray yield obtained for Cu early in the program and that noted in Figure 21. It was noted previously that in Figure 10, the X-ray conversion efficiency for Cu was about an order of magnitude larger for the Legend as compared to the Red Dragon. Note in Table 2 that the total bremsstrahlung X-ray yield for Cu is about  $1.9 \times 10^{10}$  Ph/s/ $2\pi$  sr for the Legend. The results in Figure 10 suggests that the X-ray yield for the fully compressed pulse of the Red Dragon ( $\tau = 30$ -fs FWHM) and a Cu target should be about  $1.9 \times 10^8$  Ph/s/ $2\pi$  sr. However, the X-ray yield for a 30-fs pulse, as noted from Fig. 21, is about  $1.1 \times 10^{10}$  Ph/s/ $2\pi$  sr. Thus, the yield for a Cu target is almost the same for the Legend and the Red Dragon. It is evident that something changed from the time the data were collected in Figures 10 and 21. This important point will be addressed later in this section.

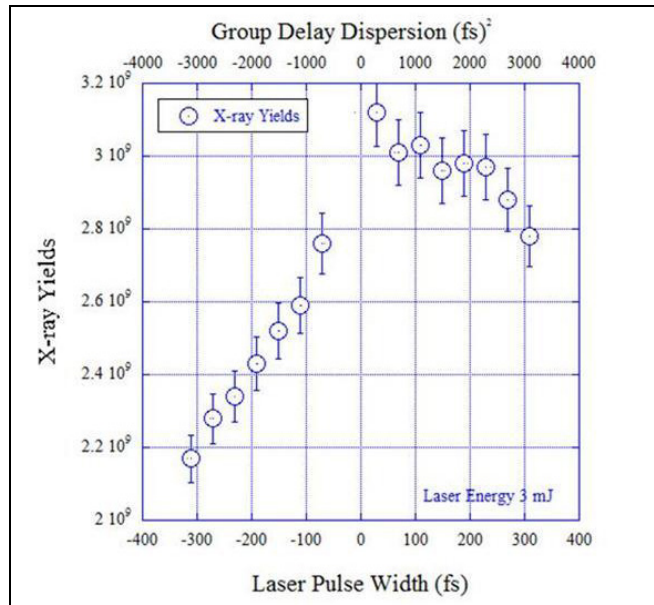


**Figure 22. Impact of chirp on X-ray yield for a glass target for energy fixed at 3.0 mJ**  
*(The laser is p-polarized)*

The dependence on X-ray yield on chirp, for the glass target shown in Figure 22, also shows a decrease in X-ray yield as the positive chirp increases; however, the decrease is much slower than that for the Cu target, as noted in Figure 21. It should be pointed out that the dependence of X-ray yield on positive chirp in Figure 22 has the same shape as that shown in Figure 14(a). It should also be noted in Figure 22, that the X-ray yield for negative chirp decreases rapidly with increasing negative chirp and has a lower magnitude than that for positive chirp.

Figure 23 shows the impact of chirp on X-ray yield for a 50- $\mu\text{m}$ -diameter water jet. The X-ray yield increases rapidly with increasing positive chirp up to a pulse width of about 230 fs, where it peaks and then begins to decrease. For increasing negative chirp the X-ray decreases, reaches a minimum at about 200 fs, and then begins to increase. This behavior of the X-ray yield with chirp is very similar to that observed by Hatanaka, et al. [2008b] from the CsCl water-sheet target, except that the maximum X-ray peak at 230 fs was for negative chirp, whereas ours was for positive chirp.

The question concerning whether the ordering of the colors in the laser pulse, chirp, or the pulse width is driving the impact can be addressed in part by examining the water-jet data in Figure 23. In reality we cannot answer this question definitively because the chirp and pulse width were not independently controlled. However, the data in Figure 23 suggest that the ordering of the colors in the laser pulse is of prime importance. For example, the X-ray yield is always larger for positive chirp than for negative chirp at the same pulse width. Since the pulse widths are the same, this would seem to imply that the order of the colors in the pulse is the important parameter--not the pulse width. However, it is strange that there are peaks in the X-ray yield. This could suggest that the pulse

width could be an important parameter. A modeling effort will be required to answer the question concerning the importance of chirp vs. pulse width to the X-ray yield.

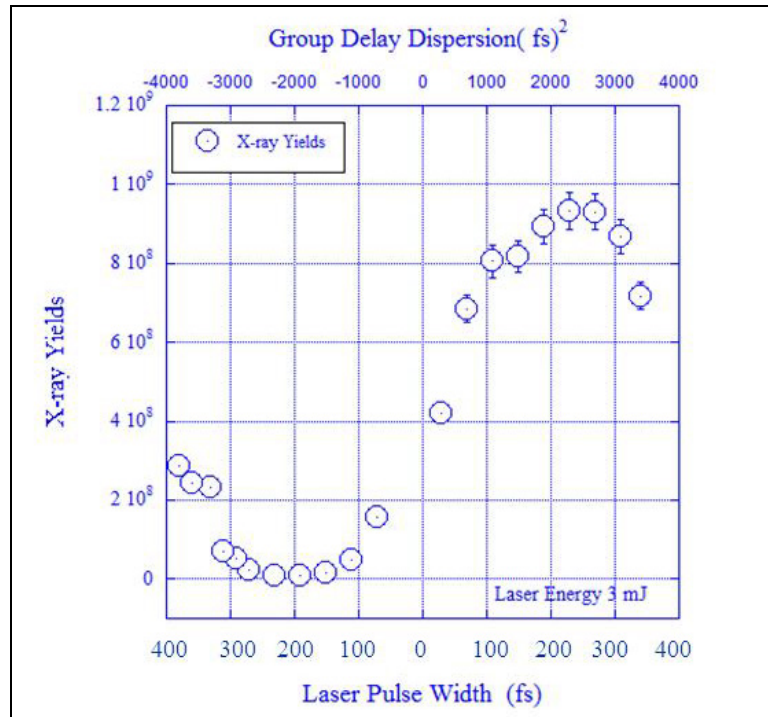


**Figure 23. Impact of chirp on X-ray yield for a 50- $\mu$ m-diameter water-jet target for a laser energy fixed at 3.0 mJ**  
(The laser is p-polarized.)

A significant difference is observed in the behavior of the X-ray yield for the positive-chirp water-target data in Figure 17 and that in Figure 23. In Figure 17(a), the X-ray yield increases with pulse width, whereas in Figure 23, the X-ray yield for positive chirp peaks at about 230 fs. Thus, the trend in these two figures is different.

A significant difference is observed in the magnitude of the X-ray emissions from Cu shown in Figure 21 and the X-ray conversion for the Cu data shown for the Red Dragon in Figure 11. As previously noted the X-ray emission for the Red Dragon was about an order of magnitude smaller than that for the Legend. However, this is not the case for the X-ray yield for the 30-fs fully compressed pulse width shown in Figure 21 where the yield was about  $1.1 \times 10^{10}$  Ph/s/ $2\pi$  sr and the total BB yield of  $1.9 \times 10^{10}$  Ph/s/ $2\pi$  sr for the Legend and Cu target in Table 3. Only the relative X-ray yields are shown for the positive chirp pulse and the Cu target in Figure 13; however, it should be pointed out that the data shown in Figures 10 and 13 were collected at approximately the same time. The data shown in Figures 10, 13, 14, 16-18, and 21-23 resulted from repeat experiments that required weeks and sometimes several months to complete. However, about one year elapsed between the taking of data shown in Figures 10-18 and those shown in Figures 21-23.

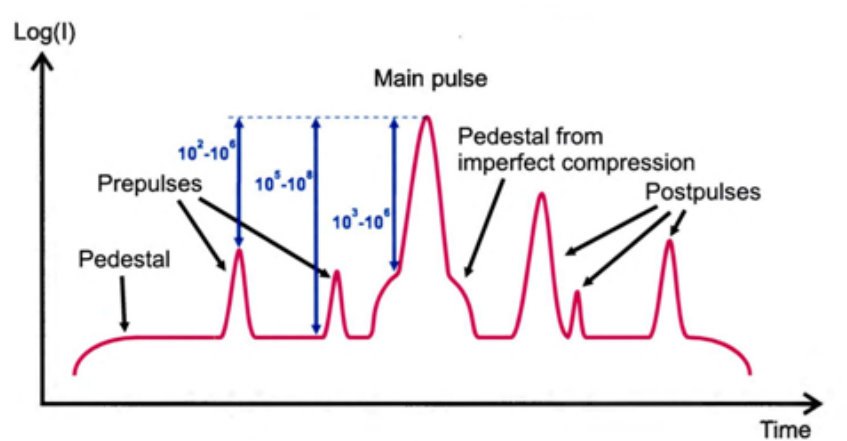


It was evident that something changed in the experiment during the one-year period in which the data in Figures 10-18 and those in Figures 21-23 were collected. During this time, the manufacturer had upgraded the Red Dragon, and it had undergone a complete realignment. Thus, it was suspected that something about the laser had changed, which resulted in the changes in X-ray yields. After some time, it was established that the laser had a prepulse at 25 ps whose magnitude could change during an alignment. The variation in this prepulse was thought to be the cause of the difference noted in the observed X-ray yield vs. chirp. The next section presents data showing how the 25-ps prepulse can change during laser alignment and its impact on X-ray yield.

### 3.6 Impact of Prepulse on X-ray Yield for Cu and Water Targets

#### 3.6.1 Impact of Natural Amplified Spontaneous Emission (ASE) on Cu and Water Targets

Prepulses are known to have a large impact on X-ray yield. Indeed, this was shown early in the program, as noted by the results shown in Figure 9 for a Ti target. In this case the prepulse was most effective at a delay of about 30 fs, and the total X-ray yield increased by a factor of almost three. Thus, the possibility existed that an inherent prepulse that could change during alignment might cause the variations in X-ray yield noted in the last section. To examine this point in some detail, it is useful to discuss the typical nature of the pulse for a femtosecond laser system.



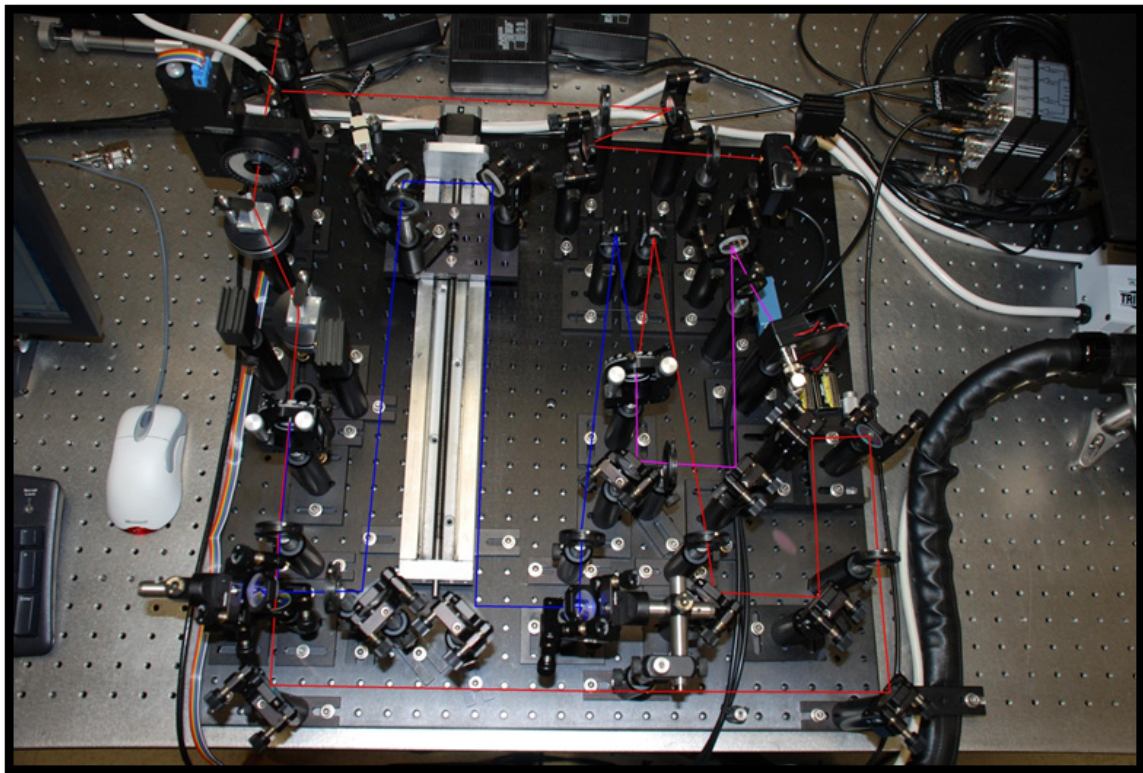
**Figure 24. Typical temporal structure of ASE from a laser pulse from a CPA system** ([from Veisz, Chap. 14, *Coherence and Ultrashort Pulse Laser Emission* by F. J. Duarte])

Figure 24 is an illustration of a typical temporal profile of a laser pulse from a CPA laser system. It consists of the main pulse located on top of a “foot” that spans several picoseconds and a very broad pedestal with a typical half-width of several nanoseconds. The broad pedestal results from ASE that typically arises in the CPA laser amplifier. Spurious reflections can also be present, which become ASE prepulses and post-pulses that have the same width as the main pulse. The intensity of the pedestal or the prepulses is usually expressed relative to the main-pulse intensity and is known as the contrast. That is, the laser contrast is defined as the ratio of the intensity of the main pulse to that of the prepulse. Typical values for contrast are shown in Figure 24.



The damage threshold of a material is a reasonable indicator of whether a prepulse can impact the X-ray yield from a target. The damage threshold is the intensity or fluence below which plasma will not form. It is dependent on the target material and the duration of the laser pulse. Values between  $10^{12}$  and  $10^{13}$  W/cm<sup>2</sup> are typical for many materials, including water and Cu. For peak intensities between  $10^{15}$  and  $10^{16}$  W/cm<sup>2</sup>, a contrast better than  $10^4$  is required to prevent prepulse ionization of the target.

The temporal structure and the contrast associated with a CPA laser system are typically measured using a third-order autocorrelator. A photograph of the third-order autocorrelator built on this program is shown in Figure 25. The autocorrelator design is based on that presented in Hong [2005].



**Figure 25. Third-order autocorrelator built on this program**

The shape of the general structure of the ASE similar to that in Figure 24 can be measured using a fast-response photodiode. The problem is that the photodiode has a nanosecond response time. To obtain quantitative measurements of the entire ASE structure, a calibration must be performed. Figure 26 is a calibrated structure of the ASE for the Red Dragon that was obtained over a 70-ns span of the laser pulse. The green trace is the response of the photodiode to the 30-fs laser pulse at time zero. The gray spikes are the corrected magnitudes estimated for the prepulses controlled to a degree by the timing of a Pockels cell. The magnitudes of the 5-ns and 13-ns peaks are sufficiently large that they could have an impact on X-ray yield. By adjusting the timing of the Pockels cell, the 5-ns and 13-ns peaks can be reduced about an additional order of magnitude from those shown in Figure 26. Some work was performed to investigate the

impact of the nanosecond prepulses on X-ray yield. However, the X-ray yield was very sensitive to the natural 25-ps prepulse. Therefore, most of the research was centered on the effect of this 25-ps prepulse.

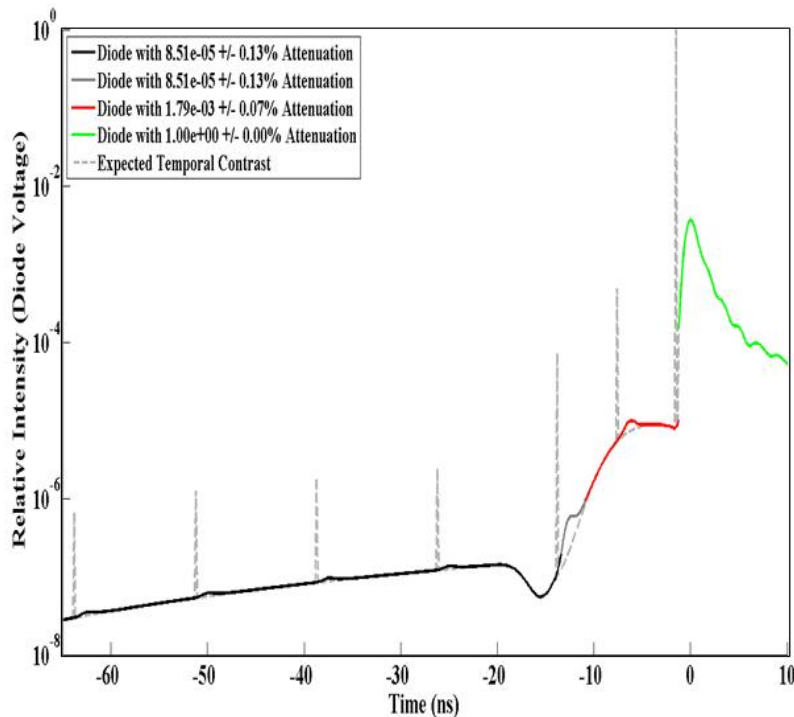


**Figure 26. Contrast of the Red Dragon laser**

*(obtained over a 70-ns time period and corrected for the 1-ns-rise-time photodiode using data from a third-order autocorrelator)*

Two third-order autocorrelation traces for the Red Dragon are shown in Figure 27. The ghost prepulses that form because of the post pulses and the third-order process have been removed from the traces. The two traces were taken about one month apart. The pulse peak-to-background ratio is  $> 10^5$ . Two original prepulses precede the main pulse at 23 and 25 ps, and their amplitudes are at least four orders of magnitude less than that of the main pulse. When the intensity of the main pulse is  $2 \times 10^{15} \text{ W/cm}^2$ , the intensities of these prepulses are approximately or less than  $10^{11} \text{ W/cm}^2$ , and the plasma expansion caused by these prepulses is negligible.

After consulting with the laser manufacturer, it was suggested that the 25-ps prepulse originated from the reflection from the internal surface of one of the Pockels cells. Changes in the 25-ps prepulse amplitude as physical adjustments were made to the Pockels cell supported this view. Thus, it was concluded that the 25-ps prepulse is an inherent characteristic of the laser. As it turned out, this was not the case. The actual cause of the 25-ps prepulse was a filter in several of the multi-pass beams that was used to flatten the peak of the main pulse. Removing this filter completely eliminated the 25-ps prepulse. Unfortunately, this was not discovered until the very end of the program. So during the program, the 25-ps prepulse was a continuous source of concern.

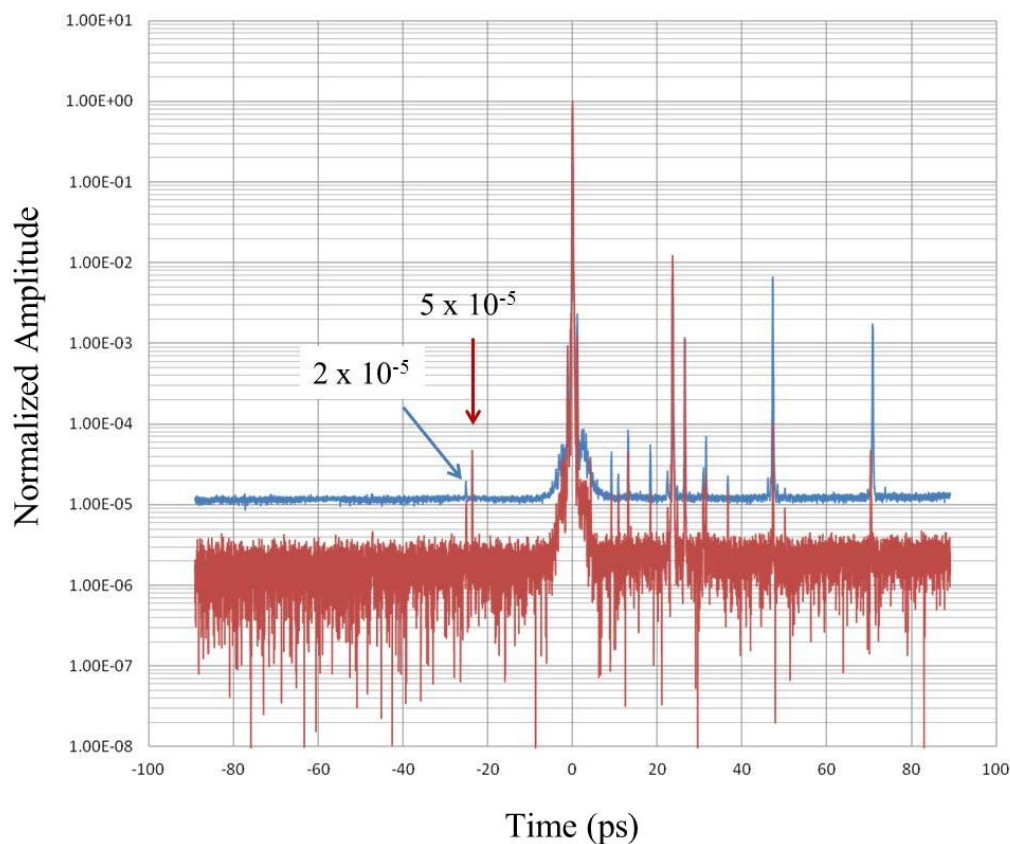


**Figure 27. Two normalized third-order autocorrelations for the Red Dragon laser taken about 1 month apart**

The magnitude of the 25-ps prepulse could change dramatically for reasons that were not always obvious, which would have a major impact on X-ray yield, as illustrated in Figure 28. Figures 28(a) and 28(c) show typical and atypical magnitudes of the 25-ps prepulse. The magnitude of the atypical peak is about 0.1% of the main peak and is about 20 times larger than the typical peak. Figures 28(b) and 28(d) illustrate that this difference in magnitude of the 25-ps prepulse can have a large impact on the X-ray yield for Cu.

The Legend was found to have several prepulses; the amplitude of some of these could have been as large as 0.1% of the main peak. Indeed, the difference in the X-ray yield from the Legend and the Red Dragon shown in Figure 11 is thought to be due to very large differences between the prepulses in the Legend and the 25-ps prepulse in the Red Dragon.

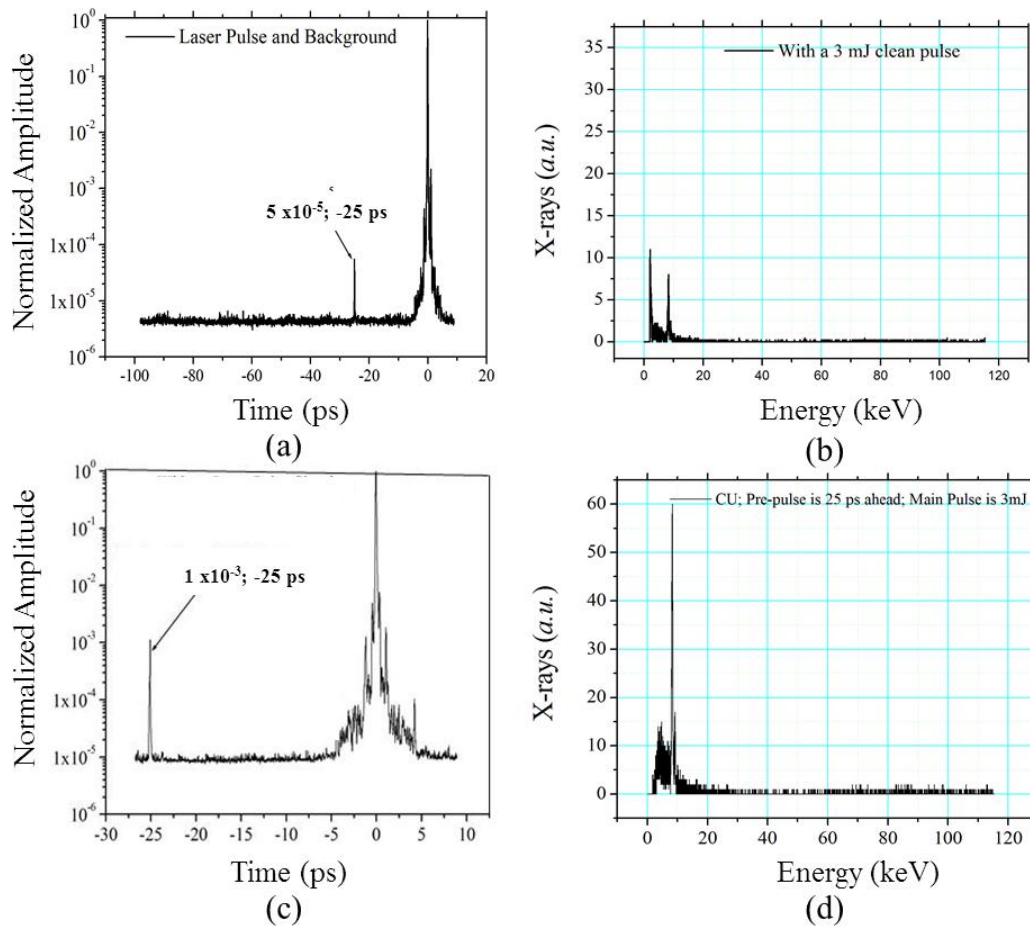


**Figure 28. Normalized third-order autocorrelation for the Red Dragon laser** (before (a) and after (c) an enhancement of the 25-ps prepulse and their respective X-ray spectra (b) and (d))

As will be shown in the subsequent sections, the X-ray yields for both Cu and water tend to peak for a 25-ps prepulse. Also, the order-of-magnitude change in X-ray yield from a Cu target, as noted for the Red Dragon in Figures 11 and 21, is thought to be due to a change in magnitude in the 25-ps prepulse. It was found that when the intensity of the 25-ps prepulse was  $< 10^{11} \text{ W/cm}^2$ , the X-ray yield was relatively low; but when the intensity of the prepulse was  $> 10^{11} \text{ W/cm}^2$ , the X-ray yield increased dramatically. Unfortunately, we could not always control the amplitude of the 25-ps prepulse. Thus, it was decided to investigate the impact of a prepulse on X-ray yield by introducing an artificial prepulse with amplitude that could be controlled.

### 3.6.2 Impact of Artificial Prepulse on X-ray Yield from Cu Target

After the realization that a 25-ps prepulse could result in a dramatic increase in X-ray yield, it was decided to investigate the impact of an artificial prepulse on X-ray yield for both Cu and water-jet targets. The experimental setup for these experiments is shown in Figure 29. The intensity of the main pulse for both the Cu and the water-jet experiments



described in Section 3.6 was about  $2 \times 10^{15} \text{ W/cm}^2$ , and the intensity of the artificial prepulse was about  $2 \times 10^{14} \text{ W/cm}^2$ . We typically started with “clean” laser pulses, which meant that the Pockels cells were adjusted so that the intensity of the 5-ns, 13-ns, and 25-ps prepulses was below  $10^{11} \text{ W/cm}^2$ . The artificial prepulse was generated by reflections from the surfaces of a beam splitter. The main pulse passed through beam splitter and was reflected from a movable mirror, which comprised an optical delay line that was used to investigate the impact of prepulse delay time on X-ray yield. The prepulse and main pulse were focused with a common lens to a 35- $\mu\text{m}$  FWHM spot.

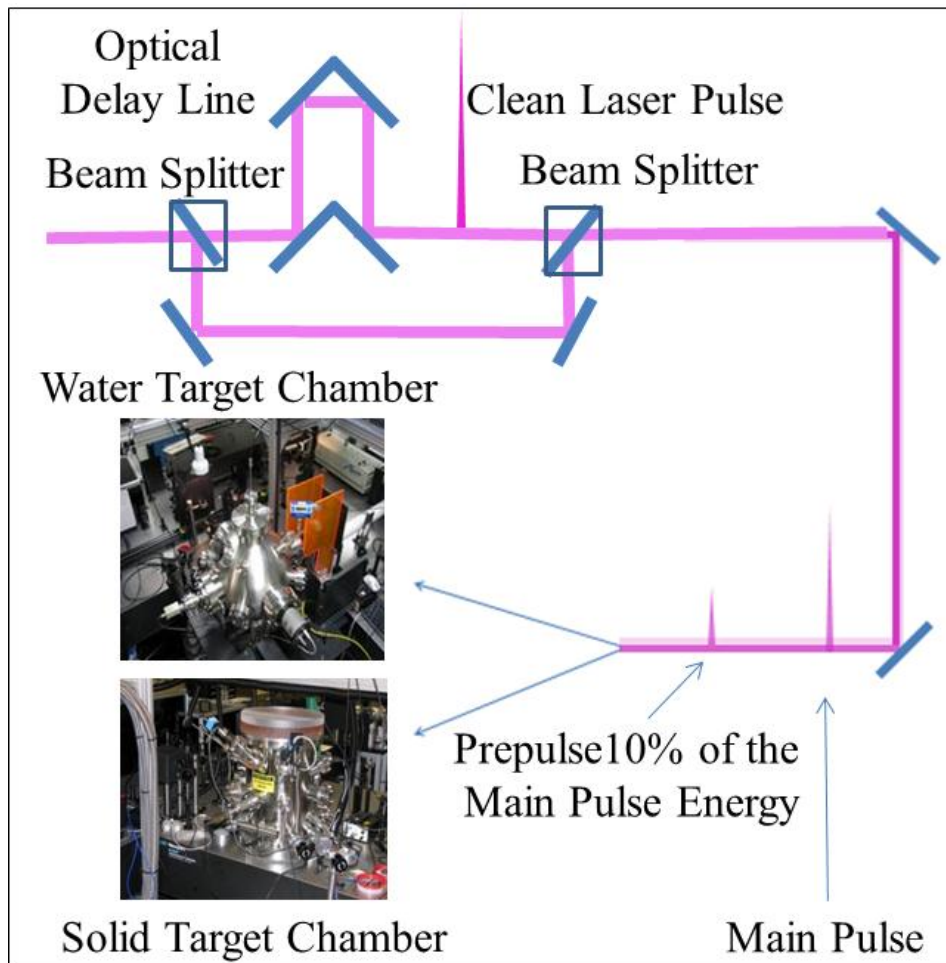


**Figure 29. Artificial prepulse optical system**

*(for producing an with a variable delay and a contrast of about 10% of the intensity of the main pulse for water and metal-target studies; yields could be enhanced using a prepulse.)*

The Cu target was made from a standard circuit board, with the copper foil about 34- $\mu\text{m}$  thick and an area of 10 cm  $\times$  10 cm. The target was mounted on a two-dimensional moving stage, as shown in Figure 7(b). The raster speed was adjusted such that each laser pulse would impact a fresh target surface. Hard X-rays were measured with an AMP TEK XR123 spectrometer that provided information on the X-ray spectrum from 2 - 120 keV as well as the integrated number of X-ray photons. A 25-micron-thick Be window of

the X-ray detector blocked the soft X-ray photons of energies less than 1 keV, and only those photons of energies above this value contributed to the spectra. To prevent X-ray signal pileup, the number of X-ray photons recorded per laser shot was controlled to be less than 0.5% by adjusting the distance between the laser focus and detector or installing one of the apertures provided by the spectrometer builder to reduce the X-ray irradiation. In experiments one or two minutes (60,000 to 120,000 laser shots) were spent to obtain one X-ray spectrum for certain laser and target conditions. Under the assumption of isotropic X-ray radiation, the X-ray yields reported here were divided by the solid angle subtended by the detector and normalized to a  $4\pi$  solid angle. During our experiments the background pressure of the target chamber was maintained at 2-Torr helium.

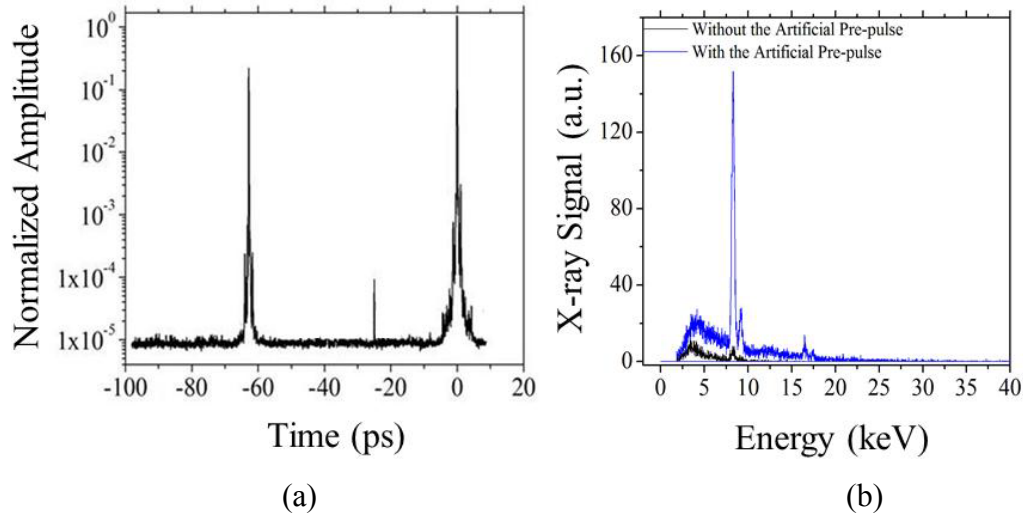


**Figure 30. Third-order-autocorrelation trace**

*((a) an artificial prepulse at 60 ps with a relative intensity of  $\approx 2 \times 10^{-1}$  and the natural prepulse at 25 ps with a contrast of about  $5 \times 10^{-5}$  obtained with the optical system illustrated in Figure 29 and (b) the X-ray yield with and without an artificial prepulse for a Cu target. The intensity of the main pulse was about  $2 \times 10^{-15}$ )*

Figure 30(a) displays a third-order-autocorrelation trace, showing the presence of a 60-ps artificial prepulse and a typical 25-ps natural prepulse. Figure 30(b) shows the  $K\alpha$  X-ray spectra of Cu with and without the artificial prepulse. It should be noted that the 60-ps artificial prepulse increases the  $K\alpha$  peak by more than a factor of 10. With a clean laser background (intensity of the background laser  $< 10^{11}$  W/cm<sup>2</sup>), no plasma formation and expansion should occur. In our experiments we observed that when the intensity of the original pre-pulse (25 ps ahead of the main pulse) was above  $10^{11}$  W/cm<sup>2</sup>, the total X-ray yield enhancement was about two to three orders of magnitude higher with the addition of the artificial pre-pulse.

Figure 30(b) shows the difference in the X-ray spectra with and without the artificial pre-pulse. The significant increase of X-ray photons and dominant  $K\alpha$  peak with the pre-pulse can be observed; correspondingly, the emission energy of  $K\alpha$  is  $\sim 30\%$  of the total X-ray emission energy. About 80% of the total X-ray energy falls in the energy range of

less than or equal to 10 keV. X-rays with energies greater than 35 keV are nearly at background level. The significant increase in X-ray yield noted in Fig. 30(b) raised the question of how a prepulse increases the X-ray yield.

Resonant absorption is often cited as the critical process responsible for an increase in X-ray yield due to a prepulse [Lu et al., 2009; Gibbon, 2005; Hatanaka et al., 2008; Silies et al., 2007]. It is generally accepted that a suitable prepulse delay,  $\Delta\tau$ , provides an appropriate time for the preplasma to expand such that the plasma length scale  $L$  (length scale of the expanded plasma from vacuum to the critical density) and angle of incidence  $\theta$  are optimized for maximum resonant absorption of the p-polarized main pulse.  $L$  is defined as:

$$L = Cs\Delta\tau, \quad (12)$$

where  $Cs$  is the sound speed and  $\Delta\tau$  the width of the laser pulse when there is no prepulse or is the delay time with a prepulse. Freidberg, et al. [1972] derived the following equation for the incidence angle ( $\theta$ ) that, when satisfied, yields the maximum resonant absorption and, presumably, the maximum X-ray yield:

$$(k_0L)^{1/3} \sin(\theta) = 0.8 \quad (13)$$

where  $k_0$  is the laser wave number in free space. Thus, it is generally thought that by using p-polarized light and varying  $\theta$  so that Eq. (13) is satisfied, one can optimize resonant absorption. This optimization is thought to result in the maximum transfer of laser energy into the production of hot electrons that pass through the critical surface into the cold, high-density region of the target, thus, generating maximum yields of Bremsstrahlung and K- $\alpha$  X-rays by collisional processes.

Experiments were performed to investigate the impact of the artificial prepulse delay time and p- and s-polarization on X-ray yield. The dependence of total and K $\alpha$  X-ray yields on the delay time is shown in Figures 31(a) and 31(b), respectively. There is less than a factor-of-two dependence of total or K $\alpha$  X-ray yield on s- and p-polarization. However, there is a very strong dependence on delay time.

The impact of the artificial prepulse on X-ray yield can be examined by noting that the zero-delay-time condition corresponds to a case where there is no prepulse. For the total X-ray yield in Figure 31(a), the total X-ray yield for the no-prepulse case is about  $4 \times 10^8$  photons/s/4 $\pi$  sr; whereas, the peak yield is about  $6 \times 10^9$  photons/s/4 $\pi$  sr for p-polarization at a delay time of about 46 ps. Thus, the prepulse with the proper delay time increased the total X-ray yield by about a factor of 15, and this increase was not strongly dependent on the polarization of the light.

The impact of the artificial prepulse on the K $\alpha$  X-ray yield was more dramatic, as noted in Figure 31(b). The K- $\alpha$  yield, with no prepulse (zero pulse delay) and for both p- and s-polarizations, was about  $2 \times 10^7$  photons/s/4 $\pi$  sr. The K- $\alpha$  yield reached a maximum value of about  $1 \times 10^9$  photons/s/4 $\pi$  sr at a delay time of 80 ps and for s-polarization and a

value of about  $8 \times 10^8$  photons/s/ $4\pi$  sr for p-polarization. Thus, the prepulse with an optimized delay time increased the K- $\alpha$  yield 50 times. Thus, the impact of an optimized prepulse had a much larger impact on the K- $\alpha$  X-ray yield than it did on the total yield, whereas the polarization of the light had a relatively small impact on optimization of either of the yields.

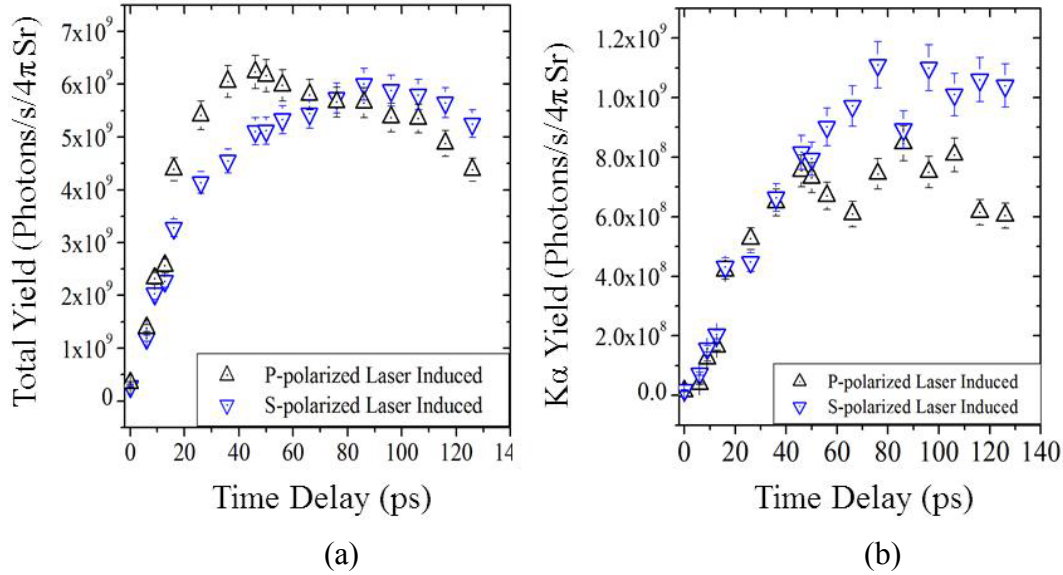


**Figure 31. Dependence of total and K $\alpha$  X-ray yields on the delay time**

((a) Total X-ray yield for Cu target as a function of delay time for an artificial prepulse for s- and p-polarized pulses, and (b) K $\alpha$  x-ray yield as a function of prepulse delay time and artificial prepulse for s- and p-polarized pulses. The main pulse intensity was  $\sim 1 \times 10^{15}$  W/cm $^2$ , and the prepulse intensity was  $\sim 1 \times 10^{14}$  W/cm $^2$ . The angle of incidence was 45°)

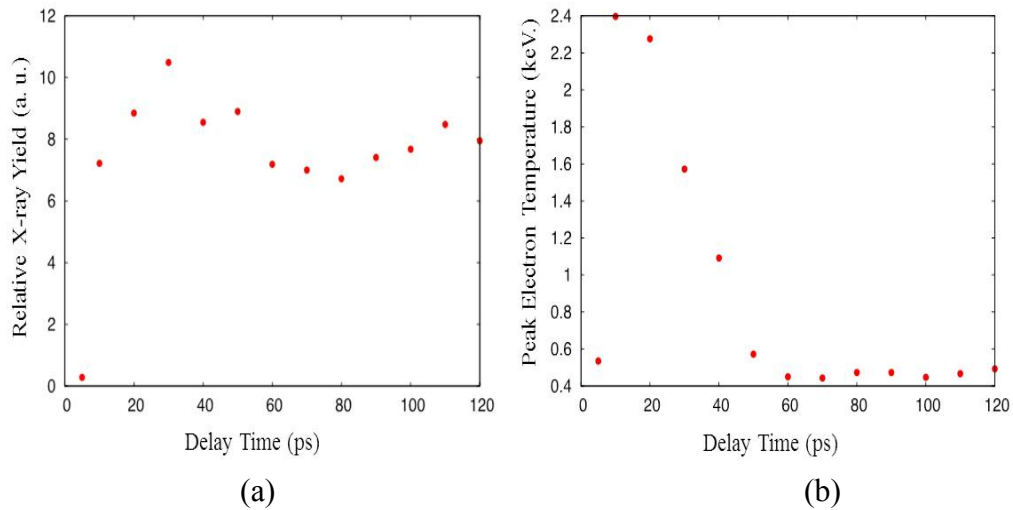


**Figure 32. Estimate of X-ray yield**

((a) Relative X-ray yield calculated as a function of prepulse delay time for conditions in Figure 31, and (b) calculated electron temperature for conditions in Figure 31. The main pulse intensity was  $\sim 1 \times 10^{15}$  W/cm $^2$ , and the prepulse intensity was  $\sim 1 \times 10^{14}$  W/cm $^2$ . The angle of incidence for the Cu target was 45°)



Reports of previous experiments on the pre-pulse effects on X-ray generation show that 20- to 30-fold enhancement in Al K-shell ( $\sim 1$  keV) emissions was achieved with a longer delay time of  $> 1$  ns [Nakano and Liesugi, 2001]. With delay times of tens to hundreds of picoseconds, less than a 10-time enhancement of the K-shell emission was observed with different targets (Si, Ti, Co, and Cu) [Ziener et al., 2002; Lu et al., 2009; Eder et al., 2000]. For the Cu K- $\alpha$  emission, a one-order enhancement was predicted in simulations; however, in experiments only four- to five-order enhancements were found [Gibbon et al., 2009].

As part of the collaboration with the University of Michigan, Ben Torralva used a 1-D HYADES model, with the Helmholtz wave solver, to estimate the X-ray yield for the above experimental conditions. Figure 32(a) illustrates that HYADES predicted a large increase in the x-ray yield from Cu when the prepulse delay was introduced. Note in Figure 32(b) that there is also a large increase in electron temperature, which peaks at about 10 ps. These hot electrons give rise to the total X-ray yield noted in Figure 32(a).

The model provided insight into processes thought to be responsible for the large increase in yield. One can think of the free electrons in the Cu as “cold over-dense plasma,” with an electron density of  $\approx 10^{23}$  electrons/cm<sup>3</sup>. The calculations indicate that when the main pulse interacts with this “cold over-dense plasma,” the laser penetrates a few tens of nanometers before being reflected, with only about 15% of the light being absorbed. When the prepulse interacts with the Cu surface, “hot” plasma expands away from the surface. In a few tens of picoseconds, it forms an exponential density ramp. When the main pulse hits, the plasma expansion has reduced the surface electron density to  $\approx 10^{19}$  electrons/cm<sup>2</sup> at about 1  $\mu\text{m}$  from the initial surface. The main pulse interacts with the expanded pre-pulse plasma, referred to as a preplasma; it penetrates a few hundred nanometers before being reflected by the critical surface, which has a density of  $\approx 10^{21}$  electrons per cm<sup>2</sup>. This increased penetration depth results in a 45% absorption of the main pulse, according to the HYADES calculations. The increased absorption increases the hot-electron number density and energy, thus increasing the electron/ion collisions. The result of this process is a large increase in the X-ray yield.

HYADES calculations attributed the increased laser absorption--and, correspondingly, the increased total X-ray yield--to an increased penetration depth of the laser before being reflected by the critical density surface. The increased penetration resulted from the prepulse changing the plasma length scale. According to the earlier discussions, the optimum length scale for optimum resonant absorption is given by Eq. (13). Using  $\theta = 45^\circ$  and  $k_0 = 2\pi/0.8 \mu\text{m}$  in Eq. (13), the optimum length scale should be  $L = 0.18 \mu\text{m}$ . Using Eq. (12) with  $\Delta\tau = 46$  ps for the total peak X-ray from Figure 31(a), the speed of sound is estimated to be about 4000 m/s. For Cu at room temperature, the speed of sound is 4600 m/s. The calculated speed using Eq. (12) is, of course, an averaged value resulting from changes in local conditions. Thus, the calculated value of 4000 m/s does not seem unreasonable. Thus, these results are consistent with the idea that an optimized prepulse, as described by Eqs. (12) and (13), could lead to maximum absorption and, thus, X-ray yield.

### 3.6.3 Impact of Artificial Prepulse on Water-Jet Target

The investigation of the impact of artificial prepulses on water-jet target was conducted with the experimental setup shown in Figure 29. The laser conditions are the same as those described in the previous section, except that the water-target chamber shown in Figure 29 was used along with the water-jet target. Also the decision was made to shift the pulse width to 230 fs with positive chirp because the pulse width resulted in a maximum X-ray yield, as noted in Figure 23. The water target was a vertically mounted, 75- $\mu\text{m}$ -diameter jet of distilled water. A syringe pump, operating at a constant pressure of 12.9 bars, provided a stable flow through a two-micron filter and then a fused-silica capillary with an inside diameter of 75  $\mu\text{m}$ . The water jet was located in a vacuum chamber that had a controlled pressure of 10 Torr. The jet was surprisingly stable for long periods of time. However, on occasions it oscillated or shifted position by about two or three microns. Normally, adjusting the flow corrected this problem. If the problem persisted, the capillary was replaced. The velocity of the jet was 7.3 m/s, which was sufficient to ensure a fresh target for each laser shot. Time-evolving movies showed that the dynamic processes associated with the laser/water-jet interaction were complete well before the next laser pulse arrived. A 1-cm-diameter tube mounted about 1 cm below the nozzle exit was used to collect the water-jet flow. The laser was focused on the water jet approximately 2 mm below the tip of the nozzle. The FWHM at the laser focus was 35  $\mu\text{m}$ .

Resonant absorption is thought to contribute to absorption of laser energy in water targets. Indeed, processes similar to those described for Cu are thought to occur for water. As noted for resonant absorption, the subsequent X-ray yield was expected to be sensitive to the laser polarization and angle of incidence. If resonant absorption were a major contributor to the X-ray yield, then the optimum X-ray emission should satisfy Eq. (13). However, there is a wide range of incident angles due to the FWHM of the focused laser and the curvature of the cylindrical water jet, as will be discussed shortly.

The sensitivity of the X-ray yield on the horizontal displacement,  $x = r \sin \theta$ , of the focal spot for p- and s-polarized light is shown in Figure 33. For each value of  $x$ , the focusing lens was traversed in and out to find the maximum X-ray yield. This maximum yield for a given  $x$  is plotted in Figure 33. As noted, there is a strong dependence on polarization with p-polarization, giving a maximum X-ray yield at  $x = 20 \mu\text{m}$ , which corresponds to  $\theta \approx 32^\circ$ , as estimated by the center of a Gaussian pulse. These characteristics are to be expected from resonant absorption. However, when one considers the range of  $\theta$  present because of the FWHM, one may arrive at a different interpretation. When one adds 17.5  $\mu\text{m}$  for the FWHM to  $x = 20 \mu\text{m}$  and computes the angle where the laser intensity has been reduced by 50%, the result is an angle of  $90^\circ$ . This means that the drop-off in the X-ray yield when  $x$  is increased beyond  $20 \mu\text{m}$  could be due, in part or totally, to the loss in laser energy. Thus, this peak may be more related to the water-jet geometry and the laser FWHM than to resonant absorption.

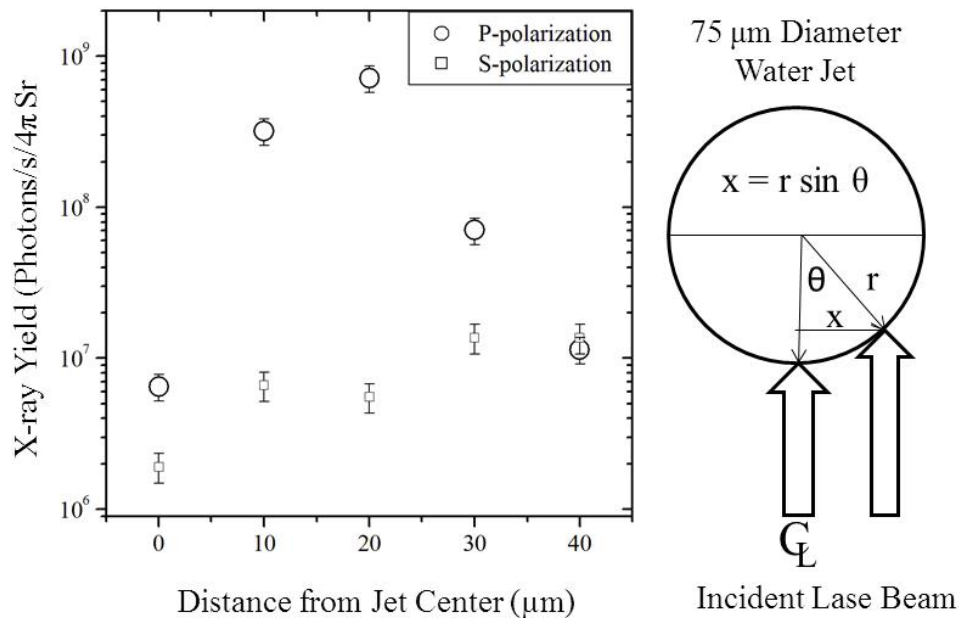


**Figure 33. Dependence of total X-ray yield on water jet distance**  
*(from the water-jet centerline for p- and s-polarization for a 75-μm-diameter water-jet target without a prepulse. The laser pulse intensity was  $\sim 2 \times 10^{15}$  W/cm<sup>2</sup>, and the pulse width was 230 fs with positive chirp)*

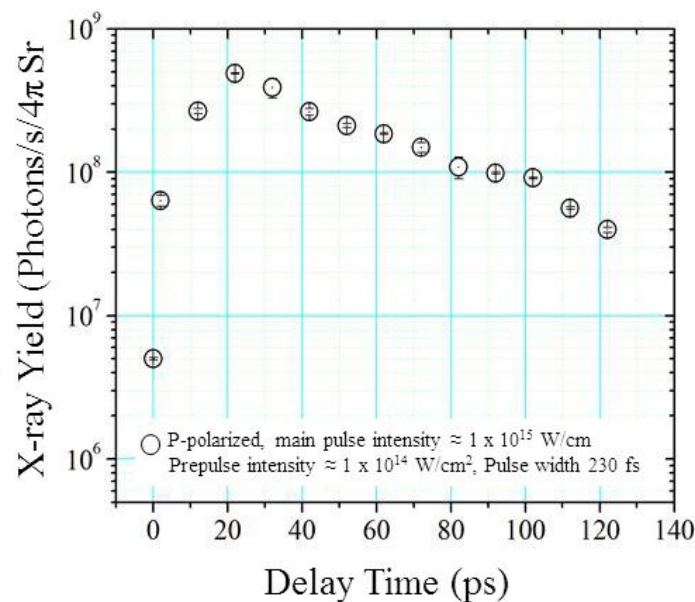


**Figure 34. Dependence of total X-ray on prepulse delay time for p-polarization for a 75-μm-diameter water-jet target**  
*(The main pulse intensity was  $\sim 1 \times 10^{15}$  W/cm<sup>2</sup>, and the prepulse intensity was  $\sim 1 \times 10^{14}$  W/cm<sup>2</sup>)*

The impact of delay time on the X-ray yield, for a 75- $\mu\text{m}$ -diameter water jet and with a 230-fs positively chirped prepulse and main pulses, is shown in Figure 34. The incoming laser beam was off-set from the jet centerline by 20  $\mu\text{m}$  and was p-polarized. Note that the X-ray was extremely sensitive to a prepulse for the water jet. Without a prepulse (delay time = 0), the X-ray yield was about  $5 \times 10^6$  photons/s/4 $\pi$  sr. With an optimum delay time of about 22 ps, the peak yield was about  $6 \times 10^8$  photons/s/4 $\pi$  sr. Thus, with an optimized prepulse delay time and with 230-fs positive chirped pulses, a two-orders-of-magnitude increase in the X-ray yield results. With Cu the prepulse increased the total yield by 15 times and the K $\alpha$  yield by 50 times, as observed from Figure 31. Indeed, for the fully compressed pulse of 30 fs and without a prepulse, it is very difficult to observe X-rays from a water-jet target at laser intensities of  $1 \times 10^{15}$  W/cm<sup>2</sup>.

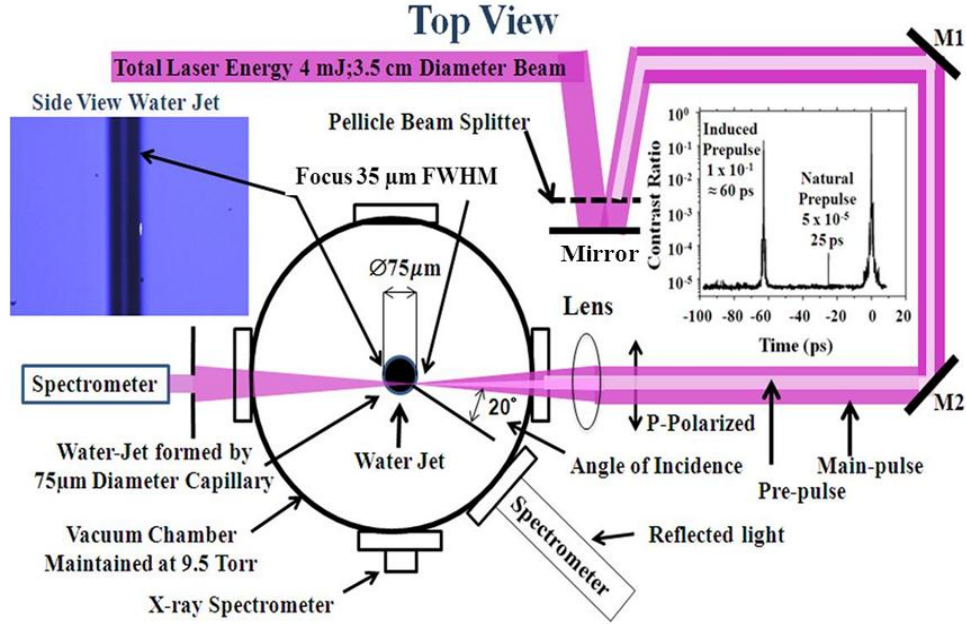
It is now understandable why the X-ray yields for both Cu and, especially, water targets were so sensitive to the natural 25-ps prepulse of the Red Dragon. The yields for both Cu and water peaked very near the 25-ps prepulse delay time, as observed in Figures 31 and 34. However, a true one-to-one comparison of the impact of prepulse on X-ray yield cannot be made from the data in Figures 31 and 34. The reason is that the main pulse and prepulses for the water-jet experiments were chirped; whereas, fully compressed pulses were used for the Cu experiment. The data in Figure 23 indicate that chirp can have a significant impact on the X-ray yield of water but did not seem to have much of an effect on the yield for Cu, as noted in Figure 21. The following experiments were conducted to investigate the impact of both prepulse and chirp on the x-ray yield from a water-jet target.

### **3.7 Impact of Artificial Prepulse and Chirp on X-ray Yield from a Water-Jet Target**

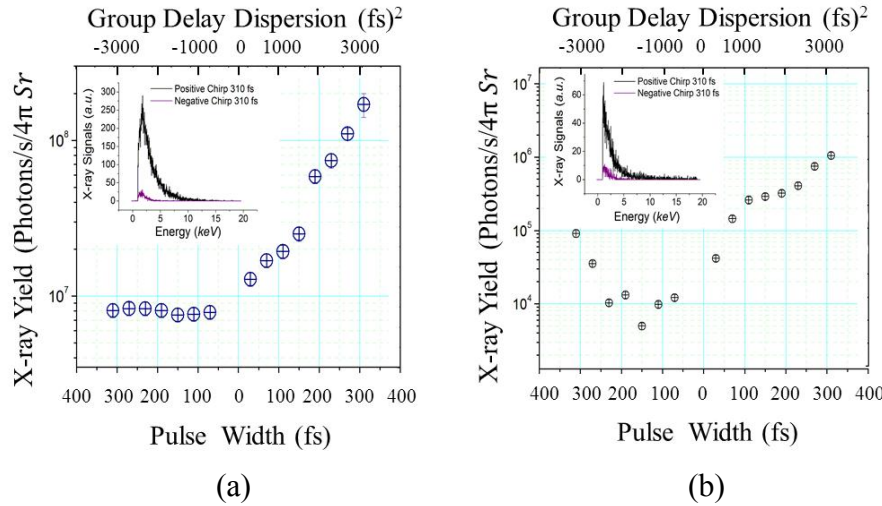
The experimental setup for studying the effects of chirp and artificial prepulse on X-ray yield is shown in Figure 35. The configuration is similar to that shown in Figure 29, with a few exceptions. The adjustable delay was replaced with a pellicle beam splitter and a mirror. An artificial prepulse was generated by reflections from the surfaces of the pellicle beam splitter. The energy of the laser prepulse was about 10% of the main pulse energy, and the time delay between the main and prepulse was fixed at  $\sim 60$  ps. The total energy of the laser was fixed at 4 mJ. The intensity of the main pulse for a 30-fs pulse width was about  $10^{16}$  W/cm<sup>2</sup> and was about  $10^{15}$  W/cm<sup>2</sup> for a pulse width of 300 fs. The pellicle-beam-splitter configuration assured spatial overlap of the main and prepulse, even though the X-ray yield was reduced by a factor of about two for a 60-ps prepulse (See Figure 34). Also, the prepulse could be eliminated without changing the optical alignment by simply removing the pellicle beam splitter. Spectrometers were used to measure the relative transmission through the water jet and the reflectance. As will be discussed shortly, a blue shift was detected from the reflected light.

The procedures employed for performing the experiments follow. Before each experiment, the displacement and the depth of the p-polarized incident beam were optimized for a positive chirped 230-fs pulse and a 60-ps prepulse. A typical displacement of the beam was about  $13 \mu\text{m} \pm 5 \mu\text{m}$  from the center of the water column. This corresponded to an incidence angle of  $\theta = 20^\circ \pm 8^\circ$ , as determined by the center of the Gaussian beam. This angle also resulted in a maximum X-ray yield for the fully

compressed 30-fs pulse with and without a prepulse. As mentioned previously, there is a large variation of the incident angle when the FWHM of the beam is considered.



**Figure 35.** Experimental setup for investigating the impact of prepulse and chirp on X-ray yield from a 75-μm-diameter water jet



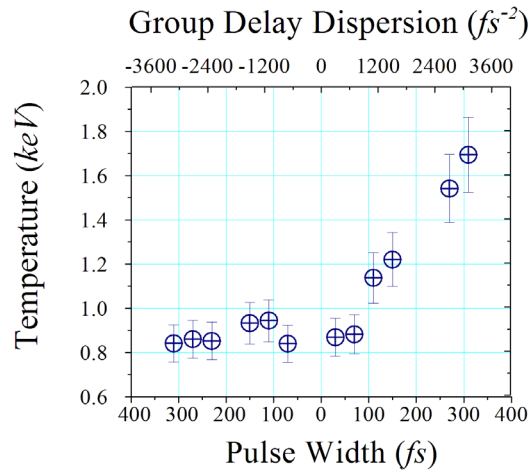
**Figure 36.** Dependence of X-ray yields on laser linear chirps and pulse widths ((a) with a prepulse and (b) without a prepulse. The target was a 75-μm-diameter water jet. The 60-ps prepulse had 10% of the energy of the main laser pulse. The inside figure shows the X-ray spectrum for positive and negative chirp with a pulse width of 310 fs)

Figure 36(a) shows the dependence of the X-ray yield on laser chirp and pulse width with the artificial 60-ps laser prepulse. The X-ray yield for a positive-chirped 310-fs pulse is about a factor of 66 times larger than that for the negative-chirped 310-fs pulse. This large difference is also illustrated by the X-ray spectra for positive and negative chirp for the 310-fs pulse widths shown by the insert in Figure 36(a). It should also be noted that as

the X-ray yield increased by a factor of about 66, the laser intensity decreased by a factor of 10 because of the laser energy being fixed. Similar behavior was noted in Figure 23. However, in Figure 23 the X-ray yield peaked for a positive-chirped pulse width of about 230 fs and had a minimum yield at a negative chirp of about 230 fs, whereas in Figure 36(a), the yield is relatively constant for negative chirp and increases with increasing positive chirp. The causes of these differences have not been determined. Indications are that both the prepulse characteristics and the procedures used in performing the experiments contribute to the dependence of the X-ray yield on chirp and possibly determine whether the yield is a maximum for positive or negative chirp. This important issue must be resolved in future studies.

Figure 36(b) shows the X-ray yield as a function of pulse width and chirp without the 60-ps prepulse. The extreme sensitivity of the X-ray yield to a prepulse can be observed by comparing Figures 36(a) and 36(b). The magnitude of the yield for the fully compressed 30-fs pulse with a prepulse [36(a)] is 375 larger than that without a prepulse [36(b)]. The maximum X-ray yields occur for a positive chirp and a pulse width of 310 fs with and without a prepulse. However, the yield is about 200 times larger with the prepulse. This clearly illustrates the extreme sensitivity of X-ray yield to prepulse for a water-jet target. Indeed, no other material we studied showed such a strong sensitivity on a prepulse.

The dependence of X-ray yield on chirp/pulse width are about the same with and without a prepulse, which can be observed by comparing the X-ray yields for the 310-fs pulse width and the 30-fs fully compressed pulse in Figures 36(a) and 36(b). An enhancement in X-ray yield due to chirp is about a factor of 10 for a prepulse and without a prepulse. A similar enhancement due to chirp is reported by Hatanake, et al. [2000b] for a liquid-sheet target of CsCl aqueous solution; however, in their case the maximum yield occurred for negative chirp.



**Figure 37. Dependence of electron temperature on linear chirp and pulse width** (for a prepulse with 10% of the energy and 60 ps ahead of the main laser pulse. The temperature is estimated from exponential curve fits to the X-ray spectra illustrated in the insert of Figure 36)

Figure 37 shows the electron temperature obtained by fitting the energy-dependent X-ray spectra, illustrated in the insert of Figure 36(a), to a Maxwellian distribution. The

temperatures range from about 0.8 keV for negative chirp to a maximum of 1.7 keV for positive chirp.

The shapes of the temperature and X-ray-yield curves in Figures 36(a) and 37 are similar, which seems reasonable since the bremsstrahlung radiation is proportional to  $n_i n_e T^{1/3}$ , where  $n_i$  and  $n_e$  are the ion and electron densities, respectively, and  $T$  is the temperature [Goldston and Rutherford, 1995]. However, it is curious that the electron temperature and X-ray yield are increasing as the laser intensity is decreasing. The observation of a blue shift, as discussed in the subsequent section, offers an explanation for this odd behavior.

The normalized spectra of the reflected light from the water target and a prepulse are shown in Figure 38. The reflected-light spectra are recorded at the same time as the X-ray data in Figure 36(a). The presentation of the spectra begins from a positive 310-fs pulse and progresses to a negative-chirped 310-fs pulse. The dashed line marks the center of just the laser pulse for positive-chirped 310-fs and 30-fs and negative-chirped 310-fs pulses, as shown by the lighter traced spectra in Figure 38.

An inverse relationship appears to exist between the magnitude of the blue shift and the X-ray yield. The blue shift begins with the positive-chirped 150-fs pulse and continues to increase as the pulse width approaches the 310-fs negative chirp. Thus, the blue shift is largest for negative-chirped pulses where the X-ray yields are small and is smaller for positive chirp pulses where the X-ray yields are large.

Figure 39 shows the normalized reflectance spectra for the water-jet target without a prepulse. The spectra progress from a positive-chirp 310-fs pulse width to the negative-chirp 310-fs pulse width. The general shapes of the spectra are very similar to those shown in Figure 38(b). The blue shift begins with the positive-chirp 150-fs pulse and increases as the chirp becomes more negative. In general, the blue shift appears to increase as the X-ray yield decreases. This also appears to be true for the negative-chirp 310-fs pulse, which actually has a relatively larger X-ray yield [see Figure 36(b)] than other negatively chirped pulses. In this case the blue shift for the main reflectance peak is relatively small (see Figure 39).

The blue shifts have been observed in ultra-short laser/target interactions with gas targets [Freeman et al., 1987; Wood et al., 1991; Singhal et al., 2005]. Model studies show that the blue shift is the result of laser ionization of the gas target [Yablonovitch, 1988; Penetrante et al., 1992]. Indeed, Wood, et al. [1991] used the blue shift to study ionization dynamics. Recently Anand, et al. [2006a] observed a blue shift in studying the X-ray yield from 15- $\mu$ m-diameter methanol drops and also attributed the observed blue shift to rapid ionization.

Significant differences exist between the blue shift in Figures 38 and 39 and those observed by Anand, et al. [2006a]. The main differences are related to the relationships among blue shift, prepulse, and X-ray yield. Their blue shift directly correlated with X-ray yields--the larger the blue shift, the larger the X-ray yield. Whereas the data in Figures 38 and 39 show that the X-ray yields are large for small blue shift and small for larger blue shifts. Also, Anand, et al. [2006b] observed a blue shift only when a 10-ns



prepulse was present. We observed blue shifts with and without a 60-ps prepulse. Their laser intensity was  $2 \times 10^{16}$  W/cm<sup>2</sup>, and the pulse width was 40 fs, which is similar to our fully compressed laser conditions.

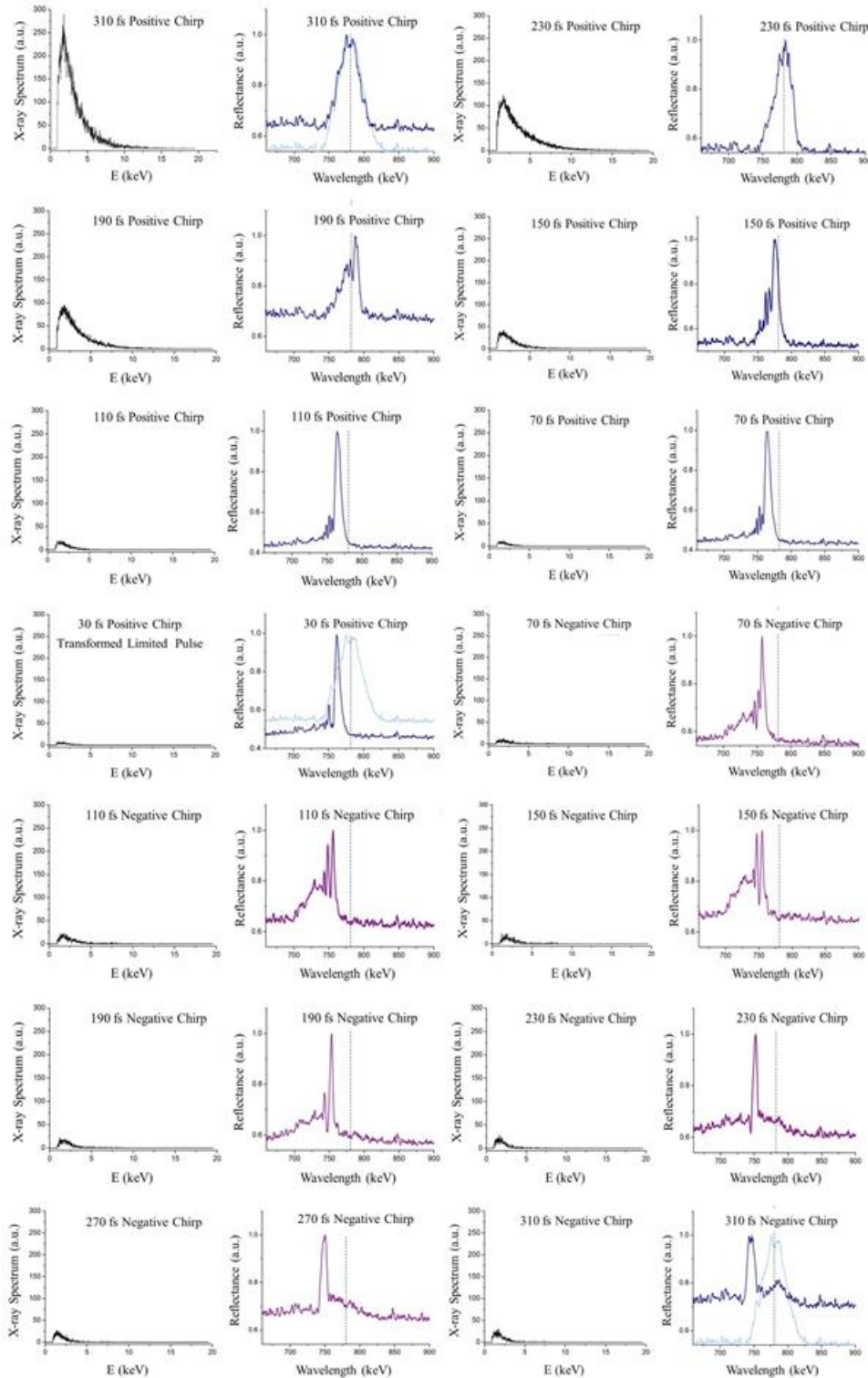


**Figure 38. X-ray and reflectance spectra for different pulse widths/chirp with a 60-ps prepulse**



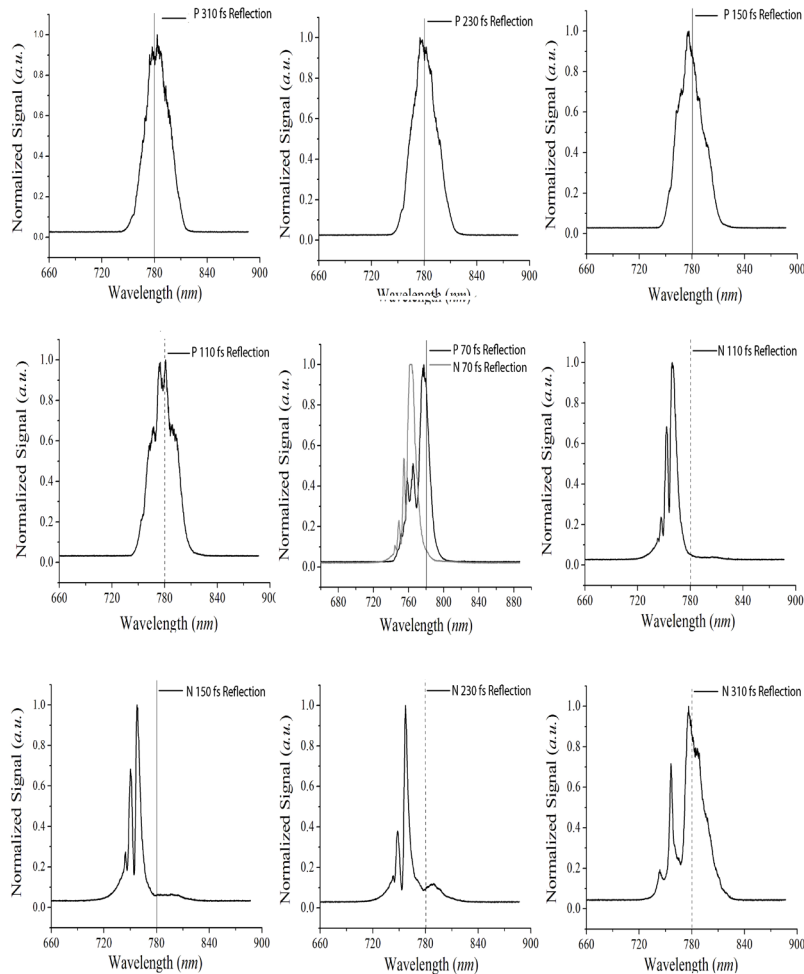


**Figure 39. Dependence of reflected laser spectra on chirp without prepulse**

A significant difference existed between the experiments of Anand, et al. [2006b] and ours. All of their observations were made with a laser that was not chirped. Our investigation appears to be the only one where the impact of the relationships among blue shift, chirp, and prepulse on X-ray generation has been studied.

In summary, a relationship among the X-ray yields, chirp, and blue shift is observed such that (1) with a positively chirped pulse with a width of 230 fs, Figure 34, the X-ray yield peaks at a prepulse delay time of 25 ps and decreases slowly over a period of 130 ps, (2) for a positive-chirped pulse with a 60-ps prepulse, Figure 36(a), the X-ray yield is  $\sim 100$  times larger than that for a negative-chirped pulse, (3) for a positive-chirped pulse with no prepulse, Figure 36(b), the X-ray yield is  $\sim 10$  times more than that for a negative-chirped pulse, (4) the blue shift is maximum and the X-ray yield is minimum for a negative-chirped pulse, as shown in Figures 38 and 39, and (5) the blue shift is minimum and the X-ray yield is maximum for positive-chirped pulse with and without a prepulse, Figures 38 and 39. When the blue shift is viewed as indicating high rates of ionization, Result (4) above seems to present a conundrum because X-ray yields are normally large

when ionization rates (blue shift) are high. This result can be explained by assuming that the high rates of ionization are producing sufficiently low-energy electrons that they cannot produce the hard X-ray measured with our spectrometer. The low temperatures extracted from the X-ray spectra for the negative-chirped pulses shown in Figure 37 support this proposition. The higher bremsstrahlung X-ray yields for Result (2) above are thought to be due, in part, to the higher electron temperatures, as indicated by the temperature obtained from the X-ray spectra of positive-chirped pulses in Figure 37.

For practical applications of laser-generated X-rays, as compared with solid targets, liquid targets are attractive because of the substantially reduced debris problems. Unfortunately, the yields from liquid targets are typically orders of magnitude lower than those of metal targets. Several studies have demonstrated how to adjust the angle of incidence, polarization, and prepulse delay time to optimize the X-ray yield. However, many laser and target parameters as well as procedures can dramatically impact the yield. This study demonstrates that the combination of prepulse and chirp can result in X-ray yields that are about an order of magnitude lower than those from metal targets. Additional gains in X-ray yields may be possible with liquid targets since relatively small changes can have major impacts on X-ray production. However, there is no comprehensive understanding of how laser, target, and procedural parameters impact yield. Future studies along this line would greatly benefit from modeling efforts that could provide a more comprehensive understanding of the important fundamental processes and how they interact to yield specific results. The following section discusses some considerations for future modeling studies.

### **3.8 Discussions of the Impact of Chirp on X-ray Generation in a Water-Jet Target**

The detailed modeling required to understand the complicated processes associated with the results presented here was beyond the scope of this study. In Section 3.6.2 a short description was presented, based on a general understanding of how resonant absorption can impact the prepulse plasma and the X-ray yield. In this section a more detailed description will be presented, beginning with the ionization processes in water, as extracted from numerous studies. These discussions are presented in the hope that the ideas discussed will be of some value to future experimental and modeling efforts in gaining a better understanding of the physics associated with these complex laser/matter interactions.

Vogel [2005, 2009], Forslund, et al. [1975], Noack and Vogel [1999], and Hammer, et al. [1996] conducted extensive studies on the ionization processes in water. The following is a synopsis of their research as thought to be important to our studies. As the leading edge of the pulse (either prepulse or main pulse) reaches an intensity of about  $10^{13}$  W/cm<sup>2</sup>, ionization is initiated by multiphoton absorption and tunneling. The ionized electrons gain energy by inverse bremsstrahlung and create additional free electrons by impact ionization. The processes of inverse bremsstrahlung and impact ionization lead to avalanche or cascade ionization in which the electron number density increases exponentially. At some depth in the plasma/water target, the light encounters the critical electron density “surface” and is reflected. Near the critical-density surface, a portion of the light is resonantly absorbed and a portion is reflected. Resonant absorption heats

some of the free electrons to temperatures that are significantly higher than those in the surrounding plasma. Some of these hot electrons, along with lower energy electrons, pass through the critical-density surface, penetrate into the colder regions of the target, and lose their energy by different scattering and absorption processes, one of which results in bremsstrahlung radiation. Hot-electron production by resonant absorption and their loss of energy in the colder water target are thought to be key processes in the production of hard X-rays in our experiment.

Resonant absorption involves effectively coupling the laser with a plasma wave that is initiated early in the ionization process. The plasma wave is the collective longitudinal oscillations (normal to the target surface) of the free electrons about the ions. Resonant absorption occurs when the laser frequency  $\omega_L$  is equal to the frequency of the plasma wave

$$\omega_p = (4\pi n_e e^2 / m_e)^{1/2} \quad (14)$$

where  $n_e$  is the electron number density,  $e$  the electron-charge, and  $m_e$  the electron mass. It takes place very near the critical-density surface. For resonant absorption to occur, a component of the electric field of the light must be in the longitudinal direction of the plasma-wave oscillation--that is, normal to the target surface. Thus, for normal incidence, where the total-electric-field vector of the light is parallel to the surface, resonance absorption is zero. However, when the electric field is p-polarized (the  $E$  vector in the same plane as the incident and reflected light) and the incidence angle is  $\theta \neq 90^\circ$ , some of the oscillating electrons near the critical-density surface gain kinetic energy by resonant absorption (as much as 50% light can be absorption [Gibbon, 2005]) and are propelled past the critical-density surface into the colder regions of the target. These hot electrons are responsible for much of the X-ray generation.

As noted in Section 3.6.2, resonant absorption is thought to be the most important process associated with the enhanced X-ray yield resulting from a prepulse. Freidberg, et al. [1972] derived the equation for the incidence angle ( $\theta$ ) that when satisfied, gives the maximum resonant absorption and, presumably, the maximum X-ray yield:  $(k_0 L)^{1/3} \sin(\theta) = 0.8$ , where  $k_0$  is the laser wave number in free space and  $L$  the length of the expanded plasma from vacuum to the critical density. The isothermal-plasma scale length  $L$  is defined as  $L = C_s \Delta\tau$ , where  $C_s$  is the sound speed and  $\Delta\tau$  the width of the laser pulse with no prepulse or the delay time with a prepulse. Thus, an optimization procedure is given in which a prepulse is used to establish a length scale  $L$  when the main pulse arrives and the angle of incidence of the laser is adjusted to give the maximum main pulse absorption and, hence, the X-ray yield. However, this procedure does not take into account the impact of chirp, which has been shown to have a significant impact on X-ray yield.

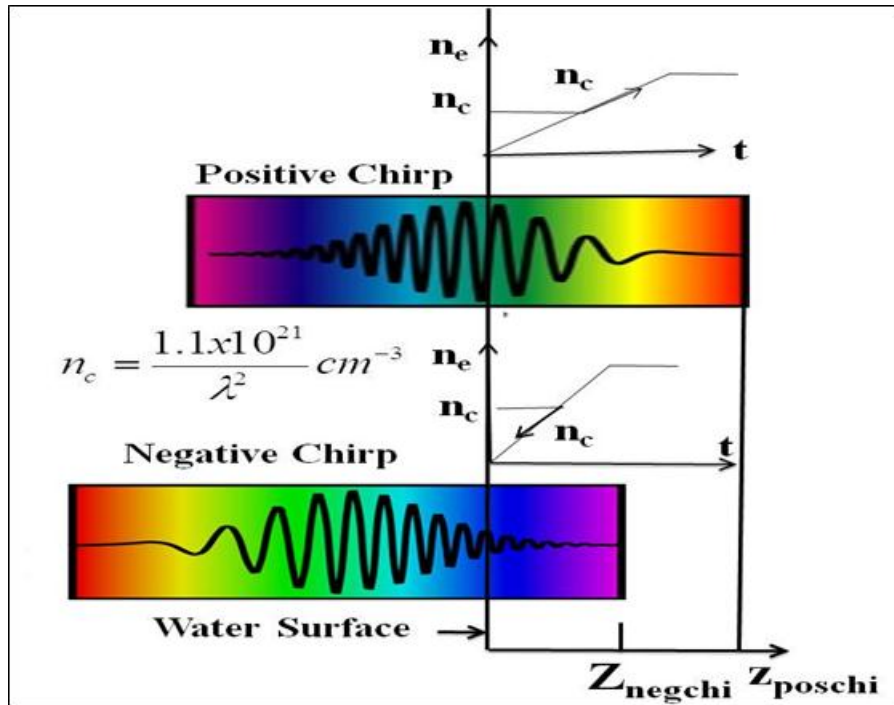


**Figure 40. Motion of critical-density surface**  
*(for positive- and negative-chirped pulses and the deeper penetration of the positive-chirped light into the water target)*

Our model for the effect of chirp on X-ray yield is illustrated in Figure 40. We consider resonant absorption to be important in explaining the chirp effect. The main idea, which is not found in the literature, is that positive-chirped pulses penetrate deeper into the water target than negative-chirped pulses. Because of the deeper penetration, the positive-chirped pulses create more hot electrons and, thus, more energetic X-rays than the negative-chirped pulses. To understand this, consider the following. For underdense plasma, the plasma length  $L$  is the distance from the initial plasma surface to the electron critical-density surface, where a portion of the light is strongly absorbed and a portion is reflected. The critical density is determined by the wavelength of the light,  $n_c \propto 1/(\lambda^2)$  and is not influenced by the electron-energy number density. For positive-chirped pulses, the leading red light reaches the critical-density surface first. Since the critical density of the shorter wavelength trailing blue light is higher than that of the red light, the blue light will penetrate deeper into the target. That is, the critical-density surface will move deeper into the fresh target as the colors of the positive-chirped pulses progress from red to blue. Although the penetration depth may be very small, it may be sufficient to continue to ionize and accelerate hot electrons as it continues to progress deeper into the fresh target. However, the opposite is true for negative-chirped pulses. The critical-density surface for the trailing red light will move in the direction opposite that of the incoming light--that is, into the already created plasma--and, thus, will be less effective in ionizing and accelerating the hot electrons needed to create X-rays. In our model positive-chirped pulses penetrate deeper into the water than negative-chirped pulses because the critical-density surface is moving deeper into the target as the pulse progresses from red to blue.

This results in the creation of a larger number density of hot electrons and, thus, higher X-ray yields. It is evident that detailed modeling of these complicated processes is needed. Our qualitative model suggests that future calculations should closely examine the impact of chirp on resonant absorption and the processes taking place near the critical-density surface.

Although the physical model presented describes the experimental observations, it does not exclude the possibility that the total conversion efficiency to energetic photons emitted in all directions is *not* significantly changed. Regardless, the experimental evidence indicates a significant enhancement in *usable* X-rays. Also, it is possible that the result of chirp and prepulse may cause redistribution in the X-ray yield in energy and angle. To our knowledge no experimental efforts have been made to obtain spectra that are resolved simultaneously in both energy and angle--much less as a function of chirp and prepulse. Indeed, detailed modeling and further experimentation are required to understand these complicated processes.

### 3.9 X-ray Emissions at Relativistic Conditions

The high yields from metal targets make them attractive for practical applications; however, they suffer from two major problems. The first is that they produce a large quantity of debris that tends to coat everything that is not protected. Second, to achieve high yields, each laser shot must interact with a fresh target. This requires that the solid must be translated and limits the number of shots before the target must be replaced. Both of these problems are exacerbated with the use of high-rep-rate lasers, which have higher average powers for a given footprint with increasing rep-rate. Potential applications that take advantage of the power density of high-rep-rate lasers would benefit from targets available at 100 kHz or even at megahertz [Frontiera et al., 2011; Kazansky et al., 2011]. Liquid targets can produce low quantities of debris and recover quickly from the disruption of a laser shot without the need to be moved. Many liquids such as melted metals [Uryupina et al., 2012], oil [Volkov et al., 2004], and water [Li et al., 2003; Fullagar et al., 2007; Hatanaka et al., 2008] have been used.

We selected water for detailed study because it is benign, easy to work with, readily available, and exhibits only bremsstrahlung emissions in the hard X-ray range, thus allowing different K and L line emissions to be obtained by dissolving salts, etc., into the water, without having a persistent line structure [Hatanaka, 2004]. The problem with water is that the X-ray yield can be very low if procedures are not taken to optimize the yield [see Figure 36(b)]. As shown, we have had some success in optimizing the X-ray yield of water.

We have demonstration that the X-ray yield for a water jet can be optimized by suitably selecting the polarization, angle of incidence, prepulse, and chirp. The X-ray yield for water, in the 1 - 15-keV range, can be increased to within a factor of  $\sim 10$  of that of Cu. These studies also provided some insight into the processes taking place and illustrated the need for detailed modeling and well-designed experiments to aid the understanding of the somewhat diverse published results. Specifically, the X-ray yields from a water-jet target have been increased to about  $10^9$  photons/s/4 $\pi$  sr, which is about an order of

magnitude less than the yield for a Cu target. However, if  $10^9$  photons/s could be delivered to a specimen, this flux would be sufficient to open the door for new extreme-light X-ray diagnostic application. The problem is that the X-rays being produced are emitted in all directions ( $4\pi$  sr), thus greatly reducing the X-ray flux that reaches the specimen.

In this section we investigate the possibility of solving the  $4\pi$  sr X-ray emissions problem by employing sufficiently large laser intensities that the electrons will be driven by the laser fields to relativistic velocities. For these large intensities, the possibility exists of creating an electron beam that can result in a beam-like source of X-rays. If this could be achieved, it would greatly enhance the X-ray yield delivered to a specimen, thus moving laser driven X-rays closer to application status.

### **3.9.1 Literature Search for Papers about Electron and X-ray Emissions Generated at Relativistic Conditions**

A particularly attractive aspect of bremsstrahlung is the fact that the angular distribution of X-rays becomes highly directional, typically in the forward direction (with respect to the motion of the electrons) if the electrons are initially at relativistic energies. For such a condition, the angular spread is proportional to  $\sim m_e c^2 / E_{\text{elec}}$ , where  $m_e$  denotes the mass of the electron,  $c$  the speed of light, and  $E_{\text{elec}}$  the initial electron energy [Jackson, 1975]. In the presence of a laser pulse, the initial energy of the free electrons is simply the ponderomotive energy defined in Eq. (1). (Note that  $m_e c^2 = 511$  keV.) Achieving relativistic electron energies is a matter of increased laser intensity, independent of the target, to  $10^{18}$  W/cm<sup>2</sup> or higher.

Because the physics of laser/target interactions at relativistic conditions is different from what we have studied, a literature survey was conducted to aid in understanding of electron and X-ray generation at relativistic conditions. The results of Rao, et al. [2007] provided insight into what may be the cause of the strong directionality of the X-rays in our experiments. They studied the annular distribution of laser-generated X-rays emitted from a Cu target and found highly peaked X-ray emissions normal to the Cu target. They demonstrated that this was the result of a highly directional beam of electrons generated by the laser/Cu-target interaction. For this reason much of our literature search involved laser-generated electrons.

The angular distribution of laser-generated electrons has received considerable attention during the last decade. Most of the studies were performed using solid targets. The results reported vary greatly; and, generally, no agreement has been reached on the description of the physical processes governing these phenomena. The resolution of this dilemma seems to depend on a variety of parameters such as laser polarization, incident angle, and intensity. Different researchers observe electrons being ejected in the laser specular-reflection direction, in the target-normal direction, and along the target surface. For example, Rao, et al. [2007, 2012] and Li, et al. [2001] recorded a single electron peak along the target normal in the backward direction, while Kodama, et al. [2001], Dusterer, et al. [2001], and Schwoerer, et al. [2001] observed a single jet along the laser specular-

reflection direction. Other researchers observed multiple peaks. For example, Chen [2008] recorded electron peaks in the target-normal and specular directions for an s-polarized laser and target-normal and along the target-surface directions for a p-polarized laser. Wang, et al. [2010] reported similar results--that is, peaks in the specular and target-normal directions, with the addition of another peak along the target surface for large incident angles. Zhang, et al. [2001], observed a peak in the target-normal direction for p-polarized light, while for s-polarization the emission was parallel to the target surface. Chen, et al. [2004] found two peaks--one in the specular direction and the other at 20 deg off the target normal toward the specular direction. Li, et al. [2006] reported three peaks: specular, forward-going normal to the target, and along the surface. Cai, et al. [2003], observed three peaks--target normal, specular, and laser backscatter. In a different experiment, Cai, et al. [2004], found two peaks--one in the specular direction and one close to the target normal (between normal and specular). Brandl, et al. [2009] reported several peaks between the target-normal and specular directions. Several other groups found that electrons were being ejected between the target-normal and specular directions and that the ejection angle was dependent on the laser intensity. Wang, et al. [2010] reported that for p-polarized light, the electrons were ejected in the specular direction for low laser intensities, while for higher intensities this peak shifted toward the target normal. For s-polarized light the peak was always in the specular direction, with the addition of another peak along the target-normal direction when a prepulse was present. More recently Tian, et al. [2012] not only observed a similar effect in an experiment but also presented a simple model explaining this effect and supported their findings with 2D particle-in-cell (PIC) simulations. Habara, et al. [2006] observed a slightly different effect--two peaks in the laser and specular directions for lower intensity that gradually shifted to one peak at the target surface for higher intensity. This question has also been studied theoretically. Ruhl, et al. [1999] derived a formula for the electron-ejection angle in the case of p-polarized laser light. This formula predicts that the electron should be ejected near the target-normal direction for most cases and in the specular direction only for ultra-relativistic electrons. Sentoku, et al. [1999] studied this question for both s- and p-polarized light and found that the electrons should be ejected in the specular direction and along the laser going into the target for s-polarization, while for p-polarized light, the answer is intensity dependent--the ejection angle is near target normal for low intensity and near the specular direction for high intensity. This is in opposition to the observations of Wang, et al. [2010]. Sheng, et al. [2000] presented another analytical formula for electron-ejection angle, which was revisited later by Chen [2006]. This formula predicted several ejection directions, including along the target surface. Given the range of results discussed above, the question of angular distribution of electrons ejected from the target during laser-matter interactions remains, for the most part, unanswered.

Very few studies have been conducted on electron angular distribution in liquid targets. Peng, et al. [2004] observed two symmetric electron jets at about 70 deg on each side, relative to the incident laser, using ethanol-droplet sprays. Liu, et al. [2009] reported a similar effect with argon clusters, where the two jets were at around 30 deg on each side, with the cross angle of two jets on the order of 60 deg. We are unaware of other studies that have been conducted on the angular distribution of hard X-rays from liquid targets.

### 3.9.2 Measurements of X-rays Generated at Relativistic Conditions

The Red Dragon laser and associated optical system were modified to achieve relativistic conditions by producing a high-quality focused beam at an intensity up to  $2 \times 10^{19}$  W/cm<sup>2</sup>. A simple plano-convex lens, previously used as a final focusing optic, was replaced with an off-axis parabolic mirror, which allowed minimization of the focal spot from  $\sim 30$   $\mu$ m down to  $\sim 2.6$   $\mu$ m [FWHM by intensity]. We installed an in-situ focal-spot monitoring system designed to check the focal-spot quality when needed. Figure 41 is an illustration of the test chamber with a 25- $\mu$ m-diameter water-jet target and the new optical system. Figure 42 shows a best-focus image obtained by our focal-spot monitoring system. In addition to this system, we installed another imaging system orthogonal to the focal-spot diagnostic. It utilizes the frequency-doubled light from the Legend laser (400 nm) and serves as the probe light in pump-probe experiments. When the two orthogonal imaging systems are used in conjunction during target alignment, the target position with respect to the laser focus can be determined within  $< 2$   $\mu$ m. Both imaging systems, as well as the parabolic mirror and the target-positioning system, are fully motorized and can be controlled remotely during the experiment. Typical laser contrast is on the order of  $10^5$  for the nanosecond prepulse and  $10^3$  for the picosecond prepulse, with a characteristic peak appearing around 25 ps before arrival of the main pulse, which is due to Pockel's-cell double passing.

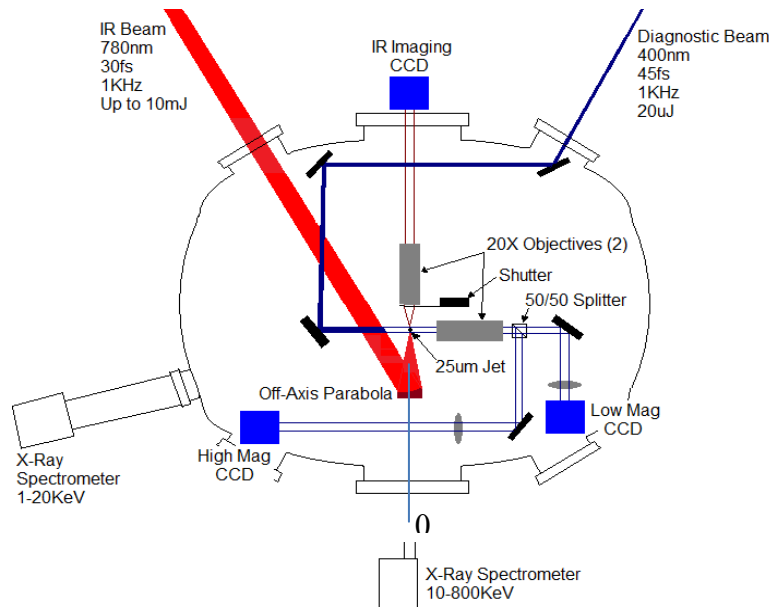


**Figure 41. Target-chamber schematic for the preliminary results presented in this document**

*(Note that both the target-normal and the specular directions are 0°)*



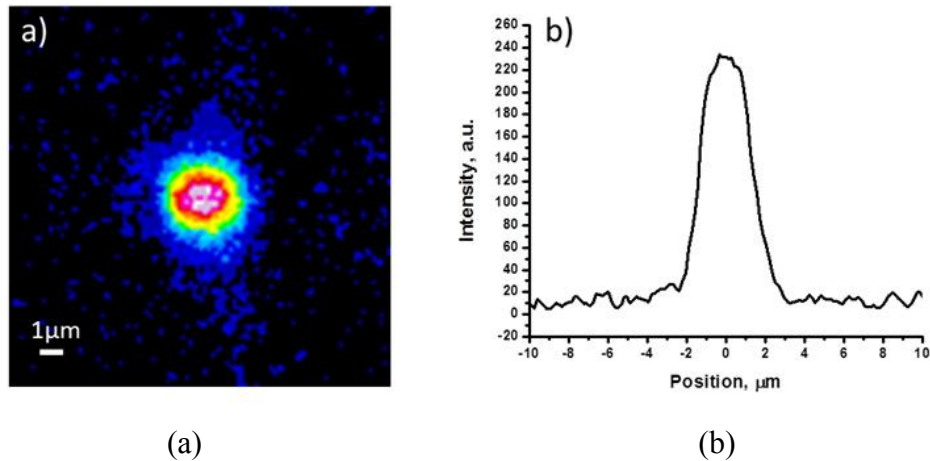


**Figure 42. Best-focus image taken by the focal-spot monitoring system**  
 ((a) The FWHM by intensity is around  $2.6\ \mu\text{m}$  and (b) lineout taken through the center of the best-focus image, showing the profile of the beam at focus.)

Preliminary measurements were made to explore whether operating at relativistic conditions would indeed influence the directionality and energy distribution of X-rays generated at these conditions. The Red Dragon was focused to a  $2.6\text{-}\mu\text{m}$ -diameter spot (FWHM) on a  $25\text{-}\mu\text{m}$ -diameter water jet. The intensity of the laser was  $\sim 10^{18}\ \text{W}/\text{cm}^2$ . These experiments revealed interesting and exciting details about the directionality and energy of the emitted radiation.

Figure 43 shows the angular distribution of human-dose equivalent (in mRem/hr) recorded by a Fluke 481 survey meter. The detector was located at a distance of about 10 cm from the chamber walls or about 50 cm from the TCC and had a low-energy cutoff of 30 keV. Each data point was obtained by averaging over at least 1 min, with a readout sampling rate of 2 Hz. The figure clearly shows a very strong peak back toward the laser ( $0^\circ$ ), with a smaller peak along the laser incident direction ( $180^\circ$ ).

We were surprised by the large dose of X-rays shown in Figure 43. As a point of reference, the typical X-ray dose outside water- and metal-target chambers during our past studies never exceeded  $\sim 30\ \mu\text{Rem}/\text{hr}$ . At relativistic conditions the emissions increased by more than a factor of  $10^4$ . Some of this increase was due to the different chamber construction, but most of it is thought to be due to an abundance of high-energy X-rays. What was even more surprising and exciting is that these energetic X-rays were highly directional in the *specular* direction *opposite* the anticipated direction, anti-parallel to the laser propagation. This is exciting because the strong directionality offers the possibility of increasing the X-ray flux delivered to a specimen, thus opening the door for more potential applications for extreme-light diagnostics.

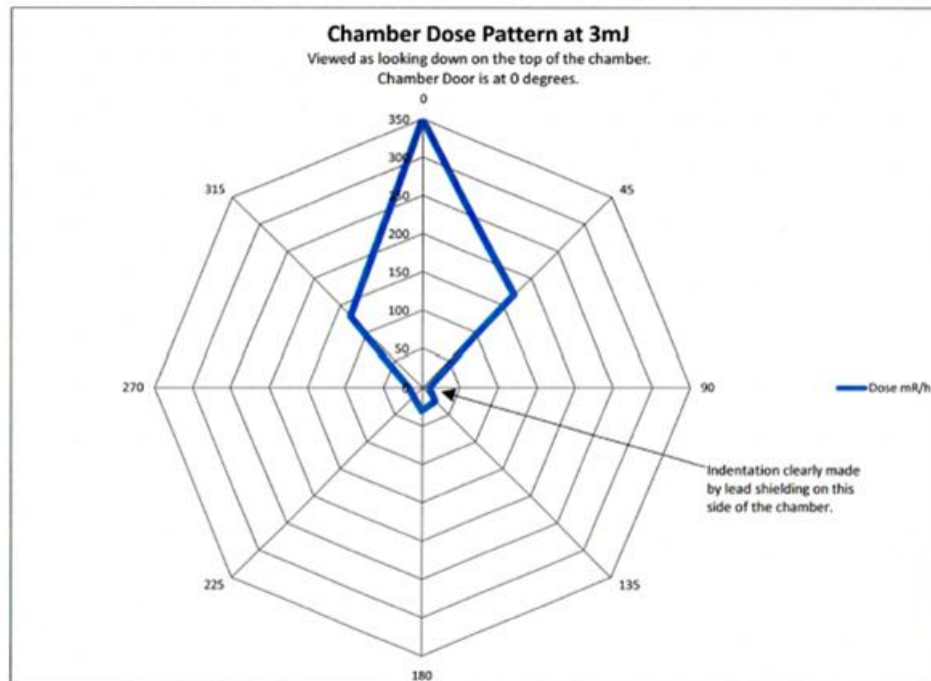


**Figure. 43. Angular distribution of human-dose equivalent (in mRem/hr) recorded by a survey meter**

*(The detector was located at a distance of about 10 cm from the chamber walls or about 50 cm from the TCC.)*

The literature review presented in Section 3.9.1 identified the work of Rao, et al. [2007] as one of the most relevant related to back emissions of electrons and X-rays. They investigated the annular distributions of X-ray emission from a 10-mm-thick, smooth Cu target. The target was irradiated by a 150-mJ, 45-fs, 2-Hz laser with an intensity of  $\approx 10^{18}$  W/cm<sup>2</sup>. The incident angle of the laser was 45°, and the X-ray detector was aligned normal to the Cu target. They observed a highly peaked bremsstrahlung radiation in the normal direction. The peak dose at a distance of 50 cm from the target was 4 mRad/hr. They found that this radiation emanated from two sources--the Cu target and the glass window of the target chamber. The laser/Cu-target interaction generated a highly directional beam of energetic electrons moving in the direction normal to the target. The loss of energy of some of these electrons in the Cu resulted in bremsstrahlung radiation from the target. The electron beam then lost all of its energy as it hit the glass window in the target chamber. This resulted in the second source of highly directional X-rays. They discovered this by measuring the X-ray dose as a function of distance from the target and using the  $1/r^2$  law for the expected decay. We repeated their experiment. The results are shown in Figure 44.

A survey meter similar to that employed by Rao, et al. [2007] was used to record data from a series of dose measurements outside the vacuum chamber along the laser axis (0° direction) as a function of distance. The results are shown in Figure 44, where  $1/(\text{dose})^{1/2}$  is plotted as a function of the distance to the TCC. In these units the dependence should be linear since the decay follows the  $1/r^2$  law. A line was fitted to the data using the least-squares method. If all X-rays were generated in the original target, then this line would

cross the X-axis at the origin. However, if an electron jet were present, two X-ray sources would exist, which would result in the “effective” X-ray source being located somewhere between the two, depending on the intensities of each source. Indeed, our fit indicates that our “effective” X-ray source was located 5.6 cm in front of the target--roughly the location of the parabolic-mirror mount. This means that the secondary X-ray source was created by the electron jet hitting the parabolic-mirror mount and that the intensity of this secondary source dominated the intensity of the original source at the TCC. The intersection of the fitted line with the X-axis shows that the “effective” X-ray source was located 5.6 cm in front of the target. These results strongly suggest that the angular distribution of the X-rays in Figure 43 is the result of a highly directional beam of electrons hitting an unintended target.

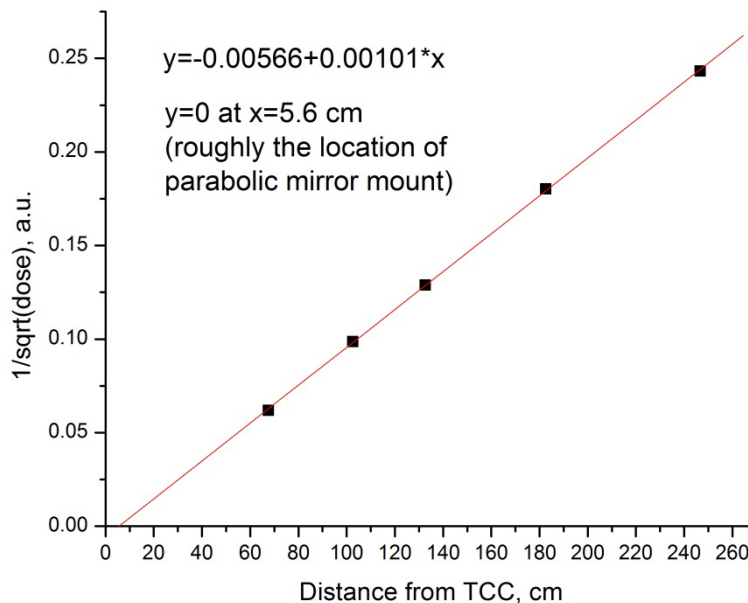


**Figure 44. Dose as a function of distance from the TCC**

*(The intersection of the fitted line with the X-axis shows that the effective X-ray source was located 5.6 cm in front of the target.)*

The results shown in Figure 43 indicate an abundance of high-energy X-rays. A question remains concerning the energy distribution of these X-rays. To characterize the X-rays emitted in our experiments, we measured the X-ray spectra at two key directions (0° and 180°) using an Amptek X-123 CdTe spectrometer. To avoid photon pile-up, the detector was placed at a distance of 10 m in the case of the 0° measurement and 7 m in the case of the 180° measurements. After deconvolution of the attenuation of the X-rays in the chamber materials and air, the processed spectra are shown in Figure 41, where the green curve represents the 180° direction and black curve, the 0° direction. We observed a peak in X-ray energies of about 100 keV, with a long decay that extended beyond the 800-keV of our instrument. The temperature taken from curve fitting the X-ray decay was in the 30 - 40 keV range. Thus, it is evident that we were producing very energetic X-rays and perhaps some gamma rays.

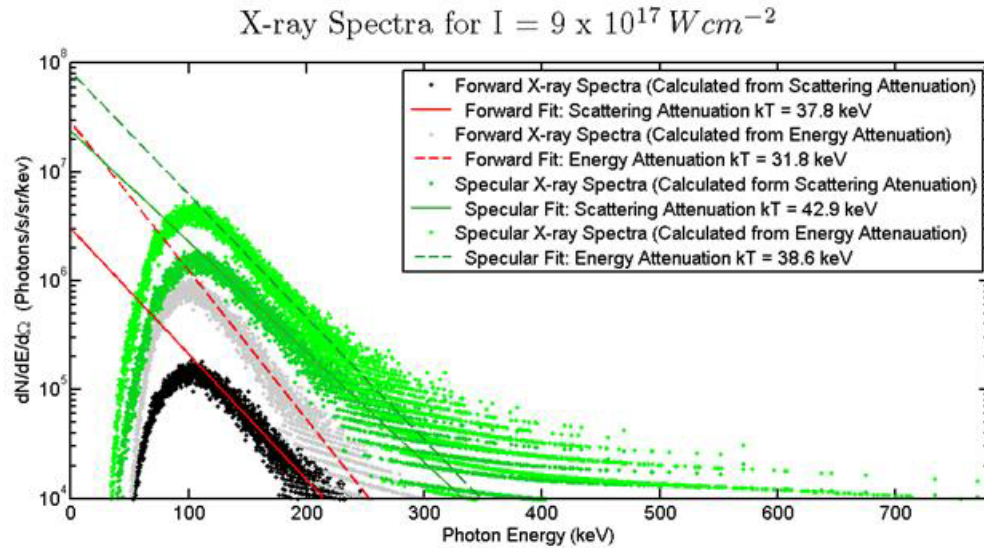


**Figure 45. Preliminary X-ray spectra along the laser axis**  
*((black and gray)  $180^\circ$  and in the specular direction (green)  $0^\circ$  obtained using a calibrated CdTe detector stack in the single-hit regime. The attenuation of the chamber and optical components is deconvolved, first assuming that any scattered photons are not detected, which results in an underestimate of the spectra (darker plots and solid-line exponential fits). The assumption that any photons not attenuated reach the detector, have only small-angle scattering events, and lose negligible energy results in an overestimate of the spectra (lighter plot and dashed exponential fits.))*

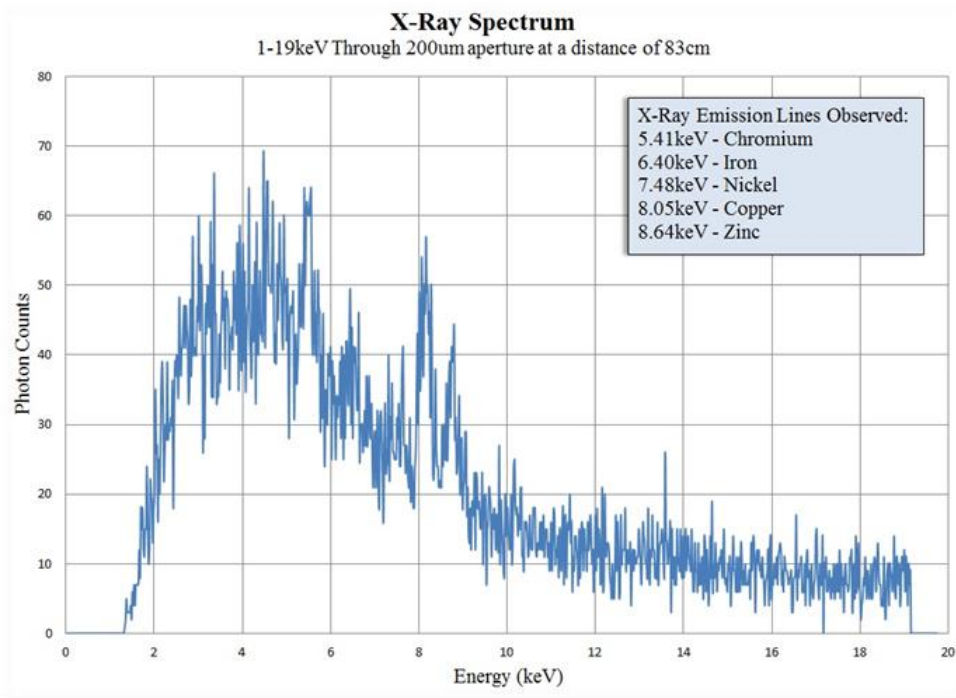


**Figure 46. Typical uncorrected raw X-ray spectrum observed from experiments**

Note in Figure 45 that we did not obtain good data below about 50 keV--a result of the 30-keV cut-off limit of the spectrometer. We attempted measurements with a single-photon-counting spectrometer that operated between 1 and 20 keV. These measurements were not successful. However, the results are presented here (in Figure 46) because they illustrate measurement problems that need to be resolved. The normal-operation mode assumes that no X-rays above the highest energy to which the detector is still sensitive are present in the spectrum. A collimator is typically used to limit the flux going to the detector--especially when the spectrometer is used in the single-photon-counting regime. Our spectrometer was equipped with a set of 2-mm-thick tungsten collimators with different aperture diameters. Caution must be taken when using such collimators for cases when the X-ray spectrum has photons with very high energies, such as shown in Figure 45. Even when the photon energy is too high to cause an event in the detector itself, scattering effects in the collimator or the detector housing can create secondary X-rays (with lower energies) that will be registered by the detector. Also, if a scattered photon loses sufficient energy, it may eventually fall into the range of detector sensitivity, even though initially it had much higher energy, and it will register as a lower energy photon. Note in Figure 46 that the spectrum contains K- $\alpha$  radiation for different metals in the collimator and aperture.

### **3.10 Visualizations of Laser/Water-Jet Interactions**

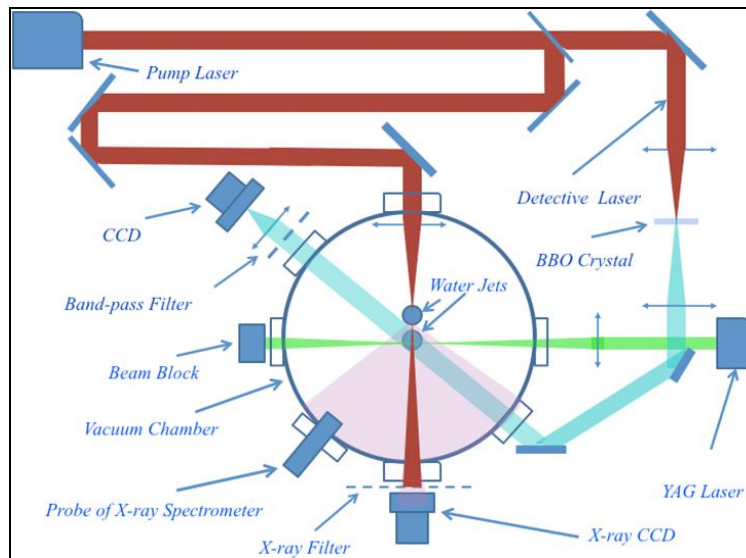
#### **3.10.1 X-ray Visualization**

Short-pulse X-ray sources generated by extreme light offer the potential to visualize the dynamics of systems that are opaque to longer wavelengths of light. Using the X-ray source developed during the current AFOSR program, we are convinced that it is possible to resolve temporally and spatially the dynamic behavior of the interaction of intense light with a liquid stream using a pump-probe technique. This is akin to the decades-old experiments where femtosecond-dye-laser pulses were used to explore the ultrafast dynamics of laser dyes. Only here the light from an extremely hot plasma is used to observe the development of extremely hot plasma systems.

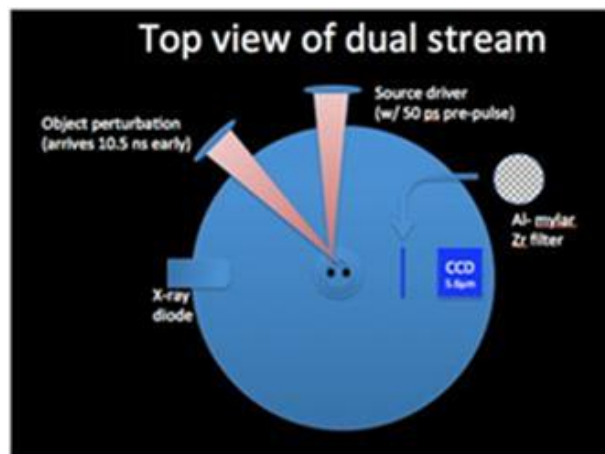
During this program we developed the ability to (1) generate X-rays from water jets, (2) perform basic X-ray imaging, and (3) perform optical pump-probe experiments with synchronization for pulses spanning the millisecond to femtosecond regime. These methods provide the tools needed to use the pump-probe technique to make extreme-light X-ray movies of dynamic processes that evolve from femtosecond to millisecond time scales. Questions remain concerning the X-ray yield and time averaging required to obtain well-resolved, high-quality X-ray images using the pump-probe technique.

The source initially used for X-ray projection in our laboratory is a solution of equal weights of CsCl and water flowing in a 20- $\mu\text{m}$  stream and irradiated by 40-fs pulses of intensity  $\sim 10^{16} \text{ W/cm}^2$ . The object is a second stream of similar description but separated from the first by 3 mm. The dual-stream setup is illustrated in Figures 47 and 48, where an intense X-ray-generating pulse is delivered (with a 50-ps prepulse) to the left-hand *source* stream, and the ablation of a weakly driven *object* stream is captured. The system in Figure 47 had a variable delay line so that laser-pumped X-ray probe studies could be

performed. The *object* is the right-hand stream in Figure 48, is irradiated by the pump laser.



**Figure 47. Experimental setup for visualizing laser/water-jet interactions**



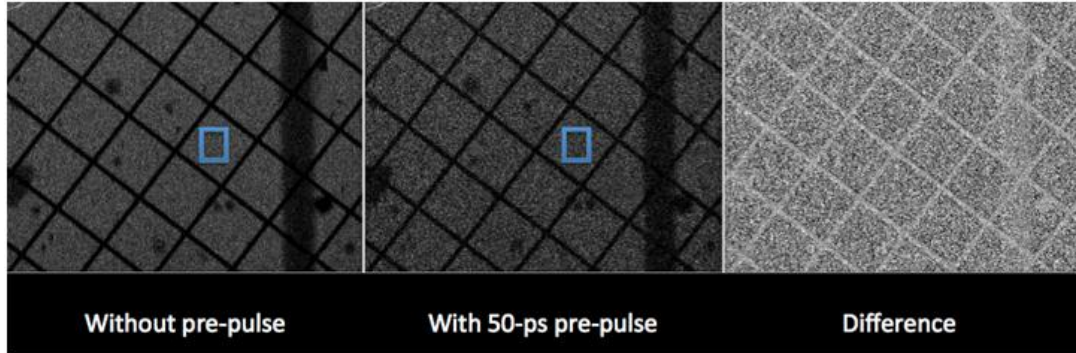
**Figure 48. Top View of dual-water-jet setup**  
(The X-ray source is the left-hand stream, pulse.)

Figure 49 shows the projections of a stream onto a CCD camera with  $9\times$  magnification and a Ni mesh with  $2\times$  magnification. The mesh has  $28\text{-}\mu\text{m}$  spars spaced  $363\text{ }\mu\text{m}$  on center, and the stream has a width of nominally  $20\text{ }\mu\text{m}$ . Each image is a sum of twelve 10-s exposures, totaling 2 min.

Following this demonstration of basic X-ray imaging with the CsCl-doped water, the X-ray source was redesigned using a significantly tighter focusing geometry to increase the intensity to more than  $10^{18}\text{ W/cm}^2$ . Optical components were also configured for enhancing the observation of the alignment of the beams on the stream to improve



positioning accuracy. The intensities available in this new geometry are similar to those used by Chen, et al. [2004] and for generation of X-rays from solid targets with efficiencies of 4 - 60 keV [Hou, et al., 2006] from  $5 \times 10^{-4}$  for Cu and Ge to  $2 \times 10^{-5}$  for Mo and Ag. These exceed by two orders of magnitude the intensities used by Tallents, et al. [2004] to obtain an efficiency of  $3 \times 10^{-4}$  for He-like Cl ( $\sim 3$  keV). For the present 10-mJ input energy, this is consistent with per-shot production of  $3 \times 10^{-6}$  J or  $\sim 10^9 - 10^{10} > 3$  keV quanta per pulse ( $10^{12} - 10^{13}$  quanta per second) from any of the elements mentioned above.



**Figure 49. Images taken without and with a 10.5-ns object-stream prepulse and the difference**

*(The boxes indicate the areas used to normalize the exposure prior to subtraction. The 20- $\mu$ m water jet passes down the right-hand side of the images.)*

Measurement of the X-ray flux that has resulted from the newly configured source suggests that we may already see a flux of  $> 10^{11}$  photons/s into  $4\pi$  sr at energies exceeding 4 keV. By imaging onto a 1.7-cm<sup>2</sup> (1.3-cm format) CCD placed 3.7 cm from the source, we will be able to collect  $10^{-3}$  of the emitted photons and record  $10^8$  photons per second, with a spectral quantum efficiency ranging between 20% and 80%. Thus, we can anticipate exposures on the order of  $10^2$  photons per second per pixel. Using a typical CCD signal calibration of  $\sim 1$  count per 50 eV of photon energy and assuming  $\sim 3$  keV photon energies, a CCD well will be very near saturation at  $10^5$  electrons per pixel using a 1-s exposure.

### 3.10.2 Shadowgraph Visualization

High-speed shadowgraph movies of laser/water-jet interactions were obtained using pump-probe experiments. The experimental setup is similar to that in Figure 47, except that the probe beam was normal to the pump beam, as shown in Figure 50. The probe-beam delay was controlled either by an optical delay line, as shown in Figure 47, or electronically, as illustrated in Figure 4. The optical-delay line could span the time before time zero when the pump hit the target to about 4 ns. Figure 51 displays visualizations of the ionization of air caused by the pump laser as it approached a water-jet target. This was one of the techniques used to determine time zero. The time resolution of the probe measurements was about 40 fs using the optical-delay line.

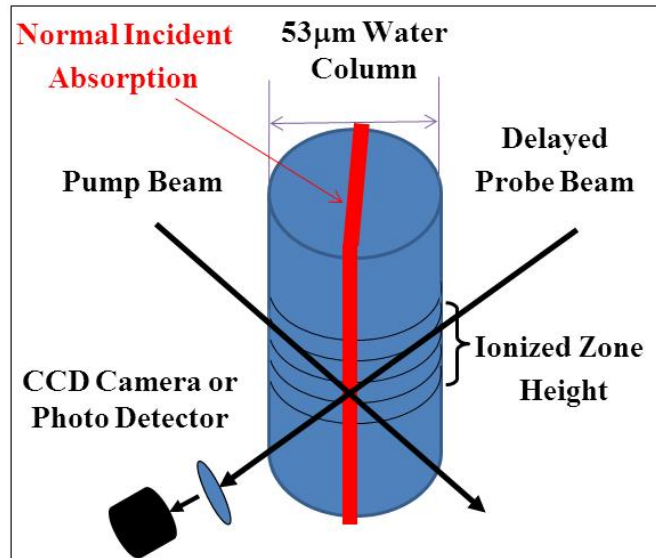


**Figure 50. Illustration of pump-probe shadowgraph experiment of a laser interacting with a water jet**

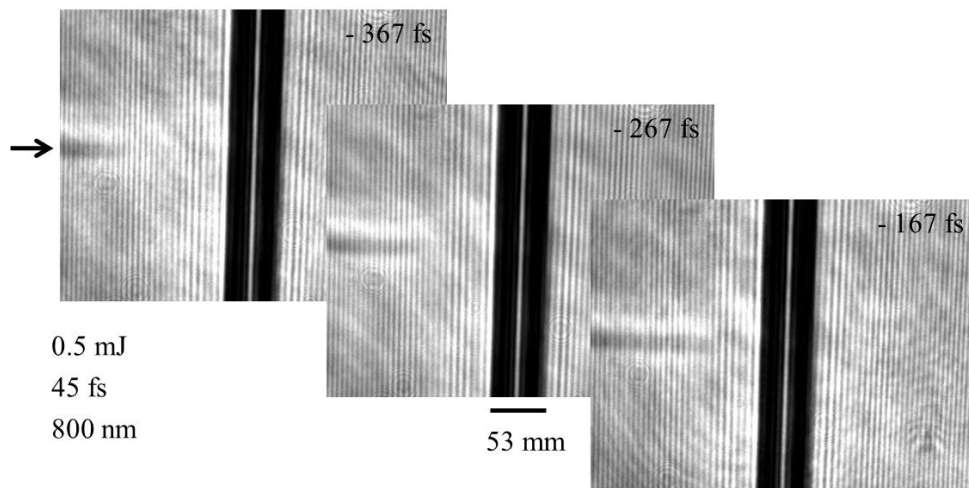


**Figure 51. Pump-probe images of the ionization of air by a probe beam approaching a water-jet target**

*(This technique was one method used to determine the time when the laser pulse hit the target. The laser is approaching from right to left.)*

High-speed movies were made for femtosecond and nanosecond laser interactions with water jets. Figure 52 shows an YAG laser with a 10-ns pulse width interacting with a 53- $\mu\text{m}$ -diameter water jet. Ten images for a given time after the pump beam hit the target were collected, and an average image was calculated. The image most like the average was selected. The selected images for a time sequence were organized into a movie using Image J, QuickTime, or a similar program. Single-shot images had a very similar appearance. This is noted in Figure 53 where three frames for 6-ns, 30-ns, and 130-ns



times were randomly selected. It should be noted that some of the details differ, but the general shape of the images is the same.

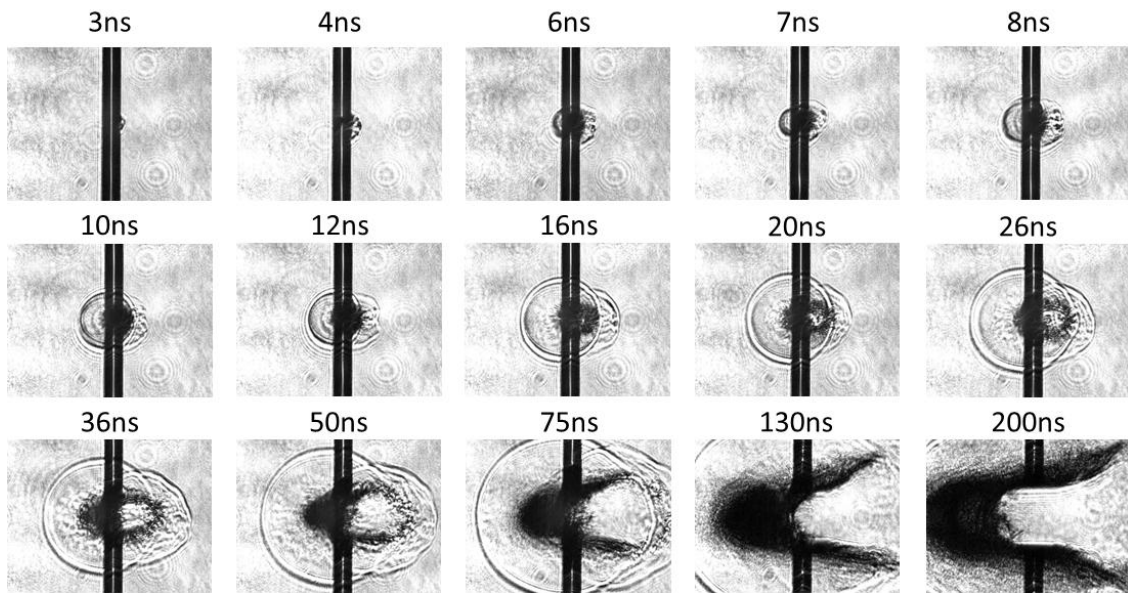


**Figure 52. Shadowgraph images of a 10-ns-pulse-width YAG laser interacting with a 53- $\mu\text{m}$ -diameter water jet in air**  
*(The probe laser had a pulse width of 45 fs. The jitter in the frame time was about  $\pm 2$  ps. The laser is approaching from right to left.)*

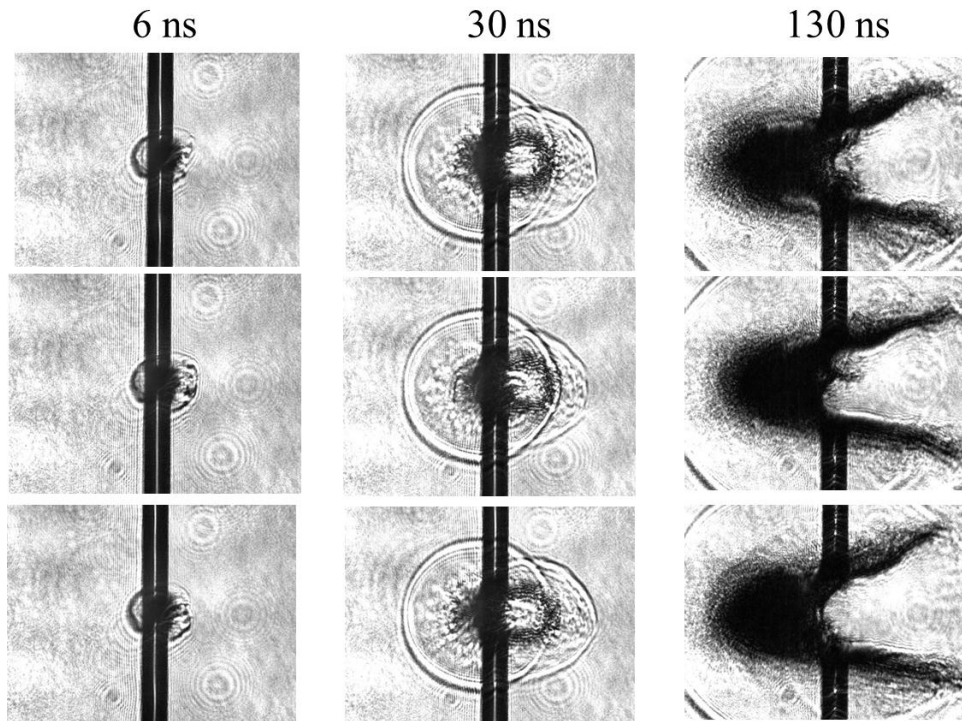


**Figure 53. Random selection of three of the single-shot images at 6 ns, 30 ns and 130 ns**

*(The images show the interaction of a YAG laser with a 53- $\mu$ m-diameter water jet, shown in Figure 52. The laser is approaching from right to left.)*

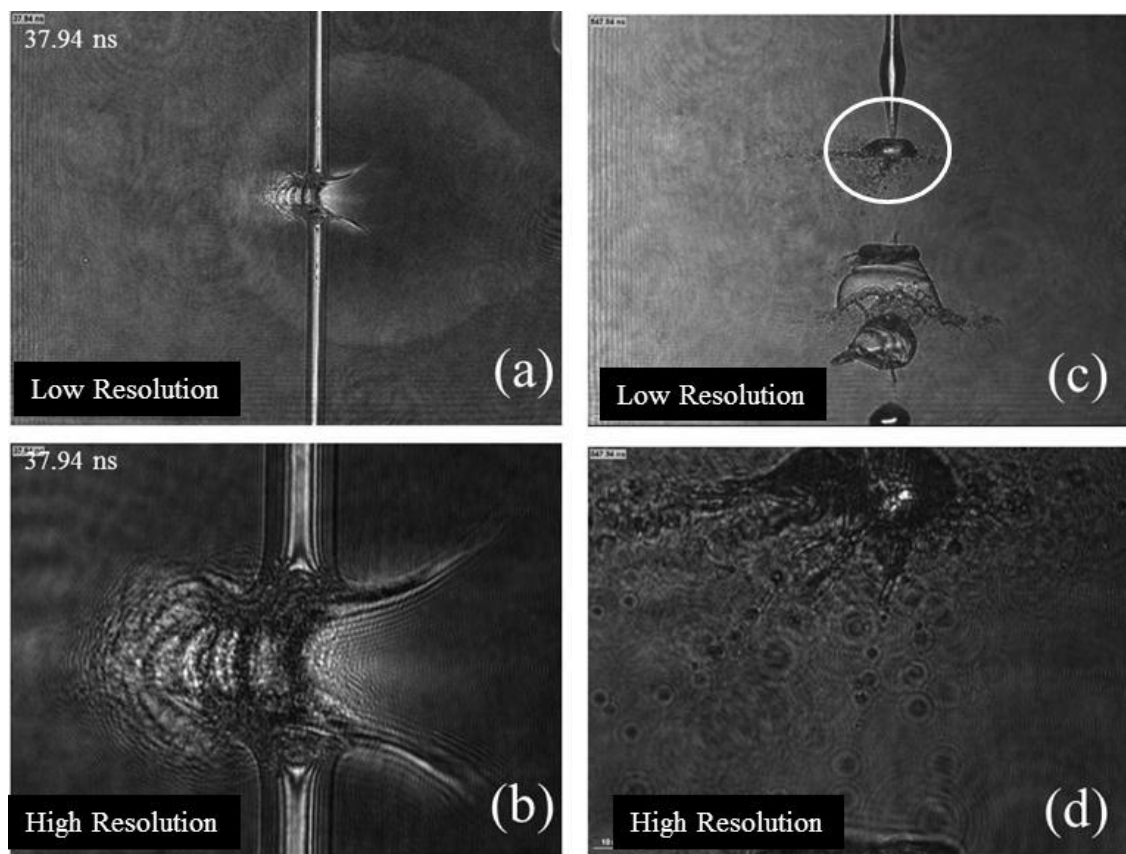


**Figure 54. Simultaneous low- and high-resolution shadowgraph images of a tightly focused 30-fs laser**

*(The intensity is about  $10^{18}$  W/cm<sup>2</sup> interacting with a 25-μm-diameter water jet [(a) and (b)] and water droplets [(c) and (d)], respectively, at 37.94 ns after the pump laser hit the target. A high resolution image of the circled region in (c) is shown in d. The laser is approaching from right to left.)*

The imaging system was modified so that high-and low-resolution shadowgraph images of the laser/target interactions could be taken at the same time. The modification involved splitting the probe beam into two beams after it passed through the target. One beam was directed through a 25× microscope objective and the other through a 10× objective. The images were then recorded with digital cameras. Examples of simultaneous low- and high-resolution images of the interaction of an intense ( $I = 10^{18}$  W/cm<sup>2</sup>), 30-fs laser pulse with a 25-μm-diameter water jet are shown in Figures 54(a) and 54(b) after an interaction time of 37.94 ns. Note that the image for the femtosecond laser interaction with a 25-μm-diameter water jet [Figure 54(b)] has about the same shape as that shown for the 130-ns image of a 10-ns YAG laser interaction with a 53-μm-diameter water jet. Figures 54(c) and 54(d) illustrate how the plasma and debris of an intense laser hitting and completely shattering a micron-size droplet were spread to much larger drops above (in white circle) and below the exploding drop, which can no longer be seen.

This program has established the procedures for making high-resolution movies that show the time and spatial evolution of laser/target interactions from the time the laser hits the target, time zero, until all dynamic processes have ceased, which is usually 10's to 100's of microseconds. These movies have provided insight into the processes taking place. For example, the images in Figure 52 illustrate that very small droplets of water can be formed during laser/water-jet interactions. These small droplets can be targets for a second laser with the goal of generated X-rays or perhaps particle-diagnostics sources. Indeed, Figures 54(c) and 54(d) illustrate how a laser-induced explosion of one drop can induce the plasma destruction of surrounding droplets. This process could provide the environment for generating radiation and particle sources. These processes should be investigated in future research efforts.

## **4.0 SUMMARY OF PUBLICATIONS AND PRESENTATIONS**

### **4.1 Development of Laser-Based X-Ray Source for Dense Spray and Soot Diagnostics**

Studies that were performed at Argonne National Laboratory have shown the utility of soft X-ray imaging as a diagnostic of dense sprays. Also, research performed by several groups has demonstrated that small-angle X-ray scattering is a useful tool for studying soot formation. However, tunable high-spectral-brightness sources of X-rays are largely limited to synchrotrons and free-electron lasers. Other research communities have shown that X-rays can be generated from the transient plasmas that are produced by the interaction of high-intensity laser pulses with matter--both gas and condensed phase. The present study was undertaken to find an efficient means of generating soft X-rays ( $\sim 9$  keV) using this approach. The output of a Ti:sapphire regenerative amplifier ( $\sim 40$  fs, 2 mJ, 1 kHz) was focused onto a liquid stream, and a silicon photodiode/mca detection unit was employed to monitor the emitted X-ray spectrum. Experiments are underway to determine X-ray yields from neat liquids (water and hydrocarbon solvents) as well as doped liquids. X-ray spectra typically show spectrally broad contributions from bremsstrahlung and narrow K-alpha characteristic lines. Some intended applications require the characteristic lines, while others require a broad spectrum. Finding ways to alter the ratio of K-alpha to bremsstrahlung contribution and "tune" the bremsstrahlung component is the key to the present research effort. The results of this study were documented by M. S. Brown, G. L. Switzer (both of ISSI), J. R. Gord, and W. M. Roquemore (both of AFRL) in an invited paper that was presented at the Gordon Research Conference on Laser Diagnostics in Combustion, which was held 31 July - 5 August 2005 in South Hadley, MA.

### **4.2 Laser-Target Generation of Soft X-Rays**

Despite the large body of work to date with respect to emission from laser-generated plasmas, current understanding is not yet sufficiently comprehensive to provide recipes for generating a specific desired X-ray spectrum with some minimum yield. In fact, some disagreement is encountered over simple single-parameter scaling laws used for empirical representation of X-ray emission. Consequently, much more research in this area is required. The overall research aim in the present study was to find--primarily through experimentation--an optimal manner in which to generate X-ray line emission in the 5-10 keV range for use for small-angle X-ray scattering of primary soot particles in flames and transmission imaging of dense-spray regions. While X-ray yields are typically largest with solid targets, droplet and stream targets offer some clear advantages. It has been noted by many researchers that solid targets result in debris that can compromise optics and detectors near the target. Also, droplets and streams provide a convenient means of changing the elemental composition in the target volume. A single solvent can be used as a carrier for multiple solutes, making the X-ray spectrum of the source discretely tunable. For these two reasons our work was initiated using a piezoelectric-driven droplet-on-demand generator that could be operated in either a droplet or stream mode. The diameter of the droplet or stream is well-defined and fixed by the nozzle tip of the generator. The results of this investigation were documented by M. S. Brown, G. Switzer (both of ISSI), J. R. Gord, W. M. Roquemore (both of AFRL), A. Bernstein, D. Symes, and T. Ditmire

(all of Texas A&M University) in a paper that was presented at the OSA Laser Applications to Chemical, Security, and Environmental Analysis Topical Meeting and Tabletop Exhibit, which was held 5-9 February 2006 in Incline Village, NV.

#### **4.3 Laser Generation of X-Rays for Air-Force Applications**

Residual-stress measurements are an important tool for diagnosing manufacturing procedures of aircraft-engine components, and nondestructive approaches are also important. One such approach makes use of X-ray diffraction. Recently, personnel at Wright-Patterson Air Force Base performed useful residual-stress measurements on coupons of turbine-blade materials using the X-ray output of a synchrotron. The goal of the present study was to provide a local and somewhat portable laser-based source of X-rays that could be used in place of the synchrotron for NDE tests such as residual-stress measurements. The generation of transient plasmas from the interaction of short, intense laser pulses with a wide range of materials leads to the emission of X-rays. The hot electrons in the laser-generated plasma produce the X-rays via bremsstrahlung or photoionization, which leads to characteristic line emission. The bremsstrahlung spectrum is broad and continuous. Line emission appears superimposed on the broad continuum. The yield and nature of the X-ray spectrum depends on the hot-electron density and energy distribution. The overall research aim of this study was to find--primarily through experimentation--an optimal manner in which to generate X-ray emission that would be suitable for Air Force applications. Line emission can be used for small-angle X-ray scattering of primary soot particles in flames and transmission imaging of dense-spray regions. Broadband emission is useful for residual-stress measurements. While X-ray yields are typically largest with solid targets, droplet and stream targets offer some advantages. Solid targets result in debris that can compromise optics and detectors. Also, droplets and streams provide a convenient means of changing the elemental composition in the target volume. A single solvent can be used as a carrier for multiple solutes, making the X-ray spectrum of the source discretely tunable. For these two reasons, the present study was initiated through the use of a piezoelectric-driven droplet-on-demand generator that can be operated in either a droplet or a stream mode. The results of this study were documented by M. S. Brown, G. L. Switzer (both of ISSI), J. R. Gord, W. M. Roquemore (both of AFRL), D. Symes, and T. Ditmire (both of the University of Texas at Austin) in a paper that was presented at the 31<sup>st</sup> Annual AIAA Dayton-Cincinnati Aerospace Science Symposium, which was held 7 March 2006 in Dayton, OH. Dr. Michael Brown (ISSI) was Chair of the Session on Fluid Dynamics III: High-Speed Flow Plasmas at this symposium. This paper was also presented in poster form at the Annual Poster Session sponsored jointly by the Dayton Section of the American Chemical Society and the Society for Applied Spectroscopy, which was held 7 March 2006 in Dayton, OH.

#### **4.4 Imaging of Laser-Generated Micro-plasmas**

X-rays are emitted from micro-plasmas created during the interaction of a tightly focused, short-pulse laser (1000 Hz, 40 fs, 2 mJ) with the surface of solid and liquid targets. The engineering development of such X-ray sources requires some knowledge of the formation and evolution of the micro-plasmas. Issues include the potential for gas breakdown prior to the laser pulse striking the target. Such breakdown can lead to

undesirable effects such as lensing and absorption of the incident energy. To gain a better understanding of such breakdown, an optical train was constructed for performing spectral interferometry in the waist region of a pulsed laser passing through helium. The interferograms provide a time-resolved image of the breakdown event, with resolution in one spatial dimension as well. The interferograms indicate the onset and degree of ionization present in the focused waist region. The emissions generated in these micro-plasmas are spatially coherent and, hence, provide a pulsed point-source for performing phase-contrast imaging with minimal use of optics. Several methods for quantitatively analyzing such images have recently been developed. Presently, the application of these techniques to current goals is being investigated. The results of this investigation were documented by M. S. Brown, C. L. Rettig, K. D. Frische (all of ISSI), J. R. Gord, W. M. Roquemore (both of AFRL), and J. A. Nees (the University of Michigan) in a paper that was presented at the 32<sup>nd</sup> Annual AIAA Dayton-Cincinnati Aerospace Science Symposium, which was held 6 March 2007 in Dayton, OH. The paper received the Best-Presentation Award at this symposium, and Dr. Michael Brown (ISSI) was Chair of the Session on Jet Flow. This paper was also presented in poster form at the Annual Poster Session sponsored jointly by the Dayton Section of the American Chemical Society and the Society for Applied Spectroscopy, which was held 1 March 2007 in Dayton, OH.

#### **4.5 Development of Laser-Generated X-Ray Source for Air-Force Applications**

The development of enhanced hardware for Air-Force applications has increased the demand on diagnostics to aid in the assessment of new systems and components. A local source of laser-generated X-rays is being developed with the near-term goal of using the X-rays to monitor soot and condensate development in combustion environments. Longer-term goals include the use of X-rays for detecting residual stress in turbine components. The X-rays are generated in transient micro-plasmas that are created when a pulsed laser (1000 Hz, 40 fs, 2 mJ) is focused onto the surface of solid and liquid targets. X-ray spectra reveal both broadband emission (via bremsstrahlung) and narrow line emission (characteristic K-alpha). The broad emission will be useful for phase-contrast imaging of sprays and particulate fields, and the narrow line emission will be useful for small-angle X-ray scattering from particulates (soot or condensates). The advantages for such a source include very high brightness and spatial coherence and extremely short pulse widths, allowing investigations into dynamics not previously possible. Current efforts are focused on the use of rotating elemental metal foils that should provide an unattended source of X-rays for 1 hr or more. Measurements of X-ray emission are being made to determine optimal conditions for enhanced yield of line and broadband emission. Key parameters include laser-focusing geometry, background gas pressure, and background gas composition. Issues for stable operation include maintaining constant, focused laser intensity on the target surface, providing fresh target material for each laser shot, and managing debris removal. The results of this study were documented by C. L. Rettig, M. S. Brown, (both of ISSI), J. R. Gord, and W. M. Roquemore (both of AFRL) in a paper that was presented at the 32<sup>nd</sup> Annual AIAA Dayton-Cincinnati Aerospace Science Symposium, which was held 6 March 2007 in Dayton, OH, and in poster form at the Annual Poster Session sponsored jointly by the

Dayton Section of the American Chemical Society and the Society for Applied Spectroscopy, which was held 1 March 2007 in Dayton, OH.

#### **4.6 Laser-Induced Breakdown Spectroscopy for Detection of Volatile Aerosols**

It is well known that aircraft exhaust contains soot particulates. Less well known is the fact that the exhaust also contains volatile aerosols and that their number density exceeds that of the soot particulates by orders of magnitude. Sulfur in the jet fuel plays a key role in the production of these volatile aerosols that are likely to have an impact on cirrus-cloud formation. To date little information has been gathered on this class of exhaust particulates. We have recently initiated a program to employ laser-induced breakdown spectroscopy (LIBS) to detect and characterize the volatile aerosols with regard to composition, number density, and size. Historically LIBS measurements of particulate size and size distributions have been executed using nanosecond-pulse-width lasers. Our experiments employed both nanosecond- and femtosecond-pulse-width lasers. A chamber is currently under construction, and future testing will permit LIBS measurements of a single chemical species in a gas phase as well as in both liquid and solid particulate form. Experiments will enable tests to determine the degree to which different phases of the same analyte can be distinguished, particularly if more than one phase is present. LIBS efforts by others have recently shown that the interaction between the initial plasma and an aerosol particle that is present in the same volume is more complex than historically thought. We are currently engaged in experiments to explore some of these issues. Shadowgraph and plasma-emission images have been acquired of LIBS breakdown on 50- $\mu$ -diameter water columns. The images were time-delayed with respect to breakdown and revealed the initial shock and blast waves. For longer delay times the shadowgraph images revealed complex fluid motion in response to the impulsive energy deposition. The results of this investigation were documented by M. S. Brown, K. D. Frische (both of ISSI), T. G. Erickson (Rensselaer Polytechnic Institute), J. R. Gord, and W. M. Roquemore (both of AFRL) in a paper that was presented at the 33<sup>rd</sup> Annual AIAA Dayton-Cincinnati Aerospace Science Symposium, which was held 4 March 2008 in Dayton, OH. Dr. Michael Brown (ISSI) was a member of the Organizing Committee (Corporate Sponsors Chair) and Chair of the Session on Innovations in Aircraft Design at this symposium. This paper was also presented in poster form at the Annual Poster Session sponsored jointly by the Dayton Section of the American Chemical Society and the Society for Applied Spectroscopy, which was held 4 March 2008 in Dayton, OH.

#### **4.7 Efficiency and Scaling of Ultrashort-Pulse, High-Repetition-Rate, Laser-Driven X-Ray Source**

The technical issues and performance of a high-repetition-rate, ultrafast-laser-based X-ray source were studied experimentally in the context of developing a dedicated laboratory-based tool for combustion diagnostics. X-ray emission from numerous elemental materials was investigated to compare with analytical-based expectations for yield and efficiency as well as to evaluate the advantages of some materials for operational issues such as debris production and degree of efficiency enhancement utilizing various illumination configurations. A weak inverse scaling of conversion efficiency with atomic number was observed. Broadband energy-conversion efficiency



of  $\sim 10^{-5}$  and yield of  $> 10^{10}$  photons/s were measured with numerous target elements. Application of a prepulse significantly enhanced conversion efficiency, and the enhancement factor was dependent on the material. Thus, previous optimizations must be performed in the atomic-number variation as well. Additionally, the efficiency enhancement associated with p-polarization incidence (relative to s-polarization) was observed to be dependent on base-material reflectivity. The results of this study were documented by C. L. Rettig (ISSI), W. M. Roquemore, and J. R. Gord (both of AFRL) in a paper that was published in *Applied Physics B* [Vol. 93, No. 2-3, pp. 365-372 (November 2008)]. The paper is included in the Appendix.

#### **4.8 An Evaluation of Femtosecond/Nanosecond-LIBS for Measuring Total Particulate Emissions**

LIBS involves the dissociation of molecular species into their atomic constituents and the subsequent emissions from the excited atoms. Using the LIBS signal from a sample, one can identify the atomic species and their relative concentrations. From this information and appropriate calibration curves, simple molecular species can be identified and their concentration estimated. This program sought to answer the critical question: Is it feasible to develop a LIBS-based technique that can be used to make a quantitative distinction between gaseous and total particulates in a multi-phase sample containing a common type atom? The approach was to investigate single- and dual-pulse, nanosecond (ns), and femtosecond (fs) LIBS techniques as a means of measuring different carbon species in gaseous, aerosol, and solid phases. The program involved a joint effort between the University of Florida and AFRL. The University of Florida investigated single ns-LIBS and dual ns/ns-LIBS, and AFRL investigated single ns-LIBS used in conjunction with dual fs/ns-LIBS. The program was partially successful in that the ratio of the ns/ns-LIBS signal and the ns-LIBS signal could be used to determine the percentage of gaseous and total particulate carbon. This approach holds promise, but the sensitivity must be improved if it is to become a practical technique. The fs/ns-LIBS technique was a disappointment. Within the parameters studied, it could not be used to determine the percent gaseous-to-particulate carbon. The reason for this is not understood but is thought to be related to the plasma dynamics. The results of this investigation were documented by M. Roquemore (AFRL), M. Brown (ISSI), and D. Hahn (University of Florida) in Final Report SERDP WP-1628 dated May 2009 on the Strategic Environmental Research and Development Program Statement of Need SON 08-05. This report is included in the Appendix.

#### **4.9 Picosecond Laser Machining of Shaped Holes in Thermal-Barrier-Coated Turbine Blades**

Increasing the operating temperature of an aircraft engine has the benefit of increasing thrust and fuel efficiency. However, increased operating temperatures can lead to temperatures in sections of the jet engine reaching or exceeding the melting point of the superalloy materials used for engine components. To maintain the structural integrity of the engine parts at the extreme operating temperatures, cooling methods must be supplied to the engine components. Cooling of the engine component is accomplished by air flow through cooling holes and through the application of thermal barrier coating (TBC). One method of fabrication for the cooling holes in turbine blades is a two-step process where

the holes are drilled in the base blade metal by either laser or electrical-discharge machining, a TBC system is applied, and the holes are drilled again to clear out and shape the TBC layer. Mound Laser and Photonics Center, Inc. (MLPC) has conducted research utilizing the ability of a picosecond-laser system to machine shaped holes through both the TBC and the underlying superalloy in a single step. The short pulse duration of the picosecond laser allows fast hole shaping and drilling without inducing spallation of the TBC or generating recast that can be encountered with high-power, long-pulse-duration lasers. The results of this study were documented by C. Druffner, L. Dosser (both of Mount Laser and Photonics Center, Inc.), W. Roquemore (AFRL), and S. Gogineni (Spectral Energies, LLC – employed by ISSI when the actual study was conducted) in Paper C2002 that was presented at the 28<sup>th</sup> International Congress on Applications of Lasers and Electro-Optics (ICALEO 2009), which was held 2-5 November 2009 in Orlando, FL. The paper was published in the Conference Proceedings and is included in the Appendix.

#### **4.10 Double-Pulse and Single-Pulse Laser-Induced Breakdown Spectroscopy for Distinguishing between Gaseous and Particulate Phase Analysis**

The use of a combination of double-pulse and single-pulse LIBS methodologies as a means of differentiating between solid-phase and gaseous-phase analytes (namely, carbon) in an aerosol stream was investigated. A range of spectral data was recorded for double-pulse and single-pulse configurations, including both nanosecond and femtosecond prepulse widths, while varying the gas-phase mass percentage of the carbon from about 10% to 90% for various fixed carbon concentrations. The carbon-emission response, as measured by the peak-to-continuum ratio, was greater for the double-pulse configuration as compared with the single-pulse response and was also enhanced as the percentage of solid carbon was increased. Using a combination of the double-pulse and single-pulse emission signals, a monotonically increasing response function was found to correlate with the percentage of gas-phase analyte. However, individual data points at the measured gas-phase percentages revealed considerable scatter from the predicted trend. Furthermore, the double-pulse to single-pulse ratio was only pronounced with the nanosecond-nanosecond configuration as compared with the femtosecond-nanosecond scheme. Overall, the LIBS methodology has been demonstrated as a potential means to discriminate between gas-phase and particulate-phase fractions of the same elemental species in an aerosol, although future optimization of the temporal parameters should be explored to improve the precision and accuracy of this approach. The results of this investigation were documented by M. Asgill (University of Florida), M. Brown (ISSI), K. Frische (ISSI), W. M. Roquemore (AFRL), and D. Hahn (University of Florida) in a paper that was published in *Applied Optics* [Vol. 49, No. 13, pp. 110-119 (May 2010)]. The paper is included in the Appendix.

#### **4.11 Hot-Electron-Dominated Rapid Transverse-Ionization Growth in Liquid Water**

Pump/probe optical-transmission measurements were used to monitor in space and time the ionization of a liquid column of water following impact of an 800-nm, 45-fs pump pulse. The pump pulse struck the 53- $\mu$ m-diameter column normal to its axis with

intensities up to  $2 \times 10^{15}$  W/cm<sup>2</sup>. After the initial photoionization and for probe delay times  $< 500$  fs, the neutral water surrounding the beam was rapidly ionized in the transverse direction, presumably by hot electrons with initial velocities 0.55 times the speed of light (relativistic kinetic energy of  $\sim 100$  keV). Such velocities are unusual for condensed-matter excitation at the stated laser intensities. The results of this study were documented by M. Brown (ISSI), T. Erickson (AFRL), K. Frische (ISSI), and W. Roquemore (AFRL) in a paper that was published in *Optics Express* [Vol. 19, No. 13, pp. 12241-12247 (June 2011)]. The paper is included in the Appendix.

## 5.0 PUBLICATIONS AND PRESENTATIONS

“Development of Laser-Based X-Ray Source for Dense Spray and Soot Diagnostics,” M. S. Brown, G. L. Switzer, J. R. Gord, and W. M. Roquemore, Invited paper presented at the Gordon Research Conference on Laser Diagnostics in Combustion, 31 July - 5 August 2005, South Hadley, MA.

“Laser-Target Generation of Soft X-Rays,” M. S. Brown, G. Switzer, J. R. Gord, W. M. Roquemore, A. Bernstein, D. Symes, and T. Ditmire, Presented at the OSA Laser Applications to Chemical, Security, and Environmental Analysis Topical Meeting and Tabletop Exhibit, 5-9 February 2006, Incline Village, NV.

“Laser Generation of X-Rays for Air-Force Applications,” M. S. Brown, G. L. Switzer, J. R. Gord, W. M. Roquemore, D. Symes, and T. Ditmire, Presented at the 31<sup>st</sup> Annual AIAA Dayton-Cincinnati Aerospace Science Symposium, 7 March 2006, Dayton, OH. Dr. Michael Brown (ISSI) was Chair of the Session on Fluid Dynamics III: High-Speed Flow Plasmas at this symposium. This paper was also presented in poster form at the Annual Poster Session sponsored jointly by the Dayton Section of the American Chemical Society and the Society for Applied Spectroscopy, 7 March 2006, Dayton, OH.

“Imaging of Laser-Generated Micro-Plasmas,” M. S. Brown, C. L. Rettig, K. D. Frische, J. R. Gord, W. M. Roquemore, and J. A. Nees, Presented at the 32<sup>nd</sup> Annual AIAA Dayton-Cincinnati Aerospace Science Symposium, 6 March 2007, Dayton, OH. The paper received the Best-Presentation Award at this symposium, and Dr Michael Brown (ISSI) was Chair of the Session on Jet Flow. This paper was also presented in poster form at the Annual Poster Session sponsored jointly by the Dayton Section of the American Chemical Society and the Society for Applied Spectroscopy, 1 March 2007, Dayton, OH.

“Development of Laser-Generated X-Ray Source for Air-Force Applications,” C. L. Rettig, M. S. Brown, J. R. Gord, and W. M. Roquemore, Presented at the 32<sup>nd</sup> Annual AIAA Dayton-Cincinnati Aerospace Science Symposium, 6 March 2007, Dayton, OH, and in poster form at the Annual Poster Session sponsored jointly by the Dayton Section of the American Chemical Society and the Society for Applied Spectroscopy, 1 March 2007, Dayton, OH.

“Laser-Induced Breakdown Spectroscopy for Detection of Volatile Aerosols,” M. S. Brown, K. D. Frische, T. G. Erickson, J. R. Gord, and W. M. Roquemore, Presented at the 33<sup>rd</sup> Annual AIAA Dayton-Cincinnati Aerospace Science Symposium, 4 March 2008, Dayton, OH. Dr. Michael Brown (ISSI) was a member of the Organizing Committee (Corporate Sponsors Chair) and Chair of the Session on Innovations in Aircraft Design at this symposium. This paper was also presented in poster form at the Annual Poster Session sponsored jointly by the Dayton Section of the American Chemical Society and the Society for Applied Spectroscopy, 4 March 2008, Dayton, OH.

“Efficiency and Scaling of Ultrashort-Pulse, High-Repetition-Rate, Laser-Driven X-Ray Source,” C. L. Rettig, W. M. Roquemore, and J. R. Gord, *Applied Physics B* [Vol. 93, No. 2-3, pp. 365-372 (November 2008)].

“An Evaluation of fs/ns-LIBS for Measuring Total Particulate Emissions,” M. Roquemore, M. Brown, and D. Hahn, SERDP WP-1628, Final Report on SERDP Statement of Need SON 08-05 (Strategic Environmental Research and Development Program, Arlington, VA, May 2009).

“Picosecond Laser Machining of Shaped Holes in Thermal Barrier Coated Turbine Blades,” C. Druffner, L. Dosser, W. Roquemore, and S. Gogingeni, Paper C202 presented at the 28<sup>th</sup> International Congress on Applications of Lasers and Electro-Optics (ICALEO 2009), 2-5 November 2009, Orlando, FL, and published in the Conference Proceedings.

“Double-Pulse and Single-Pulse Laser-Induced Breakdown Spectroscopy for Distinguishing between Gaseous and Particulate Phase Analytes,” M. Asgill, M. Brown, K. Frische, W. M. Roquemore, and D. Hahn, *Applied Optics* [Vol. 49, No. 13, pp. 110-119 (May 2010)].

“Hot Electron Dominated Rapid Transverse Ionization Growth in Liquid Water,” M. Brown, T. Erickson, K. Frische, and W. Roquemore, *Optics Express* [Vol. 19, Issue No. 13, pp. 12241-12247, June 2011].

## 6.0 REFERENCES

- Albert, O., Wang, H., Liu, D., Chang, Z., and Mourou, G. (2000) "Generation of relativistic intensity pulses at a kilohertz repetition rate," *Optics Letters* **25**(15), 1125-1127.
- Anand, M., Gibbon, P., and Krishnamurthy, M. (2006a) "Large spectral blue shifts in intense laser irradiation of microdroplets," *Optics Express* **14**(12), 5502-5507.
- Anand, M., Sandhu, A. S., Kahaly, S., Kumar, G. Ravidra, Gibbon, P., and Krishnamurthy, M., (2006b), "Prepulse dependence in hard x-ray generation from microdroplets" 3<sup>rd</sup> Int. Conf. on Superstrong Fields in Plasma, Edited by Batani and M. Lontano, American Institute of Physics, 0-7354-0319-8/06.
- Babonneau, D., Primout, M., Girard, F., Jadaud, J.-P., Naudy, M., Villette, B., Depierreux, S., Blancard, C., Faussurier, G., Fournier, K. B., Suter, L., Kauffman, R., Glenzer, S., Miller, M. C., Grün, J., and Davis, J. (2008) "Efficient multi-keV x-ray sources from laser-exploded metallic thin foils," *Physics of Plasmas* **15**(9), 092702-1 - 092702-15.
- Banerjee, S., Powers, N. D., Ramanathan, V., Ghebregziabher, I., Brown, K. J., Maharjan, C. M., Chen, S., Beck, A., Lefebvre, E., Kalmykov, S. Y., Shadwick, B. A., and Umstadter, D. P. (2012) "Generation of tunable, 100–800 MeV quasi-monoenergetic electron beams from a laser-wakefield accelerator in the blowout regime," *Physics of Plasmas* **19**(5), 056703-1 – 056703-8.
- Bargheer, M., Zhavoronkov, N., Gritsai, Y., Woo, J. C., Kim, D. S., Woerner, M., and Elsaesser, T. (2004) "Coherent atomic motions in a nanostructure studied by femtosecond x-ray diffraction," *Science* **306**, 1771-1773.
- Bell, A. R. and Kingham, R. J. (2003) "Resistive collimation of electron beams in laser-produced plasmas," *Physical Review Letters* **91**(3), 035003-1 – 035003-4.
- Boschetto, D., Mourou, G., Rousse, A., Mordovanakis, A., Hou, B., Nees, J., Kumah, D., Clarke, R. (2007) "Spatial coherence properties of a compact and ultrafast laser-produced plasma keV x-ray source," *Applied Physics Letters* **90**, 11106-1 – 11106-03.
- Brandl, F., Hidding, B., Osterholz, J., Hemmers, D., Karmakar, A., Pukhov, A., and Pretzler, G. (2009) "Directed acceleration of electrons from a solid surface by sub-10-fs laser pulses," *Physical Review Letters* **102**(19), 195001-1 – 195001-4.
- Brown, M. S., Erickson, T., Frische, K., and Roquemore, W. M. (2011) "Hot electron dominated rapid transverse ionization growth in liquid water," *Optics Express* **19**(13), 12241-12247.

Brunel, F. (1987) “Not-so-resonant, resonant absorption,” *Physical Review Letters* **59**(1), 52-55.

Cai, D. F., Gu, Y. Q., Zheng, Z. J., Wen, T. S., Chunyu, S. T., Wang, Z. B., and Yang, X. D. (2003) “Experimental study for angular distribution of the hot electrons generated by femtosecond laser interaction with solid targets,” *Physics of Plasmas* **10**(8), 3265-3269.

Cai, D. F., Gu, Y. Q., Zheng, Z. J., Zhou, W. M., Yang, X. D., Jiao, C. Y., Chen, H., Wen, T. S., and Chunyu, S. T. (2004) “Double-peak emission of hot electrons generated by femtosecond laser interaction with solid targets,” *Physical Review E* **70**(6), 066410-1 – 066410-5.

Calegari, F., Stagira, S., D’Andrea, C., Valentini, G., Vozzi, C., Nisoli, M., De Silvestri, S., Poletto, L., Villoresi, P., Faenov, A., and Pikuz, T. (2006) “Table-top soft x-ray imaging of nanometric films,” *Applied Physics Letters* **89**(11), 111122-1 – 111122-3.

Chen, L. M., Forget, P., Toth, R., Kieffer, J. C., Krol, A., Chamberlain, C. C., Hou, B. X., Nees, J., and Mourou, G. (2003) “Laser-based intense hard x-ray source for mammography,” *Medical Imaging 2003: Physics of Medical Imaging*, *Proceedings of SPIE* **5030**, 923-928.

Chen, L. M., Forget, P., Fourmaux, S., Kieffer, J. C., Krol, A., Chamberlain, C. C., Hou, B. X., Nees, J., and Mourou, G. (2004a) “Study of hard x-ray emission from intense femtosecond Ti:sapphire laser–solid target interactions,” *Physics of Plasmas* **11**(9), 4439-4445.

Chen, L. M., Forget, P., Toth, R., Fourmaux, S., Kieffer, J. C., Krol, A., Chamberlain, C. C., Hou, B. X., Nees, J., and Mourou, G. (2004b) “Experimental study of hard x-ray emission from intense femtosecond laser-solid target interactions,” *Proceedings of SPIE* **5196**, 337-343.

Chen, M., Sheng, Z.-M., and Zhanga, J. (2006) “On the angular distribution of fast electrons generated in intense laser interaction with solid targets,” *Physics of Plasmas* **13**(1), 014504-1 – 014504-4.

Chen, L. M., Kando, M., Xu, M. H., Li, Y. T., Koga, J., Chen, M., Xu, H., Yuan, X. H., Dong, Q. L., Sheng, Z. M., Bulanov, S. V., Kato, Y., Zhang, J., and Tajima, T. (2008) “Study of x-Ray emission enhancement via a high-contrast femtosecond laser interacting with a solid foil,” *Physical Review Letters* **100**(4), 45004-1 – 045004-4.

Chen, S., Powers, N. D., Ghebregziabher, I., Maharjan, C. M., Liu, C., Golovin, G., Banjeree, S., Zhang, J., Cunningham, N., Moorti, A., Clarke, S., Pozzi, S., and Umstadter, D. P. (2013) “MeV-energy x-rays from inverse Compton scattering with laser-Wakefield accelerated electrons,” *Physical Review Letters* **110**(15), 155003.

Cobble, J. A., Schappert, G. T., Jones, L. A., Taylor, A. J., Kyrala, G. A., and Fulton, R. D. (1991) "The interaction of a high irradiance, subpicosecond laser pulse with aluminum: The effects of the prepulse on x-ray production," *Journal of Applied Physics* **69**(5), 3369-3371.

Corkum, P. B. (1993) "Plasma perspective on strong-field multiphoton ionization," *Physical Review Letters* **71**(13), 1994-1997.

Croft, M., Jisrawi, N., Zhong, Z., Jorvath, K., Holtz, R. L., Shepard, M., Lakshmipathy, M., Sadananda, K., Skaritka, J., Shukla, V., Sadangi, R. K., and Tsakalakos, T. (2008) "Stress gradient induced strain localization in metals: High resolution strain cross sectioning via synchrotron x-ray diffraction," *Journal of Engineering Materials and Technology* **130**(2), 021005-1 – 021005-10.

Ditmire, T. (2002) "Laser fusion on a tabletop," *Optics and Photonics News* **13**(5), 28-32.

Dobosz, S., Doumy, G., Stabile, H., D'Oliveira, P., Monot, P., Réau, F., Hüller, S., and Martin, Ph. (2005) "Probing hot and dense laser-induced plasmas with ultrafast XUV pulses," *Physical Review Letters* **95**(2), 025001-1 – 025001-4.

Donnelly, T. D., Rust, M., Weiner, I., Allen, M., Smith, R. A., Steinke, C. A., Wilks, S., Zweiback, J., Cowan, T. E., and Ditmire, T. (2001) "Hard x-ray and hot electron production from intense laser irradiation of wavelength-scale particles," *Journal of Physics B: Atomic, Molecular, and Optical Physics* **34**(10), L313 - L320.

Düsterer, S., Schwoerer, H., Behrens, R., Ziener, C., Reich, C., Gibbon, P., Sauerbrey, R. (2001) "Hard x-rays and nuclear reactions from laser produced plasmas," *Contributions to Plasma Physics* **41**(2-3), 171-174.

Eder, D. C., Pretzler, G., Fill, E., Eidmann, K., Saemann, A. (2000) "Spatial characteristics of  $K\alpha$  radiation from weakly relativistic laser plasmas," *Applied Physics B* **70**, 211-217

Feurer, T., Morak, A., Uschmann, I., Ziener, Ch., Schwoerer, H., Förster, E., Sauerbrey, R. (2001) "An incoherent sub-picosecond X-ray source for time-resolved X-ray-diffraction experiments," *Applied Physics B* **72**, 15-20.

FIERO, "Frontiers in Extreme Relativistic Optics" (2013) Workshop held at The Ohio State University, February 20-21, Columbus, OH.

Forslund, D. W., Kindel, J. M., Lee, K., Lindman, E. L., and Morse, R. L. (1975) "Theory and simulation of resonant absorption in a hot plasma," *Physical Review A* **11**(2), 679-683.

Freidberg, J. P., Mitchell, R. W., Morse, R. L., Rudinski, L. I., (1972) "Resonant absorption of laser light by plasma targets," *Physical Review Letters* **28**(13), 795-799.



Freeman, R. R., Bucksbaum, P. H., Milchberg, H., Darach, S., Schumacher, D., and Geusic, M. E., (1987), *Physical Review Letters* **59**, 1092.

Froom, D. A. (1989), “Maneuverable N-ray system acceptance tests,” *Proceedings of the Third World Conference*, Osaka, Japan, pp. 741-748.

Froula, D. H., Clayton, C. E., Döppner, T., Marsh, K. A., Barty, C. P. J., Divol, L., Fonseca, R. A., Glenzer, S. H., Joshi, C., Lu, W., Martins, S. F., Michel, P. A., Mori, W. B., Palastro, J. P., Pollock, B. B., Pak, A. E., Ralph, J. E., Ross, J. S., Siders, C.W., Silva, L. O., and Wang, T., (2009) “Measurements of the critical power for self-injection of electrons in a laser Wakefield accelerator,” *Physical Review Letters* **103**(21), 215006-1 – 215006-4.

Frontiera, R. R., Henry, A.-I., Gruenke, N. L., and Van Duyne, R. P., (2011) “Surface-enhanced femtosecond stimulated Raman spectroscopy,” *Journal of Physical Chemistry Letters* **2**(10), 1199-1203.

Fullagar, W., Harbst, M., Canton, S., Uhlig, J., Walazak, M., Wahestrom, C.-G., and Sundstrom, V. (2007) “A broadband laser plasma x-ray source for application in ultrafast chemical structure dynamics,” *Review of Scientific Instruments* **78**(11), 115105-1 – 115105-9.

Gibbon, P. (2005) *Short Pulse Laser Interactions with Matter, an Introduction* (Imperial College Press, London).

Gibbon, P., Mašek, M., Teubner, U., Lu, W., Nicoul, M., Shymanovich, U., Tarasevitch, A., Zhou, P., Sokolowski-Tinten, K., and von der Linde, D. (2009) “Modelling and optimization of fs laser-produced Ka sources,” *Applied Physics A* **96**(1), 23-31.

Goldston, R. J., and Rutherford, P. H., (1995), *Introduction to Plasma Physics*, Institute of Physics Publishing, Bristol and Philadelphia, 1-500.

Habara, H., Adumi, K., Yabuuchi, T., Nakamura, T., Chen, Z. L., Kashihara, M., Kodama, R., Kondo, K., Kumar, G. R., Lei, L. A., Matsuoka, T., Mima, K., and Tanaka, K. A. (2006) “Surface acceleration of fast electrons with relativistic self-focusing in preformed plasma,” *Physical Review Letters* **97**(9), 095004-1 – 095004-4.

Hagedorn, M., Kutzner, J., Tsilimis, G., and Zacharias, H. (2003) “High-repetition-rate hard x-ray generation with sub-millijoule femtosecond laser pulses,” *Applied Physics B* **77**(1), 49-57.

Hammer, D. X., Thomas, R. J., Noojin, G. D., Rockwell, B. A., Kennedy, P. K., and Roach, W. P. (1996) “Experimental investigation of ultrashort pulse laser-induced breakdown thresholds in aqueous media,” *IEEE Journal of Quantum Electronics* **32**(4), 670-678.

- Hatanaka, K., Miura, T., and Fukumura, H. (2004) "White x-ray pulse emission of alkali halide aqueous solutions irradiated by focused femtosecond laser pulses: a spectroscopic study on electron temperatures as functions of laser intensity, solute concentration, and solute atomic number," *Chemical Physics* **299**(2-3), 265-270.
- Hatanaka, K., Ono, H., and Fukumura, H. (2008a) "X-ray pulse emission from cesium chloride aqueous solutions when irradiated by double-pulsed femtosecond laser pulses," *Applied Physics Letters* **93**(6), 064103-11 – 064103-3.
- Hatanaka, K., Ida, T., Ono, H., Matsushima, S., Fukumura, H., Juodkazis, S., and Misawa, A. (2008b) "Chirp effect in hard x-ray generation from liquid target when irradiated by femtosecond pulses," *Optics Express* **16**(17), 12650-12657.
- Hegelich, B. M., Albright, B. J., Cobble, J. A., Flippo, K., Letzring, S., Paffett, M., Ruhl, H., Schreiber, J., Schulze, R. K., and Fernández, J. C. (2006) "Laser acceleration of quasi-monoenergetic MeV ion beams," *Nature* **439**(7075), 441-444.
- Higginson, D. P., McNaney, J. M., Swift, D. C., Bartal, T., Hey, D. S., Kodama, R., Le Pape, S., Mackinnon, A., Mariscal, D., Nakamura, H., Nakanii, N., Tanaka, K. A., and Beg, F. N. (2010) "Laser generated neutron source for neutron resonance spectroscopy," *Physics of Plasmas* **17**, 100701-1 – 100701-4.
- Hombourger, C. (1998) "An empirical expression for K-shell ionization cross section by electron impact," *Journal of Physics B: Atomic, Molecular, and Optical Physics* **31**(16), 3693-3702.
- Hong, K. (2005) "Generation and measurement of >108 intensity contrast ratio in a relativistic kHz chirped-pulse amplified laser," *Applied Physics B* **81**, 447-457.
- Hou, B., Nees, J., Mordovanakis, A., Wilcox, M., Mourou, G., Chen, L. M., Kieffer, J. C., Chamberlain, C. C., and Krol, A. (2006) "Hard x-ray generation from solids driven by relativistic intensity in the lambda-cubed regime," *Applied Physics B* **83**(1), 81-85.
- Jackson, J. D. (1975) "Bremsstrahlung, method of virtual quanta, radiative beta processes," *Classical Electrodynamics*, Second Edition (John Wiley & Sons, Inc., New York), Chapter 15, pp.701-738.
- Jiang, Y., Li, W., Cao, G., Lee, T., Ketwaroo, G., Rose-Petruck, Ch. (2001) "Applications of X-rays generated from lasers and other bright sources II," *Proceedings of SPIE* **4504**.
- John, R., Buchanan, D. J., Caton, M. J., and Sushant, K. (2010) "Stability of shot peen residual stresses in IN100 subjected to creep and fatigue loading," *Science Digest, Procedia Engineering* **2**(1), 1887-1893.

- Kazansky, P. G., Shimotsuma, Y., Sakakura, M., Beresna, M., Gecevičius, M., Svirko, Y., Akturk, S., Qiu, J., Miura, K., and Hirao, K. (2011) "Photosensitivity control of an isotropic medium through polarization of light pulses with tilted intensity front," *Optics Express* **19**(21), 20657-20664.
- Keldysh, L. V. (1965) "Ionization in the field of a strong electromagnetic wave," *Soviet Physics JEPT* **20**(5), 1307-1314.
- Kim, K. Y., Alexeev, I., Antonsen, T. M., Gupta, A., Kumarappan, V., Milchberg, H. M., (2005) "Spectral redshifts in the intense laser-cluster interaction," *Physical Review A* **71**, 01120-1 – 01120-4.
- Kodama, R., Mochizuki, T., Tanaka, K. A., and Yamanaka, C. (1987) "Enhancement of keV x-ray emission in laser-produced plasmas by a weak prepulse laser," *Applied Physics Letters* **50**(12), 720-722.
- Kodama, R., Mima, K., Tanaka, K. A., Kitagawa, Y., Fujita, H., Takahashi, K., Sunahara, A., Fujita, K., Habara, H., Jitsuno, T., Sentoku, Y., Matsushita, T., Miyakoshi, T., Miyanaga, N., Norimatsu, T., Setoguchi, H., Sonomoto, T., Tanpo, M., Toyama, Y., and Yamanaka, T. (2001) "Fast ignitor research at the Institute of Laser Engineering, Osaka University," *Physics of Plasmas* **8**(5), 2268-2274.
- Krol, A., Kieffer, J.-C., Ichalaleb, Z., Jiang, Z., Chamberlain, C. C., and Scalzetti, E. (2001) "Experimental and theoretical studies of dual energy subtraction angiography (DESA) performed using laser-based x-ray source," *Applications of x-rays generated from lasers and other bright sources II, Proceedings of SPIE* **4504**, 227-233.
- Krol, A., Kieffer, J.-C., Nees, J. A., Chen, L., Toth, R., Hou, B., Kincaid, R. E., Coman, I. L., Chamberlain, C. C., Lipson, E. D., and Mourou, G. A. (2003) "Development of novel ultrafast-laser-based micro-CT system for small-animal imaging," DOI:10.1109/NSSMIC.2003.1352271, *Proceedings of the IEEE 2003 Nuclear Science Symposium* **3**, 1993-1996.
- Larsen, J. T., and Lane, S. M. (1994) "Hyades - A plasma hydrodynamics code for dense plasma studies," *Journal of Quantitative Spectroscopy and Radiative Transfer* **51**(1-2), 179-186.
- Leemans, W. P., Nagler, B., Gonsalves, A. J., Toth, Cs., Nakamura, K., Geddes, C. G. R., Esarey, E., Schroeder, C. B., and Hooker, S. M. (2006) "GeV electron beams from a centimetre-scale accelerator," *Nature Physics* **2**, 696-699.
- Leggett, D. (1994) "Feasibility study of using neutron diagnostics for turbine engine structural measurements," Final Technical Report WL-TR-94-2054 (Wright Laboratory, Wright-Patterson Air Force Base, OH) (ADA292791).

Li, Y. T., Zhang, J., Chen, L. M., Mu, Y. F., Liang, T. J., Wei, Z. Y., Dong, Q. L., Chen, Z. L., Teng, H., Chun-Yu, S. T., Jiang, W. M., Zheng, Z. J., and Tang, X. W. (2001) "Hot electrons in the interaction of femtosecond laser pulses with foil targets at a moderate laser intensity," *Physical Review E* **64**(4), 046407-1 – 046407-6.

Li, Y. T., Zhang, J., Sheng, Z. M., Teng, H., Liang, T. J., Peng, X.Y., Lu, X., Li, Y. J. and Tang, X. W. (2003) "Spatial distribution of high-energy electron emission from water plasmas produced by femtosecond laser pulses," *Physical Review Letters* **90**, 165002.

Li, Y. T., Zhang, J., Sheng, Z. M., and Zheng, J. (2004) "High-energy electrons produced in subpicosecond laser-plasma interactions from subrelativistic laser intensities to relativistic intensities," *Physical Review E* **69**, 036405.

Li, Z., Daido, H., Fukumi, A., Sagisaka, A., Ogura, K., Nishiuchi, M., Orimo, S., Hayashi, Y., Mori, M., Kado, M., Bulanov, S. V., Esirkepov, T. Zh., Oishi, Y., Nayuki, T., Fujii, T., Nemoto, K., Nakamura, S., and Noda, A. (2006) "Measurements of energy and angular distribution of hot electrons and protons emitted from a p- and s-polarized intense femtosecond laser pulse driven thin foil target," *Physics of Plasmas* **13**(4), 043104-1 – 043104-6.

Liu, Y., Dong, Q., Peng, X., Jin, Z., and Zhang, J., (2009) "Soft x-ray emission, angular distribution of hot electrons, and absorption studies of argon clusters in intense laser pulses," *Physics of Plasmas* **16**(4), 043301-1 – 043301-5.

Lu, W., Nicoul, M., Shymanovich, U., Tarasevitch, A., Zhou, P., Sokolowski-Tinten, K., von der Linde, D., Masek, M., Gibbon, P., and Taubner, U. (2009) "Optimized K $\alpha$  x-ray flashes from femtosecond-laser-irradiated foils," *Physical Review E* **80**(2), 026404-1 - 026404-10.

Lytle, A. L., Zhang, X., Peatross, J., Murnane, M. M., Kapteyn, H. C., and Cohen, O. (2007) "Probe of high-order harmonic generation in a hollow waveguide geometry using counterpropagating light," *Physical Review Letters* **98**(12), 123904-1 – 123904-4.

Mourou, G., and Umstadter, D. (2002) "Extreme light," *Scientific American* **286**(5), 81-86.

Nakano, H., Liesugi, N., (2001) "Enhanced K-shell X-ray line emissions from Aluminum plasma created by a pair of femtosecond laser pulses," *Applied Physics Letters* **79**(1), 24-26.

Noack, J., and Vogel, A. (1999) "Laser-induced plasma formation in water at nanosecond to femtosecond time scales: Calculation of thresholds, absorption coefficients, and energy density," *IEEE Journal of Quantum Electronics* **35**(8), 1156-1167.

Norreys, P. A., Santala, M., Clark, E., Zepf, M., Watts, I., Beg, F. N., Krushelnick, K., Tatarakis, M., Dangor, A. E., Fang, X., Graham, P., McCanny, T., Singhal, R. P.,

Ledingham, K. W. D., Creswell, A., Sanderson, D. C. W., Magill, J., Machacek, A., Wark, J. S., Allott, R., Kennedy, B., and Neely, D., (1999) "Observation of a highly directional g-ray beam from ultrashort, ultraintense laser pulse interactions with solids," *Physics of Plasmas* **6**(5), 2150-2156.

OECD (Organization for Economic Co-operation and Development) (2002) "OECD Global Science Forum: Workshop on Compact High-Intensity, Short-Pulse Lasers: Future Directions and Applications."

Penetrante, B. M., Bardsley, J. N., Wood, W. M., Siders, C. W., Downer, M. C., (1992) "Ionization-induced frequency shifts in intense femtosecond laser pulses," *Journal of the Optical Society of America B* **9**(11), 2032-2040.

Peng, X. Y., Zhang, J., Jin, Z., Liang, T. J., Sheng, Z. M., Li, L. I., Yu, Q. Z., Zheng, Z. Y., Wang, Z. H., Chen, Z. L., and Zhong, J. Y., (2004) "Energetic electrons emitted from ethanol droplets irradiated by femtosecond laser pulses," *Physical Review E*, **69**(2), 26414-1 – 026414-5.

Perelomov, A. M., Popov, V. S., and Terent'ev, M. V. (1966) "Ionization of atoms in an alternating electric field: I," *Soviet Physics JETP* **23**(5), 924.

Perelomov, A. M., Popov, V. S., and Terent'ev, M. V. (1966) "Ionization of atoms in an alternating electric field: II," *Soviet Physics JETP* **24**(1), 207-217.

Perry, M. D., and Mourou, G. (1994), "Terawatt to petawatt subpicosecond lasers," *Science* **264**, 917-924.

Petwal, V. C., Bapna, S. C., Sandha, R. S., Kotaiah, S., and Subbaiah, K. V. (2007) "Bremsstrahlung converter for high power EB radiation processing facility," APAC 2007, Indore, India, pp. 767-679.

Pogany, A., Gao, D., and Wilkins, S. W. (1997) "Contrast and resolution in imaging with a microfocus x-ray source," *Review of Scientific Instruments* **68**(7), 2774-2782.

Poola, R., Powell, C. F., Yue, Y., Gupta, A., McPherson, A., and Wang, J. (2000) "Development of a quantitative measurement of a diesel spray core using synchrotron x-rays," Eighth International Conference on Liquid Atomization and Spray Systems, Pasadena, CA.

Popov, V. S., Kuznetsov, V. P., and Perelomov, A. M. (1968) "Quasiclassical approximation for nonstationary problems," *Soviet Physics JETP* **26**(1), 222-232.

Powell, C. F., Yue, Y., Cheong, S.-K., Narayanan, S., Cuenca, R., Ciatti, S., Shu, D., Wang, J. (2003) “Effects of ambient pressure on fuel sprays as measured using x-ray absorption,” ILASS Americas, 16th Annual Conference on Liquid Atomization and Spray Systems, Monterey, CA., May.

Rao, B. S., Naik, P. A., Arora, V., Khan, R. A., and Gupta, P. D. (2007) “Angular distribution and dose measurements of hard x-ray emission from intense laser-plasma interaction,” *Journal of Applied Physics* **102**(6), 063307-1 – 063307-4.

Rao, B. S., Arora, V., Naik, P. A., and Gupta, P. D. (2012) “Study of fast electron jet produced from interaction of intense laser beam with solid target at oblique incidence,” *Physics of Plasmas* **19**(11), 113118-1 – 113118-6.

Reich, Ch., Gibbon, P., Uschmann, I., and Forster, E. (2000) “Yield optimization and time structure of femtosecond laser plasma *Ka* Sources,” *Physical Review Letters* **84**(2), 4846-4849.

Rettig, C. L., Roquemore, W. M., and Gord, J. R. (2008) “Efficiency and scaling of an ultrashort-pulse high-repetition-rate laser-driven x-ray source,” *Applied Physics B*, **93**(), 365-372.

Rose-Petruck, C., Jimenez, R., Guo, T., Cavalleri, A., Siders, C. W., Raksi, F., Squiers, J. A., Walker, B. C., Wilson, K. R., and Barty, C. P. J. (1999) “Picosecond-milliangstrom lattice dynamics measured by ultrafast x-ray diffraction,” *Nature* **398**(6725), 310-312.

Rousse, A., Rischel, C., Fourmaux, S., Uschmann, I., Förster, E., Audebert, P., Geindre, J. P., Gauthier, J. C., and Hulin, D. (2001) “Time-resolved femtosecond x-ray diffraction by an ultra-short pulse produced by a laser,” *Measurement Science and Technology* **12**(11), 1841-1846.

Rozmus, W., and Tikhonchuk, V. T. (1990) “Skin effect and interaction of short laser pulses with dense plasmas,” *Physical Review A* **42**, 7401-7412.

Rozmus, W., Tikhonchuk, and V. T., Cable, R. (1996) “A model of ultrashort laser pulse absorption in solid targets,” *Physics of Plasmas* **3**, 360-367.

Ruhl, H., Sentoku, Y., Mima, K., Tanaka, K. A., and Kodama, R. (1999) “Collimated electron jets by intense laser-beam-plasma surface interaction under oblique incidence,” *Physical Review Letters* **82**(4), 743-746.

SAUUL (The Science and Applications of Ultrafast, Ultraintense Lasers) (2002) National Workshop, Washington, DC, 17-19 June.

- Schlegel, Th., Bastiani, S., G émillet, L., Geindre, J. P., Audebert, P., Lefebvre, E., Bonnaud, G., Delettrez, A. J., (1999) "Comparison of measured and calculated X-ray and hot-electron production in short-pulse laser solid interactions at moderate intensities," *Physical Review E* **60**(2), 220-2217
- Schworer, H., Gibbon, P., Düsterer, S., Behrens, R., Ziener, C., Reich, C., and Sauerbrey, R. (2001) "MeV x rays and photoneutrons from femtosecond laser-produced plasmas," *Physical Review Letters* **86**(11), 2317-2320.
- Sentoku, Y., Ruhl, H., Mima, K., Kodama, R., Tanaka, K. A., and Kishimoto, Y. (1999) "Plasma jet formation and magnetic-field generation in the intense laser plasma under oblique incidence," *Physics of Plasmas* **6**(7), 2855-2861.
- Sheng, Z.-M., Sentoku, Y., Mima, K., Zhang, J., Yu, W., and Meyer-ter-Vehn, J. (2000) "Angular distributions of fast electrons, ions, and Bremsstrahlung x/g-rays in intense laser interaction with solid targets," *Physical Review Letters* **85**(25), 5340-5343.
- Siders, C. W., Cavalleri, A., Sokolowski-Tinten, K., Tóth, Cs., Guo, T., Kammler, M., Horn von Hoegen, M., Wilson, K. R., von der Linde, D., and Barty, C. P. J. (1999) "Detection of nonthermal melting by ultrafast x-ray diffraction," *Science* **286**(5443), 1340-1342.
- Silies, M., Linden, S., Witte, H., and Zacharias, H. (2007) "The dependence of the Fe K $\alpha$  yield on the chirp of the femtosecond exciting laser pulse," *Applied Physics B* **87**(4), 623-627.
- Silies, M., Witte, H., Linden, S., Kutzner, J., Uschmann, I., Förster, E., and Zacharias, H. (2009) "Table-top kHz hard x-ray source with ultrashort pulse duration for time-resolved x-ray diffraction," *Applied Physics A* **96**(1), 59-67.
- Singhal, H., Arora, V., Naik, P. A., Gupta, P. D., (2005) "Spectral blueshifts in laser light scattered from argon-gas-cluster plasmas," *Physical Review A* **72**, 043201-1 – 043201-7.
- Snively, R. A., Key, M. H., Hatchett, S. P., Cowan, T. E., Roth, M., Phillips, T. W., Stoyer, M. A., Henry, E. A., Sangster, T. C., Singh, M. S., Wilks, S. C., MacKinnon, A., Offenberger, A., Pennington, D. M., Yasuike, K., Langdon, A. B., Lasinski, B. F., Johnson, J., Perry, M. D., and Campbell, E. M. (2000) "Intense high-energy proton beams from petawatt-laser irradiation of solids," *Physical Review Letters* **85**(14), 2945-2948.
- Sokolowski-Tinten, K., Blome, C., Dietrich, C., Tarasevitch, A., Horn von Hoegen, M., von der Linde, D., Cavalleri, A., Squier, J., and Kammler, M. (2001) "Femtosecond x-ray measurement of ultrafast melting and large acoustic transients," *Physical Review Letters* **87**(22), 225701-1 – 225701-4.

Sokolowski-Tinten, K., Blome, C., Blums, J., Cavalleri, A., Dietrich, C., Tarasevitch, A., Uschmann, I., Forster, E., Kammiller, M., Horn-von-Hoegen, M., and von der Linde, D. (2003) "Femtosecond x-ray measurement of coherent lattice vibrations near the Lindemann stability limit," *Nature* **422**(6929), 287-289.

Strickland, D., and Mourou, G. (1985) "Compression of amplified chirped optical pulses," *Optics Communications* **56**(3), 219-221.

Tallents, G., Pestehe, J., Turcum, E., Abou-Ali, Y., Hirst, G., Powers, M., and Shaikh, W. (2004) "Efficiency of 1.5 - 4.5 keV x-ray production from laser plasmas," *Proceedings of SPIE* **5196**, 185-193.

Thomas, A. G. R., Sherlock, M., Kuranz, C., Ridgers, C. P., and Drake, R. P. (2013) "Hybrid Vlasov-Fokker-Planck-Maxwell simulations of fast electron transport and the time dependence of K-shell excitation in a mid-Z metallic target," *New Journal of Physics* **15**(015017), 1-20.

Tian, Y., Liu, J., Wang, W., Wang, C., Deng, A., Xia, C., Li, W., Cao, L., Lu, H., Zhang, H., Xu, Y., Leng, Y., Li, R., and Xu, Z. (2012) "Electron emission at locked phases from the laser-driven surface plasma wave," *Physical Review Letters* **109**(11), 115002-1 – 115002-5.

Umstadter, D. (2001) "Review of physics and applications of relativistic plasmas driven by ultra-intense lasers," *Physics of Plasmas* **8**(5), 1774-1785.

Uryupina, D. S., Ivanov, K. A., Brantov, A. V., Savel'ev, A. B., Bychenkov, V. Yu., Povarnitsyn, M. E., Volkov, R. V., and Tikhonchuk, V. T. (2012) "Femtosecond laser-plasmas interaction with prepulse-generated liquid metal microjets," *Physics of Plasmas* **19**(1), 013104-1 – 013401-8.

Uspenskii, Yu. A., Levashov, V. E., Vinogradov, A. V., Fedorenko, A. I., Kondratenko, V. V., Pershin, Yu. P., Zubarev, E. N., and Fedotov, V. Yu. (1998) "High-reflectivity multilayer mirrors for a vacuum-ultraviolet interval of 35–50 nm," *Optics Letters* **23**(10), 771-773.

Vogel, J. (2005) "Mechanisms of femtosecond laser nanosurgery of cells and tissues," *Applied Physics B* **81**(8), 1015-1047.

Vogel, A. (2009) "Roles of tunneling, multiphoton ionization, and cascade ionization for optical breakdown in aqueous media," Final Report, AFOSR International Research Initiative Project SPC 053010/EOARD (ADA521817).

Volkov, R. V., Gordienko, V. M., Mikheev, P. M., Savel'ev, A. B., Uryupina, D. S. (2004) "High-temperature plasma produced on a free liquid surface by femtosecond laser pulses," *Quantum Electronics* **34**(2), 135-138.



- Wang, W., Liu, J., Cai, Y., Wang, C., Liu, L., Xia, C., Deng, A., Xu, Y., Leng, Y., Li, R., and Xub, Z. (2010) “Angular and energy distribution of fast electrons emitted from a solid surface irradiated by femtosecond laser pulses in various conditions,” *Physics of Plasmas* **17**(2), 023108-1 – 023108-8.
- Wieland, M., Frueke, R., Wilhein, T., Spielmann, C., Pohl, M., and Kleineberg, U. (2002) “Submicron extreme ultraviolet imaging using high-harmonic radiation,” *Applied Physics Letters* **81**(14), 2520-2522.
- Wieland, M., Spielmann, Ch., Kleineberg, U., Westerwalbesloh, Th., Heinzmann, U., and Wilhein, T. (2005) “Toward time-resolved soft x-ray microscopy using pulsed fs-high-harmonic radiation,” *Ultramicroscopy* **102**(2), 93-100.
- Wilks, S. C., Langdon, A. B., Cowan, T. E., Roth, M., Singh, M., Hatchett, S., Key, M. H., Pennington, D., MacKinnon, A., and Snavely, R. A. (2001) “Energetic proton generation in ultra-intense laser–solid interactions,” *Physics of Plasmas* **8**(2), 542-549.
- Wood, W. M., Siders, C. W., Downer, M. C., (1991) “Measurement of femtosecond ionization dynamics of atmospheric density gases by spectral blue shifting,” *Physical Review Letter* **67**(25), 3523-3526.
- Workman, J., Cobble, J., Flippo, K., Gautier, D. C., Montgomery, D. S., and Offermann, D. T. (2010) “Phase-contrast imaging using ultrafast x-rays in laser-shocked materials,” *Review of Scientific Instruments* **81**(10), 10E520-1 – 10E520-3.
- Yablonovitch, E., (1988) “Energy conservation in the picosecond and subpicosecond photoelectric effect,” *Physical Review Letters* **60**(9), 795-796.
- Yamanouchi, K. (2002) “The next frontier,” *Science* **295**(1), 1659-1660.
- Zhang, P., Liang, T.-J., Chen, L.-M., Chen, Y.-T., Li, D.-B., He, Z.-H., Wei, J.-T., Wang, Z.-Y., Tang, L., Zhang, X.-W., Liang, J., Chen, T.-J., Chen, Y.-T., Li, Z.-H., He, J.-T., Tang, L., and Zhang, J. (2001) “Effects of polarization on super-hot electron generation in femtosecond laser-plasma interaction,” *Chinese Physics Letters* **18**(10), 1374-1376.
- Zhang, P., Ovchinnikov, V. M., Frische, K., and Roquemore, W. M. (2013) “Correlation between hard x-ray yields and self-phase modulation from water plasmas excited by linearly chirped femtosecond laser,” To be published in *Optics Express*.
- Zheng, J., Tanaka, K. A., Sato, T., Yabuuchi, T., Kurahashi, T., Kitagawa, Y., Kodama, R., Norimatsu, T., and Yamanaka, T. (2004) “Study of hot electrons by measurement of optical emission from the rear surface of a metallic foil irradiated with ultraintense laser pulse,” *Physical Review Letters* **92**(16), 165001-1 – 165001-4.

Ziener, Ch., Uschmann, I., Stobrawa, G., Reich, Ch., Gibbon, P., Feurer, T., Morak, A., Düsterer, S., Schwoerer, H., Förster, E., Sauerbrey, R., (2002) "Optimization of  $K\alpha$  bursts for photon energies between 1.7 and 7 KeV produced by femtosecond-laser-produced plasmas of different scale length," *Physical Review E* **65**(8), 066411-1 -066411- 8.

## APPENDIX – Presentations and Publications

# Efficiency and scaling of an ultrashort-pulse high-repetition-rate laser-driven X-ray source

C.L. Rettig · W.M. Roquemore · J.R. Gord

Received: 24 December 2007 / Revised version: 7 May 2008 / Published online: 21 August 2008  
© Springer-Verlag 2008

**Abstract** Technical issues and performance of a high-repetition-rate ultrafast-laser-based X-ray source have been studied experimentally in the context of developing a dedicated laboratory-based tool for combustion diagnostics. X-ray emission from numerous elemental materials have been investigated to compare with analytical based expectations for yield and efficiency, as well as to evaluate advantages of some materials for operational issues such as debris production and degree of efficiency enhancement utilizing various illumination configurations. A weak inverse scaling of conversion efficiency with atomic number was observed. Broadband energy conversion efficiency of approximately  $10^{-5}$  and yield greater than  $10^{10}$  photons/s have been measured with numerous target elements. Application of a pre-pulse significantly enhances conversion efficiency, and the enhancement factor depends on material. Thus, previous optimizations must be performed in the atomic number variation as well. Additionally, the efficiency enhancement associated with p-polarization incidence (relative to s-polarization) is observed to depend on base material reflectivity.

**PACS** 52.38.Ph · 52.38.Dx

C.L. Rettig (✉)  
Innovative Scientific Solutions, Inc., 2766 Indian Ripple Rd,  
Dayton, OH 45440, USA  
e-mail: [curt.rettig@spectra-physics.com](mailto:curt.rettig@spectra-physics.com)

*Present address:*

C.L. Rettig  
Spectra-Physics, a Division of Newport, Mountain View, CA,  
USA

W.M. Roquemore · J.R. Gord  
Air Force Research Laboratory, Propulsion Directorate,  
Wright-Patterson Air Force Base, Dayton, OH 45433, USA

## 1 Introduction

Laser-based X-ray sources, made possible by the high radiation intensity of ultrashort-pulse lasers, possess unique and advantageous capabilities for use in a wide variety of applications and are potentially more accessible than synchrotron-based X-ray facilities [1–5]. Important combustion diagnostic applications that will benefit from availability of a short-pulse X-ray point source include: (1) imaging of micron-scale spray droplets in the injector region of a combustor where the optical depth at longer wavelengths is very short, (2) small-angle X-ray scattering from soot precursors to gauge their size and elucidate the physics of their growth, and (3) surface and bulk measurements of residual stress by X-ray diffraction of critical high-value gas turbine engine components. It is anticipated that diagnostics, such as (1), will require a short pulse-length and high repetition rate, while others, such as (2), will require highly coherent beams in space and energy and (3) will require extremely high brightness. Pulsed laser driven X-ray sources have the potential to provide X-rays with many of these preferential characteristics.

When a laser pulse is focused to sufficiently high intensity on a metallic target, X-rays are generated through a multi-step process. First, incident radiation ionizes the surface into a near-solid-density plasma. Absorption mechanism of the laser energy into the plasma varies somewhat with intensity, but always proceeds through the electron channel. Since typical target surfaces are initially highly conductive, absorption occurs within a skin-depth, the skin depth shrinking rapidly within the first several cycles of the laser light. The partition of the laser energy into the hot thermal and/or non-thermal electrons determines the efficiency to which the laser energy is converted into hot electron energy and especially into how efficiently the electron

energy is subsequently converted into X-rays. At modest laser intensity ( $<10^{15}$  W/cm<sup>2</sup>) almost all of the absorbed laser energy transfers through collisional processes such as inverse bremsstrahlung; at higher intensity, absorption occurs through collisionless processes, including resonance absorption and the anomalous skin effect [6]. A hot electron distribution is created with effective temperature in the range 1–5 keV, possibly including a nonthermal component at higher energy [7]. Finally, energetic electrons, incident on the metallic target, lose energy via collisions within the substrate, slowing down within a mean-free path of the surface. High-energy thermal and nonthermal electrons generate both continuum (bremsstrahlung) radiation through scattering events and characteristic (line) radiation by ionizing inner shell electrons of target atoms. Both processes are analogous to X-ray generation in conventional X-ray tubes. Emission originates from a spot size characterized by the laser focus convolved with the electron mean free path in the solid. The temporal pulse length is characterized by the slowing-down time in the substrate and the dynamics of re-absorption [8]. Thus, at least three unique characteristics of the radiation from such an X-ray source are possible: (1) very short pulse length,  $<1$  ps [8], (2) very small spot size, on the order of 10  $\mu$ m or less (which translates to high spatial coherence), and (3) very high instantaneous brightness, due to the high incident energy density. A short X-ray pulse length has enabled studies of phase transition [9] and chemical reaction dynamics [2, 10], while a small source size allows high spatial resolution imaging and phase contrast imaging to be utilized to achieve enhanced image fidelity for a given X-ray yield [11]. Efforts to improve efficiency for the overall conversion to X-rays concentrate on the absorption of the laser energy, as conversion from electron energy to X-rays allows very little to change.

Recent research on laser driven X-ray sources has successfully utilized high repetition rate lasers for generation of ultrashort X-ray pulses at high rep-rate [12–17]. Lasers operating with pulse energy of 0.1–300 mJ and focused intensity in the range  $10^{15}$ – $10^{18}$  W/cm<sup>2</sup> have been utilized to generate X-rays with demonstrated conversion efficiency in the range  $10^{-9}$ – $10^{-4}$ , as summarized by Hagedorn [14]. A significant goal of the research is to increase the conversion efficiency or absolute yield of X-ray emission while retaining ultrashort pulse length. Emission has been measured to be isotropic in a cone around the target normal, making single point measurements of conversion efficiency generally accurate [18, 19]. Targets in the form of moving tape, rotating disc, stationary substrate, liquid metal jet, and drawn wire have been utilized. In these ranges of experiments, conversion efficiency depends approximately quadratic on incident laser intensity, though substantial variation between experiments can be noted [14, 16, 19–21]. However, experimental evidence and theoretical considerations suggest the

existence of an optimal intensity above which X-ray yield decreases with increasing intensity [21, 22]. Enhanced conversion efficiency has been demonstrated when low-energy pre-pulses ( $<10\%$  of the main pulse energy) are applied [21, 23, 24]. On the other hand, some experiments have shown increased yield when care was taken to ensure that the laser possessed high contrast ratio on the picosecond timescale [13]. In most cases, the illumination angle of incidence has been normal to the surface, but in several experiments oblique incidence and *p*-polarization have been utilized with improved efficiency [25]. For slightly longer laser pulses and *p*-polarized illumination, it has been found that resonance absorption is a significant mechanism in creating superthermal electrons and fast ions and the X-ray conversion efficiency is correspondingly increased [19, 26]. Thus, spatial and temporal dynamics of the illumination are critically important to the success of the technology, and an optimum configuration has yet to be identified.

In the present study, the yield and characteristics from a high-rep-rate laser X-ray source were investigated by varying illumination geometry, and spatial and temporal dynamics. To compare yield scaling with models, targets were fabricated from numerous different elements to quantify the scaling with atomic number. To optimize the illumination configuration, polarization and pre-pulse dynamics were varied. The well-known *p*-polarization enhancement varied significantly over the different target materials in a way that correlated inversely with reflectivity. Thus, while the polarization dependence is usually attributed to resonance absorption, this indicates that the basic power available to the cutoff layer may vary with basic material optical properties. Finally, the pre-pulse enhancement was of the order of a factor of 3, and this possessed a more sharp dependence on delay time than previously observed, and the optimum time depended on target material. Numerous effects have been identified to further improve the source brightness and yield, including intensity, polarization, and pulse temporal dynamics.

## 2 Experimental configuration

In these experiments, we utilized a commercial Ti:sapphire laser that employs chirped-pulse amplification to achieve high intensity. It consists of a stable, low-power seed oscillator and a single regenerative amplifier that operates at a repetition rate of 1 kHz. The pulse length was  $\sim 45$  fs (FWHM), and the pulse energy, incident on the target, was  $\sim 1.8$  mJ. Parasitic pre-pulses are known to arise from reflections off environmental chamber surrounding the crystal. For most of the results shown here, the beam was focused by a 16 cm focal-length plano-convex lens. The beam was first passed through an expansion telescope to increase the numerical

aperture to  $NA = 0.25$ . The resulting focus was  $\sim 12 \mu\text{m}$  in diameter (FWHM), and the associated peak intensity was  $\sim 4 \times 10^{16} \text{ W/cm}^2$ . The laser incidence angle onto the target was, unless stated otherwise, 45 degrees to the surface, and p-polarized. X-ray yield and spectra were recorded with a cooled and temperature-stabilized Si-PIN photodiode and a multichannel analyzer to perform energy dispersive spectroscopy (EDS).

Due to the large numerical aperture required to achieve high focus intensity, the depth of focus is on the order of  $100 \mu\text{m}$ , which requires even shorter scale target positioning tolerance. Long integration times further exacerbate this requirement as the position must be maintained through target translation. Targets were fabricated as thin disks, 0.001–0.030 in. thick, cut from high-purity rolled stock and cleaned of oxides and residue that may interfere with surface optical properties, while the runout could be controlled to the required tolerance. The focus lens could be stepped along the beam axis with resolution of less than  $10 \mu\text{m}$  to precisely control the focal plane position relative to the target surface. The disk was moved such that the interaction point swept out a tight spiral pattern with typically  $50 \mu\text{m}$  between tracks and  $40 \mu\text{m}$  between points to cleanly separate consecutive pulses.

The final focus lens, installed inside the vacuum chamber, is vulnerable to coating by debris ablated from the target. While several techniques of debris mitigation were tested including rotating transparent membranes, the most effective method of mitigating debris was use of a buffer gas and larger standoff. The buffer gas used was helium at several Torr pressure, while a pressure of greater than approximately 10 Torr resulted in significant yield reduction. In this arrangement, no measurable coating formed on the lens after several hours of operation at full laser power. Since the volume of debris from higher power sources is expected to increase proportionately with the power, a more effective method of active debris elimination or reactive passivation will be essential.

### 3 X-ray characteristics

#### 3.1 Target materials

Targets were fabricated from twelve different elements to determine atomic number scaling and the most appropriate target material for specific applications. For each target, at least one characteristic X-ray line was observed that uniquely identified elemental composition. Characteristic lines in the measured energy range (2–10 keV) are associated with *K-shell* transitions for elements from the fourth row of the periodic table and with *L-shell* transitions for elements in the fifth and higher rows. In most cases, alpha

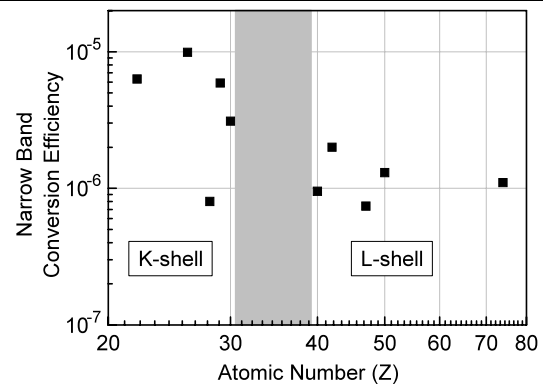


**Fig. 1** Atomic-number ( $Z$ -) dependence of narrow-band conversion efficiency measured at constant energy. Note that the line emission evaluated is from a K-shell transition on the left and from an L-shell transition on the right. The grayed out region indicates elements with no emission lines between 2 and 10 keV

and beta components of the series were observed simultaneously. Mu-metal and stainless steel radiated multiple-line spectra with three or more components, although the intensity of each line was not proportional to the elemental concentration. Such a multiple-line source could be useful for differential absorption spectroscopy or phase contrast imaging. The atomic number dependence of the principal line emission for numerous elements is shown in Fig. 1. It must be noted that for species with atomic number  $Z < 33$ , the line strength plotted corresponds to K-shell emission, while radiation from elements with  $Z > 40$  corresponds to L-shell emission, because these are the ranges that fell within the measurement range of the detector system. The scaling trend of reducing conversion efficiency with increasing  $Z$ - for constant laser energy is generally consistent with expectations [22].

Line emission, requiring a minimum electron energy for ionization of an inner shell electron, scales somewhat differently than bremsstrahlung emission. Figure 2 shows the  $L_{\alpha}$  photon yield and electron temperature,  $T_e$ , at various locations as the focal plane is scanned through a molybdenum target. At the centermost position where target surface intensity is greatest, the yield is greatest.  $T_e$  is calculated by fitting the energy dependent yield in the continuum portion of the photon energy spectrum at each position. The characteristic or line radiation exhibits a quasi-threshold dependence on the intensity, as it increases more rapidly after a delayed onset. The collisional ionization cross section for the  $2s$  electron (whose vacancy results in L-shell photon emission) peaks at energies well above those measured in the experiments here, approximately three times its binding energy [27], which is shown by the dotted line in Fig. 3. Thus, only tail electrons contribute to line emission in these experiments. Clearly, higher temperatures by use of higher intensity are required for optimum line emission yield as confirmed in numerical analysis [22]. Note that on one side

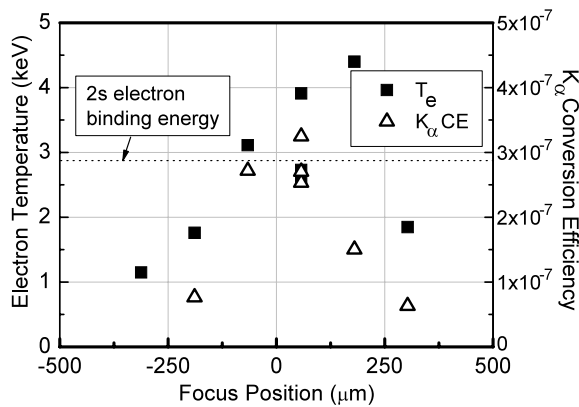


**Fig. 2** Electron temperature plotted as a function of the focus position while the focal plane is scanned through a molybdenum target. For comparison, the dotted line indicates the binding energy for the 2s electron of Mo. Conversion efficiency (CE) of laser energy to  $K_{\alpha}$  photon energy is also shown

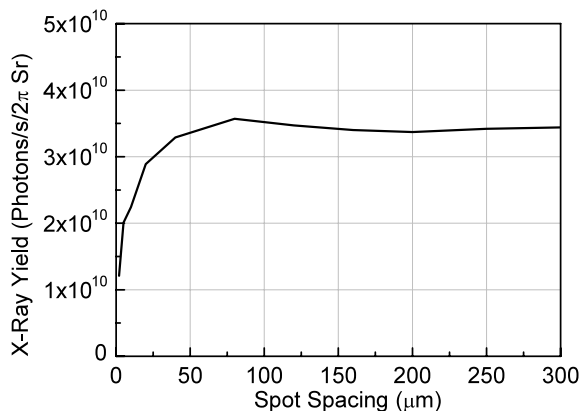


**Fig. 3** X-ray yield from an Fe target for different values of spacing between adjacent pulses. The rate is roughly constant above the FWHM spot size of 20  $\mu\text{m}$ , although variation up to 50  $\mu\text{m}$  indicates significant energy outside Gaussian defined spot size

of the optimum X-ray yield, the temperature actually increases. Speculation to explain this might focus on creation of a slightly underdense (than optimum) plasma above the surface which can reach higher temperature, but has insufficient density to act as X-ray targets. Asymmetries in the intensity emission characteristics centered about the surface have been noted for some time.

### 3.2 X-ray yield and conversion efficiency

While establishing consistent target conditions, it was found that the X-ray yield depends sensitively on the spacing between consecutive pulses on the solid target. The importance of presenting new target material to the focus for each pulse was investigated by varying the spot spacing on the target. In Fig. 3, the X-ray yield from an Fe target is shown as the pulse separation on target is varied from well less than the spot size ( $\sim 12$  microns) to more than 10 times the spot size.

As the spacing decreases less than a spot size resulting in overlap of adjacent pulses, the yield reduces rapidly. The X-ray yield is reduced even when each point on the target receives an average of just two pulses. Thus, to ensure maximum output and efficiency from a laser-driven X-ray source, it is extremely important to illuminate a new flat target with each laser pulse, as we have done in all subsequent scaling studies. This degradation does not result from the axial displacement of the interaction point by creation of a crater since the crater depth was measured to be  $\sim 5$   $\mu\text{m}$  per pulse. Rather, it may well be that the increased crater area left by a previous pulse effectively reduces the incident intensity, resulting in reduced efficiency. Thus, if the incident intensity were greater than the optimum, repetitive hits might result in increased efficiency. Other speculation as to the origin of the degraded yield typically concerns roughening of the surface. However, in some experiments enhanced yield from multiple-pulse overlap have been observed when utilizing a tape target [21].

The X-ray yield represents the measured photon rate extrapolated into a *hemisphere* and with energy greater than  $\sim 2$  keV. As mentioned, great care was taken to ensure that longitudinal motion of the rotating and translating target was less than the Rayleigh range throughout integration.

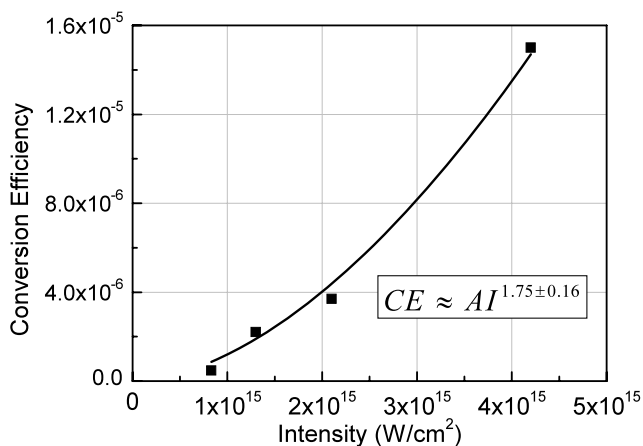
Note that we normalize emission into a hemisphere because backward-pointing emission into a planar target is unrecoverable—although there is no evidence that it is any less intense. Thus, we took a conservative accounting of the emission, and conversion-efficiency values reported here should be doubled when compared to results based upon emission into a sphere. Table 1 lists the broadband and narrowband yield and conversion efficiency for all of the materials investigated so far in this work.

A more quantitative determination of the X-ray yield dependence on intensity has been performed by varying the incident pulse energy while maintaining a fixed focus position and size. In Fig. 4, the measured conversion efficiency from a copper target is plotted as a function of incident laser intensity for pulse energy in the range 0.1–1.8 mJ. The conversion efficiency is fit by a power-law scaling with intensity, i.e.,  $CE = aI_{\text{inc}}^{\gamma}$ , where  $I_{\text{inc}}$  is the incident laser intensity,  $a$  is a proportionality constant, and  $\gamma$  is the exponent fit parameter. As noted in Fig. 4, the best fit to the data points occurs with an exponent of  $\gamma \approx 1.74 \pm 0.16$ . Similar measurements performed for titanium, molybdenum, and copper targets indicated that  $\gamma$  lies within experimental uncertainty of  $\gamma = 1.8$  for each element. Note that this value is a similar magnitude to that determined by numerous other authors utilizing lasers with similar available intensity [13, 14, 16, 19, 21]. As the laser intensity increases and approaches the optimum for X-ray production, the exponent must decrease as laser energy partitions into higher energy X-rays which may be created and absorbed deep in the substrate or other high energy products.



**Table 1** X-ray emission characteristics for several materials studied. Note that yield and conversion efficiency values are defined for emission into a hemisphere

Element	Z	Broadband yield (ph/s/2 $\pi$ Sr)	Broadband conversion efficiency	$E_{ph}$	$K_{\alpha}$ ( $L_{\alpha}$ ) yield (ph/s/2 $p$ Sr)	$K_{\alpha}$ ( $L_{\alpha}$ ) CE
Ti	22	$4.8 \times 10^{10}$	$2.4 \times 10^{-5}$	4.5	$2.7 \times 10^{10}$	$1.1 \times 10^{-5}$
V	23	$2.3 \times 10^{10}$	$1.3 \times 10^{-5}$	4.95	$1.1 \times 10^{10}$	$4.9 \times 10^{-6}$
Fe	26	$4.7 \times 10^{10}$	$2.3 \times 10^{-5}$	6.41	$1.5 \times 10^{10}$	$8.6 \times 10^{-6}$
Ni	28	$1.3 \times 10^{10}$	$4.3 \times 10^{-6}$	7.48	$3.6 \times 10^9$	$2.4 \times 10^{-6}$
Cu	29	$1.9 \times 10^{10}$	$1.4 \times 10^{-5}$	8.05	$6.5 \times 10^9$	$4.6 \times 10^{-6}$
Zn	30	$1.8 \times 10^{10}$	$1.3 \times 10^{-5}$	8.64	$4.1 \times 10^9$	$3.1 \times 10^{-6}$
Zr	40	$2.5 \times 10^{10}$	$1.4 \times 10^{-5}$	2.01 (La)	$5.2 \times 10^9$	$9.5 \times 10^{-7}$
Mo	42	$3.3 \times 10^{10}$	$1.5 \times 10^{-5}$	2.29 (La)	$9.8 \times 10^9$	$2.0 \times 10^{-6}$
Ag	47	$9.6 \times 10^9$	$3.7 \times 10^{-6}$	3.0 (La)	$3.0 \times 10^9$	$8.2 \times 10^{-7}$
Sn	50	$2.2 \times 10^{10}$	$1.1 \times 10^{-5}$	3.44 (La)	$4.1 \times 10^9$	$1.3 \times 10^{-6}$
W	74	$2.6 \times 10^{10}$	$1.4 \times 10^{-5}$	8.4 (La)	$1.5 \times 10^9$	$1.1 \times 10^{-6}$

**Fig. 4** Conversion-efficiency dependence on focus intensity for a copper target. For clarity, several data points have been averaged to each point plotted. A power-law fit to the data is shown as a solid line

### 3.3 Dependence on incident polarization

While the primary laser absorption mechanism at intensities  $\lesssim 10^{14}$  W/cm<sup>2</sup> is inverse bremsstrahlung, its absorption coefficient reduces with decreasing collisionality at higher intensity. At intensities greater than  $\sim 1\text{--}5 \times 10^{15}$  W/cm<sup>2</sup>, collisionless processes including resonance absorption become dominant [28]. Physically, resonance absorption involves a p-polarized wave that tunnels through to the critical surface where it resonantly excites a plasma wave which grows until it in turn is damped by collisions or particle trapping and wave breaking [28, 29]. A p-polarized component of the incident light is necessary to produce an oscillating electric field along the density gradient. Thus, with our oblique incidence illumination geometry, we have a crude method of determining what role, if any, resonance absorption plays in X-ray generation. This experiment is somewhat complicated by the issue of whether the incident light is actually p-polarized in the vicinity of the critical layer (within sev-

eral wavelengths) and its uniformity over the full wavefront. For example, with micro-structured targets, local variations in the target normal and associated plasma density gradient result in wide variation of the local polarization relative to the density gradient; thus, polarization issues can be complicated beyond resolution.

With our flat targets, we have tested for the possible role of resonance absorption by varying the illumination polarization between s- and p-incidence at 45 degree incidence illumination angle. Figure 5a shows the X-ray conversion efficiency as a function of the focus position for separate scans in which the incident light is p-polarized and s-polarized. To determine whether other differences in the two cases might account for the enhanced yield associated with p-polarization, we repeated the scans with the target rotated to normal incidence in which case the polarizations are degenerate. No significant difference in the yields was measured, as shown in the inset of Fig. 5a. Furthermore, the intensity scaling dependence for s- and p-polarization illumination was found to be significantly different. Figure 5b shows the conversion efficiency for a Fe target as a function of intensity when the illumination is in the s- and p-polarizations, indicating that the intensity dependence is significantly stronger for the p-polarization. Also note that this is merely an average dependence over the range of intensities studied here; a power scale fit to the p-polarization yield vs. intensity curve ignores the salient features of resonance absorption, but the difference is strongly suggestive of an additional mechanism in the case of p-polarized illumination.

Another clue to the origin of the polarization dependence is that the enhancement varies with target material. For example, emission from titanium was a factor of 3 greater for p-polarized incidence than for s-polarized incidence, whereas virtually no difference was evident when silver targets were used. Among the materials tested, the largest discrepancy measured was for materials with low surface re-



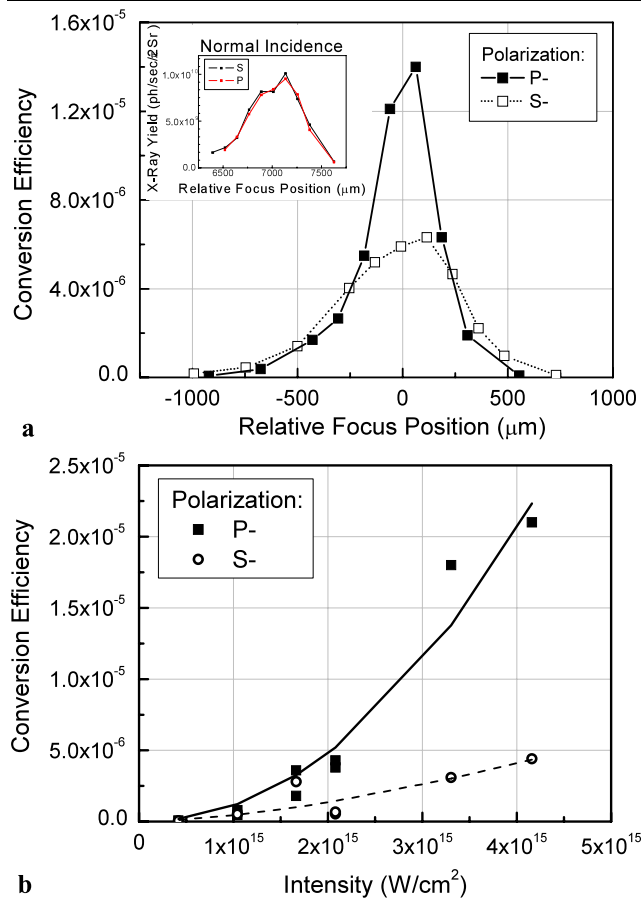


**Fig. 5** (a) Conversion efficiency of laser energy to X-ray energy as a function of axial focus position, measured for both s- and p-polarization illumination. In the inset, the same comparison is shown for a configuration in which the illumination is at normal incidence; thus, the polarizations are indistinguishable and the yields are nearly identical. (b) Conversion efficiency dependence on intensity for s- and p-polarization shows increased yield for p-polarization as intensity increases into the range predicted for resonance absorption

flectivity. Figure 6 shows a plot of the p-polarization incidence yield normalized to the s-polarization incidence yield for numerous target materials as a function of the base metal reflectivity (measured for each actual target). It is understood that low-power reflectivity varies considerably with surface conditions, including smoothness of finish and cleanliness and may have little direct relevance to the high-intensity (ionized) reflectivity. Analogy might be made to dielectric coatings in which lower reflectivity surfaces have greater differences between s- and p-polarization reflectivity. Thus, more power can leak through to the cutoff layer when the incidence is p-polarized and indeed there is even a minimum in the reflection dependence at the Brewster angle.

### 3.4 Efficiency scaling with pre-pulse illumination

Pre-pulses offer a promising technique for enhancing X-ray conversion efficiency. The potential improvement arises

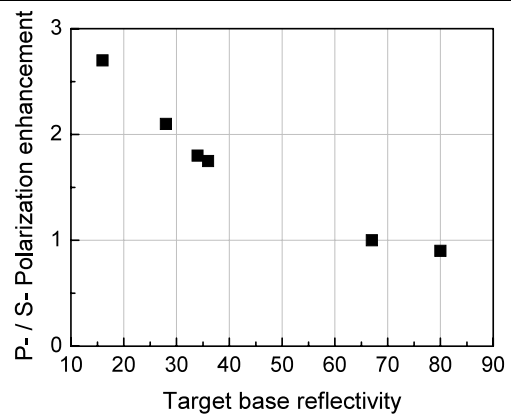


**Fig. 6** Ratio of X-ray yield with p-polarization illumination relative to that with s-polarization illumination, as a function of (low power) target reflectivity for various materials. P-polarization enhancement is most significant for materials with low reflectivity

from somewhat poor laser light coupling to the absorption region in the very steep density profiles which are characteristic of solid targets. Primary absorption occurs in the regions related to the cutoff, where the local electron density,  $n_e$ , equals the critical density,  $n_{cr}$ , for the incident light

$$n_{cr} = \frac{mc^2}{\lambda^2 e^2},$$

where  $m$  is the electron mass,  $\lambda$  is the incident light vacuum wavelength, and  $e$  is the electron charge. The salient action of the pre-pulse is to create high-density plasma in front of the target. During the intervening delay before the main pulse arrives, the density profile evolves through collisional and convective transport due to the high local temperature. Coupling to the absorption region can be optimized if the density gradient scale length leading up to it can be made sufficiently long, e.g., on the order of the vacuum wavelength. During the delay, the scale length increases but the peak density decreases and the pre-pulse plasma becomes under-dense and less effective for coupling. Thus, the optimum pre-pulse delay represents a compromise between creating a well-matched layer and sustaining sufficient peak density as to affect good coupling. Previous experiments which have demonstrated improved yield with pre-pulses have utilized delays on the order of 10–100 ps.

To ensure stable timing with delays on the order of 10–100 ps, the pre-pulse must be derived from the same source as the main pulse by splitting the laser output into a main and pre-pulse beam. The pre-pulse beam was sent through a delay line which could be varied over a 300 ps range, while the main pulse was delayed by the maximum delay of the variable delay line. The main pulse was also rotated into s-polarization while the pre-pulse remained in p-polarization and the pulses were then re-combined through a polarizing beamsplitter. To accommodate the re-

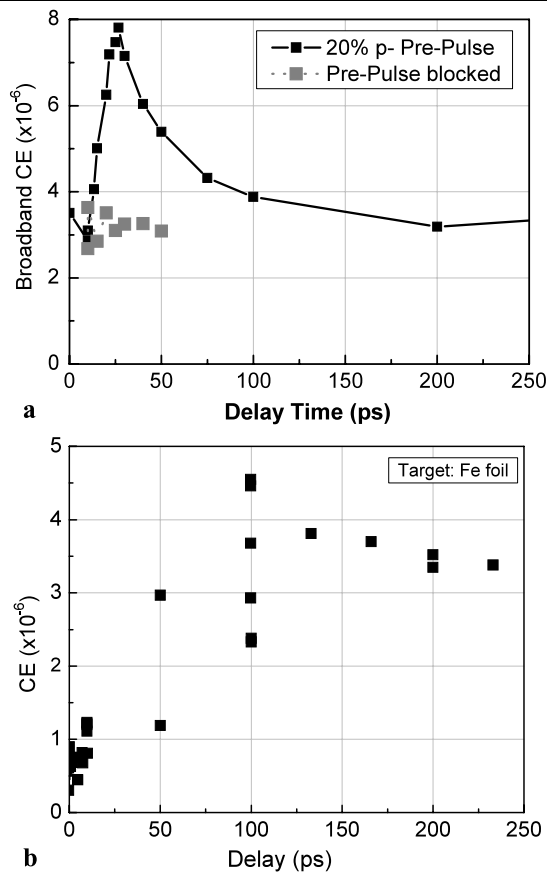


**Fig. 7** Broadband conversion efficiency as a function of time delay following a small amplitude (approximately 20%) pre-pulse for (a) Ti target and (b) Fe target. Conversion efficiency calculation accounts for the pre-pulse energy. Points shown in gray have the pre-pulse beam blocked and the enhancement goes away as expected

duced aperture of the polarizer, the beam waist and subsequent focus numerical aperture were reduced, resulting in reduced peak intensity and reduced absolute conversion efficiency. Approximately 80% of the energy was carried in the main pulse. Figure 7 is a plot of the measured conversion efficiency from a Ti target as a function of the pre-pulse delay time, i.e., the delay time between pre-pulse and main pulse. Note that when the pre-pulse was blocked, the conversion efficiency reduced to nearly the same value as when the delay is very long. Thus, quite a small perturbation results in a significant yield enhancement. The conversion efficiency in each case is calculated based upon the total energy incident on target, pre-pulse included or omitted, as the case may be. The optimum delay is approximately 30 ps for Ti. When the target material was changed to Fe, the optimum delay increased to approximately 100 ps and the shape of the yield dependence around the optimum was significantly wider, indicating significantly different transport in the plasma associated with the Fe target.

### 3.5 Discussion

X-ray generation from a high-intensity laser pulse that is incident on a solid target is a multi-step process, each step having independent optimization conditions and losses. First, laser light must be coupled into the metallic target substrate. Losses include reflection prior to ionization (usually insignificant for femtosecond pulses), reflection from the discontinuous plasma boundary (especially if the density scale-length is too short), and reflection from a parasitic pre-pulse plasma that couples poorly to the electron thermal distribution. Inverse bremsstrahlung and resonance absorption (RA) both create energetic electron populations, although the population associated with RA is predicted to have a stronger tail due to damping of the resonantly driven plasma wave on electrons [26]. Second, energetic electrons interact with the dense substrate to create (1) continuum radiation when interacting by low angle Coulomb collisions and (2) characteristic radiation if a collision happens to ionize an inner shell electron. In either case, interactions occur between electrons and the substrate. Losses in this step include electrons which are born into trajectories away from the target (although this is reduced by ambipolar charging) and losses into heating the substrate. Typical conversion efficiency from electron-beam energy to X-ray energy is of the order of  $10^{-3}$  in a conventional X-ray tube. Thus, if the overall conversion efficiency in a laser driven source is  $10^{-6}$ , then the conversion efficiency of light to electron kinetic energy is on the order  $10^{-3}$ . Although this assessment is admittedly very approximate, the physical mechanism of X-ray generation from energetic electrons is common and well known, so it places the challenge for further improvements in improving laser absorption and perhaps into tailoring the driven electron distribution.

### 4 Summary

Utilizing an ultrafast laser, we have demonstrated a frequency-agile X-ray point source that is suitable for applications in combustion diagnostics when scaled to higher power. The source can be configured to emit narrow-band radiation in nearly any region of the soft X-ray spectrum because solid-state targets allow utilization of many different elements and alloys. The narrowband conversion efficiency and yield for most elements investigated decreased gradually with atomic number and was  $>10^{10}$  photons/s into  $2\pi$  Sr, with energy conversion-efficiency greater than  $10^{-5}$ . For applications requiring monoenergetic X-rays, titanium would be an excellent target material because of its strong coherent peak in relation to the continuum background. Investigation of numerous elements has demonstrated atomic number scaling

of yield that is consistent with theoretical predictions. Further details of enhanced yield arising from optimized polarization and pre-pulses have been found. For example, the pre-pulse delay time dependence of the X-ray yield has been shown to be very sharp in at least one element, and the optimum delay varies with element. The greatest factor in conversion efficiency in the high-rep-rate, low-intensity regime of operation ( $<10^{16}$  W/cm<sup>2</sup>) was previously known to be incident intensity, but as more high rep-rate lasers achieve optimum intensity, polarization, pre-pulses, pulse dynamics and other factors will assume prominence.

While the presently available X-ray flux is sufficiently large that imaging over many pulses can be considered, significant advantages in combustion diagnostics can be realized if the flux can be increased sufficiently to allow much shorter integration time. The current generation of high-rep-rate laser drivers can produce more than five times the pulse energy as our present laser and with approximately one-half the pulse length, producing an order of magnitude higher intensity. This is close to the optimum intensity for most of the materials investigated. Additionally, low loss mode correction by deformable mirror adaptive optics, as demonstrated by many researchers, increases the intensity by more than an order of magnitude. This is expected to be sufficient for radiography of a fuel spray with averaging of less than 100 ms. Further advantages are possible by employing phase contrast imaging in the diagnostic, possible because of the high spatial coherence of the source.

**Acknowledgements** The authors wish to express appreciation to Kyle Frische for significant assistance in the experimental work especially in maintenance and performance enhancement of the laser systems. We would also like to thank Sivaram Gogineni and Keith Grinstead for assistance in the experiments. The support of Dr. Anne Matsuura and the Physics and Electronics Division of the Air Force Office of Scientific Research is gratefully acknowledged.

## References

- Ch. Rose-Petruck, R. Jimenez, T. Guo, A. Cavalleri, C.W. Siders, F. Rksi, J.A. Squier, B.C. Walker, K.R. Wilson, C.P.J. Barty, *Nature* **398**, 310 (1999)
- K. Sokolowski-Tinten, C. Blome, C. Dietrich, A. Tarasevitch, M. Horn von Hoegen, D. von der Linde, A. Cavalleri, J. Squier, M. Kammler, *Phys. Rev. Lett.* **87**, 225701 (2001)
- M. Croft, I. Zakharchenko, Z. Zhong, Y. Gurlak, J. Hastings, J. Hu, R. Holtz, M. DaSilva, T. Tsakalakos, *J. Appl. Phys.* **92**, 578 (2002)
- K. Sokolowski-Tinten, D. von der Linde, *J. Phys. Condens. Matter* **16**, R1517 (2004)
- C.W. Siders, A. Cavalleri, K. Sokolowski-Tinten, Cs. Toth, T. Guo, M. Kammler, M. Horn von Hoegen, K.R. Wilson, D. von der Linde, C.P.J. Barty, *Science* **286**, 1340 (1999)
- W. Rozmus, V.T. Tikhonchuk, *Phys. Rev. A* **42**, 7401 (1990)
- W. Rozmus, V.T. Tikhonchuk, R. Cauble, *Phys. Plasmas* **3**, 360 (1996)
- T. Feurer, A. Morak, I. Uschmann, Ch. Ziener, H. Schwöerer, E. Förster, R. Sauerbrey, *Appl. Phys. B* **72**, 15 (2001)
- A. Rousse, C. Rischel, S. Fourmaux, I. Uschmann, E. Förster, P. Audebert, J.P. Geindre, J.C. Gauthier, D. Hulin, *Meas. Sci. Technol.* **12**, 1841 (2001)
- Y. Jiang, W. Li, G. Cao, T. Lee, G. Ketwaroo, Ch. Rose-Petruck, Applications of X-rays generated from lasers and other bright sources II, in *Proc. SPIE (The International Society for Optical Engineering)*, vol. 4504, ed. by G. Kyrall, J.-C. Gauthier (SPIE, Bellingham, 2001)
- D. Boschetto, G. Mourou, A. Rousse, A. Mordovanakis, B. Hou, J. Nees, D. Kumah, R. Clarke, *Appl. Phys. Lett.* **90**, 11106 (2007)
- Y. Jiang, T. Lee, W. Li, G. Ketwaroo, C.G. Rose-Petruck, *Opt. Lett.* **27**, 963 (2002)
- N. Zhavoronkov, Y. Gritsai, G. Korn, T. Elsaesser, *Appl. Phys. B* **79**, 663 (2004)
- M. Hagedorn, J. Kutzner, G. Tsilimis, H. Zacharias, *Appl. Phys. B* **77**, 49 (2003)
- G. Korn, A. Thoss, H. Stiel, U. Vogt, M. Richardson, T. Elsaesser, M. Faubel, *Opt. Lett.* **27**, 866 (2002)
- B. Hou, J.A. Nees, W. Theobald, G. Mourou, L.M. Chen, J.-C. Kieffer, A. Krol, C.C. Chamberlain, *Appl. Phys. Lett.* **84**, 2259 (2004)
- O. Albert, H. Wang, D. Liu, Z. Chang, G. Mourou, *Opt. Lett.* **25**, 1125 (2000)
- R.J. Tompkins, I.P. Mercer, M. Fettweis, C.J. Barnett, D.R. Klug, L.G. Porter, I. Clark, S. Jackson, P. Matousek, A.W. Parker, M. Towrie, *Rev. Sci. Instrum.* **69**, 3113 (1998)
- U. Teubner, C. Wülker, W. Theobald, E. Förster, *Phys. Plasmas* **2**, 972 (1995)
- L. Chen, P. Forget, R. Toth et al., Laser generated and other lab. X-ray and EUV sources, in *Proc. SPIE*, vol. 5196 (SPIE, Bellingham, 2004), p. 337
- J. Kutzner, M. Silies, T. Witting, G. Tsilimis, H. Zacharias, *Appl. Phys. B* **78**, 949 (2004)
- Ch. Reich, P. Gibbon, I. Uschmann, E. Förster, *Phys. Rev. Lett.* **84**, 4846 (2000)
- K. Sokolowski-Tinten, C. Blome, J. Blums, A. Cavalleri, C. Dietrich, A. Tarasevitch, D. von der Linde, *AIP Conf. Proc.* **634**, 11 (2002)
- M. Berglund, L. Rymell, H.M. Hertz, *Appl. Phys. Lett.* **69**, 1683 (1996)
- L.A. Gizzi, D. Giulietti, A. Giulietti, P. Audebert, S. Bastiani, J.P. Geindre, A. Mysyrowicz, *Phys. Rev. Lett.* **76**, 2278 (1996)
- D.D. Meyerhofer, H. Chen, J.A. Delettrez, B. Soom, S. Uchida, B. Yaakobi, *Phys. Fluids B* **5**, 2584 (1993)
- H. Deutsch, K. Becker, B. Gstir, T.D. Märk, *Int. J. Mass Spectrom.* **213**, 5 (2002)
- V.L. Ginzburg, *The Propagation of Electromagnetic Waves in Plasmas* (Pergamon, New York, 1964)
- P. Gibbon, E. Förster, *Plasma Phys. Control. Fusion* **38**, 769 (1996)

## **APPENDIX AB**



# **An Evaluation of fs/ns-LIBS for Measuring Total Particulate Emissions**

**SERDP WP-1628**

Final Report  
May 2009

Dr. Mel Roquemore  
Air Force Research Laboratory

in collaboration with

Dr. Mike Brown  
Innovative Scientific Solutions, Inc. (ISSI)

and

Professor David Hahn  
University of Florida

Approved for public release; distribution unlimited.

## Table of Contents

List of Figures .....	104
1.0 Executive Summary .....	106
2.0 Introduction .....	108
3.0 Background .....	109
3.1 Conventional ns-LIBS .....	109
3.2 Femtosecond fs-LIBS .....	113
4.0 Results and Discussion .....	114
4.1 Experimental Methods for University of Florida Activities .....	114
4.2 fs/ns LIBS at Propulsion Directorate Air Force Research Laboratory.....	119
4.2.1 Experimental Set-up.....	119
4.2.2 LIBS signal acquisition and processing .....	121
4.2.3 ns-LIBS with gas-phase carbon .....	123
4.2.4 ns-LIBS with solid –phase carbon (aerosol particles) .....	128
4.2.5 ns-LIBS with solid-phase carbon (polystyrene spheres).....	129
4.2.6 fs-ns dual-LIBS with gas and solid-phase carbon (CO <sub>2</sub> and aerosol particles) .....	130
5.0 Summary and Observations .....	136
6.0 Recommendations.....	138
7.0 Acknowledgement .....	140

## List of Figures

Figure 3.1. ns-LIBS spectrum of sulfuric acid aerosols in the vicinity of the three sulfur emission lines used for concentration measurements. (Taken from Nunez 2000.) .....	110
Figure 3.2. Calibration of ns-LIBS signal for sulfur emission taken from sulfuric acid aerosols. The ns-LIBS signal scales linearly with the sulfur concentration in the parent liquid (by weight %) and with the sulfuric acid mass density in the probe volume. (Taken from Nunez 2000.).....	111
Figure 3.3. Particle size histogram determined from LIBS signals recorded in a stream of Ca-based particles with co-flow of nitrogen at 1 atm. The bars indicate the LIBS-based particle size measurements. The solid line indicates the size results obtained using a commercial particle sizer. (Taken from Hahn 2000.) .....	111
Figure 3.4. The elemental metal composition of the exhaust stream of a biomass coal burner for three different fuels obtained from ns-LIBS measurements. The spectral features of 8 different metals were monitored simultaneously. (Taken from Blevins 2003.) .....	112
Figure 3.5. LIBS spectra for different sources of carbon All the spectra have the same scale and have been shifted vertically for clarity. (From Hohreiter 2005.) .....	113
Figure 3.6. Calibration curves based on C atomic emission line for 5 carbon analyte sources. (From Hohreiter 2005.) .....	113
Figure 4.1.1 and 4.1.2. 1000-shot average LIBS spectra for 10% gas-phase carbon (left) and for 90% gas-phase carbon (right) for both single-pulse and dual-pulse LIBS.....	116
Figure 4.1.3 and 4.1.4. LIBS calibration curves for 90% gas-phase carbon (left) and for 10% gas-phase carbon (right) for both single-pulse and dual-pulse LIBS configurations.....	116
Figure 4.1.5. Individual slopes of the LIBS calibration curves as a function of the percent gaseous carbon ranging from 10% to 90%, for both the single and dual-pulse cases. ....	117
Figure 4.1.6. Ratio of the dual-pulse to single-pulse calibration curve response as predicted from the trend lines of Figure 4.1.5 and as measured from the individual calibration curves, as a function of the percent gaseous carbon ranging from 10% to 90%. ....	118
Figure 4.2.1. Schematic of the dual laser system LIBS setup used for this study. As indicated by “path 1” and “path 2” labels, two LIBS signal collection geometries were employed. For path 1 the LIBS signal was collected at 90-degrees to the incident laser beams and for path 2 the signal was collected in the backward direction using a pierced mirror. For clarity, only the mirrors directing the collected LIBS emission are shown. See text for details.....	120
Figure 4.2.2. LIBS chamber used for all data collection presented here. Design based on work by Dr. Hahn and co-workers. ....	121
Figure 4.2.3. Graphical representation of Peak and Baseline. The peak-to-base ratio (P/B) is defined as the ratio of the peak area to the midpoint value (value at line center) of the baseline. ....	122
Figure 4.2.4. Measured peak-to-base ratios for two pulse energies compared with results from (Hohreiter and Hahn, 2005) (Univ. of Fla.). (Backward light collection.) Error bars equal to size of markers.....	124
Figure 4.2.5. Linear fits to the data of Figure 4.2.4. Slope for corresponding work by Hahn et al = $1.16 \times 10^{-4}$ .....	124
Figure 4.2.6. Measured peak-to-base ratios as a function of gate delay for three values of the gate width...	125
Figure 4.2.7. Measured peak carbon signal as a function of gate delay and gate width. Compare with Figure 4.2.6. ....	126
Figure 4.2.8. Schematic indicating the aperturing of the LIBS plasma volume by the entrance slit of the spectrometer. (Slit indicated by the gray rectangular box.) The LIBS plasma appears as an ellipsoid with the long axis collinear with the propagation axis of the laser, b). c) and d) indicate the portion of the ellipsoid that passes through the spectrometer slit for backward, c), and 90-degree, d), light collection. (See Figure 4.2.1 for light collection geometry.).....	127
Figure 4.2.9. Measured peak-to-base ratios versus mass loading for 90-degree light collection (path 1 in Figure 4.2.1). Compare with Figure 4.2.4. Ns-LIBS on solid-phase carbon (aerosol particles).....	127

Figure 4.2.10. Comparison of peak-to-base ratios for carbon in aerosol form (oxalic acid) versus mass loading for the data collected with the setup at WPAFB and at the Univ. of Florida (Hahn). Backward light collection. ....	128
Figure 4.2.11 Particle size distribution determined by a differential mobility analyzer for the Duke Scientific 50-nm polystyrene spheres. Agglomeration above an effective diameter of 225 nm is unknown as these sizes lie outside the operating range of the analyzer. Compare with Figure 4.2.12. ....	129
Figure 4.2.12. Peak-to-base ratios for the LIBS signals associated with the particle size distributions shown in Figure 4.2.11. ....	130
Figure 4.2.13. Timeline for the dual-pulse LIBS experiments. For the work done at the Univ. of Fla., both pulses were delivered from a ns laser. For the work done at WPAFB, the first pulse was delivered from an fs laser and the second from a ns laser. ....	131
Figure 4.2.14. Images of fs and ns laser sparks collected at 90-degrees. The spark images have been displaced vertically for clarity. The fs spark appears 750 $\mu\text{m}$ behind the location of the peak ns spark plasma emission. ....	132
Figure 4.2.15. Peak-to-base ratios for fs-ns and ns-only excitation of carbon in gaseous phase as a function of the mass loading in the chamber. ....	133
Figure 4.2.16. Peak-to-base ratios for fs-ns and ns-only excitation of carbon in aerosol phase as a function of the mass loading in the chamber. ....	134
Figure 4.2.17. Peak-to-base ratios for fs-ns and ns-only excitation of carbon in $\text{CO}_2$ /aerosol mixtures as a function of the percent of gaseous carbon present. Downward slopes are indicative of stronger LIBS signals from the aerosol phase. For each mixture, the total mass loading of all carbon present was held to 5000 $\mu\text{g}/\text{m}^3$ . ....	134
Figure 4.2.18. Ratio of peak-to-base values for the fs-ns configuration to the ns-only configuration. Data in figure was constructed using the data in Figure 4.2.17. ....	135

## 1.0 Executive Summary

This report describes the research performed on a one year seed program that resulted from the SERDP Statement of Need, SON 08-05. SERDP seed programs involve innovative approaches that entail high technical risk. Their purpose is to develop the data necessary to provide for risk reduction and/or a proof of concept. The following research question was raised in this Statement of Need (SON), “How can one accurately measure the total particulate emissions, including the volatile contribution?” This study investigated the feasibility of using Laser Induced Breakdown Spectroscopy (LIBS) as an approach to addressing this question.

LIBS involves the ionization or dissociation of molecular species into their atomic constituents and the subsequent emissions from electrically excited atoms. Using the LIBS signal from an unknown sample, one can identify the atomic ions, neutrals, and their relative concentrations. This information can then be used to estimate the molecular (parent) species and their concentrations in the original sample. This approach has been applied to gas, liquid, and solid samples and in some cases mixtures of molecules in different states or physical phase. However, there is a potential problem. How can one use LIBS to distinguish between a species in a multi phase mixture? The premise of quantitative LIBS is that the sample is completely dissociated into the constituent atoms by the laser/plasma/sample interactions regardless of the molecular state or phase of the target species. This premise would discourage the use of LIBS for distinguishing between gaseous and particulate species; however, recent studies by Prof. David Hahn at the University of Florida, obtained data that suggested this premise is not correct for certain aerosol and solid particle samples. In their work, LIBS calibration curves were generated for gas, liquid aerosol, and solid particles containing carbon. It was noted that the calibration curves were the same for different gaseous samples. However, it was demonstrated that calibration curves of LIBS signal vs carbon concentration depend, not only on the phase of the carbon sample, but on particle size and composition of the original particulates containing the carbon atoms. This raises the question: can the differences in LIBS response be used to determine the total particulates in a multi-phase sample with molecules containing a common type of atom? This is an important question because the exhaust of a gas turbine engine can have the same atomic species in multiple phases and in different types of molecules.

This program explored the question: is it feasible to develop a LIBS based technique that can distinguish between gaseous and particulate species in a way that the total particulates can be determined in a multiphase sample? The approach was to explore the use of nanosecond (ns,  $10^{-9}$  s) and femtosecond (fs,  $10^{-15}$  s) LIBS in ways that would take advantage of the difference in LIBS response to species in gaseous and particulate states. Carbon was selected for study because it is relatively straight forward to generate gaseous and particulate sample streams and because there are published results documenting the different in LIBS response for carbon in multi-phase samples. The conditions studied were not those expected in a gas turbine engine exhaust but those that were conducive to exploring new concepts for in situ measurements of total particulates. If a concept proved feasible, then it would be evaluated in more realistic environments.

The program involved a joint effort between Prof. David Hahn and the Air Force Research Laboratory (AFRL). Dr Hahn investigated a combined single- and dual-pulse ns-LIBS technique for overcoming the multi-phase problem. AFRL investigated using single ns-LIBS and dual fs/ns-LIBS techniques. The idea of using fs-LIBS resulted from literature studies that suggest fs lasers, can dissociate



a sample more efficiently than a ns laser. AFRL also investigate the question: can a fs/ns-LIBS technique provide a solution to the multi-phase sampling and partitioning problem?

This program was partly successful because of a new and innovative idea put forward by Prof. Hahn. His group demonstrated that single ns-LIBS and dual ns/ns-LIBS measurements could be used, in a unique way, to estimate the percentage of gaseous and total particulate carbon in a mixture of air, CO<sub>2</sub>, and carbon particulates. The idea followed from the observation that the dual ns/ns-LIBS signal increased with increasing particulate carbon concentration at a different rate than the traditional single ns-LIBS signal. They obtained calibration curves that quantitatively related the dual-pulse ns/ns-LIBS and single-pulse ns-LIBS signals with the percentage of gaseous and particulate carbon. Using these calibration curves, it was demonstrated that the ratio of the dual- to single-pulse LIBS signals could be used to estimate the percentage of gaseous and total particulate carbon in a multiphase mixture. Although the sensitivity of the technique needs to be improved, Prof. Hahn's group demonstrated an approach that shows promise for distinguishing between gas and particle species. In an attempt to improve the sensitivity of Prof. Hahn's approach, AFRL investigated replacing the dual ns/ns-LIBS with fs/ns LIBS. A fs/ns-LIBS capability was established at AFRL. To demonstrate this capability, several of Prof. Hahn's critical experiments were successfully repeated using the conventional ns-LIBS technique. Single-pulse ns-LIBS and dual-pulse fs/ns LIBS were then used to obtain calibration curves for: (1) carbon dioxide, (2) oxalic acid, and (3) mixtures of air and these species. The results were similar to those of Prof. Hahn's group in that both the single and dual LIBS techniques gave a larger response to carbon from particulates than that from gases. However, the slopes of the linear calibration curves were nearly the same for the single and dual LIBS techniques. The impact was that the ratio of the fs/ns-LIBS to the ns-LIBS signals was almost independent of percent gaseous carbon. Thus, Prof. Hahn's use of single and dual LIBS to determine the percentage of gaseous and total particulate carbon did not seem to apply to the dual fs/ns-LIBS in place of the ns/ns-LIBS for the conditions studied. The cause of the difference in sensitivity of the dual ns/ns-LIBS and the fs/ns LIBS techniques is not clearly understood at this time but it is likely related to the significantly reduced interaction volume and plasma dynamics associated with the fs laser generated plasma.

## 2.0 Introduction

The EPA considers PM<sub>2.5</sub> (particulate matter with particle sizes of 2.5 microns or less) to be the most important air pollutant because they can cause significant environmental and health problems. On 17 October 2006, the EPA issued the final amendments to the National Ambient Air Quality Standards (NAAQS) that reduce the PM<sub>2.5</sub> 24-hour standard from 65  $\mu\text{g}/\text{m}^3$  to 35  $\mu\text{g}/\text{m}^3$  (Federal Register: Oct. 17, 2006, 71, 200). This could pose problems for DoD air bases because almost all of the particles produced in gas turbine engines are PM<sub>2.5</sub> emissions. They include solid particulates (soot) and volatile aerosols formed from condensed gases and chemi-ions. To date, attention has been directed primarily at the carbonaceous particulate matter. However most of the particulate emissions in aircraft exhaust are in the form of condensed volatile aerosols. These particulates can grow via continuing condensation and agglomeration. They consist mostly of acids, such as  $\text{H}_2\text{SO}_4/\text{H}_2\text{O}$ ,  $\text{HNO}_3/\text{H}_2\text{O}$  and  $\text{H}_2\text{O}/\text{H}_2\text{SO}_4/\text{HNO}_3$ , as well as neat  $\text{H}_2\text{O}$ . These aerosols can have a significant impact on both the local and global environment by providing surface areas for heterogeneous chemistry and sinks for already present atmospheric condensable gases. These effects are not understood nor have they been adequately characterized. This was recognized in the SERDP SON 08-05 in which the following research question was raised, “How can one accurately measure the total particulate emissions, including the volatile contribution?”

### 3.0 Background

A literature search was performed to identify promising diagnostic techniques for distinguishing the phase of solid and volatile aerosol particles in gas turbine engine exhaust. Laser-Induced Breakdown Spectroscopy (LIBS) was identified as a promising technique because it has the potential of measuring: total mass, composition, number density, and particle size of both solid and aerosol particles. There are numerous ns-LIBS studies involving the detection of solid particles and aerosols. Some of the papers involved in sulfur particles are reviewed in this section. There are relatively few studies involving using ns-LIBS to obtain quantitative analysis of a species in different phases (gaseous, liquid, and solid) in the same sample. The difficulties of multiphase ns-LIBS measurement that are most relevant to this study are illustrated in the research performed by Prof. David Hahn at the University of Florida. Important aspects of his research are also discussed in this section. In recent years fs-LIBS has evolved as an important diagnostic tool but it has not been extensively investigated as a quantitative method of analysis. Some background on fs-LIBS is also provided in this section.

#### 3.1 Conventional ns-LIBS

Radzlemski *et al* [1983] were the first to determine the atomic species composition of aerosols using LIBS. However, it has been only in the last 10 years that LIBS has been used to obtain total mass, composition, and size distributions of particles [Hahn, 1997; Hahn, 1998]. Since this revelation, LIBS has been used in numerous solid and aerosol particle studies. Some background on LIBS and the results from several relevant LIBS studies are presented in this section to illustrate its potential for making both solid and aerosol particulate measurements. Most LIBS studies use ns pulse lasers. Thus, conventional LIBS is sometimes referred to as ns-LIBS to distinguish it from fs-LIBS performed with fs pulse lasers.

LIBS is an atomic emission spectroscopy technique that makes use of transient laser-induced micro-plasmas that serves as both the sample volume and excitation source [Hahn, 2000; Lee, 2004; Song, 1997]. All molecules and particles less than 10  $\mu\text{m}$  are dissociated in the micro-plasma. The optical emission consists of a plasma continuum and atomic emission lines corresponding to the elemental composition of the sample. The wavelength of the individual emission lines identifies the elemental composition and their relative intensity indicates the concentration of the individual species. The emitting atoms and ions are excited through collisions with hot electrons, ions, and other atoms. The plasma exists for a few  $\mu\text{s}$  to ms. While the plasma kinetics are quite complex, knowledge of the details of the dynamics is generally not needed to effectively use LIBS. The sensitivity and quantifiable nature of LIBS measurements are made through systematic calibration of individual LIBS instruments. Attributes of the technique include *in situ* operation, multi-elemental analysis, relatively simple data reduction, high sensitivity, and space- and time-resolved real-time measurements. For most species, detection limits lie in the few ppm and below. LIBS has been used for analysis on solid surfaces, soil samples, gas samples, ice particles [Arp 2004], and aerosols. Measurements are readily made in harsh ambient environments such as reacting flows. The spatial distribution of H and O atoms in hydrogen/air diffusion flames has been measured and favorably compared with simulations [Itoh 2001]. Trace metals have been detected at ppm levels in industrial boilers and furnaces [Blevins, 2003]. More recently, LIBS was demonstrated as a means for engine health monitoring via the detection of seeded Mg [Baldwin, 2006]. In addition to the seeded Mg, Fe from actual engine wear was also detected in this proof-of-concept study.

A recent study has demonstrated that LIBS can be used to determine the composition and total mass of sulfuric acid aerosols produced in controlled homogeneous nucleation experiments [Nunez, 2000]. Even though the measurements were made in a controlled environment, this is an important demonstration because most of the particulate emissions from gas turbine engines are in the form of condensed volatile material with the dominant aerosol species being  $\text{H}_2\text{SO}_4/\text{H}_2\text{O}$  [Karcher, 1998-b; Penner, 1999]. Aviation fuels contain sulfur that is largely emitted in the nascent exhaust as  $\text{SO}_2$ . Through a series of chemical kinetic steps, the gaseous  $\text{SO}_2$  becomes  $\text{H}_2\text{SO}_4/\text{H}_2\text{O}$  (sulfuric acid) forming the most abundant volatile aerosols. Nunez [2000] generated the aerosol droplets at room temperature by passing bulk liquid sulfuric acid of varying concentrations through a nebulizer into a bath of either air or argon.

A sample LIBS spectrum of three S emission lines obtained by Nunez *et al* [2000] is presented in Figure 3.1. Such spectra were recorded over a range of known sulfuric acid concentrations permitting an absolute concentration calibration. The results of the calibration run are shown in Figure 3.2. From the calibration work, the researchers determined a sulfur detection limit of 0.38 ppm of sulfuric acid aerosol with their experimental setup. The authors noted that this *does not* represent the absolute lower limit of detection. Their detection limit was dictated by hardware limitations and not the LIBS technique itself. In Figure 3.2 the S ns-LIBS signal is correlated with both sulfur concentration by weight and the sulfuric acid mass density.

Aerosol size distributions can also be determined from LIBS signals [Hahn, 2000]. Figure 3.3 shows the size distribution of Ca-based particles determined by ns-LIBS measurements. The results are presented as a histogram and compared with the particle size distribution as determined by a commercial particle sizer using a light scattering methodology. The agreement between the two techniques is quite good. Individual particle diameters were determined from the calibrated linear relationship between mass concentration and LIBS signal, the measured plasma volume (sample volume), and the known density of individual Ca particles.

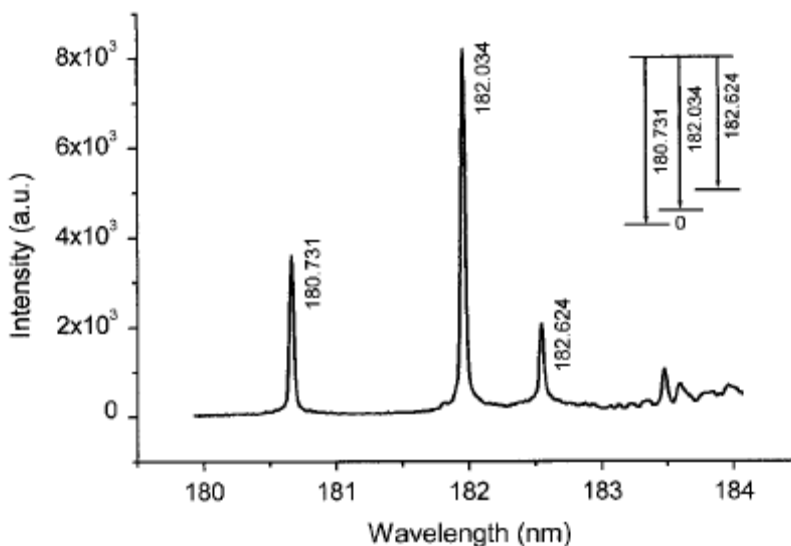


Figure 3.1. ns-LIBS spectrum of sulfuric acid aerosols in the vicinity of the three sulfur emission lines used for concentration measurements. (Taken from Nunez 2000.)

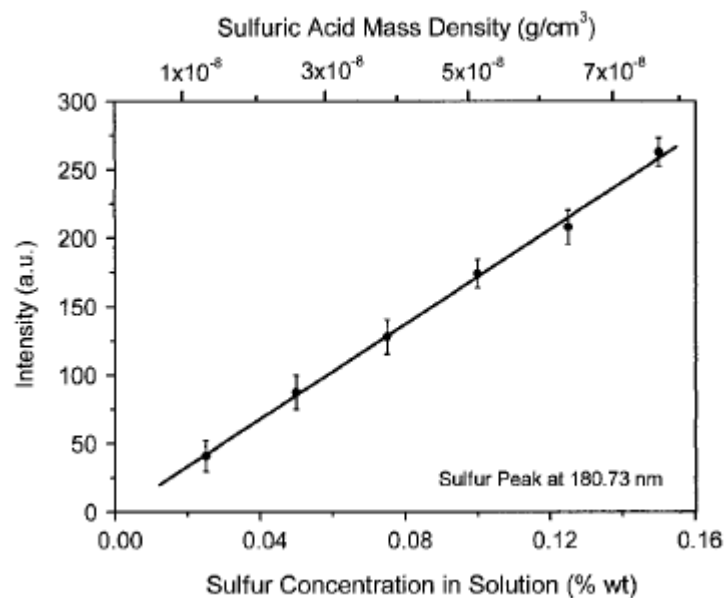


Figure 3.2. Calibration of ns-LIBS signal for sulfur emission taken from sulfuric acid aerosols. The ns-LIBS signal scales linearly with the sulfur concentration in the parent liquid (by weight %) and with the sulfuric acid mass density in the probe volume. (Taken from Nunez 2000.)

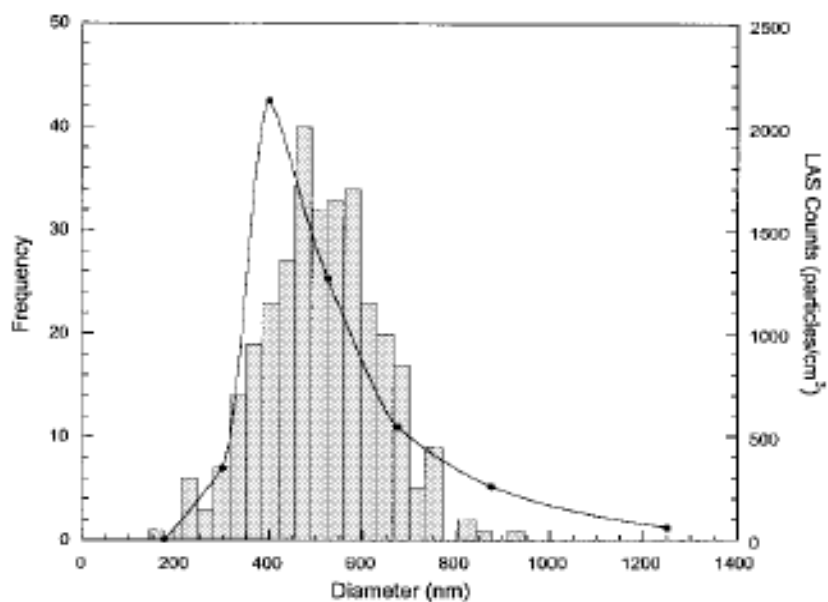


Figure 3.3. Particle size histogram determined from LIBS signals recorded in a stream of Ca-based particles with co-flow of nitrogen at 1 atm. The bars indicate the LIBS-based particle size measurements. The solid line indicates the size results obtained using a commercial particle sizer. (Taken from Hahn 2000.)

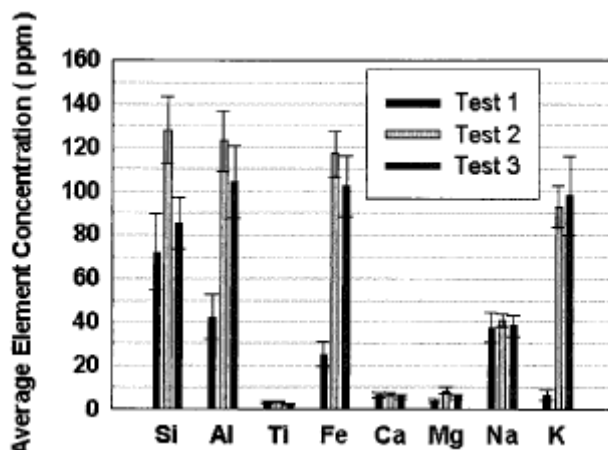


Figure 3.4. The elemental metal composition of the exhaust stream of a biomass coal burner for three different fuels obtained from ns-LIBS measurements. The spectral features of 8 different metals were monitored simultaneously. (Taken from Blevins 2003.)

It is clear from the above that ns-LIBS can be used to determine the mass concentration and individual particle size of particulates and aerosols. Composition of multi-component flows can be determined as well. This is illustrated by the work of [Blevins, 2003] who simultaneously detected 8 trace metals in the exhaust of a biomass coal burner at 1170 K. Thus, there is significant research that illustrates LIBS can be used to obtain particle size distributions and identify the particle composition. What has not been clearly demonstrated is whether LIBS can be used to distinguish between an analyte in gas, liquid aerosol and solid particles in the same sample like would occur in the exhaust plume of a gas turbine engine.

A critical issue is whether fs/ns-LIBS can distinguish between gases, liquid aerosols, and solid particles in simple and complex environments. Recent results obtained by [Hohreiter, 2005; Hohreiter, 2006] suggests this is a real problem. They investigated the LIBS spectra of carbon in gas and solid phases. The gas phase carbon was in the form of  $\text{CO}_2$ ,  $\text{CO}$ , and  $\text{CH}_4$ . The solid carbon was in the form of 30-nm polystyrene ( $\text{C}_8\text{H}_8$ ) and oxalic acid  $(\text{COOH})_2$  particles. As noted in Figure 3.5, the intensities of the carbon spectra lines are different for the different forms of carbon. Figure 3.6 shows how the carbon spectral intensity changes with carbon concentration. Note that all the LIBS intensities, for carbon in the gas phase, are on the same curve. However, the curve for the LIBS C intensities, for the higher density oxalic acid ( $1.9 \text{ g/cm}^3$ ) particles, has a larger slope than that for the polystyrene particles with a density of  $1.0 \text{ g/cm}^3$ .

The issue raised by Hohreiter and Hahn of whether LIBS can always distinguish between gas, liquid, and solid phase of an analyte is the main focus of this paper. Their results were obtained using ns-LIBS. An important issue to address is whether the same problem would occur using fs-LIBS, which is a relatively new field. A short background of fs-LIBS is given in the next section.

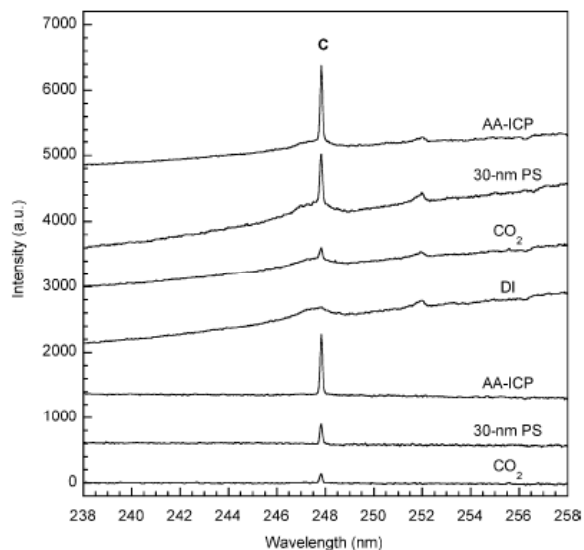


Figure 3.5. LIBS spectra for different sources of carbon. All the spectra have the same scale and have been shifted vertically for clarity. (From Hohreiter 2005.)

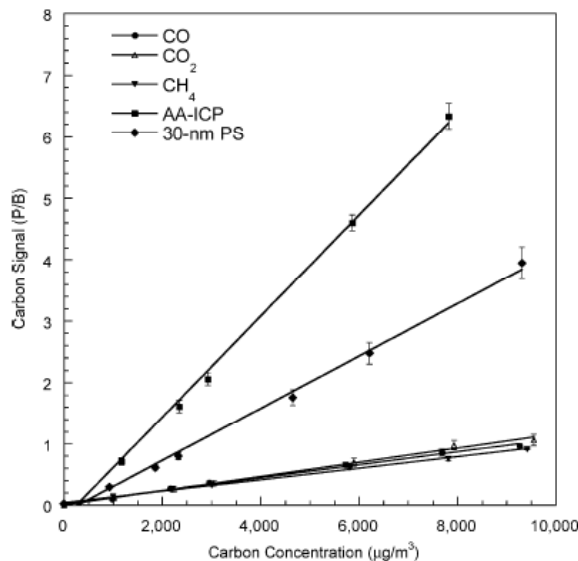


Figure 3.6. Calibration curves based on C atomic emission line for 5 carbon analyte sources. (From Hohreiter 2005.)

### 3.2 Femtosecond fs-LIBS

Historically, LIBS became a popular diagnostic technique because of the availability of reliable nanosecond pulsed lasers in the 1970s. For example, excimer and Nd:YAG ns pulse lasers produce a plasma by achieving focused intensities of  $>10^9$  W/cm<sup>2</sup>, which are above the breakdown potential of most samples. This results in electron temperatures of about 15,000 K. Today, a new generation of LIBS is evolving because of breakthroughs in laser technology. The invention of chirped-pulse amplification and reliable femtosecond lasers has resulted in the availability of tabletop, fs pulse lasers, with focused intensities greater than  $10^{19}$  W/cm<sup>2</sup>. Such ultra-short-pulse, ultra-intense focused intensities, referred to as extreme light [Mourou, 2002], interact with matter in completely new ways that can be advantageous to LIBS. For example, the plasma created with extreme light results from field ionization of both the outer and inner electrons in a sample. This results in plasmas with a higher density of electrons and higher collision rates than that produced by a ns laser. This is important because the higher collision rate of the electrons with the atomic species can result in more intense, richer emission spectra. The net result of this is that fs-LIBS has the potential of having higher signal to noise ratios and higher accuracy than ns LIBS. This has been demonstrated in some recent fs-LIBS studies [see for example Margetic 2000]. Ppm detection limits for minor species in Al alloys have been demonstrated [Le Drogoff 2001].

## 4.0 Results and Discussion

This program explored the question: is it feasible to develop a LIBS based technique that can be used to obtain the percentage of particulates in a gaseous/particulate multi-phase mixture? The approach was to explore the use of nanosecond (ns,  $10^{-9}$  s) and femtosecond (fs,  $10^{-15}$  s) LIBS in ways that would take advantage of the different in LIBS response to species in gaseous and particulate states as observed by [Hohreiter and Hahn, 2005]. The approach involved a joint effort between Prof. David Hahn and the Air Force Research Laboratory (AFRL). Dr Hahn investigated different ns-LIBS techniques that might be used to overcome the multi-phase problems. The literature suggests that a femtosecond (fs,  $10^{-15}$  s) pulse laser decomposes a sample into constituent atoms more efficiently than a ns laser. AFRL investigated using fs-LIBS techniques along with a combined fs/ns-LIBS techniques as a means of solving the multi-phase problem. The results of these studies are presented in this section.

Carbon was selected as the species to study because it is relatively straight forward to generate gaseous and particulate sample streams and because there are published results documenting the different in LIBS response for carbon in multi-phase samples. The conditions studied were not those expected in a gas turbine engine exhaust but those that were conducive to exploring new concepts for in situ measurements of total particulates. If a concept proved feasible, then it would be evaluated in more realistic environments..

### 4.1 Experimental Methods for University of Florida Activities

Dual and single-pulse LIBS measurements were made using various mixtures of gaseous and particulate carbon. Single-pulse LIBS measurements were recorded using a 1064-nm Nd:YAG laser (denoted Laser 1) with 300 mJ/pulse energy operating at 5 Hz repetition rate. All analyte samples flowed through a standard six-way vacuum cross at atmospheric pressure, which functioned as the LIBS sample chamber. A gaseous co-flow of 44 lpm of purified air was used for all experiments. The air was passed through an activated alumina dryer, a coarse particle filter, an additional desiccant dryer, and finally a HEPA filter cartridge prior to entering the sample chamber. All flow rates were controlled with digital mass flow controllers. The aerosolized carbon particles were made by nebulizing a solution of oxalic acid at a rate of about 0.15 ml/min using a gas flow of 5 lpm through a pneumatic type nebulizer (Hudson model #1724). The carbon solutions were prepared by diluting ICP-grade analytical standards of 10,000  $\mu\text{g C/ml}$  [SPEX CertiPrep] to the desired concentration using ultrapurified deionized water. The solution concentrations were adjusted to provide a range from about 3 to 20  $\mu\text{g C/liter}$  of gas through the LIBS sample chamber. Based on previous TEM measurements using the current configuration, the average aerosol particle size following droplet desolvation (i.e. solid analyte phase) is expected to be less than about 100 nm, while agglomerate formation is considered insignificant. For gaseous-phase carbon, carbon was introduced to the sample chamber as a specified flow of carbon dioxide using an additional mass flow controller. Experimental conditions were adjusted such that the percentage of solid-carbon to gaseous-carbon could be varied from 10% gas-phase carbon and 90% particulate phase carbon (as elemental carbon by mass) to 90% gas-phase carbon and 10% particulate phase carbon. Specific conditions tested were 10/90 (gas/solid percentages), 25/75, 50/50, 75/25 and 90/10 gas/solid percentages. For each gas/solid mixture, the overall carbon concentration was then increased while the percentage was held constant.



For all experiments, the plasma was created in the center of the sample chamber using a 50-mm diameter, 75-mm focal length lens. The plasma emission was collected on axis with the incident laser beam (Laser 1) using a pierced mirror and 75-mm focal length condensing lens. The plasma emission was then fiber-coupled to a 0.275-m spectrometer (2400 groove/mm grating, 0.15-nm resolution). Spectral data were recorded using an intensified CCD detector array. For all experiments, the ICCD was synchronized to the laser Q-switch, and the detector delay and integration times were set to 8  $\mu$ s and 5  $\mu$ s, respectively. For the dual-pulse configuration, an additional laser-induced plasma was created using a similar 1064-nm, 300 mJ/pulse laser (denoted as Laser 2) oriented orthogonal to the first laser such that the laser-induced plasma was created at the exact same focal volume as created for Laser 1. For all dual-pulse experiments, Laser 2 was fired 1  $\mu$ s prior to Laser 1, which was estimated to be an optimal separation based on extensive previous dual-pulse measurements [Windom, 2006]. For each carbon concentration and gas/solid mixture, each measurement was recorded using six individual 1000-shot averages spread over multiple days for both the single-pulse LIBS (Laser 1 only), and the dual-pulse LIBS (Laser 2 1  $\mu$ s prior to Laser 1) configurations. All data were processed using the 247.9-nm carbon I atomic emission integrated over the full-width, and normalized to the adjacent continuum plasma emission (Bremsstrahlung emission), to yield the final Peak-to-Base ratio (P/B) as the analyte signal.

Figures 4.1.1 and 4.1.2 show representative single- and dual-pulse LIBS spectra that correspond to 90% gas-phase carbon and 10% solid-phase carbon (90/10). Also, 10% gas-phase carbon and 90% solid-phase carbon (10/90) are also shown. Several features are noted in these spectra, which were consistent for all of the experiments performed. First, for all cases the absolute intensity of the dual-pulse configuration was reduced with respect to the corresponding single-pulse condition. This was observed for all gas/solid carbon mixtures. This effect is consistent with previous experiments [Windom, 2006], and corresponds to the fact that the first laser-induced plasma (Laser 2) creates a rarefied condition into which the second laser (Laser 1) is fired. The rarefaction created by the first laser reduces the resulting plasma emission from the plasma created by the second laser. For analysis of *solids* via dual-pulse LIBS, the rarefaction created above the solid by the first laser helps to “clear” the target from the cover gas, thereby creating better coupling from the second pulse into the target, resulting in more analyte emission from the solid target, and less continuum emission from the ambient gas. However, with pure gaseous breakdown as in the current study, the rarefaction serves to significantly lower the plasma continuum emission because the continuum arises primarily from the gas-phase species, which have been subsequently rarefied by the first plasma event. The second observation is that the 247.9-nm carbon emission signal was observed to increase when increasing the percentage of carbon as particulate solid carbon (i.e. decreasing the gas/solid carbon mixture fraction). This trend was observed for both solid and dual-pulse LIBS configurations. To quantify the data, the P/B ratio was calculated for all total carbon concentrations and for all gas/solid carbon mixtures.

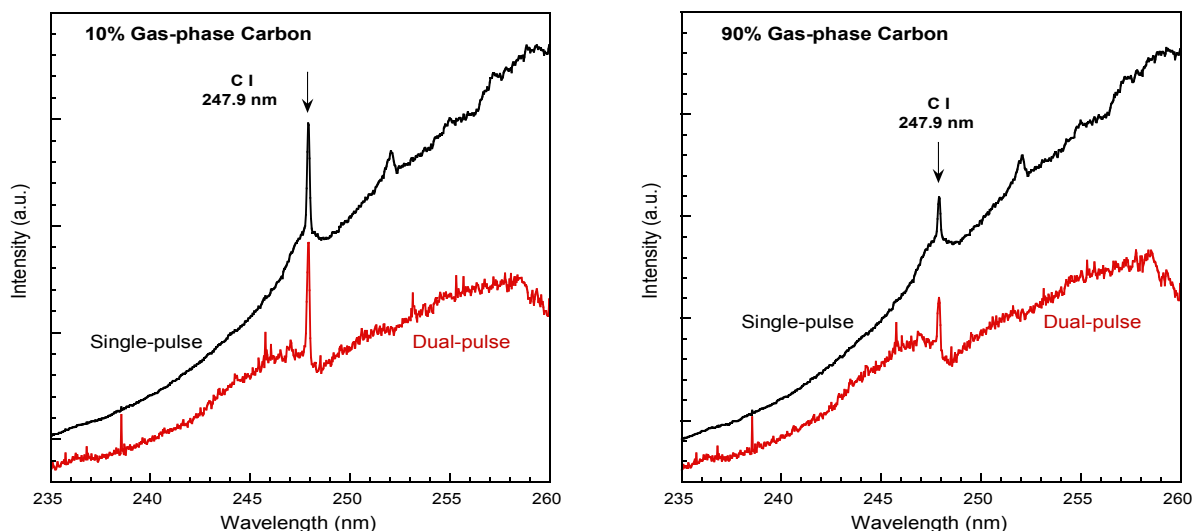


Figure 4.1.1 and 4.1.2. 1000-shot average LIBS spectra for 10% gas-phase carbon (left) and for 90% gas-phase carbon (right) for both single-pulse and dual-pulse LIBS.

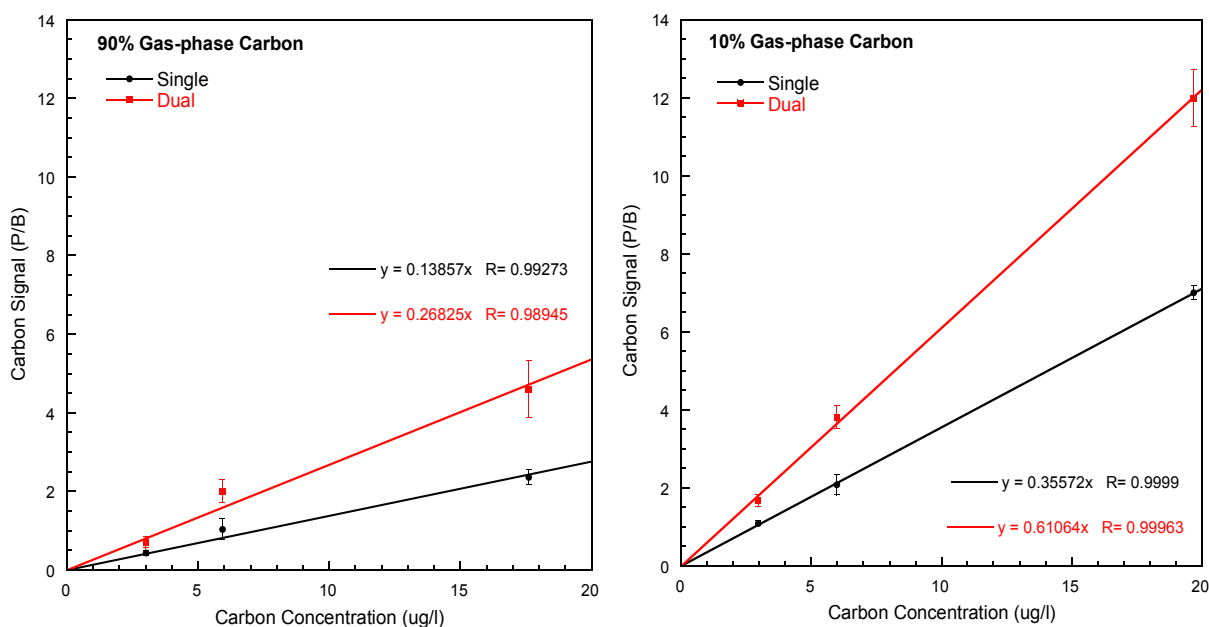


Figure 4.1.3 and 4.1.4. LIBS calibration curves for 90% gas-phase carbon (left) and for 10% gas-phase carbon (right) for both single-pulse and dual-pulse LIBS configurations.

By varying the overall carbon content while maintaining a constant gas/solid carbon mixture fraction, calibration curves were prepared for each specific mixture using both the dual-pulse and single-pulse configurations. Two such calibration plots are presented in Figures 4.1.3 and 4.1.4 for the 10% gas-phase and 90% gas-phase carbon conditions, respectively. All calibration curves yielded excellent linearity and a nearly zero y-intercept value, although a slight trend of reduced correlation coefficients was observed with increasing gas/solid content ratio. It is noted that a zero y-intercept value is required for a robust analytical calibration curve.

The above calibration curves reveal an increased slope with increasing solid carbon content (i.e. decreasing gas/solid mixture fractions), which is in agreement with the above discussions regarding Figures 4.1.1 and 4.1.2. *Clearly the carbon signal is enhanced with increasing percentage of solid-phase analyte.* While it was not so apparent in the raw spectra, it is also observed that the carbon P/B signal is in fact *enhanced* with the dual-pulse configuration as compared to the single-pulse configuration for both gas-phase mixtures presented above, as evidenced by the increase in slope when comparing the dual-pulse calibration plot to the single-pulse calibration plot for a given gas/solid mixture. The above calibration plots were also prepared for the 25/75, 50/50, and 75/25 gas/solid carbon mixtures, yielding results consistent with the above trends. To examine the overall behavior of carbon response over the entire experimental matrix, the resulting calibration curve slopes are presented in Figure 4.1.5 as a function of gas/solid carbon mixture fractions for both the single and dual-pulse configurations. As observed in

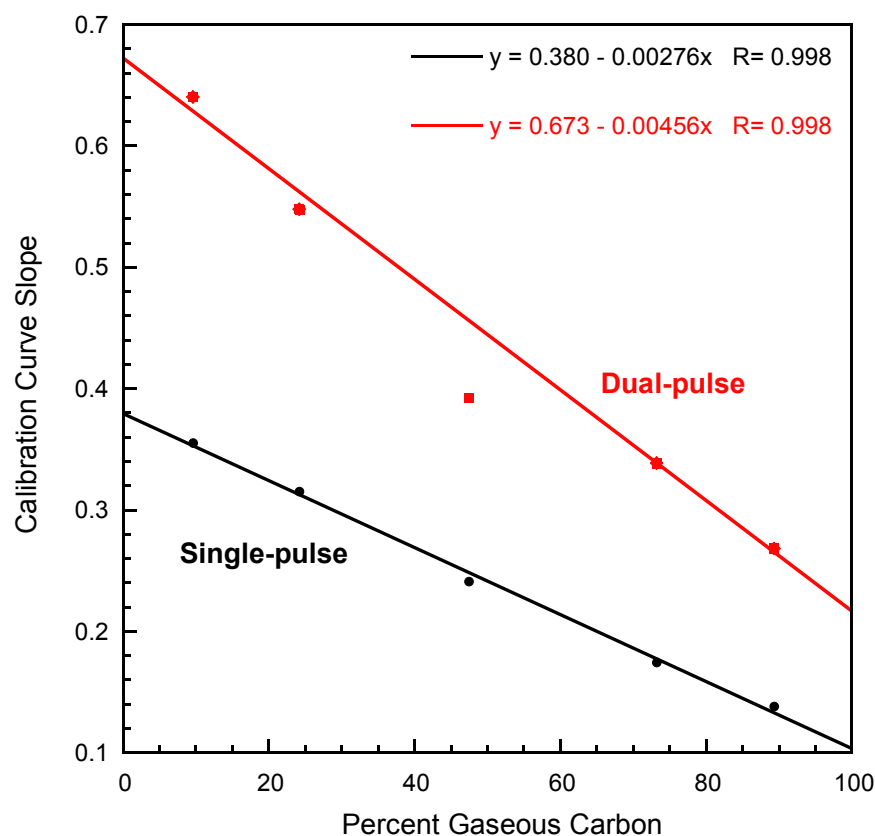


Figure 4.1.5. Individual slopes of the LIBS calibration curves as a function of the percent gaseous carbon ranging from 10% to 90%, for both the single and dual-pulse cases.

Figure 4.1.5 for any given percentage of gaseous carbon, the slope of the dual-pulse LIBS calibration curve always exceeds the single-pulse LIBS calibration curve slope. For a given configuration (i.e. single or dual-pulse), the calibration curve slope is always observed to increase as the percentage of gaseous carbon is decreased (i.e. increasing solid carbon content). Furthermore, the trend line fit to the calibration curves slopes of the single-pulse LIBS experiments is very linear over the range of gaseous/solid mixtures explored. The corresponding curve fit to the dual-pulse experiments is also rather linear in nature; although the 50/50 data point (50% gas phase/50% solid phase) does sit somewhat below the linear trend line. This behavior was consistently observed, and the offset is well outside the expected error bars.

The results presented in Figure 4.1.5 suggest an interesting observation, namely, that the ratio of the single-pulse to dual-pulse response (as reflected by the calibration curve results) reveals a steady trend as the percentage of gaseous carbon varies over the range of 10% to 90%. The concept was further evaluated by using the two trend lines to calculate the ratio of the dual-pulse to single-pulse response as a function of percentage of gaseous carbon. A plot of this dual/single carbon response is presented in Figure 4.1.6 over the range of experimental conditions. In addition, the actual calibration curve slopes are included for the 10/90, 25/75, 75/25 and 90/10 gas/solid cases. *Most importantly, the ratio of the dual/single pulse response does display a monotonic response over the range from 10% to 90% gaseous carbon.* While the

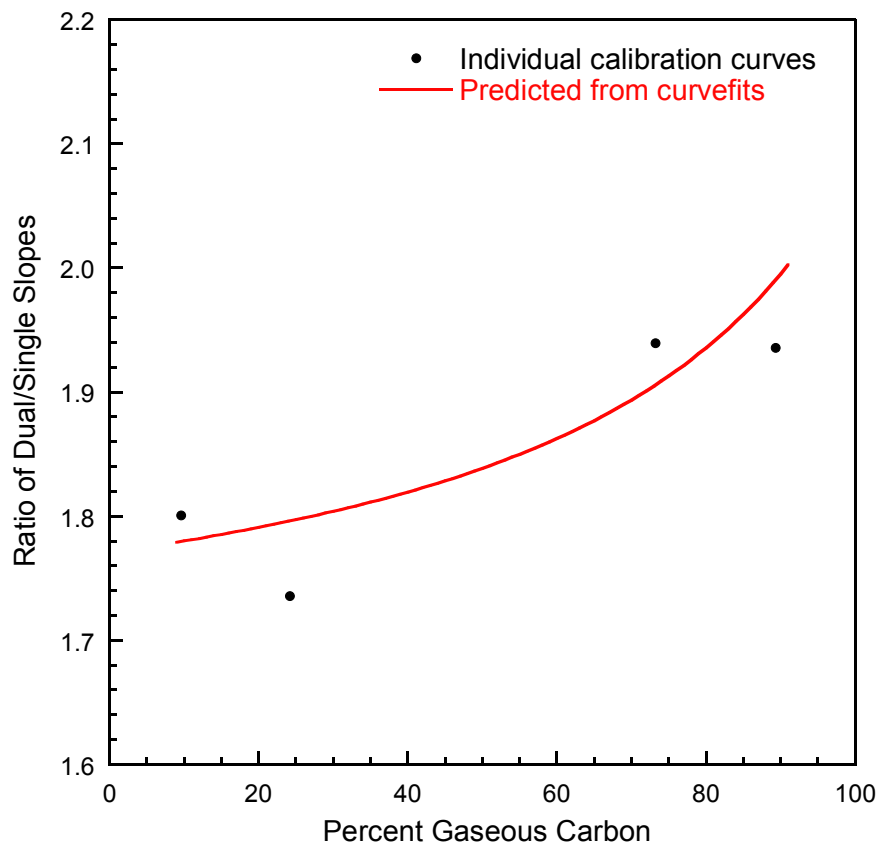


Figure 4.1.6. Ratio of the dual-pulse to single-pulse calibration curve response as predicted from the trend lines of Figure 4.1.5 and as measured from the individual calibration curves, as a function of the percent gaseous carbon ranging from 10% to 90%.

individual calibration curve points show some variation, they also follow this general trend. It is rather remarkable that given the considerable variation in LIBS response of the carbon line when comparing single or dual-pulse configurations, or when comparing the various percentages of gaseous carbon, the ratio of dual/single pulse LIBS response is remarkably consistent, and furthermore, displays a monotonic response over the mixture fraction range examined in the current study.

Figure 4.1.6 illustrates that the ratio of dual- and single-pulse LIBS signals can be used to estimate the percentage of gaseous and total particles in a multi-phase sample. This technique utilized the result that gaseous, liquid aerosol, and solid particulates result in a different calibration curves for dual and single pulse LIBS. As observed in this and previous studies, there exist significant differences in the LIBS

response of solid-phase analyte as compared to gaseous-phase analyte [Hohreiter, 2005], with the former being more pronounced. In addition, the dual-pulse configuration provides an enhanced analyte response (as measured by the P/B ratio) although the absolute signal levels are reduced. Such an effect is consistent with the rarefaction produced by the first laser-induced plasma, and the fact that particulate-phase species are somewhat resistant to the rarefaction relative to gas-phase species. When these two observations are combined, the use of the dual/single pulse LIBS response is shown to be a potentially useful method for measuring the total particulate and gaseous species containing carbon. However additional studies are needed to determine the full potential of this technique.

#### **4.2 fs/ns LIBS at Propulsion Directorate Air Force Research Laboratory**

The research at AFRL differed from that at the University of Florida in that a combined fs/ns LIBS system was set-up so that independent measurements could be made using either fs or ns LIBS. The fs and ns lasers could also be electronically coupled so that one could be used as a pre-pulse and the other the main pulse. This system was used to reproduce the importance results of Hohreiter and Hahn, 2005. Once their results had been reproduced, the combined system was used to investigate the feasibility of using the dual LIBS technique described in Section 4.1 to distinguish between the gas and solid carbon analyte but using the fs laser as the pre-pulse and the YAG as the main LIBS pulse. This research is described in this section.

##### **4.2.1 Experimental Set-up**

A schematic of the optical setup for the work reported here is shown in Figure 4.2.1. Two laser systems were employed in the measurements enabling measurements in both a one-pulse and two-pulse format. The single-pulse measurements were made using a 10-Hz frequency-doubled Nd:YAG laser delivering 6-ns pulses at 532 nm with pulse energies ranging from 290 – 680 mJ. The double-pulse measurements combined the output of the Nd:YAG laser with the output of a Ti:sapphire regenerative amplifier delivering 45-fs pulses at 1 kHz with a central wavelength of 800 nm. The pulse energy was varied from 400 – 750  $\mu$ J. The laser pulses from the two systems were synched to each other electronically using a master/slave arrangement. The Ti:sapphire laser operated as a master clock controlled by its intrinsic electronics. A clock pulse from these electronics was input to a custom-built divide-by box the output of which delivered 10-Hz pulses to a delay generator. Two output pulses from the delay generator triggered the flashlamp and Q-switch of the Nd:YAG laser. The same delay generator also triggered the controller for the ICCD camera used to acquire the LIBS signals.

Beams from both lasers were combined using a dichroic mirror and directed through a pierced mirror to a common focusing lens that placed the focus of both beams at the center of the LIBS chamber. The dichroic mirror transmitted the 800-nm light and reflected the 532-nm light. Most of the single-pulse gas-phase carbon data was acquired using a 150-mm focusing lens placed exterior to the chamber. The single-pulse solid-phase carbon data along with all of the double-pulse data was collected using a 40-mm focusing lens placed inside one arm of the LIBS chamber. The arrival time of the laser pulses in the sample chamber was monitored using a photodiode placed near the chamber.

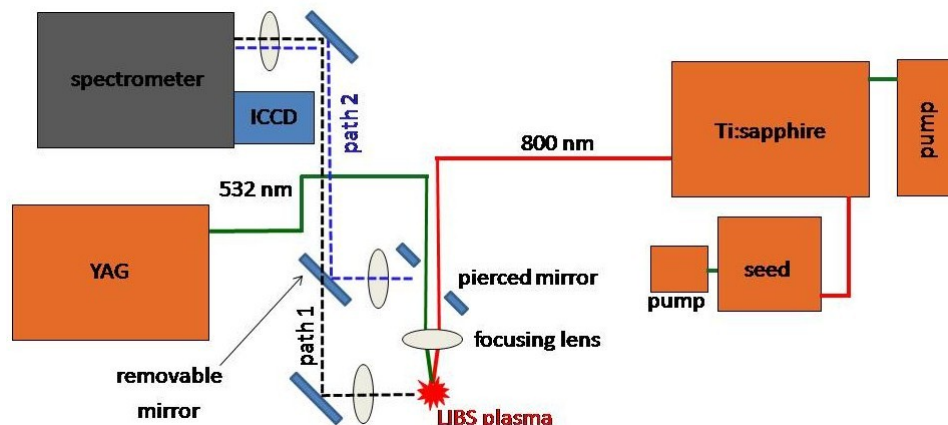


Figure 4.2.1. Schematic of the dual laser system LIBS setup used for this study. As indicated by “path 1” and “path 2” labels, two LIBS signal collection geometries were employed. For path 1 the LIBS signal was collected at 90-degrees to the incident laser beams and for path 2 the signal was collected in the backward direction using a pierced mirror. For clarity, only the mirrors directing the collected LIBS emission are shown. See text for details.

The pierced mirror permitted the collection of the LIBS signal in the backward emission direction. (See path 2 in Figure 4.2.1.) This geometry enables collection of the LIBS signal from nearly the entire plasma volume reducing sensitivity to shot-to-shot changes in the axial location of the LIBS plasma breakdown location. For this collection path, the focusing lens doubles as the collection lens. The optical setup also included signal collection at 90-degrees with respect to the propagation axis of the lasers through the chamber. (See path 1 in Figure 4.2.1.) All of the double-pulse data was collected using this. Switching between collection paths was achieved simply by removing or replacing the “removable mirror” shown in Figure 4.2.1. The collection lenses for both signal collection paths collimate the LIBS signal which is then directed by mirrors to a common lens (350-mm) that focuses the light into the  $\frac{3}{4}$ -m single-grating spectrometer. The exit slit of the spectrometer was removed and replaced with an intensified charge-coupled device (ICCD) camera that served as the detector. The ICCD was operated in imaging mode yielding a 2-D signal map with wavelength along one axis and spatial location on the orthogonal axis. The recorded spatial dimension is normal to the propagation axis of the laser pulse for both collection axes.

The target chamber (see Figure 4.2.2) was constructed following the design of [Hahn, 2001] and suspended between two laser tables in the laboratory room. The incident laser beams were focused at the center of a six-way cross. The four equatorial arms were fitted with quartz windows to permit straight-thru passage of the laser beams as well as signal collection and visualization of the laser sparks. The top of the cross was open to an active exhaust hood that drew the sample flow effluent out of the room. The bottom of the cross was connected to the analyte/solute delivery system. Solid-phase carbon samples in the form of aerosols were delivered into the target area using a commercial medical-grade nebulizer made by Hudson. Carbon in the form of dilute oxalic acid [atomic absorption grade supplied by Spex Certiprep] was loaded into the nebulizer by unscrewing the reservoir from its top. A 5 l/min supply of dry nitrogen (99.999% pure) was fed into the nebulizer from a computer-controlled mass-flow-controller. At this gas flow rate 0.15 ml/min of fluid was introduced into the drying tube. The resultant mass loading of carbon in the sample chamber was altered by repeated dilution of the oxalic acid with de-ionized water. Solid carbon in the form of polystyrene spheres was also introduced into the chamber by placing samples of the

spheres (also diluted with de-ionized water) into an atomizer that was plumbed in place of the nebulizer. To prevent sample-to-sample contamination, individual nebulizers were used for each sample type and for each carbon concentration. For gas-phase carbon measurements, no material was placed inside the nebulizer reservoir. The nebulizer simply acted as a pass-through for carbon-containing gas delivered through the 5 l/min mass flow controller. Most of these measurements were made using a research-grade bottle of 100 ppm CO<sub>2</sub> in N<sub>2</sub>. The output of nebulizer was directed through a hole cut in the center of the sintered metal disk.

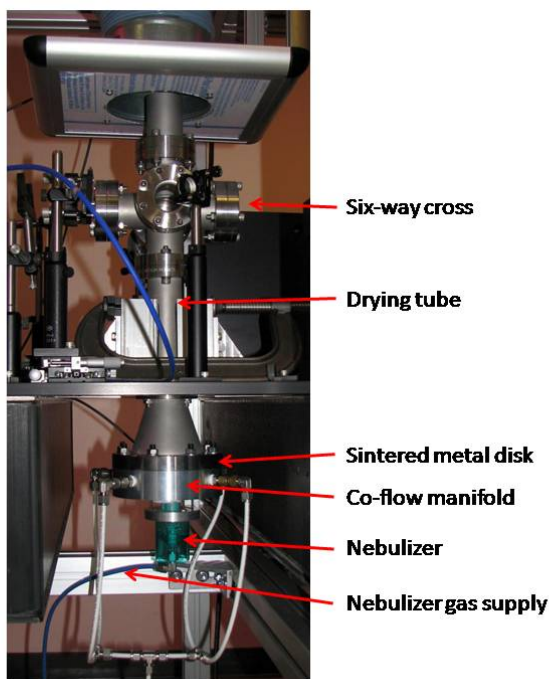


Figure 4.2.2. LIBS chamber used for all data collection presented here. Design based on work by Dr. Hahn and co-workers.

Further dilution and delivery of the nebulizer effluent was accomplished using a co-flow of N<sub>2</sub> (99.999% pure) metered by a 50 l/min mass flow controller. The co-flow passed through the sintered metal disk ensuring laminar flow in the drying tube. The co-flow rate was varied to maintain a total gas flow rate into the chamber of 40 – 45 l/min. The combination of this total flow rate and the length of the drying tube insured that dry aerosol particles of carbon entered the laser focus area with mean diameters of less than 100 nm as determined by Hahn's group using the original test chamber based on the same design [Hohreiter, 2005]. We note that all measurements regardless of analyte source were made at atmospheric pressure. Similarly all measurements were made under flowing conditions.

#### 4.2.2 LIBS signal acquisition and processing

A LIBS signal consists of one or more atomic lines from the emitting analyte superimposed on the broadband plasma emission. The broadband emission consists largely of bremsstrahlung from the free electrons as they cool along with some recombination emission. If the LIBS signal is acquired over a large wavelength range (many tens of nm or more) atomic (and molecular) features associated with the



environmental gas (e.g. air) are typically present as well. For most of the work reported here, carbon served as the analyte. In Figure 4.2.3 the strong 248-nm emission line from the neutral carbon atom is shown sitting on top of the broadband plasma. The broadband emission is present in all LIBS measurements at varying degrees of intensity. Consequently, LIBS signals are typically reported as peak-to-base ratios (P/B). As shown in the Figure 4.2.3, the peak is given by the integrated area of the analyte emission line above the broadband emission (baseline or base). For the data reported here, we adopt the definition used by Hahn's research group for the base [Hohreiter, 2005]. Numerically, the base is given by the value of the baseline at line center. The peak-to-base ratios shown in the figures that follow represent averages over multiple laser shots, typically 600-1000 depending on the strength of the signal.

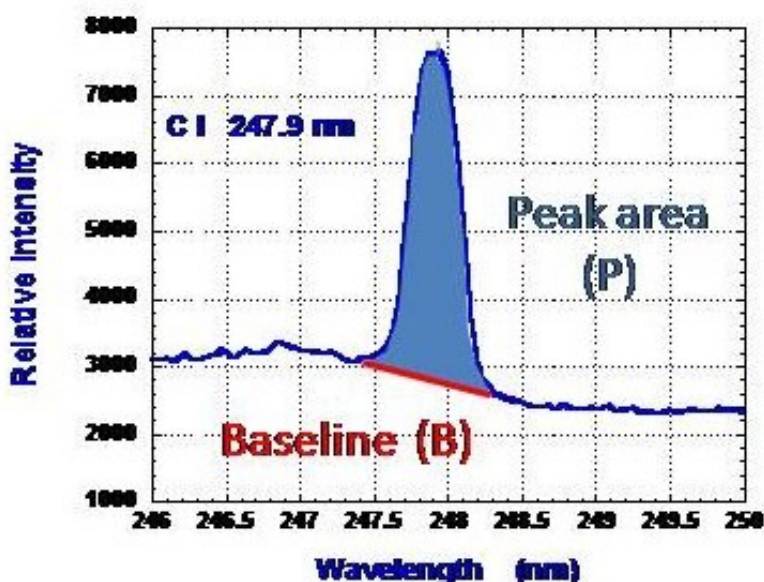


Figure 4.2.3. Graphical representation of Peak and Baseline. The peak-to-base ratio (P/B) is defined as the ratio of the peak area to the midpoint value (value at line center) of the baseline.

For each experimental condition of carbon source and solute, three types of ICCD images were acquired: (1) a background image acquired with the laser blocked, (2) a “blank” image of just the analyte, and (3) a signal images of the analyte/solute source at varying conditions of the test parameter. The test parameters included laser pulse energy, detection gate delay and gate width, solute phase, and solute concentration. For each experimental condition, a background and blank image were recorded at both the beginning and end of the parametric run. All four of these images were recorded using the same number of laser shots as the parametric signal images. The pre- and post-run background and blank images were compared to ensure that no systematic signal collection changes had occurred during the parametric run. No sign of such systematic drift was ever seen indicating the robustness of the setup. This observation is consistent with the findings of Dr. Hahn and his group.

The acquired ICCD images were processed using custom routines written in Matlab. The background image was subtracted from each blank and signal image to remove electronic noise. The background-corrected blank and signal images were then processed to produce corresponding spectra. This was accomplished by summing the individual rows in the images along the spatial dimension. Care was taken



to exclude the rows which lay outside the region of strong emission. This has an indirect effect of improving signal-to-noise ratios. The signal spectra were processed with the corresponding blank spectra. The baseline of the signal spectra were subtracted from the desired atomic line emission using the blank spectra (scaled as need be). The baseline-corrected signal spectra were integrated across the atomic emission feature to yield a numerical value for the peak. The line center value of the blank spectrum was used for the base and the peak-to-base ratio was then calculated. This procedure was repeated for each signal image acquired in each parametric study. The Matlab routines were constructed to either process a single signal image or batch process a collection of related images. All of the data presented in the following figures was processed in this way and is presented in the form of peak-to-base ratio (P/B) versus the test parameter.

#### **4.2.3 ns-LIBS with gas-phase carbon**

Gas-phase carbon LIBS measurements excited by ns pulses provided a good means to verify common results between the work done at WPAFB and the Univ. of Fla. Figure 4.2.4 shows the peak-to-base ratios for gas-phase carbon LIBS signals from CO<sub>2</sub>/N<sub>2</sub> mixtures as a function of carbon mass loading in units of micrograms per cubic meter. Three sets of measurements are shown: two made at WPAFB using pulse energies of 350 and 680 mJ/pulse, and the third at the Univ. of Fla. using a pulse energy of 290 mJ.

As seen, the signal strength has at most a weak dependence on the pulse energy. This is consistent with the current wisdom of the LIBS community. More importantly, the slopes of the P/B ratios versus mass loading are nearly identical between our two collaborative working groups (see Figure 4.2.5). The agreement between the two sets of measurements ensures that the hardware setups in both laboratories yields similar measurement environments and that the signal processing routines yield common numerical results.

Work at the Univ. of Fla. has shown that all gas-phase sources of carbon yield a common LIBS signal (P/B) dependence on mass loading in a common solute (air in this instance). Hence, we can comfortably assume that our results shown in Figure 4.2.4 and Figure 4.2.5 are transferable to any gas-phase carbon source such as methane, carbon monoxide, or the vapor of any heavy hydrocarbon fuel.

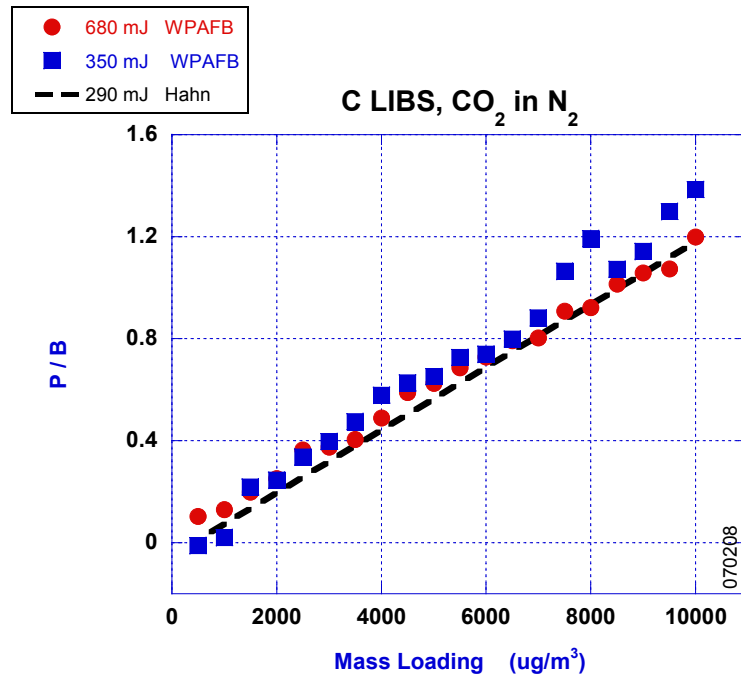


Figure 4.2.4. Measured peak-to-base ratios for two pulse energies compared with results from (Hohreiter and Hahn, 2005) (Univ. of Fla.). (Backward light collection.) Error bars equal to size of markers.

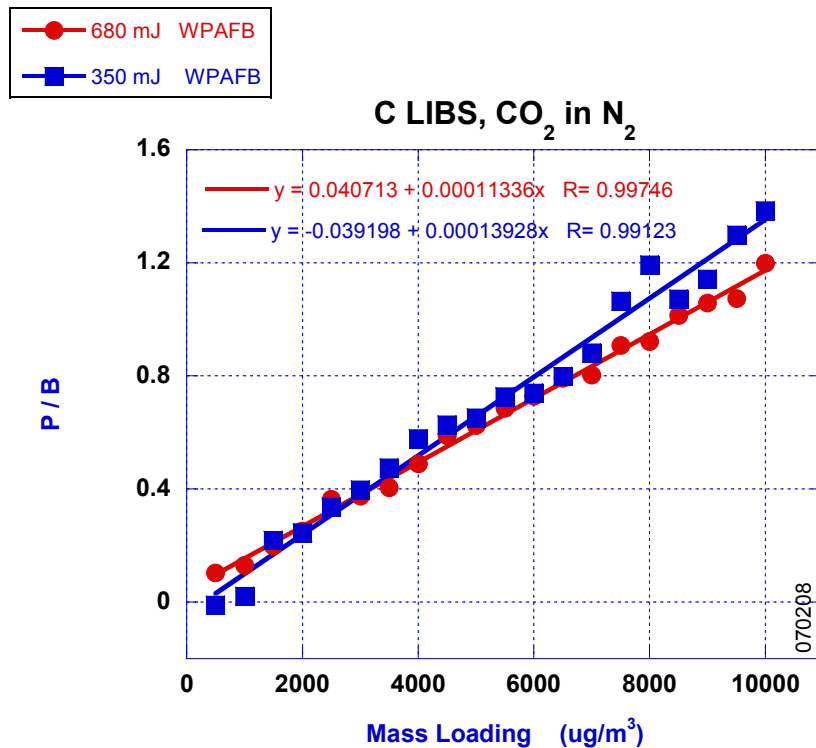


Figure 4.2.5. Linear fits to the data of Figure 4.2.4. Slope for corresponding work by Hahn et al =  $1.16 \times 10^{-4}$ .

Two of the key experimental parameters for LIBS measurements are the detector delay and gate width. The delay is with respect to the arrival of the excitation laser pulse in the sample chamber (Refer to Figure 4.2.13 ignoring the first laser pulse). The temporal characteristics of the plasma emission and atomic analyte emission typically differ as the plasma evolves. The initially hot electrons cool largely via bremsstrahlung and later, after having lost much of their initial kinetic energy, they collisionally excite the desired atomic emission. While individual electrons may lose their energy at differing rates with a well-defined statistical loss rate for the ensemble, generally speaking, most lose much of their energy early in the plasma evolution. As a consequence, the background plasma emission tends to decay faster than the atomic emission of interest. We examined this for a fixed mass loading of carbon from a  $\text{CO}_2/\text{N}_2$  mixture by measuring the peak-to-base ratios and the peak ratios as a function of gate delay for three settings of the gate width (3, 6 and 12  $\mu\text{s}$ ). Results of these measurements are shown in Figure 4.2.8. Consistent with published results, the peak-to-base ratios increase with increasing delay until a maximum value is reached and the ratios decrease rapidly for greater delays. Over the same range of gate delays the peak signal (wavelength-integrated emission) decreases and consequently the signal-to-noise ratio decreases. Selection of detector gate delay is then a matter of compromise between peak-to-base and signal-to-noise ratios. For the work presented here, the gate delay was typically set to 10 or 12  $\mu\text{s}$ .

The dependence of the observed LIBS signal on gate width is much weaker than that on the gate delay. As seen in Figure 4.2.6 and Figure 4.2.7, increasing the gate width by a factor of 4 only increases the measured signal by a factor of  $\sim 20\%$  or less. Most of the data reported here was recorded with a gate width of 10-12  $\mu\text{s}$ .

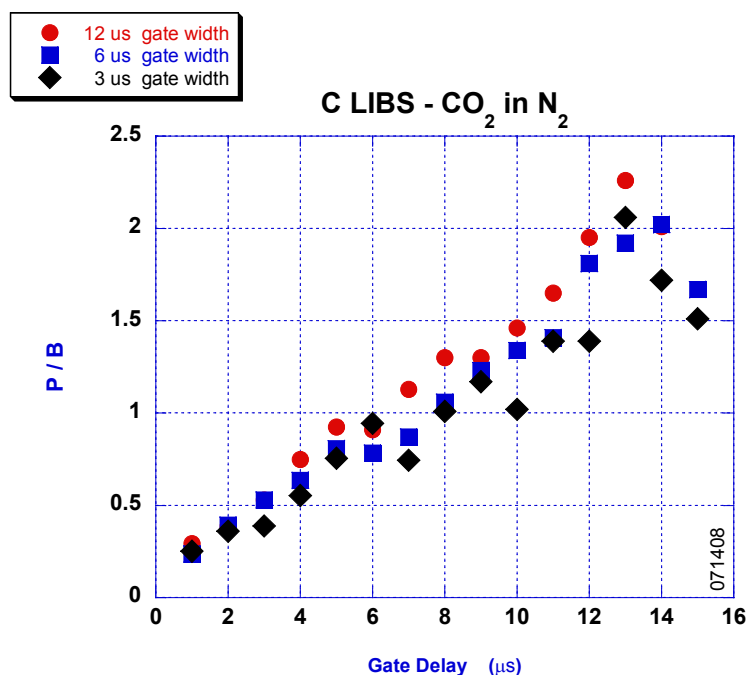


Figure 4.2.6. Measured peak-to-base ratios as a function of gate delay for three values of the gate width.

The LIBS plasma volume is best characterized as an ellipsoid with the long axis lying on the propagation direction of the incident laser pulse. Regardless of the signal collection direction with respect to laser propagation axis, the entrance slit of the spectrometer acted as a limiting aperture. Figure 4.2.9 indicates the relative relationship between the LIBS plasma volume and the sub-volume passed through the spectrometer. The plasma volume is characterized by gradients in electron temperature and density. Both are greatest near the center of the ellipsoid and decrease radially and longitudinally with distance from the center. Therefore, changes in signal collection direction that in turn change the effective aperture lead to a sampling of somewhat different plasma conditions for the same laser spark.

The data shown in Figure 4.2.4, Figure 4.2.5, Figure 4.2.6, and Figure 4.2.8 was recorded using the backward collection geometry (path 2 of Figure 4.2.1). In this geometry, the slit passes all emission along the beam propagation axis simply eliminating the side lobes of the emission region (c in Figure 4.2.9). In this way both cold and hot regions of the plasma contribute to the recorded LIBS signal. With the 90-degree geometry the slit preferentially selects the hot region of the plasma (d in Figure 4.2.9) and this impacts the observed signal. Figure 4.2.10 shows the peak-to-base ratios for gas-phase carbon versus mass loading taken with the 90-degree collection geometry. Comparing with equivalent ratios recorded in the backward geometry (Figure 4.2.5) we see that peak-to-base ratios are of nearly equal value. The difference lies in the slope which is 13% less for the 90-degree collection data set. While this is not a large difference it is statistically significant and emphasizes the fact that LIBS calibration procedures need to be executed using the same geometry planned for the measurements of unknown analyte concentration.

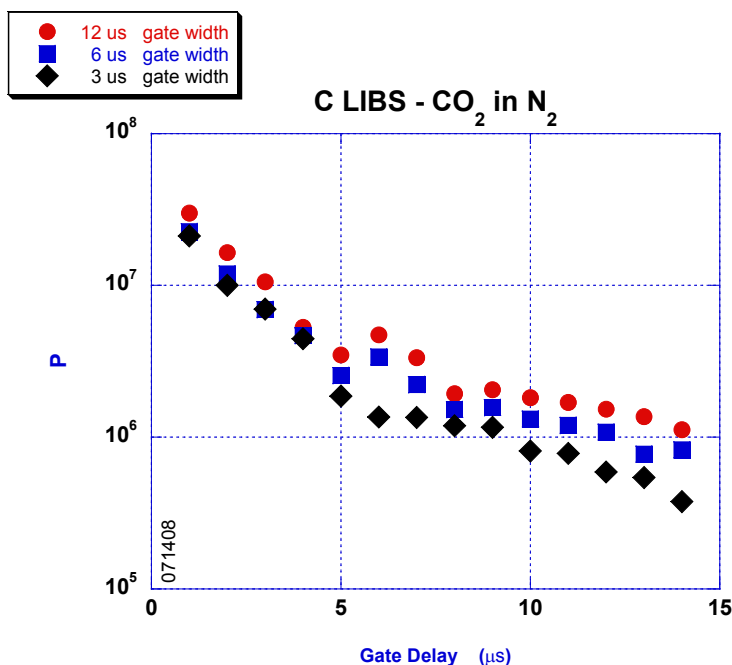


Figure 4.2.7. Measured peak carbon signal as a function of gate delay and gate width. Compare with Figure 4.2.6.

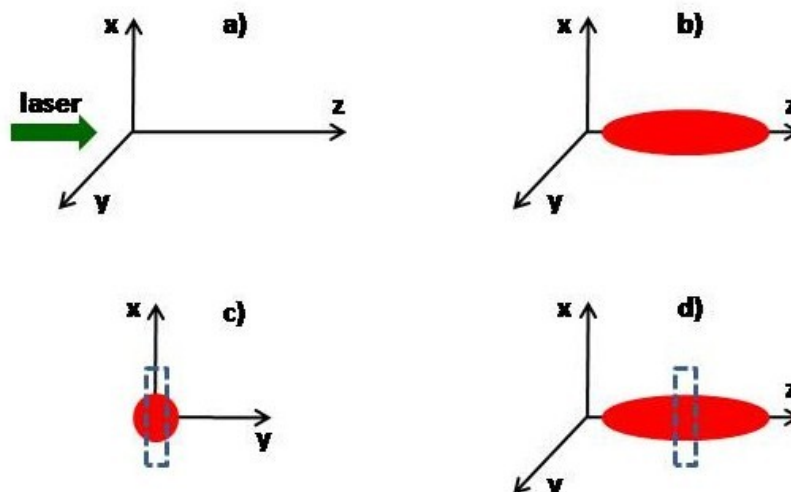


Figure 4.2.8. Schematic indicating the aperturing of the LIBS plasma volume by the entrance slit of the spectrometer. (Slit indicated by the gray rectangular box.) The LIBS plasma appears as an ellipsoid with the long axis collinear with the propagation axis of the laser, b). c) and d) indicate the portion of the ellipsoid that passes through the spectrometer slit for backward, c), and 90-degree, d), light collection. (See Figure 4.2.1 for light collection geometry.)

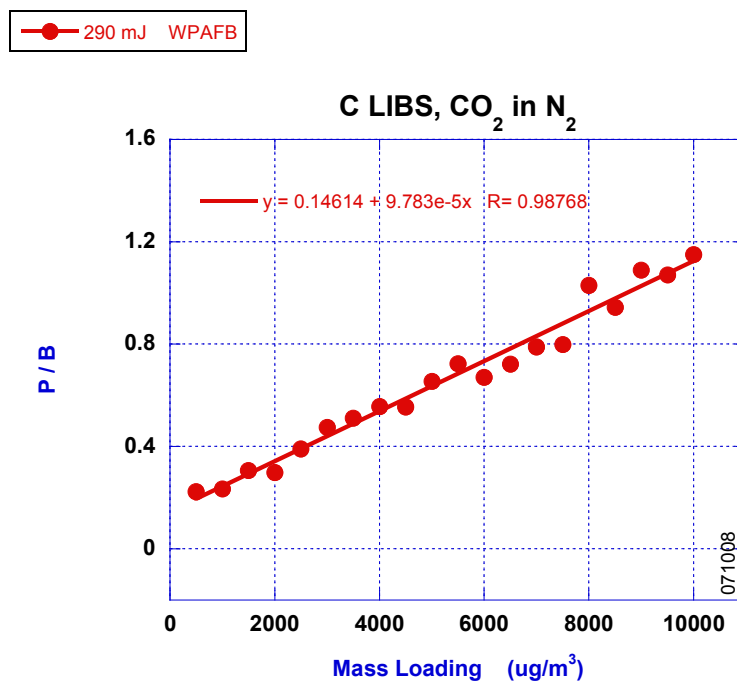


Figure 4.2.9. Measured peak-to-base ratios versus mass loading for 90-degree light collection (path 1 in Figure 4.2.1). Compare with Figure 4.2.4. Ns-LIBS on solid-phase carbon (aerosol particles)

#### 4.2.4 ns-LIBS with solid –phase carbon (aerosol particles)

LIBS measurements on solid-phase carbon particles were executed by loading dilute samples of oxalic acid in the nebulizer. The high-purity stock sample of oxalic acid (1000 mg of C per ml) was obtained from Spex Certi-prep and varying mass loadings were obtained through dilution with de-ionized water. Using the flow rates noted in section 4.2.1, carbon in the form of small aerosol particles was delivered into the sample volume in a flowing manner. Based upon previous studies by Hahn and coworkers at the Univ. of Fla., the aerosol particles are known to have diameters of less than 200 nm. Peak-to-base ratios for our work and the work at the Univ. of Fla. are shown in Figure 4.2.10. The slopes of the signals are roughly seven times that of the gas-phase carbon signal (see Figure 4.2.5) over the same range of mass loadings. This confirms the observation by Hahn and coworkers and Chang and coworkers that LIBS signals of the same analyte are dependent upon the physical phase of the analyte. This difference is related to the details of how the energy in the incident laser pulse is transported into the sample volume, and the hydrodynamic response of the plasma. For gas-phase samples the excitation of individual analyte atoms occurs via direct electron impact excitation or electronic energy cascade following recombination of an electron and an analyte ion. For aerosol particles, excitation energy must first be transported macroscopically into the interior of the aerosol via thermal transport.

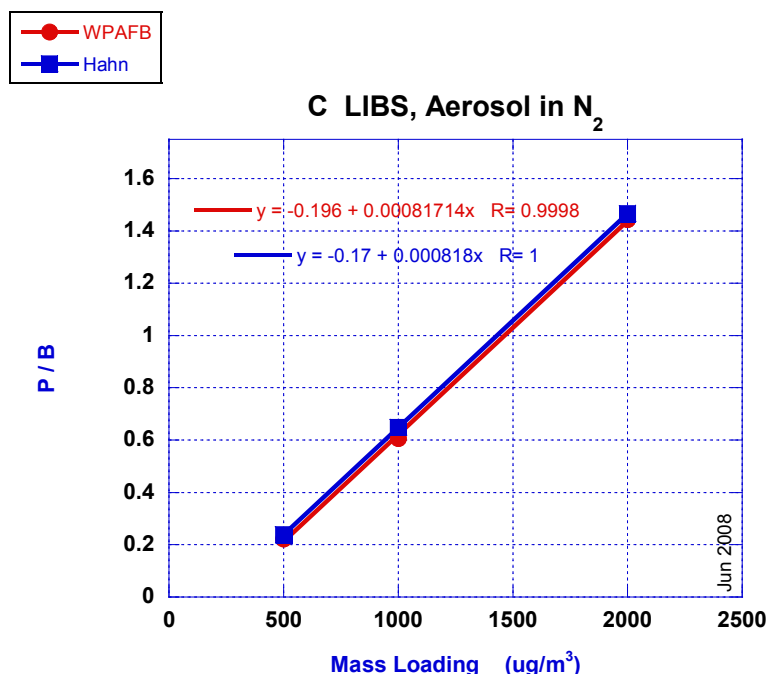


Figure 4.2.10. Comparison of peak-to-base ratios for carbon in aerosol form (oxalic acid) versus mass loading for the data collected with the setup at WPAFB and at the Univ. of Florida (Hahn). Backward light collection.

It is well-known that when energy is impulsively deposited at a single geometric point, the subsequent gas dynamic response generates radial gradients in the pressure, temperature and density of the surrounding medium as a blast wave emanates from the point of energy deposition [Zeldovich, 1966]. While the LIBS spark is spatially distributed (on the scale of tens of microns) it is very likely that such a blast wave will sweep material radially outward from the initial spark volume. The lighter gas-phase

material will be more easily swept out than the solid-phase material which will offer inertial resistance to such movement. Consequently, on the spatial scale of the initial LIBS spark, the mass density of solid-phase analyte will be closer to that of the pre-spark state than that of the gas-phase analyte. Both the details of energy transport and hydrodynamic response could play a role in the observed difference of LIBS signals for gas and solid-phase analytes over similar ranges of mass loading. An important part of this research effort is finding ways to exploit this phase-dependent aspect of the LIBS signal, since the aircraft exhaust environment is characterized by individual analytes in multiple phases.

#### 4.2.5 ns-LIBS with solid-phase carbon (polystyrene spheres)

LIBS measurements were made on solid-phase carbon in the form of polystyrene spheres. For this work, the nebulizer was replaced with a TSI atomizer. Monodispersed samples of known carbon concentration were purchased from Duke Scientific. The atomizer was loaded with fixed concentrations of carbon on a mass basis. In order to characterize the sample within the LIBS spark volume, a differential mobility analyzer (DMA) was connected to an extractive sampling tube the end of which was placed within the flowing sample stream about one cm away from the spark location. The DMA was

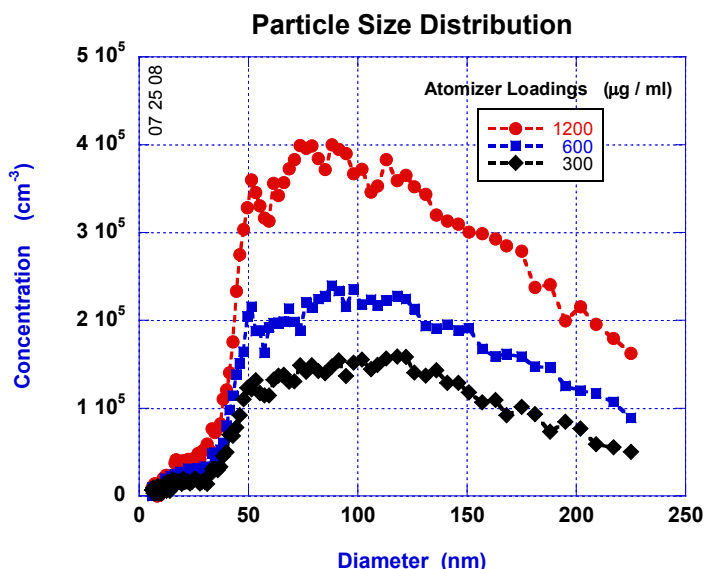


Figure 4.2.11 Particle size distribution determined by a differential mobility analyzer for the Duke Scientific 50-nm polystyrene spheres. Agglomeration above an effective diameter of 225 nm is unknown as these sizes lie outside the operating range of the analyzer. Compare with Figure 4.2.12.

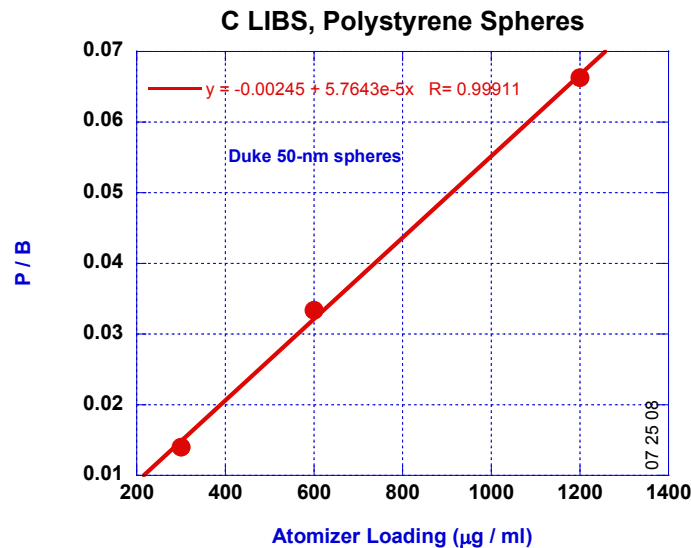


Figure 4.2.12. Peak-to-base ratios for the LIBS signals associated with the particle size distributions shown in Figure 4.2.11.

paired with a particle counter and the combination provided a particle size distribution in the form of concentration (number of polystyrene spheres per cubic centimeter) per mean particle diameter. The particle size distribution for the 50-nm polystyrene spheres is shown in Figure 4.2.11 for three atomizer mass loadings. Clearly the mono-dispersed sample is heavily agglomerated. The reason for this is that the sample did not contain a surfactant (which contained carbon) for keeping the particles dispersed. We attempted to disperse the polystyrene spheres by mixing for many hours but were not successful. Polystyrene is a dielectric and small spheres can easily acquire enough charge to electrostatically cling to one another. In principle it is possible to determine the carbon mass loading within the LIBS spark using the particle size distribution. However, the DMA configuration prevented detection of agglomerated spheres with effective diameters greater than 225 nm. The size-limited particle size distribution is insufficient to confidently recover the mass loading in the LIBS target volume. However, it is meaningful to report the LIBS peak-to-base ratios as a function of atomizer mass loading. This is done in Figure 4.2.12 for the sample reported in Figure 4.2.11. Note that the P/B ratios are a linear function of atomizer loading. This suggests that it is possible to make quantitative LIBS measurements on agglomerated analyte particles.

#### 4.2.6 fs-ns dual-LIBS with gas and solid-phase carbon (CO<sub>2</sub> and aerosol particles)

As evidenced by the work done by our collaborators at the Univ. of Fla., dual-pulse LIBS based on two ns pulses delayed with respect to each other yields a means to quantitatively determine the relative amounts of gas-phase and solid-phase carbon in a mixed sample over a range of total mass loadings. We examined another dual-pulse approach using a combination of fs and ns pulses. While the fs pulses deliver much less energy than the ns pulses (0.5 mJ vs 300 mJ), their peak field intensity is orders of magnitude higher and they efficiently ionize the target sample via the tunneling mechanism. The lower pulse energy also produces plasma that is much shorter lived – tens of ns as compared to tens of µs. However, in principle, a LIBS detection scheme that begins with a fs pulse that is closely followed by a ns pulse (see Figure 4.2.13) may yield complimentary phase discrimination. The leading fs pulse can



potentially influence the LIBS signal by either rarifying the sample volume hydrodynamically or by producing a pre-ionized sample volume that more readily absorbs more energy from the second ns pulse than if the fs pulse were not present.

The LIBS spark produced by the fs laser pulse is significantly smaller than that produced by the ns laser pulse. Like the ns-pulse-excited spark, the fs-pulse-excited spark is elliptical in shape with the long axis collinear with the laser propagation direction. To ensure that any preconditioning produced by the fs pulse was taken advantage of fully, the two incident laser beams were combined (see Figure 4.2.1) and focused with a common optic (singlet) along a common propagation axis. A singlet lens was used for this purpose. To compensate for the different focal lengths of the lens at 532 and 800 nm, two-lens telescopes were placed in both laser beam paths to alter the divergence of the two beams as they entered the singlet. (Recall that a singlet will focus “blue” light faster than “red” light.) Images of the two laser sparks appear in Figure 4.2.14. The two spark images have been displaced vertically for clarity. They do in fact lie on a common axis. The ns-pulse-excited spark is not entirely symmetric along the propagation axis. The peak plasma emission tends to appear closer to the leading edge of the spark than the trailing edge. With this in mind, the beam telescopes were adjusted to get the fs spark to lie as close as possible to the location for peak emission within the ns spark. The distance between the center of the fs spark and the peak emission point of the ns spark was minimized to 750  $\mu\text{m}$ . Any further reduction of this spatial separation will require the use of a custom-designed air-spaced doublet or triplet. Since breakdown of the surrounding medium does not necessarily happen right at the waist of the focused ns beam, (Breakdown can initiate

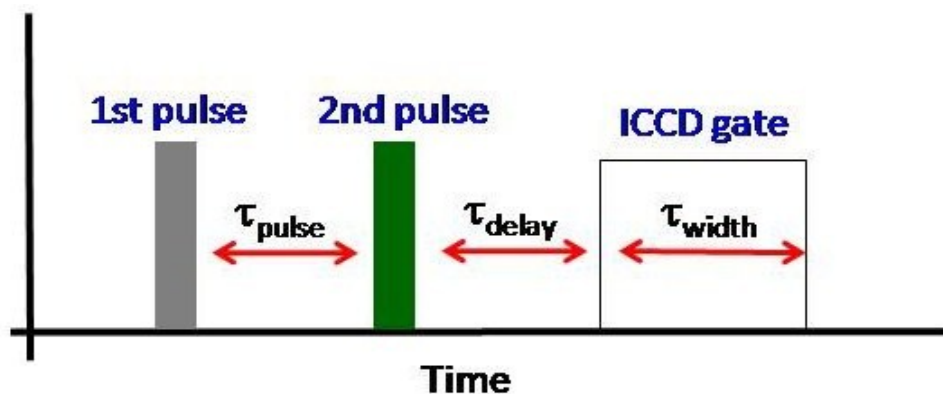


Figure 4.2.13. Timeline for the dual-pulse LIBS experiments. For the work done at the Univ. of Fla., both pulses were delivered from a ns laser. For the work done at WPAFB, the first pulse was delivered from an fs laser and the second from a ns laser.

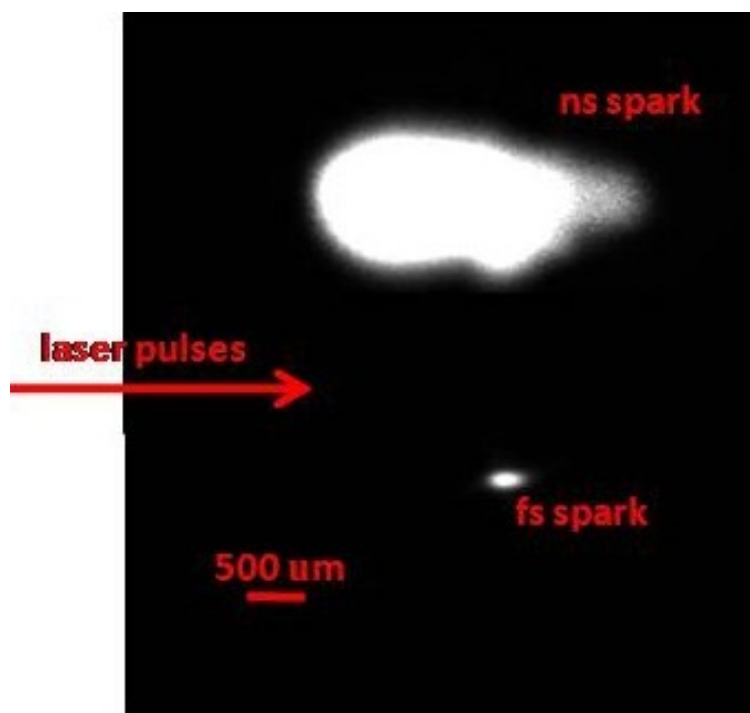


Figure 4.2.14. Images of fs and ns laser sparks collected at 90-degrees. The spark images have been displaced vertically for clarity. The fs spark appears 750  $\mu\text{m}$  behind the location of the peak ns spark plasma emission.

upstream of the waist position), care must be taken in this design to permit some independent user adjustment of the two spark locations.

It is well known that focused fs pulses with intensity characteristics of the laser used in this work ( $>10^{14} \text{ W/cm}^2$ ) yield forward and backward emission due to self-phase modulation and stimulated Raman processes. Such emission may offer its own unique diagnostic utility, particularly for even larger focused intensities. For the work reported here, we chose to collect the LIBS signal at 90-degrees to ensure that we only studied signals attributable to the dual-pulse setup. The collection optics were arranged such that the spatial location of the fs spark and the back end of the ns spark were imaged into the spectrometer. The LIBS signal from this spatial location will necessarily exhibit the largest dual-pulse effects but is unlikely to be the region of greatest emission. In this sense the data was collected using an optical compromise given the restrictions of the hardware available to the program.

With the two laser sparks overlapped as noted, measurements were taken of the peak-to-base ratios for gas-phase carbon ( $\text{CO}_2$  in  $\text{N}_2$ ) as a function of delay between the two pulses for two values of the fs pulse energy – 500 and 750  $\mu\text{J}$ . The detector gate delay and gate width were both held fixed at 10  $\mu\text{s}$ . The gate delay with respect to the ns pulse is indicated in Figure 4.2.13. For both pulse energies the difference between the dual and single-pulse LIBS signals peaked for a pulse delay of 500 ns. This delay setting was then used for all of the P/B measurements as a function of mass loading and phase mixture fraction. Based on these measurements we cannot say with certainty whether the influence of the fs pulse on the LIBS signal is due to ratification or pre-ionization. Such discernment would require a much more extensive fundamental study.

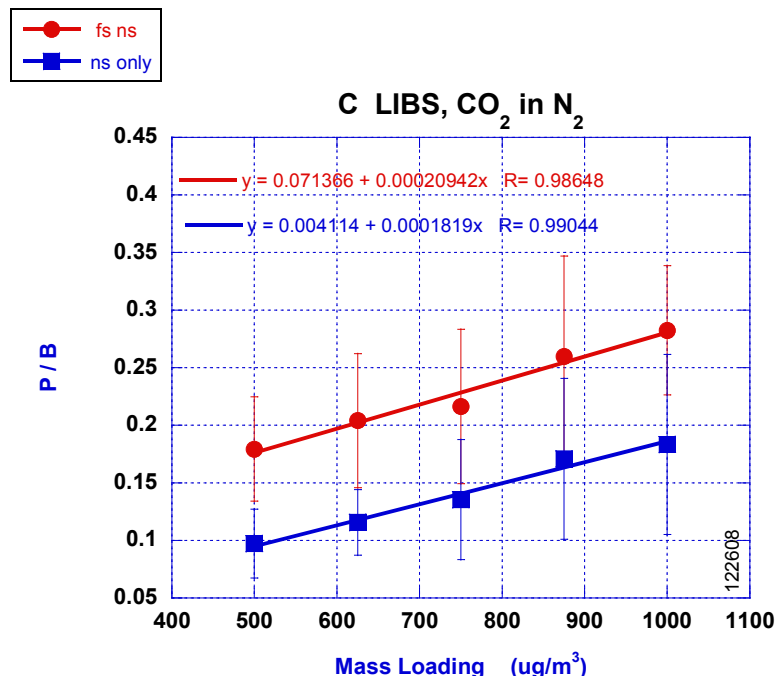


Figure 4.2.15. Peak-to-base ratios for fs-ns and ns-only excitation of carbon in gaseous phase as a function of the mass loading in the chamber.

The peak-to-base ratios for the dual pulse (fs-ns) and single pulse (ns-only) measurements on gas-phase and solid-phase (aerosol) carbon are shown in Figures 4.2.15 and 4.2.16, respectively. Similar to the results found by our collaborators at the Univ. of Fla. using two ns pulses, the dual-pulse LIBS signal is larger than the single-pulse signal. As anticipated, both modes exhibit a linear relationship between the LIBS signal and the mass loading. Also, as seen in the dual-pulse approach with two ns pulses, the signal increases faster for the solid-phase sample as a function of mass loading. We note that the dual-pulse work involving two ns pulses was performed at higher carbon mass loadings. For example, a mass loading of 10  $\mu\text{g/L}$  on the ns-ns data (see fig x and fig y) corresponds to a mass loading of 10,000  $\mu\text{g/m}^3$  on Figure 4.2.15 and Figure 4.2.16. However, given the linearity of LIBS signals over very large ranges of mass loadings as reported in the literature, it is very unlikely that this difference affects the conclusions reached in this study.

Following the measurements on samples of single-phase carbon, dual and single-pulse LIBS measurements were made on mixtures of gas and solid-phase carbon at a fixed total mass loading. Results for a total mass loading of 5000  $\mu\text{g/m}^3$  are shown in Figure 4.2.17. The data are plotted as a function of the percentage of the total mass in gas phase. Just as for the study using the two ns pulses, the LIBS signals decrease with increasing percentage of gas-phase carbon. Likewise, the dual-pulse signal (fs-ns) is larger than the single-pulse (ns-only) signal. The difference lies in the relative slopes between the fs-ns case and the ns-only case. The two calibration curves are very parallel to each other. This is highlighted by examining the ratio of the signals in the two cases. As seen in Figure 4.2.18, within the measurement uncertainties, the ratio of the two signals for the two modes (dual-pulse and single-pulse) is constant as a function of percent gaseous carbon. Hence, at least for the stated measurement conditions it would be difficult to determine the relative amounts of gas and solid-phase carbon using an fs-ns dual-pulse LIBS measurement.

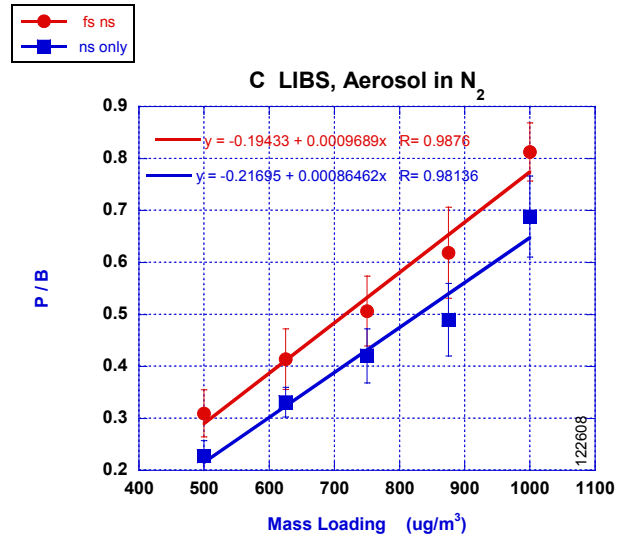


Figure 4.2.16. Peak-to-base ratios for fs-ns and ns-only excitation of carbon in aerosol phase as a function of the mass loading in the chamber.

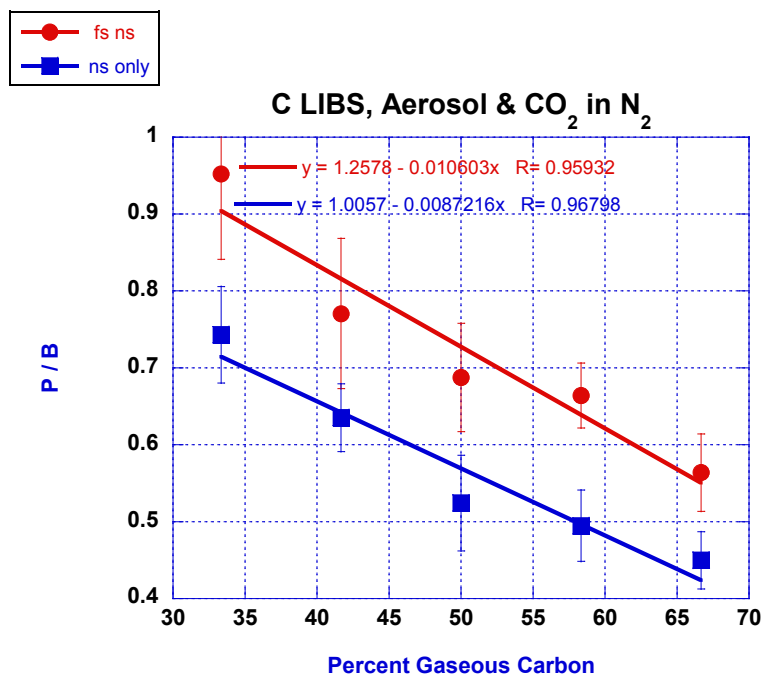


Figure 4.2.17. Peak-to-base ratios for fs-ns and ns-only excitation of carbon in CO<sub>2</sub>/aerosol mixtures as a function of the percent of gaseous carbon present. Downward slopes are indicative of stronger LIBS signals from the aerosol phase. For each mixture, the total mass loading of all carbon present was held to 5000 µg/m<sup>3</sup>.

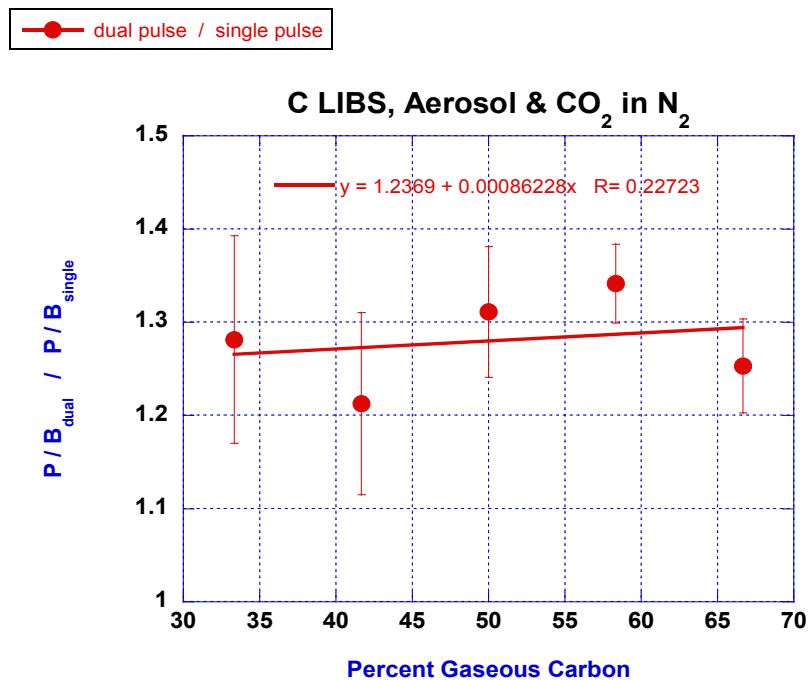


Figure 4.2.18. Ratio of peak-to-base values for the fs-ns configuration to the ns-only configuration. Data in figure was constructed using the data in Figure 4.2.17.

## 5.0 Summary and Observations

This program explored the feasibility of developing a LIBS based technique for measuring total particulates in a sample containing carbon in gas and particulates species. The program was partly successful in that a LIBS technique was demonstrated for measuring the percentage of gaseous carbon and total particulate carbon in a multi-phase sample. The technique involves establishing a calibration curve that relates the ratio of dual to single-pulse ns-LIBS signals to the percentage of gaseous or total particulate carbon in a multi-phase sample. The program is considered only partly successful because additional research is required to improve the sensitivity so it is a viable technique for other species and for broader ranges of solid and gas ratios.

The program involved research at the University of Florida and at the Air Force Research Laboratory (AFRL). The success of this program was based on the continuation of concepts developed by Prof. Hahn at the University of Florida. In previous research, [Hohreiter and Hahn, 2005] showed that there were significant differences in the LIBS response of carbon contained in solid particles, liquid aerosol particles, and gaseous molecules, with the solid particle response being more pronounced for the same carbon concentration. On this program, Prof. Hahn explored ways of exploiting these differences in sensitivity to determine total particulates in a multi-phase sample. The approach was to investigate the use of single- and dual-pulse ns-LIBS. Calibration curves of LIBS signal, as measured by the peak (P) to base (B) ratio vs. carbon concentration, were obtained for gas and particulate carbon samples. As observed previously, there existed significant differences in the LIBS response of particulate-phase analyte as compared to gaseous-phase analyte. It was also observed that dual-pulse, as compared to single-pulse, ns-LIBS technique provided an enhanced analyte response (as measured by the P/B ratio). These observations were used to formulate a promising technique for measuring total particulates. It was shown that the ratio of dual- to single-pulse LIBS singles has promise for estimating the percentage of total particulates in a multi-phase sample. However, for this to become a viable technique the sensitivity of the technique needs to be improved.

Literature results suggested that the sensitivity of Professor Hahn's technique might be improved by replacing the ns pre-pulse laser with a fs pre-pulse laser, the idea being that the increased intensity of the fs pre-pulse would more readily ionize the sample. This approach was investigated at the Air Force Research Laboratory (AFRL). An experimental system capable of conducting both ns- and fs-LIBS was constructed at the Propulsion Directorate of AFRL. First, gaseous and solid carbon calibration experiments, similar to those conducted at the University of Florida, were repeated with the AFRL ns-LIBS system. Excellent repeatability of Dr. Hahn's results established that the experimental platform and data processing procedures used by AFRL and the University of Florida were equivalent. Next, measurements, complimentary to and in collaboration with those of Prof. Hahn, were executed using a combination of dual and single-pulse LIBS setups, with a fs pre-pulse being used in the AFRL dual-pulse experiments. In general, the results were similar to those at the University of Florida, in that the fs dual-pulse fs/ns-LIBS P/B ratio was always larger than the corresponding single ns pulse LIBS P/B ratio for gaseous and particulate carbon samples. Unfortunately, for the experimental conditions explored, the *ratio* of the LIBS signal from the fs pre-pulse and the ns main pulse was independent of the percentage of total carbon particulates. The physics associated with this less than expected result is not understood but is believed to be related to the total energy deposited in the plasma generated by the fs pre-pulse and the time duration for depositing the energy. Basically, we speculate that the ns pre-pulse creates a rarefied or low-density plasma with a compression wave that tends to clear the gaseous ions from the region of the

plasma responsible for the LIBS signal; whereas, a fs pre-pulse creates a much smaller, high density plasma in which the gaseous species are ionized so quickly that they are not selectively transported to the outer region of the plasma but remain concentrated in the region of the plasma responsible for the LIBS signal.

## 6.0 Recommendations

The problem of developing an in situ technique for characterizing and studying PM<sub>2.5</sub> liquid aerosol and solid particulates in aircraft exhaust type environments is very important because of the impact that PM<sub>2.5</sub> have on the environment as well as on people's health. It is also an extremely difficult measurement problem. Professor Hahn's idea of using the ratio of dual and single pulse LIBS signals to determine the total percentage of carbon particulates in a multi-phase sample is a new, innovative approach that we feel is worth investigating further. However, the ultimate sensitivity of the technique remains a concern. The following recommendations are for research to investigate ways to improve the sensitivity of Professor Hahn's technique. Recommendations are also presented on other approaches for measuring particulates that resulted during the course of this program.

Figure 4.1.6 indicates that the sensitivity of the technique increases as the percentage of gaseous carbon increases; whereas, the technique is weakly dependent on the percentage of gaseous carbon, when the particulate carbon is greater than about 70%. This suggests that for samples with the high particulate loading, the signal is primarily due to carbon from the particulates, a finding consistent with previous research. If this is the case, then either single or dual LIBS could be used to determine the total concentration of carbon with reasonable accuracy because almost all of the analyte signal would come from the particulates. Indeed, the use of dual and signal pulse LIBS may provide a quantitative way of determining when a LIBS signal is basically due to particulates. If this is the case, this would greatly enhance the potential of the single- and dual-pulse ns-LIBS. This point was not fully realized until all of the data were analyzed and summarized; hence resources were not available during the original scope of the work to further investigate the potential. It is therefore recommended that future research on this technique investigate this point.

There are potential ways for increasing the sensitivity of the signal and dual pulse ns-LIBS. It is recommended that additional studies investigate the effect of temporal variations in both the dual-pulse laser-to-laser delay (currently fixed at 1  $\mu$ s), and the temporal gating of the detector gate (currently fixed at a delay of 8  $\mu$ s). As more is learned about the temporal nature of analyte dissociation and diffusion within the laser-induced plasma [Diwakar, 2007], additional analyte sensitivity may be realized by further exploiting the differences in solid and gaseous-phase response, and in single and dual-pulse response.

The approach of using a fs pre-pulse to improve the sensitivity of Prof. Hahn's technique did not produce the expected benefits. There is another approach that could be more successful. The idea involves a new method of remote sensing called filament induced breakdown Spectroscopy (FIBS) [Stelmaszczyk, 2004]. When FIBS is used with a LIDR detection technique it can be an effective remote sensing tool that has the potential of providing spatially resolved particulate measurements along a line. It is recommended that FIBS be explored as a way to obtain total percentage of particulates. In particular, the interaction of filaments with aerosol particulates and the resulting analyte response is largely unexplored in the literature. Hence future efforts should include the investigation of using FIBS as the pre-pulse in conjunction with a ns main LIBS pulse at a focal location of the filament.

While conducting this program, several other ideas surfaced as a means of measuring total particulates. In earlier studies, the interaction of lower energy laser pulses with aerosol particles was noted to yield molecular fragments from the particle that are liberated in the excited electronic state [Omenetto, 2000; Damm, 2001; Dalyander, 2008]. It was also noted that these pulses do not create full



laser-induced plasma. In general, this technique is referred to as photofragmentation spectroscopy, and may be considered a complementary technique to LIBS. One advantage of photofragmentation is the ability to pick up volatile organic species and aerosols, notably sulphur-containing species that are historically difficult to detect via LIBS. Future work that combines the photofragmentation and LIBS techniques in a novel multi-pulse sequence could bring additional analytical power to the problem of multi-phase volatile species monitoring.

## **7.0 Acknowledgement**

The authors wish to think Mr. Kyle Frische and Mr Thomas Erickson for the excellent job they did in setting up, checking out, and operating the fs/ns-LIBS system at AFRL. Their help on this project is most appreciated. The authors would also like to think Mr. Michael Asgill for his work at the University of Florida on this project and Dr. Meng-Dawn Cheng of the Oak Ridge National Laboratory for his very helpful editorial comments. The authors are most grateful to Ms. Angela Wedding for editing this report and putting it into an acceptable format. The authors also wish to thank Mr. Charles Pellerin and Mr. Bruce Sartwell for their support of this program.

## 8.0 References

- Arp, Z. A., Cremers, D. A., Wiens, R. C., Wayne, D. M., Salle, B., and Maurice, S., "Analysis of Water Ice and Water Ice/Soil Mixtures Using Laser-Induced Breakdown Spectroscopy: Application to Mars Polar Exploration," *Appl. Spectrosc.* 58, pg. 897, 2004.
- Baldwin, C., "Particulate Detection in Turbine Exhaust Using Laser-Induced Breakdown Spectroscopy," *Proc. of SPIE* 6379, 2006.
- Blevins, L. G., Shaddix, C. R., Sickafoose, S. M., and Walsh, P. M., "Laser-Induced Breakdown Spectroscopy at High Temperatures in Industrial Boilers and Furnaces," *Appl. Opt.* 42, pg. 6107, 2003.
- Boucher, O., "Air Traffic May Increase Cirrus Cloudiness," *Nature* 397, pg. 30, 1999.
- Braun, A., Korn, G., Liu, X., Du, D., Squier, J., and Mourou, G., "A LIDAR Technique to Measure the Filament Length Generated by a High-Peak Power Femtosecond Laser Pulse in Air," *Opt. Lett.* 20, pg. 73, 1995.
- Calibration," *TSI Quarterly*, 4(2): 3-8.
- Chin, S. L., et al. "The Propagation of Powerful Femtosecond Laser Pulsed in Optical Media: Physics, Applications, and New Challenges", *Can. J. Phys.* 83: 863-905, 2005.
- Dalyander, P.S., D.W. Hahn. *Applied Spectroscopy*, 62:1028-1037 (2008).
- Damm, C. J., D. Lucas, R.F. Sawyer, and C.P. Koshland, *Appl. Spectrosc.* 55, 1478 (2001).
- Diwakar, P.K., P.B. Jackson, D.W. Hahn, Investigation of Multi-component Aerosol Particles and the Effect on Quantitative Laser-induced Breakdown Spectroscopy: Consideration of Localized Matrix Effects, *Spectrochimica Acta Part B*, 62:1466-1474 (2007).
- Gibbon, Paul, Short Pulse Laser Interaction with Matter: An Introduction, Imperial College Press (2005).
- Gunaratne, T., Kangas, M., Singh, S., Gross, A., and Dantus, M., "Influence of Bandwidth and Phase Shaping on Laser Induced Breakdown Spectroscopy with Ultrashort Laser Pulses," *Chem. Phys. Lett.* 423, pg. 197, 2006.
- Hahn, D. W., et al., "Discrete Particle Detection and Metal Emissions Monitoring Using Laser-Induced Breakdown Spectroscopy," *Appl. Spectrosc.* 51: 1836-1844, 1997.
- Hahn, D. W., "Laser-Induced Breakdown Spectroscopy for Sizing and Elemental Analysis of Discrete Aerosol Particles," *Appl. Phys. Letters*, 72L2960-2962, 1998.
- Hahn, D. W. and Lunden, M. M., "Detection and Analysis of Aerosol Particles by Laser-Induced Breakdown Spectroscopy," *Aerosol Sci. Technol.* 33, pg. 30, 2000.
- Hahn et al. Aerosol generation system, *Rev. Sci. Instrum.* 72(9) 3706, 2005.
- Hidalgo, M., Núñez, P. Cavalli, G. Petrucci, and N. Omenetto, *Appl. Spectrosc.* 54, 1805 (2000).

Hohreiter V., and D.W. Hahn. Calibration effects for laser-induced breakdown spectroscopy of gaseous sample streams: Analyte response of gaseous phase species vs. solid phase species, *Analytical Chemistry*, 77:1118-1124 (2005).

Itoh, S., Shinoda, M., Kitagawa, K., Arai, N., Lee, Y-I., Zhao, D., and Yamashita, H., "Spatially Resolved Elemental Analysis of a Hydrogen-Air Diffusion Flame by Laser-Induced Plasma Spectroscopy (LPIS)," *Microchemical Journal* 70, pg. 143, 2001.

Iwasaki, A., Akozbek, N., Ferland, B., Luo, Q., Roy, G., Bowden, C. M., and Chin, S. L., "A LIDAR Technique to Measure the Filament Length Generated by a High-Peak Power Femtosecond Laser Pulse in Air," *Appl. Phys. B* 76, pg. 231, 2003

Jin, Z., Zhang, J., Xu, M. H., Lu, X., Li, Y. T., Wang, Z. H., Wei, Z. Y., Yuan, X. H., and Yu, W., "Control of Filamentation Induced by Femtosecond Laser Pulses Propagating in Air," *Opt. Express* 13, pg. 10424, 2005.

Karcher, B., Yu, F., Schroder, F. P., and Turco, R. P., "Ultrafine Aerosol Particles in Aircraft Plumes: Analysis of Growth Mechanisms," *Geophys. Res. Lett.* 25, pg. 2793 (1998).

Karcher, B., Busen, R., Petzold, A., Schroder, F. P., and Schumann, U., "Physiochemistry of Aircraft-Generated Liquid Aerosols, Soot, and Ice Particles 2. Comparison with Observation and Sensitivity Studies," *J. Geophys. Res.* 103, pg. 17129, 1998-b.

Kasparian, J et al, "White Light Filaments for Atmospheric Analysis," *Science* 301, pg. 61, 2003.

Le Drogoff, B., Margot, J., Chaker, M., Sabsabi, M., Barthelemy, O., Johnston, T. W., Laville, S., Vidal, F., and von Kaenel, Y., "Temporal Characterization of Femtosecond Laser Pulses Induced Plasma for Spectrochemical Analysis of Aluminum Alloys," *Spectrochem. Acta B* 56, pg. 987, 2001.

Lee, W-B., Wu, J., Lee, Y-I., and Sneddon, J., "Recent Applications of Laser-Induced Breakdown Spectrometry: A Review of Material Approaches," *Appl. Spectrosc. Rev.* 39, pg. 27, 2004.

Margetic, V., Pakulev, A., Stockhaus, A., Bolshov, M., Niemax, K., and Hergenroder, R., "A Comparison of Nanosecond and Femtosecond Laser-Induced Plasma Spectroscopy of Brass Samples," *Spectrochem. Acta B* 55, pg. 1771, 2000.

Nunez, M. H., Cavalli, P., Petrucci, G., and Omenetto, N., "Analysis of Sulfuric Acid Aerosols by Laser-Induced Breakdown Spectroscopy and Laser-Induced Photofragmentation," *Appl. Spectrosc.* 54, pg. 1805, 2000.

Penner, J. E., Lister, D. H., Griggs, D. J., and Dokken, D. J. eds., "Aviation and the Global Atmosphere," Intergovernmental Panel on Climate Control, [www.grida.no/climate/ipcc/aviation/index.htm](http://www.grida.no/climate/ipcc/aviation/index.htm), 1999.

Petzold, A. and Schroder, F. P., "Jet Engine Exhaust Aerosol Characterization," *Aerosol Sci. Technol.* 28, pg. 62 (1998)

Putaud, J-P., *et al*, “A European Aerosol Phenomenology—2: Chemical Characteristics of Particulate Matter at Kerbside, Urban, Rural and Background Sites in Europe,” *Atmospheric Environment* 38. pg. 2579 (2004).

Radzlemiski, L. J., *et al*, “Time-Resolved Laser-Induced Breakdown Spectrometry of Aerosol,” *Anal. Chem.* 55, 1246-1252, 1983.

Rogers, D. C., DeMott, P. J., Kreidenweis, S. M., and Chen, Y., “Measurements of Ice Nucleating Aerosols During SUCCESS,” *Geophys. Res. Lett.* 25, pg. 1383 (1998).

Schafer, K., *et al*, “Nonintrusive Optical Measurements of Aircraft Engine Exhaust Emissions and Comparison with Standard Intrusive Techniques,” *Appl. Opt.* 39, pg. 441, 2000.

Schumann, U., Arnold, F., Busen, R., Curtiss, J., Karcher, B., Kiendler, A., Petzold, A., Schlager, H., Schroder, F., and Wohlrrom, K. H., “Influence of Fuel Sulfur on the Composition of Aircraft Exhaust Plumes: The Experiments SULFUR 1-7,” *J. Geophys. Res.* 107, pg. 4247, 2002.

Sirven, J. B., Bousquet, B., Canioni, L., and Sarger, L., “Time-Resolved and Time-Integrated Single-Shot Laser-Induced Plasma Experiments Using Nanosecond and Femtosecond Laser Pulses,” *Spectrochim. Acta B* 59, pg. 1033, 2004.

Song, K., Lee, Y-I., and Sneddon, J., “Applications of Laser-Induced Breakdown Spectrometry,” *Appl. Spectrosc. Rev.* 32, pg. 183, 1997.

Stelmaszezyk, K., Rohwetter, P., and *et al*. “Long-distance Remote Laser-Induced Breakdown Spectroscopy Using Filamentation in Air”, *Appl. Phys. Lett.*, 85, 18, 3977-3979, 1 Nov. 2004.

Twohy, C. H. and Gandrud, B. W., “Electron Microscope Analysis of Residual Particles from Aircraft Contrails,” *Geophys. Res. Lett.* 25, pg. 1359 (1998).

Wilson, C. W., Petzold, A., Nyecki, S., Schumann, U., and Zellner, R., “Measurement and Prediction of Emissions of Aerosols and Gaseous Precursors from Gas Turbine Engines (PartEmis): an Overview,” *Aerospace Sci. Technol.* 8, pg. 131, 2004.

Windom, B.C., P.K. Diwakar, D.W. Hahn. Dual-Pulse LIBS for Analysis of Gaseous and Aerosol Systems: Plasma-Analyte Interactions, *Spectrochimica Acta Part B*, 61:788-796 (2006).

Zeldovich and Raizer, Vol.1. Physics of Shock Waves and High-Temperature Hydrodynamic Phenomena (AP,1966).

# APPENDIX AC

## PICOSECOND LASER MACHINING OF SHAPED HOLES IN THERMAL BARRIER COATED TURBINE BLADES

Paper (C202)

Carl Druffner<sup>1</sup>, Larry Dosser<sup>1</sup>, William Roquemore<sup>2</sup>, Sivaram Gogineni<sup>3</sup>

<sup>1</sup>Mound Laser & Photonics Center Inc. Miamisburg, Ohio 45343, USA

<sup>2</sup>Air Force Research Laboratory, Propulsion Directorate, WPAFB, Ohio, 45433, USA

<sup>3</sup>Spectral Energies LLC, Dayton, Ohio 45431, USA

### Abstract

Increasing the operating temperature of an aircraft engine has the benefit of increasing thrust and fuel efficiency. However, increased operating temperatures can lead to temperatures in sections of the jet engine reaching or exceeding the melting point of the superalloys materials used for engine components. In order to maintain the structural integrity of the engine parts at the extreme operating temperatures, cooling methods must be supplied to the engine components. Cooling of the engine component is accomplished by air flow through cooling holes and through the application of thermal barrier coatings. One method of fabrication for the cooling holes in turbine blades is a two step process where the holes are drilled in the base blade metal by either laser or electrical discharge machining, a thermal barrier coating (TBC) system is applied and the holes are drilled again to clear out and shape the TBC layer. Mound Laser & Photonics Center, Inc. (MLPC) has conducted research utilizing the ability of a picosecond laser system to machine shaped holes through both the TBC and underlying superalloy in a single step. The short pulse duration of the picosecond laser allows for fast hole shaping and drilling without inducing spallation of the TBC or generating recast that can be encountered with high power, long pulse duration lasers.

### Introduction

Modern turbine engines are being operated at extremely high temperatures where maintaining the component temperature is critical to the integrity of the engine. If a blade or turbine vane is allowed to reach too high of a temperature, then structural failure can occur which can result in a cascading failure of the engine. Component cooling is achieved in multiple ways, one way is by the machining of air flow cooling channels and secondly by the application of Thermal Barrier Coatings (TBC). Air flow cooling is applied both internally and through boundary film cooling. Air flows through internally created channels inside of the component and exits through shaped surface holes.

The exiting air flows along the surface of the material resulting in an insulating boundary layer, keeping the hot gas from the engine component. Figure 1 illustrates the internal air flow channel and surface holes of a typical turbine blade [1].

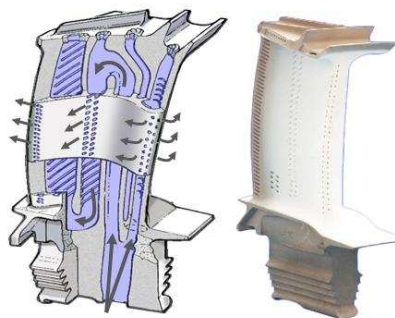


Figure 1: Schematic of air flow channels and holes on a modern TBC coated turbine blade

The internal cooling channels are cast during fabrication of the engine component with the surface holes being machined into the component after it has been fabricated. The air flowing through the surface holes generates the boundary layer cooling and also aids in minimizing hot spots and maintains a uniform temperature flow throughout the engine. A modern jet engine has hundreds of thousands of cooling holes with the number of holes per component varying from 25 to over 40,000 as seen in Table 1. [2] An additional aspect of the hole cutting is shaping of the hole outlet (in either metal or TBC) to keep the air flow laminar and close to the material surface.

Table 1: Cooling Holes Per Component

Component	Dia. (mm)	Thickness (mm)	Angle (deg)	# of holes
Blade	0.3-0.5	1.0-3.0	15	25-200
Vane	0.3-1.0	1.0-4.0	15	25-200

Afterburner	0.4	2.0-2.5	90	40,000
Base plate	0.5-0.7	1.0	30-90	12,000
Seal Ring	1.0	1.5	50	180
Cooling Ring	0.8	4.0	80-90	4200

There are several ways to machine the cooling holes into the engine materials. These methods range from Electrical Discharge Machining (EDM), Laser drilling (both laser trepanning and laser percussion), Electron Beam Drilling (EBD) or Electro-Chemical Drilling (ECD). Typically either EDM or laser drilling is used for cutting the holes in nickel superalloys. Mechanical drilling is difficult on nickel superalloys and typically is used for larger holes over several millimeters in diameter [3].

Electrical discharge machining (EDM) is a thermal erosion process in which material is removed by a series of recurring electrical discharges between a cutting tool electrode, and a conductive work piece in the presence of a dielectric fluid. The discharge occurs in a small gap between the EDM electrode and the work piece. An increasing voltage is applied between the electrode and the work piece until electrical breakdown occurs and a spark discharges across the gap. Heat from the discharge vaporizes minute particles of the work piece which are then washed from the cut by continuously flushing dielectric fluid. EDM generates very high temperatures in the region of the breakdown spark. During EDM drilling, both the electrode and the material get eaten away. EDM has the advantage of being able to machine multiple holes simultaneously with fingered electrodes. The drawback of EDM is that the material must be conductive so while bare engine components can be drilled, TBC coated materials, which are not conductive, cannot be drilled. EDM can have quality issues with recast and microcracking as can laser machining.

Laser drilling for aerospace applications can be accomplished by either percussion or trepan drilling. Trepanning is where the laser beam or part is rotated about the hole being cut. Percussion drilling is accomplished by repetitive shots of the laser pulse until a hole is produced. Trepanning will yield a better quality holes but percussion drilling can drill a hole faster than trepanning. Percussion drilling can be done with the part movement synchronized to the laser firing to further decrease cycle times by allowing "fire on the fly" techniques. The number of holes to be

drilled, the location, shape and quality of the finished hole will usually determine which laser method is used. The advantages of laser drilling are the ability to drill both conductive and non-conductive materials, the ability to machine small holes, machine at angles and fast processing. The downsides for laser drilling is tapering on the hole cut long pulse (ms,ns,us) and high power lasers can generate recast and a heat affected zone which can result in microcracking issues.

Industrial laser drilling is typically done with high power longer pulse duration (microsecond) Nd-Yag lasers system where peak power can be in the 100kW's of Watts and a hole can be cut with only few laser pulses. These high power lasers can eject a molten spray of material resulting in recast on the surface so steps may have to be taken to minimize the recast from sticking during machining [4] or removal of the recast after machining. Drilling with high laser powers can also generate microcracking or coating delaminations [5,6]

Mound Laser & Photonics Center, Inc. has undertaken a study to investigate the drilling of holes and shaping in TBC coated Hastelloy X, a nickel superalloy. Currently laser drilling of TBC coated components with industrial (millisecond-nanosecond) lasers can results in cracking or spallation of the TBC coating. Recast and heat damage is also a concern with longer pulse duration lasers and these affects should be minimized with shorter pulse duration lasers. The goals were to investigate and demonstrate picoseconds laser drilling of shaped and angled holes through TBC coated material.

## Experimental Setup

### Laser System

The laser drilling trials were conducted with a Lumera SuperRapid Laser. This laser has pulse duration of ~12ps with a repetition rate of 10-640 kHz. The pulse duration in the picosecond range is short enough to limit thermal effects. Ablation occurs through absorption of the laser light by the free electrons at the material surface, which leads to bond break and fast plasma expansion as opposed to more aggressive thermally driven vaporization as seen with longer pulse duration lasers. A picoseconds laser pulse will not have the same heat affected zone as longer pulse duration lasers. The laser is capable of 2 different firing modes. A single shot firing mode and a burst pulse mode where a packet of pulses separated by 20ns are released on the single pulse firing frequency. This study investigated machining with both 355nm and 1064nm wavelengths in both single and burst pulse mode. For this laser, the power increases with

repetition rate for 1064nm while the 355nm output has a peak at about 160 kHz as shown in Figure 2.

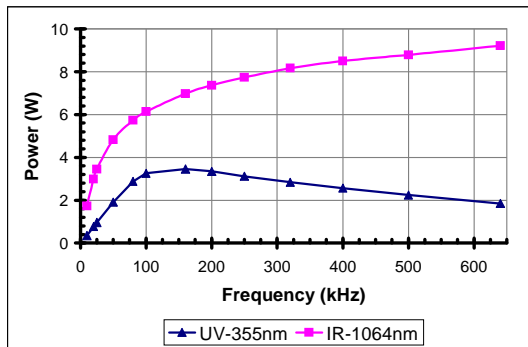


Figure 2: Power versus repetition rate for the laser

## Material

The drilling tests were conducted on Hastelloy X. The typical composition of this aerospace alloy is shown in Table 2. Hastelloy X is a nickel based superalloy widely used in gas turbine engines for combustion zone components. It is also used in industrial furnace applications because of its excellent resistance to oxidizing, reducing and neutral atmospheres. The Hastelloy coupons were 25mm wide x 50mm long and thicknesses of 0.02" (0.5mm) and 0.05" (1.27mm) thick. The base metal had up to 0.43mm of thermal barrier coatings applied.

Table 2: Hastelloy X Composition

Nominal Chemical Composition, Weight Percent								
Ni	Cr	Fe	Mo	Co	W	C	Mn	Si
47 <sup>a</sup>	22	18	9	1.5	0.6	0.10	1 <sup>*</sup>	1 <sup>*</sup>

<sup>a</sup>As balance <sup>\*</sup>Maximum

The thermal barrier coating system consisted of a base and top coat which was plasma sprayed onto the coupons. The base coat, or bond coat for the TBC, consisted of nickel chromium, aluminium, and yttrium which forms a diffusion layer of nickel aluminide. The bond layer has the temperature and corrosion resistance of a ceramic with the thermal expansion coefficients of a metal so that the top layer can lattice match well to the base metal. The top coat of the thermal barrier coating was yttria stabilized zirconia (YSZ). The function of the TBC is to reduce the temperature of the airfoil material so either the engine can be operated at higher temperatures or the service life of the parts is increased. Table 3 shows the thickness ranges of the coating applied to the metal coupons.

Table 3: Thermal Barrier Coating Thickness

Base Metal Hastelloy X thickness	Bond Coat, NiCrAlY thickness	Top Coat YSZ thickness
0.02" (0.5mm)	0.002"-0.004" (0.05-0.1mm)	0.004"-0.008" (0.1-0.2mm)
0.05" (1.27mm)	0.002"-0.004" (0.05-0.1mm)	0.010"-0.013" (0.25-0.33mm)

## Micromachining Station

The micromachining station used for this study has precision Aerotech stages allowing for XYZ movement and attachments for part fixturing at an angle were added as needed. The system has multiple optical trains with ScanLab galvanometer scanners which allow fast (100s mm/sec) precise scanning of the laser beam across the part. The general system layout is shown in Figure 3. Programming of the laser beam movement and stage placement is done through a combination of software controlling the stages and beam movement. Pattern cutting was done with a combination of beam and part movement.

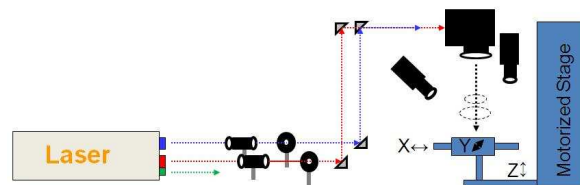


Figure 3: Laser Micromachining Schematic

## Experimental Results

The first item for evaluation using the picosecond laser system was to investigate the effects of laser machining the material in 355nm or 1064nm. The system has significantly more IR power so a true hole drilling comparison between wavelengths could not be accomplished. Ablation rate removal data was collected by machining a series of 1mm steps into the material. These steps were then analysed by white light interferometer to measure the amount of material removed. Due to the large possible sets of processing parameters, the data collection was done with a standardized overlap of 75% and using a selection of



laser repetition rates. For 1064nm those repetition rates were 80, 160, 250, 400, and 500 kHz with the average power being adjusted from 0.25 to 5W. For 355nm the repetition rates were 80, 160, 250, and 500 kHz with the power range of 0.25 to 2W during testing. In addition testing was done at a middle and high power level to evaluate the effect of adding burst pulses to the machining. The ablation squares were run at a series of increasing passes such as 12/24/36/48/60/72 to investigate how repeated passes would affect the material removal rate and surface finish at the bottom of the depth well.

There were several interesting affects found during the ablation rate study. Regardless of laser wavelength, or the power input the bottom surface of the shallow test squares would develop a pitted appearance as seen in Figure 4. It is not known if the alloyed composition of the metal was responsible for these pits seen in the metal surface. The amount of pitting varied and a connection between laser power or repetition rate and the pitting was not able to be made. The pitting seemed to be a function of the number of passes as it increased with number of passes.

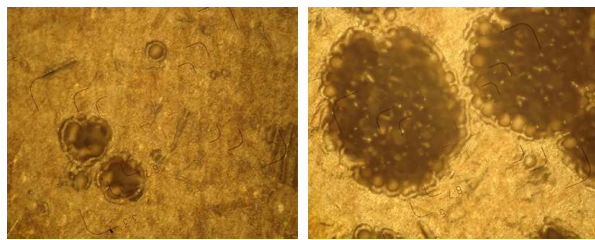


Figure 4: Bottom surface of ablation test marks

It was found that pulse burst mode did increase the overall removal rate and it did result in a more uniform bottom surface to the ablation wells. It was found there was a limit to the additional benefit of adding more burst pulses as seen in Figure 5. Burst pulse mode in IR resulted in an increase of the average power being directed at the part where as pulse mode in UV resulted in a drop of power which was attributed to the affects of burst on the harmonic crystal efficiency.

On the metal removal rate, it was found that either wavelength could be used to effectively machine the material but due to the higher power available in IR, cutting of test holes would be done in 1064nm. It was also found that 1064nm did a better job at removing the TBC layer in a uniform manner where as 355nm tended to dig in and leave a much rougher surface.

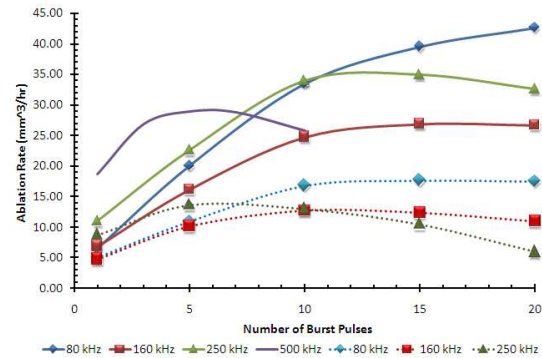


Figure 5: Affect of Burst Pulse Mode on Material Removal. Solid lines are at 4W while the dotted lines are at 2W average power

Drill testing started with holes being cut normal to the surface through both bare and coated coupons. The laser repetition rate and power used were based upon the data gathered during the ablation removal work. The holes were examined for entrance/exit size, quality of the hole and surface finish. Holes were cut at 0.8, 0.5, and 0.25mm in diameter. Figure 6 below shows the entrance and exit holes cut in 0.5mm thick bare Hastelloy. The entrance hole diameter is 0.8mm with an outlet of 0.67mm. No recast build up was found on the top or bottom surface. Drill time was 21 seconds per hole and hole to hole consistency was found to be very good.

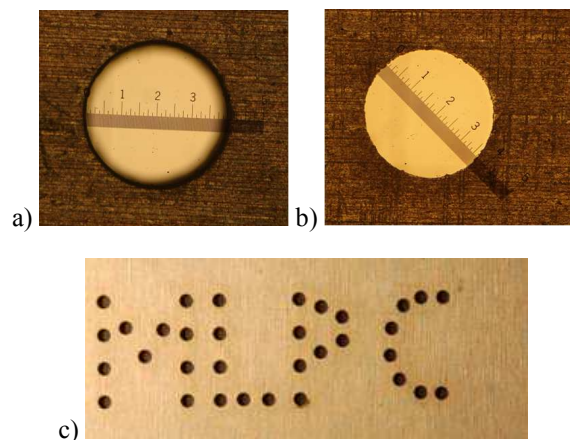


Figure 6: Holes at 90 degrees in a bare Hastelloy coupon (a) inlet surface, (b) outlet surface, (c) series of holes for repeatability

No cleaning of the sample was necessary. Hole machining was done with and without gas to observe the changes to the cut time/material removal rate. A gas assist had a negligible effect on cut time and did not appear to change the surface finish.

Figure 7 is the TBC coated material with a 0.8mm diameter hole drilled through it. With the TBC coating, the material thickness has increased to 0.8mm. The outlet holes were slightly smaller at 0.625mm than the thinner bare metal and the cut time was 27 seconds per hole. The TBC directly at the edge of the hole does pick up some minor machining debris in it. No delamination of the TBC was found to occur. Comparative samples were drilled utilizing a nanosecond laser system and the longer pulse duration did result in noticeable heat damage around the holes.

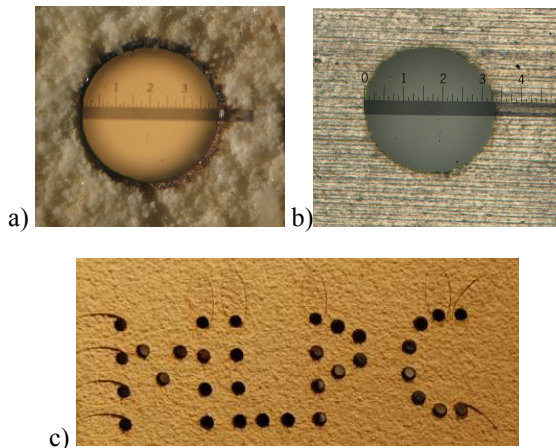


Figure 7: Holes at 90 degrees in a TBC coated Hastelloy coupon (a) inlet surface (b) outlet surface, (c) series of holes for repeatability

The time to machine the hole is relative to the hole diameter and the material thickness. Although the machining time is somewhat long when compared to long pulse duration laser drilling, the goal of this project was to investigate combining processing steps so that longer cycle time could be acceptable if other steps could be removed from the process or if tighter hole tolerance could be accomplished. Tighter hole size tolerances and placement would allow better utilization of the engine capabilities.

A series of angled hole were drilled starting at 45 degree on both the bare and coated samples. Figure 8 shows the 45 degree angled drilling relative to the surface into the bare material and TBC coated material. Due to the angle of the cut, the overall thickness being cut is increased to ~1.5mm to ~1.9mm for the angled samples. The 45 degree holes had sharp clean entrances and exits. The cut time had increased to 45 sec and 51 seconds for the bare and coated materials, respectively.

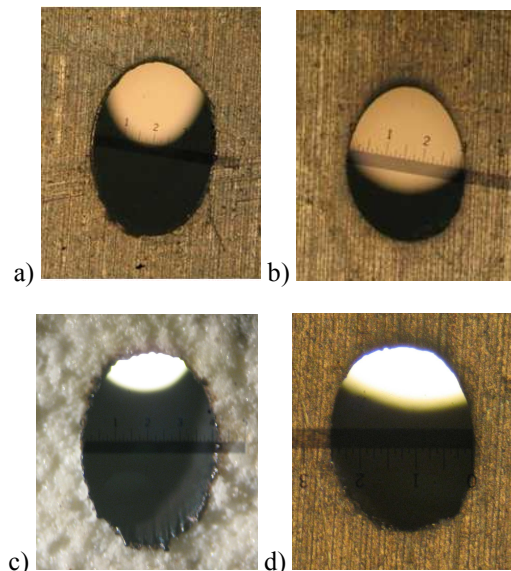


Figure 8: (a) Inlet & (b) outlet surface on bare metal compared to the (c) inlet on TBC coated & (d) outlet on TBC coated material at a cut angle of 45 degrees

The diameter of entrance hole was 0.8mm with exit holes roughly 0.6 and 0.55mm. Additional angle testing was done at 30, 20 and 15 degree. It was found that the minimum angle the laser could effectively cut into the surface was approximately 17 degrees. Below this angle the laser beam appeared skim along the surface of the material instead of cutting into it. Figure 9 illustrates the 30 angled cut.

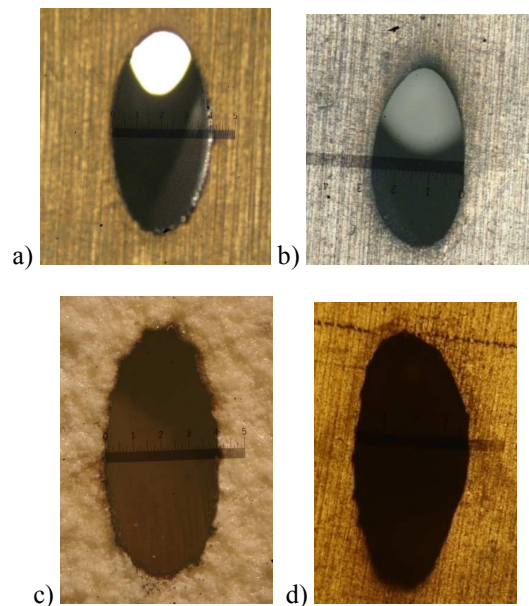


Figure 9: (a) Inlet surface and (b) outlet surface of bare material compared to (c) inlet TBC coated and (d) outlet of TBC material at a cut angle of 30 degrees.



Due to the angle of the cut, the overall thickness being cut is increased to 2.3mm to 3.0 mm for the different samples. The 30 degree holes had sharp clean entrances and the exits on the bare metal but the TBC coated material began to exhibit a poorer edge quality on the exits. The cut time had increased to 72 sec and 92 seconds for the bare and coated materials, respectively.

Another aspect of this study was to investigate the ability of the picosecond laser to shape the TBC without cracking or debonding it. Several different designs were micromachined into the TBC as shown in Figure 10. The bottom design in Figure 10 was a simple removal of the TBC coating in a sloped oval. The deepest part of the oval shape is 0.150mm with the overall length of 3.4mm by 1.5mm wide. This shape could be machined into the TBC material in 6 seconds with the laser.



Figure 10: Simple slope shaping of the TBC

Further investigation into TBC shaping is shown in Figure 11 where a larger 3.5mm complex design was micromachined into the TBC. This design had three 0.5mm wide arrow strips left behind to better examine the interaction of the laser and the TBC.



Figure 11: Complex TBC shaping with finger design.

The design shown in Figure 11 can be machined with 35 second of laser time. There appeared to be no cracking or spallation of the coating when machining of this arrow design although further SEM analysis is ongoing.

The good results in utilizing the picoseconds laser to shape and drill TBC and Hastelloy led to two further demonstrations. Silicon Carbide and composites are potential material choices for future next generation aerospace components. Figure 12 is a 0.8mm hole drilled through 0.5mm thick silicon carbide. The exit hole is 0.6mm and the drill time on the hole was 21

second. Figure 12 also illustrates the excellent cut quality on the edge lines.

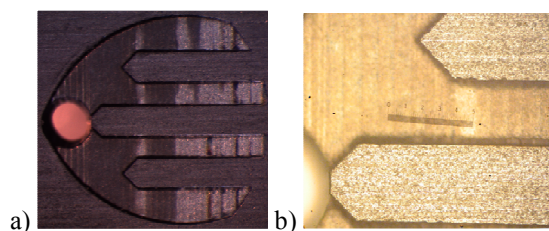


Figure 12: Drilled and shaped Silicon Carbide.

The cutting of nozzle shapes for fuel injectors was also investigated. The machining algorithm was programmed to cut a nozzle shape through 0.5mm of Hastelloy. The inlet of the nozzle was 0.3mm with an outlet size of 0.075mm. The nozzle would change taper at about 0.35mm through the material with a sharp angled outlet from that point downward. Very sharp and small 75 micron outlet holes were produced as seen in Figure 13. Cross sectioning of the samples revealed a change in angle was accomplished in accordance with the programmed cut.

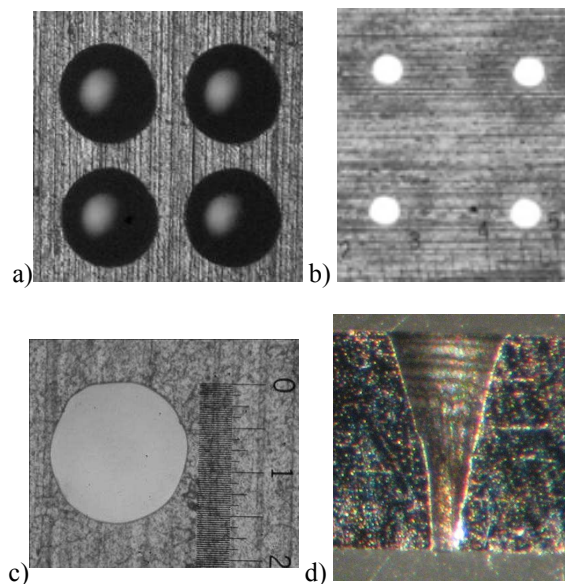


Figure 13: Nozzle shaped cut with a 75 micron outlet. (a) inlet surface (b) outlet surface (c) magnified view of a single outlet, scale 0-1=50microns and (d) is a cross sectioned view of the nozzle shape

## Summary

In this work, laser drilling of TBC coated Hastelloy was investigated. It was found that the picosecond laser could effectively drill turbine coupons with reasonable drill time based on the power rating available at the time of this study. This laser machining

resulted in very good hole quality and almost no recast on the inlet or outlet surfaces. MLPC has demonstrated the ability to machine both shaped holes and complex surface structures without cracking of the TBC coating. Unique machining algorithms allow for efficient drilling with minimal heat damage. The technology for laser machining of these materials has been demonstrated as transferable to other material like silicon carbide for next generation components.

### References

1. Michael Cervenka, T.A.t.D.-E.T., Office of the Chief Engineer, Rolls-Royce plc, The Rolls-Royce Trent Engine 10 November 2000. @ <http://www.msm.cam.ac.uk/phasetrans/mphil/Trent1/sld032.htm>,
2. Bostanjoglo, G.; Sarady, I.; Beck, T.; Weber, H. (1996) Processing of Ni-based aero engine components with repetitively Q-switched Nd:YAG-lasers. Proceedings of the SPIE - The International Society for Optical Engineering High-Power Lasers: Applications and Emerging Applications v 2789, p.145-57
3. Smaller Holes Bigger Challenges (2006), Manufacturing Engineering March 2006 Vol. 136 No. 3
4. Low, D.K.Y., Li, L., Byrd, P.J. (2003) Spatter prevention during the laser drilling of selected aerospace materials, Journal of Materials Processing Technology 139, p. 71-76
5. Corcoran, A., Sectron, L., Seaman, B., Ryan, P. Byrne, G., (2002) The laser drilling of multi-layer aerospace material systems, Journal of Materials Processing Technology 123, p. 100-106
6. Voisey, K.T., Clyne, T.W., (2004) Laser drilling of cooling holes through plasma sprayed thermal barrier coating Surface and Coating Technology 176, p. 296-306

### Acknowledgements

The authors would like to thank the Air Force Research Laboratory at Wright Patterson Air Force Base in Dayton Ohio for their input, guidance and funding assistance on this project. The work was funded through an AFRL Phase II SBIR contract number F33165-01-C-5700

### Meet the Authors

Carl Druffner is currently working as a Research Specialist at Mound Laser & Photonics Center Inc. He is involved in both commercial and government research and development projects involving laser micromachining at MLPC. He has a Masters Degree in Materials Engineering and Bachelors Degree in Chemical Engineering from the University of Dayton.

Dr. Larry Dosser, President and CEO of MLPC, possesses has more than forty years of hands-on experience in laser applications and physical chemistry with proven success in numerous laser-based technology areas. He is a force for economic and workforce development in his local community and the laser materials processing industry, and is an active member of several educational and commercial development boards to promote Science, Technology Engineering & Mathematics (STEM) education and enhance the collaboration between defense, commercial, and educational institutions.

## APPENDIX AD

# Double-pulse and single-pulse laser-induced breakdown spectroscopy for distinguishing between gaseous and particulate phase analytes

Michael E. Asgill,<sup>1</sup> Michael S. Brown,<sup>2</sup> Kyle Frische,<sup>2</sup> William M. Roquemore,<sup>3</sup>  
and David W. Hahn<sup>1,\*</sup>

<sup>1</sup>Department of Mechanical and Aerospace Engineering, University of Florida,  
Gainesville, Florida 32611, USA

<sup>2</sup>Innovative Scientific Solutions, Inc., Dayton, Ohio 45440, USA

<sup>3</sup>Propulsion Directorate, Wright-Patterson AFB, Ohio 45433, USA

\*Corresponding author: dwhahn@ufl.edu

Received 7 October 2009; revised 16 February 2010; accepted 17 February 2010;  
posted 18 February 2010 (Doc. ID 118273); published 9 March 2010

We explore the use of a combination of double-pulse and single-pulse laser-induced breakdown spectroscopy (LIBS) methodologies as a means of differentiating between solid-phase and gaseous-phase analytes (namely, carbon) in an aerosol stream. A range of spectral data was recorded for double-pulse and single-pulse configurations, including both ns and fs prepulse widths, while varying the gas-phase mass percentage of the carbon from about 10% to 90% for various fixed carbon concentrations. The carbon emission response, as measured by the peak-to-continuum ratio, was greater for the double-pulse configuration as compared with the single-pulse response and was also enhanced as the percentage of solid-phase carbon was increased. Using a combination of the double-pulse and single-pulse emission signals, a monotonically increasing response function was found to correlate with the percentage of gas-phase analyte. However, individual data points at the measured gas-phase percentages reveal considerable scatter from the predicted trend. Furthermore, the double-pulse to single-pulse ratio was only pronounced with the ns–ns configuration as compared with the fs–ns scheme. Overall, the LIBS methodology has been demonstrated as a potential means to discriminate between gas-phase and particulate-phase fractions of the same elemental species in an aerosol, although future optimization of the temporal parameters should be explored to improve the precision and accuracy of this approach. © 2010 Optical Society of America

OCIS codes: 300.6365, 300.6210.

### 1. Introduction

Laser-induced breakdown spectroscopy (LIBS) is an analytical technique that utilizes atomic emission to identify and quantify the composition of an analyte sample, which may be in the solid, liquid, or gaseous state [1–4]. With LIBS, a pulsed laser beam is fo-

cused onto the sample in question with sufficient irradiance to form a laser-induced plasma, thereby causing the constituent molecules to dissociate. Within the ensuing plasma, the excited state of the liberated atoms and ions results in atomic emission, which is then collected and analyzed to determine the composition of the sample. The concentration of each constituent can also be quantified using calibration, since the intensity of the atomic emission is proportional to the mass concentration of the

emitting atoms and ions in the sample plasma. However, calibration with LIBS can present challenges, given that matrix effects can be present in all sample types. For example, with LIBS analysis of aerosol systems, which is the focus of the present study, several calibration issues have been noted. Hohreiter and Hahn [5] reported a different analyte response for gas-phase and particle-phase carbon samples, finding a stronger response for the solid particulate fraction of the aerosol. Such an effect is most likely due to the rarefaction of gas-phase species in the resulting plasma. Other studies have found calibration effects within the particulate fraction as well, including upper size limits for complete vaporization [6,7] and particle matrix effects in which concomitant mass within an aerosol particle perturbs the analyte response of other species [8]. In contrast, others have observed rather limited size effects in the nanometer-size regime for relatively long plasma delay times [9]. As noted in several of the above studies and others [10,11], the temporal aspects of particle dissociation and atomic diffusion are important, making quantitative analysis of aerosol systems a problem in which the physical nature of the analyte must be carefully considered.

Double-pulse LIBS involves the use of two lasers with a delay between the two laser pulses. In many instances, the double-pulse configuration has been shown to increase the analyte signal for solids analysis [12–15], generally by using the first pulse to rarefy the gas above the sample, thereby enabling better coupling of the second laser pulse into the solid [16]. Windom *et al.* [17] explored double-pulse LIBS for analysis of purely gaseous and aerosol systems at atmospheric pressures. They found that the peak-to-continuum ( $P/B$ ) ratio of double-pulse LIBS departs very little from that of traditional single-pulse LIBS for a purely gaseous-phase analyte, attributing this to the fact that the second laser pulse was poorly coupled (nearly 100% transmission) to the rarefied initial plasma at moderate delay times. However, for aerosol analysis, with the analyte bound in the solid particulate phase, the  $P/B$  ratio for a double-pulse configuration was significantly higher (factor of 4) than that for single-pulse LIBS. This was attributed to the similar effects as observed with double-pulse analysis of solid targets, namely, the gaseous phase of the aerosol is rarefied, leaving a more analyte-rich (i.e., solid-phase) signal behind, although temporal timing is important.

Given the range of results above, namely, a differing response for gas-phase and particulate-phase fractions of an aerosol system, as well as different responses for these same fractions with single-pulse and double-pulse LIBS, one might be led to explore the combined effects of these two findings as a means to discriminate between solid and gaseous analyte signals. A useful analyte to explore is carbon, given its ubiquitous nature. For example, carbon is an important species to study when characterizing a combustion system. The presence of carbon dioxide is an

indicator of complete combustion, while particulate carbon is a marker of fuel-rich combustion, either localized or overall. LIBS has also been successfully explored for analysis of hydrocarbon and combustion gases [18,19]. These two carbon sources are also important from an emissions standpoint as carbon dioxide is a greenhouse gas, and particulate matter, such as solid carbon soot, is a carcinogen and environmental pollutant. Overall, the ability to distinguish between the particulate and gaseous forms of any analyte would be of use for many applications. The purpose of this study is to determine whether LIBS is capable of differentiating between solid-phase and gaseous-phase carbon-based analytes.

## 2. Experimental Methods

Two double-laser platforms were used in the study and are described sequentially below. The first platform employed two Q-switched Nd:YAG lasers (8–10 ns pulse widths), both operating at a frequency of 5 Hz. Both beams were expanded and collimated to allow for a tighter focus. A schematic of the system is given in Fig. 1 and details of the lasers are provided in Table 1. The first laser (Big Sky CFR 400), denoted Laser 1, was used for all of the single-pulse measurements. The second laser (Continuum PRII 8000), denoted Laser 2, was added for the double-pulse measurements, always firing prior to Laser 1. Both lasers were spatially oriented such that their focal points coincided within a standard six-way vacuum cross sample chamber (15.2 cm across, 3.5 cm ID). The flashlamp of Laser 2 was used to trigger a digital delay generator (SRS DG535), which then triggered the flashlamp of Laser 1. Both Q switches were internally triggered. The delay between the firing of Laser 2 and Laser 1 was kept constant at 1  $\mu$ s. A delay of 1  $\mu$ s was selected in an effort to maximize the  $P/B$  difference with the double-pulse configuration for a solid-phase analyte and minimize the double-pulse response for a gaseous analyte based on previous work [17]. Specifically, in the previous study it was found that the enhancement with a double-pulse configuration was maximized for the particulate phase of an aerosol in this temporal delay regime, while such enhancements were minimal for the gaseous fraction. A digital oscilloscope (2.5 Gsample/s) and fast-response phototube (Hamamatsu R1193U-51, 200 ps rise time) were used to continuously measure the actual pulse-to-pulse delay throughout the experiment and maintain the value at 1  $\mu$ s. This laser platform will be referred to as the ns–ns system, based on the pulse widths of each laser.

The second laser platform employed a similar sequential prepulse timing scheme, but using a fs-pulse laser for Laser 2 (Continuum Legend) and a frequency-doubled Q-switched Nd:YAG laser for Laser 1 (Spectra Physics GCR3). As with the first platform, Laser 1 is present in all measurements, and Laser 2 was added for all of the double-pulse measurements. The fs pulse was provided by a



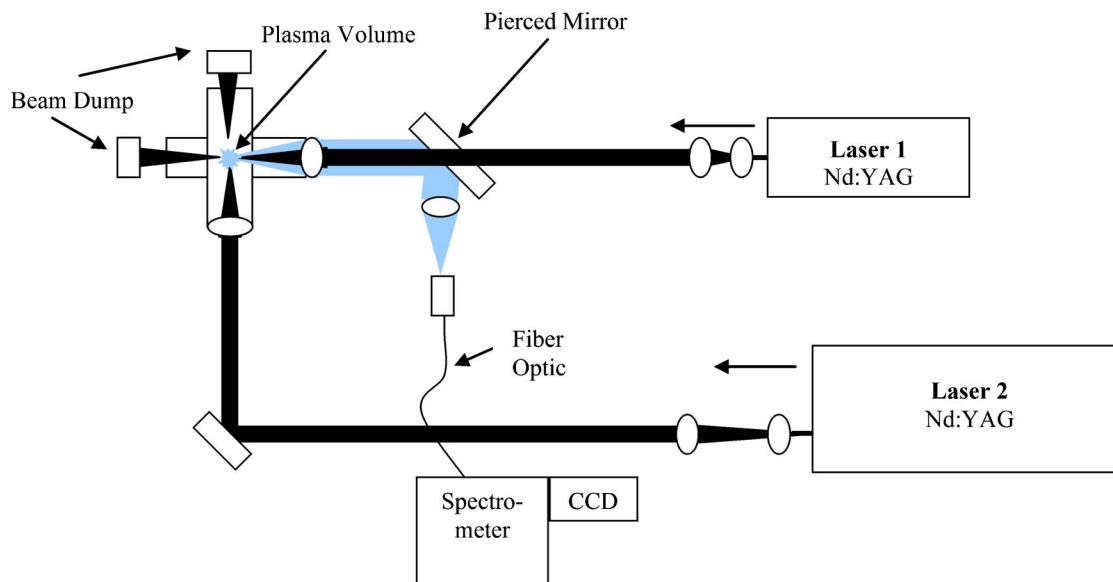


Fig. 1. (Color online) Experimental apparatus for the double-pulse and single-pulse ns-ns LIBS configuration.

Ti:sapphire regenerative amplifier with a pulse width of 45 fs. Although the fs pulses deliver much less energy than the ns pulses (0.5 mJ versus 300 mJ), their peak field intensity is orders of magnitude higher; hence they efficiently ionize the target sample via the tunneling mechanism [20]. The lower pulse energy also produces a plasma that is much shorter lived—tens of nanoseconds as compared with tens of microseconds for the ns-pulse plasma. However, the leading fs pulse can potentially influence the LIBS signal by either rarefying the sample volume hydrodynamically or by producing a pre-ionized sample volume that more readily absorbs energy from the second ns pulse.

The LIBS spark produced by the fs laser pulse is significantly smaller than that produced by the ns laser pulse. Like the ns-pulse-excited spark, the fs-pulse-excited spark is elliptical in shape with the long axis collinear with the laser propagation direction. To ensure that any rarefaction or preconditioning produced by the fs pulse was taken advantage of fully, the two incident laser beams were combined and focused with a common optic (singlet, biconvex, 40 mm focal length) along a common propagation axis. To compensate for the different focal lengths of the singlet lens at 532 and 800 nm, telescopes

(fs beam: −200 mm focal length plano-concave, +100 mm focal length plano-convex; ns beam: −125 mm focal length plano-concave, +100 mm focal length plano-convex) were placed in both laser beam paths to alter the divergence of the two beams as they entered the singlet. To assist with the overlap of the two sparks, magnified images were collected at 90 deg with respect to the common propagation axis. The beam telescopes were adjusted to place the fs spark as close as possible to the location for peak emission within the ns spark. The distance between the center of the fs spark and the peak emission point of the ns spark was minimized to 0.75 mm.

The overlapped fs and ns sparks were placed at the center of a second six-way cross also serving as a LIBS sample chamber. For two values of the fs pulse energy, 0.5 and 0.75 mJ, the difference between the double- and single-pulse LIBS signals peaked for a pulse delay of 500 ns for carbon-containing analytes. This pulse delay was used for all measurements reported here. Similarly, the detector gate delay and width were both held fixed at 10 μs with respect to Laser 1. This platform will be referred to as the fs-ns configuration. The significant characteristics of the two systems are summarized in Table 1.

For both laser platforms, carbon was the analyte species of interest for all experiments and was introduced as either a gaseous phase, a particulate phase (i.e., solid phase), or a mixture of the two phases. For the gas-phase analyte, CO<sub>2</sub> (Praxair 4.0 Instrument Grade) was the source of carbon, it having been well established in the literature that for gas-phase species, the analyte signal is independent of the molecular source [5,21,22]. To generate the solid-phase analyte, a dilute solution of carbon (as oxalic acid in water) was nebulized, which produces a high number density aerosol of carbon-rich particulates following droplet desolvation, with a mean size of about 100 nm [23]. The carbon solutions were prepared

Table 1. Parameters for the ns-ns and fs-ns Platforms

	ns-ns Platform	fs-ns Platform
Laser 1 Wavelength	1064 nm	532 nm
Laser 2 Wavelength	1064 nm	800 nm
Laser 1 Energy	300 mJ/pulse	300 mJ/pulse
Laser 2 Energy	300 mJ/pulse	0.5 to 0.75 mJ/pulse
Orientation of lasers	Perpendicular	Collinear
Prepulse delay	1 μs	500 ns
Gate delay	8 μs	10 μs
Gate width	5 μs	10 μs

by diluting ICP-grade analytical standards of  $10,000\text{ }\mu\text{g C/ml}$  (SPEX CertiPrep) to the desired concentration using ultrapurified de-ionized water. A pure nitrogen (Praxair 99.7%  $\text{N}_2$ , <32 ppm  $\text{H}_2\text{O}$ ) co-flow was used as the balance for all experiments. All gaseous flows were passed through HEPA filters and were metered with digital mass flow controllers (Alicat Scientific MC-20SLPM-D, MC-10SLPM-D, and MC-50SLPM-D and Matheson Gas Products 8272-0434) appropriately sized to the relevant flow rates for high accuracy. The diluted carbon solutions were nebulized at a rate of about  $0.15\text{ ml/min}$  using a flow of  $5\text{ lpm}$  of nitrogen through a pneumatic type nebulizer (Hudson model #1724) and mixed with a nitrogen co-flow of  $43.7\text{ lpm}$ . The exact nebulization rates were measured by gravimetric analysis using the initial and final mass of solution in the nebulizer. The combination of analyte concentration in solution, the exact nebulization rate, and total gas flow rates was used to determine the true concentration ( $\mu\text{g/l}$ ) of analyte in the test chamber.

LIBS measurements were conducted using the fs–ns platform in single-pulse (ns only) mode to ensure consistent calibration with respect to previously reported data using the ns–ns platform in single-pulse mode [5]. Excellent agreement between the two platforms was established for peak-to-continuum ratios, for both gas-phase and solid-phase carbon samples, as a function of total carbon mass loading, thereby enabling direct comparison of the measurements discussed in this paper.

For the ns–ns laser platform, the total carbon concentrations (gaseous and solid phase) were adjusted to provide a range of about  $3$  to  $20\text{ }\mu\text{g C/l}$  of gas. For each total carbon concentration, the gaseous-to-solid carbon ratio was increased by increasing the flow rate of the carbon dioxide stream while proportionately decreasing the concentration of carbon in the nebulized solution. This allowed the total carbon concentration in the sample stream to remain constant while investigating the effects of analyte phase. The conditions were adjusted to vary the percentage of solid carbon and gaseous carbon from about 10% gas-phase carbon and 90% solid-phase carbon as elemental carbon mass (designated 10/90) to about 90% gas-phase carbon and 10% solid-phase carbon (designated 90/10). For all five total carbon concentrations investigated, the exact gas/solid mass concentration ratios tested were 9.6/90.4, 24.2/75.8, 47.4/52.6, 73.2/26.8, and 89.3/10.7 with relative standard deviations of 0.60%, 0.82%, 1.82%, 1.17%, and 0.62%, respectively.

For the fs–ns laser platform, the total carbon concentration was varied between  $0.5$  and  $5.0\text{ }\mu\text{g C/l}$  of gas. The ratio of gas to solid-phase analyte was adjusted as noted above keeping the total mass concentration fixed. Five gas/solid mixture ratios were used over the range of 32.5/67.5 (gas% to solid%) to 67.5/32.5. Deviations between the ns–ns and fs–ns platforms regarding total carbon concentration and gas/solid ratios were dictated by differences between

operation limits of the particular flowmeters employed.

For all the ns–ns experiments, the plasma was created in the center of the sample chamber using a  $50\text{ mm}$  diameter,  $75\text{ mm}$  focal length plano-convex lens ( $1064\text{ nm}$  antireflection coating). Spectral emission from the plasma was collected by backscatter on the axis with Laser 1 through a pierced mirror and coupled through a fiber optic cable into the spectrometer. The light was dispersed by a  $0.275\text{ m}$  spectrometer (Acton Research Corp. Spectra Pro-275,  $2400$  grooves/mm and  $0.15\text{ nm}$  resolution) and recorded by an intensified CCD (ICCD) array (Princeton Instruments 1024MLDS). The ICCD was triggered by the Q-switch sync from Laser 1, with the delay and width set to  $8\text{ }\mu\text{s}$  and  $5\text{ }\mu\text{s}$ , respectively, and fixed with respect to Laser 1 for both single- and double-pulse configurations, as shown in Fig. 2. For the single-pulse experiments, Laser 2 was shuttered. For each carbon concentration and gas/solid percentage, data were recorded using six individual  $1000$ -shot averages spread over multiple days for both single-pulse and double-pulse configurations. All data were processed using the  $247.9\text{ nm}$  carbon I atomic emission line ( $21,648\text{--}61,982\text{ cm}^{-1}$ ) integrated over the full-width and normalized to the adjacent continuum plasma emission (Bremsstrahlung and recombination emission) to attain the final peak-to-base ratio ( $P/B$ ) as the analyte signal. In addition, the signal-to-noise ratio (SNR) was calculated as the ratio of the full-width peak area to the RMS noise of the adjacent

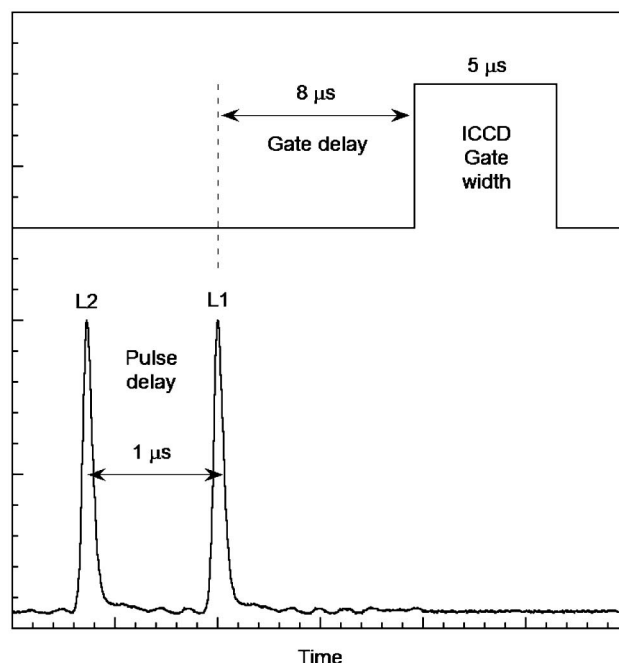


Fig. 2. Timing schematic for the double-pulse and single-pulse experiments employing the double ns–ns laser platform. For the fs–ns laser platform the pulse delay was shortened to  $500\text{ ns}$  (fs pulse preceding the ns pulse) and the ICCD gate delay and width were each set to  $10\text{ }\mu\text{s}$ .



featureless continuum intensity, as evaluated over the same number of pixels.

Focused fs pulses with peak irradiance  $>10^{14}$  W/cm<sup>2</sup>, such as the one used for the fs–ns experiments, yield forward and backward emission due to self-phase modulation and stimulated Raman processes. Therefore, the LIBS signal was collected at 90 deg to the beam propagation axis for the fs–ns work reported here to ensure that only signals attributable to the double-pulse setup were analyzed. The signals were collected using the same carbon I line noted above using similar signal averaging procedures. The signals were collected using a free-space lens pair (two plano-convex lenses 50 mm in diameter; +150 mm focal length near the chamber and +350 mm focal length near the spectrometer), dispersed through a 0.5 m spectrometer (SPEX 500 M) and captured using a second ICCD (Princeton Instruments PI-MAX). The oscillator seeding the regenerative amplifier was used as the master clock driving a delay generator (Highland P400 and SRS DG535) that provided the trigger signals for the Nd:YAG (flash-lamp and Q switch) and the ICCD. Overall, data was collected for similar configurations and analyte loadings for both the ns–ns and fs–ns systems.

### 3. Results and Discussion

Figure 3 shows representative single-pulse and double-pulse (ns–ns configuration) LIBS spectra corresponding to 89.3% gas-phase carbon and 10.7% solid-phase carbon (referred to as 90/10) and 9.6% gas-phase carbon and 90.4% solid-phase carbon (referred to as 10/90), all at a fixed total carbon concentration of  $5.8 \mu\text{g/L}$ . Two significant features are noted in these spectra, which were consistent for all of the gas/solid percentage values examined. First, both the carbon emission peak intensity and

the continuum emission intensity of the single-pulse measurements are greater than the corresponding values of the double-pulse measurements. These values will be quantified below in terms of both the  $P/B$  and SNR values. Overall, this finding is consistent with previous work [17] and is attributed to the fact that the first laser-induced plasma (Laser 2) creates a rarefied condition into which the second laser (Laser 1) is fired. When the second laser pulse interacts with the existing plasma, the coupling effects are different for the gas-phase and solid-phase species, with the gas-phase species showing less effect due to the second laser pulse, as noted in detail by Windom *et al.* [17]. However, since the overall species density is reduced due to the high temperatures of the first plasma, the continuum emission is also subsequently reduced with the double-pulse configuration. Second, as the percentage of particulate carbon increases in the sample (i.e., from 10% to 90% particulate carbon in Fig. 3), the overall emission intensity of the carbon line increases for both the single-pulse and double-pulse configurations. This trend is consistent with previous work exploring the effects of the analyte phase [5], in which it was found that the analyte response of particulate-phase species was greater than the analyte response of gaseous-phase species for aerosol LIBS measurements. The single- and double-pulse fs–ns measurements showed the same qualitative behavior as the ns–ns measurements, as discussed below.

While the exact mechanisms responsible for the noted behavior are not fully understood, several processes likely contribute to these findings. Gas-phase species undergo rarefaction in the hot, expanding plasma; hence the number density of emitting species at the time of the analytical measurements (typically some microseconds following breakdown)

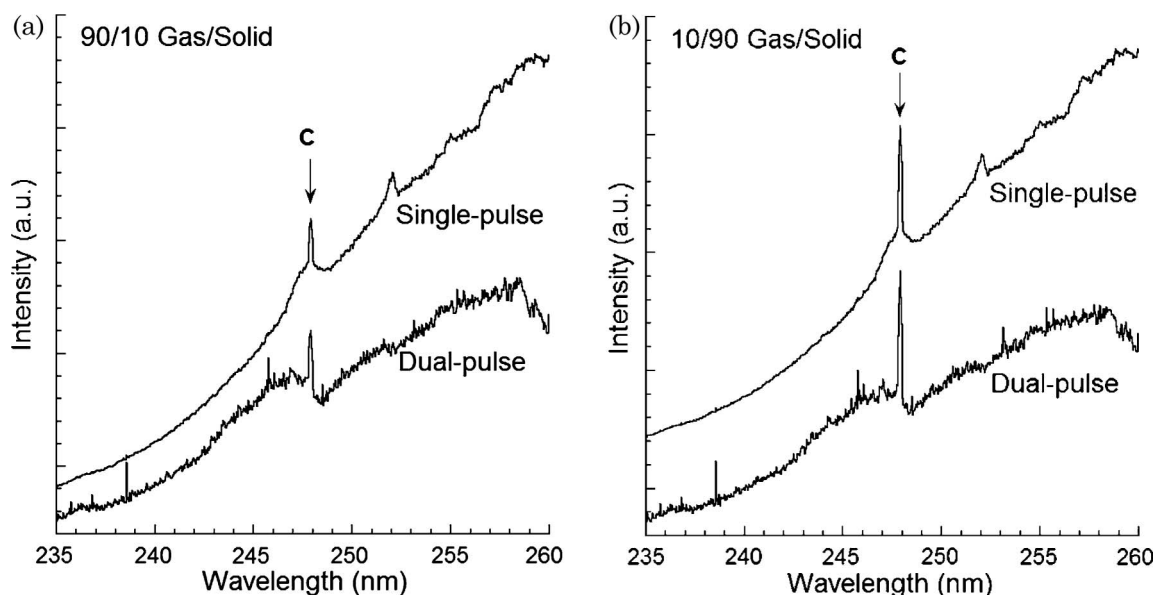


Fig. 3. 1000-shot average LIBS spectra for (a) 90% gas-phase carbon and (b) 10% gas-phase carbon for both single-pulse and double-pulse using the ns–ns configuration. All data were recorded at a fixed total carbon concentration of  $5.8 \mu\text{g/L}$ . The spectra have been offset and do not have the same intensity scales.

are reduced from the original ambient values. However, due to the considerable mass and required times for particle vaporization [24], particulate-phase species are expected to lag behind with respect to rarefaction of the gas-phase, therefore yielding an enrichment of analyte species derived from the particulate phase. For the fs–ns platform, the incident fs prepulse deposits significantly less energy than the ns pulse due to the significant difference in incident energies (0.5 mJ as compared with 300 mJ). Consequently, the rarefaction effect may be reduced. However, the extremely high peak pulse irradiance of  $\sim 10^{14}$  W/cm<sup>2</sup> leads to very efficient ionization via strong field effects such as tunneling [20]. In this case the difference in analyte phase response may lie in part in the details of the plasma kinetics associated with the two phases.

Overall, the effects of gas and particulate-phase in combination with the single- and double-pulse configurations (ns–ns platform) are quantified below in terms of the  $P/B$  and SNR values. Specifically, the  $P/B$  ratios were calculated for all carbon concentrations, gas/solid ratios, and single- and double-pulse configurations. By holding the gas/solid mixture fraction constant and varying the overall carbon concentration, calibration curves were created for each gas/solid mixture fraction for both single-pulse and double-pulse configurations. Figure 4 presents the resulting calibration curves for the 10/90 (i.e., 10% gas-phase) and the 90/10 (i.e., 90% gas-phase) carbon mixtures. Overall, the curves display nice linearity, with all correlation coefficients greater than 0.982, and with the typical value greater than 0.99, although the variability was observed to increase with increasing gas-phase carbon content. The overall trends of the calibration curves are consistent with the spectral data of Fig. 3. Namely, the double-pulse calibration curves are all characterized by a greater slope than the respective single-pulse

curve for a given gas/solid percentage. For example, the slope of the 10% gas-phase calibration curve (Fig. 4 data) is  $0.36 \pm 0.02$  (standard deviation) for the single-pulse data and  $0.62 \pm 0.04$  for the double-pulse data. Similarly, the slope values are  $0.15 \pm 0.02$  and  $0.28 \pm 0.04$  for the single- and double-pulse configurations, respectively, for the 90% gas phase. This is consistent with a greater carbon emission peak as compared with the continuum emission with the double-pulse configuration, although the signal-to-noise values are actually reduced, as discussed below. This trend held for all gas-phase carbon mixtures, but as the percentage of gaseous carbon increased, the difference between the two signals decreased. Another important characteristic of the calibration curve data is a lessened overall analyte response, as measured by the calibration curve slope, when shifting from 10% gas phase (primarily solid-phase carbon) to 90% gas phase for either pulse configuration (i.e., single-pulse or double-pulse). This is consistent with the spectral data as well (see Fig. 3), is in agreement with previous findings as discussed above [5], and clearly shows that the overall signal increases with an increasing percentage of solid-phase analyte.

The calibration curves for the fs–ns laser platform are similar to those of the ns–ns platform. As shown in Fig. 5, the  $P/B$  ratio as a function of mass loading is greater for the double-pulse case than for the single-pulse case for both pure gas-phase and pure solid-phase carbon. Likewise, the slopes for the calibration curves are somewhat greater for the double-pulse case than for their single-pulse counterparts. The difference between the double- and single-pulse calibration slopes for the fs–ns platform is not as great as for the ns–ns platform, as observed in Fig. 5.

From an analytical point of view, it is important to note the difference between the peak-to-base ratio and the signal-to-noise ratio, noting the former

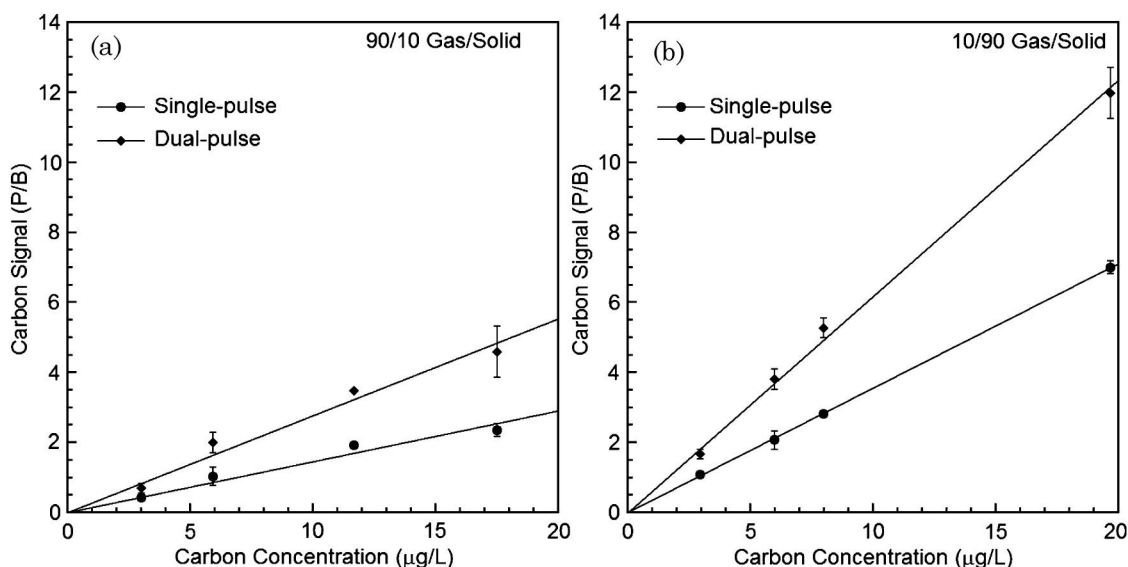


Fig. 4. LIBS calibration curves for (a) 90% gas-phase carbon and (b) 10% gas-phase carbon for both single-pulse and double-pulse ns–ns configurations. Error bars represent one standard deviation.

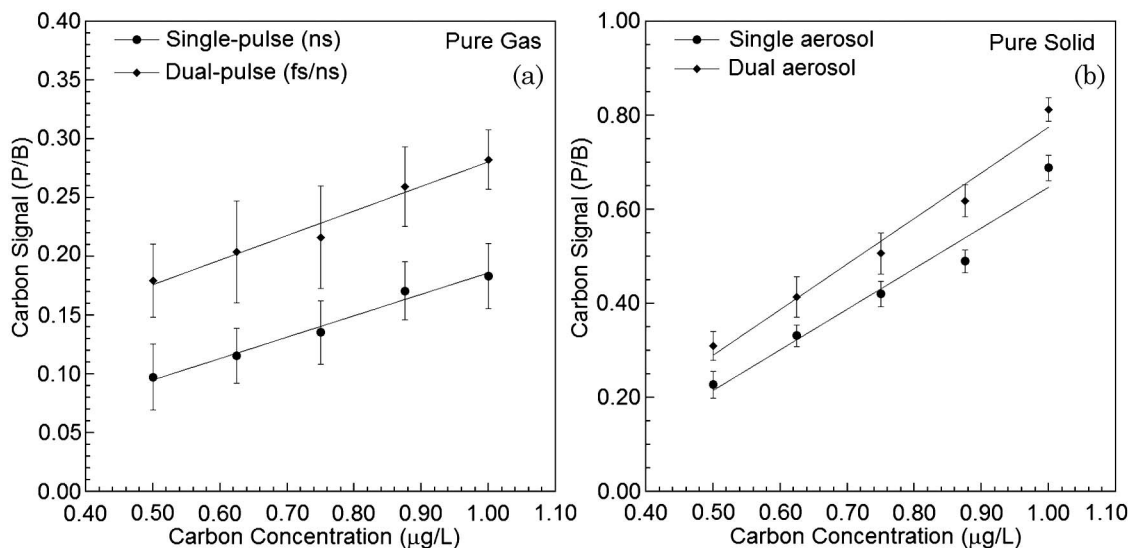


Fig. 5. Peak-to-base ratios for fs-ns and ns-only excitation of carbon in (a) pure gaseous phase and (b) pure particulate (i.e., aerosol) phase as a function of the mass loading in the chamber. Error bars represent one standard deviation.

quantity provides a self-normalization with regard to the plasma emission and is therefore a useful parameter for calibration, while the latter better reflects the quality of the signal and is more useful in the context of detection limits. The SNR values for the ns-ns platform are presented in Fig. 6 as a function of percent gaseous carbon for a fixed total carbon concentration of  $5.8 \mu\text{g/l}$ . Note that the limiting data points at about 10% and 90% gas-phase carbon correspond to the spectral data of Fig. 3. As expected, the signal-to-noise ratio increases as the percentage of solid-phase carbon increases (i.e., gas-phase carbon decreases). This trend is in agreement with the calibration curve data and reflects the enhanced

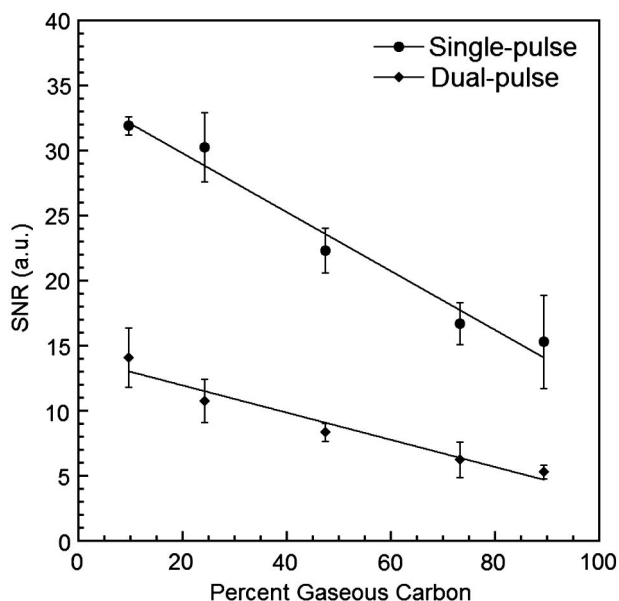


Fig. 6. Signal-to-noise ratio as a function of the percentage of gaseous carbon for a fixed total carbon concentration of  $5.8 \mu\text{g/l}$  for the ns-ns configuration. Error bars represent one standard deviation.

analyte response with the solid-phase as compared with the gaseous-phase carbon. In contrast to the  $P/B$  data, the SNR is greater for the single-pulse LIBS data than for double-pulse data at any given gas-phase concentration. This trend was consistent for all gas/solid mixtures and all concentrations and is in qualitative agreement with the spectral data of Fig. 3, which reveal a greater amount of spectral noise in the continuum emission relative to the signal level of the carbon line. Although the  $P/B$  ratio does correctly reflect the value of atomic emission intensity relative to the continuum emission intensity, the overall signal levels were greatly diminished with the double-pulse configuration. Hence the spectral signals are moving toward the noise-limited regime with the double-pulse configuration, which is reflected with the diminished SNR values. Overall, the SNR data trends of decreasing SNR with increasing gas-phase carbon at a fixed mass loading and of increasing single-pulse SNR with respect to the double-pulse value, were also observed in the fs-ns laser platform measurements.

As a summary of the overall data and trends characteristic of combined effects of single- and double-pulse configurations and gas-phase and solid-phase partitioning, Fig. 7 presents the slopes of the individual calibration curves (e.g., see Fig. 4) as a function of the gas-phase percentage for both the double-pulse and single-pulse ns-ns experiments. The plot shows that for all of the gas-phase carbon percentages investigated, the slopes of the double-pulse LIBS  $P/B$  calibration curves are higher than the respective single-pulse calibration slopes, which is consistent with the above results and reflects the enhanced atomic emission with respect to the continuum emission with the double-pulse approach, noting the reduced overall intensity levels as reflected in the SNR values. In addition, it is observed that the calibration curve slopes decrease as the gas-phase

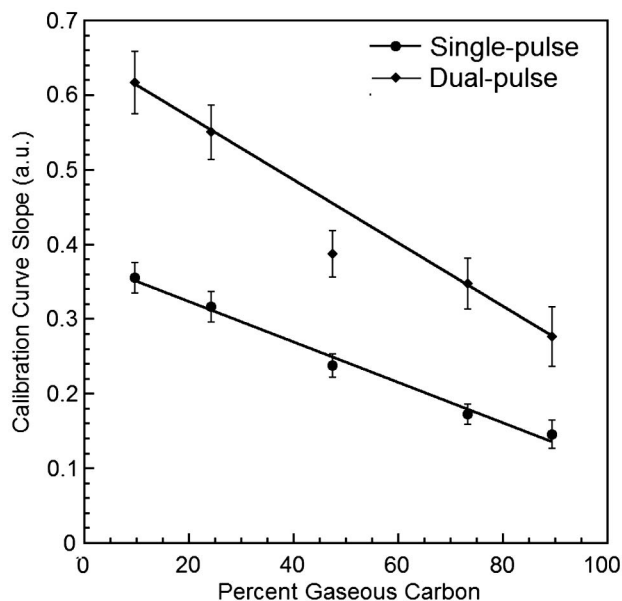


Fig. 7. Slopes of the calibration curves as a function of percent gas-phase carbon for the single-pulse and double-pulse ns-ns LIBS configurations. Error bars are based on the average standard deviation over all concentrations for each respective calibration curve.

percentage increases for both double-pulse and single-pulse configurations, thereby reflecting the overall decrease in analyte response of gas-phase species with respect to particulate-phase species. Overall, both curve fits show high linearity, with the single exception being the approximately 50% gas/solid mixture for the double-pulse configuration. No explanation is apparent for the departure of this particular value, but it was excluded from the linear fit for the double-pulse data.

In light of the trends highlighted above, the ratio of the slope of the double-pulse LIBS calibration curves to the slope of the single-pulse calibration curves was calculated for the ns-ns laser platform as a function of the gas-phase carbon percentage over the full range of experimental values. In addition, this ratio was also calculated using the two linear trend lines of Fig. 7, which enables calculation of a continuous ratio function rather than the discrete experimental values. The results are presented in Fig. 8. Using the linear trend lines to generate the continuous ratio reveals a monotonically increasing function, in which the ratio of the double-pulse to single-pulse LIBS response does correlate with the percentage of gas-phase analyte. This finding is rather novel in that it is the first time to our knowledge that a LIBS methodology has been demonstrated as a means to discriminate between gas-phase and particulate-phase fractions of the same elemental species in an aerosol. Caution is noted, however, in that the superposition of the individual data measurements at each gas-phase percentage reveals considerable scatter, notably so with the approximately 50% gas/solid fraction data point, which is clearly affected by the reduced slope of the double-pulse calibration curve at this fraction, as noted in the discussion of

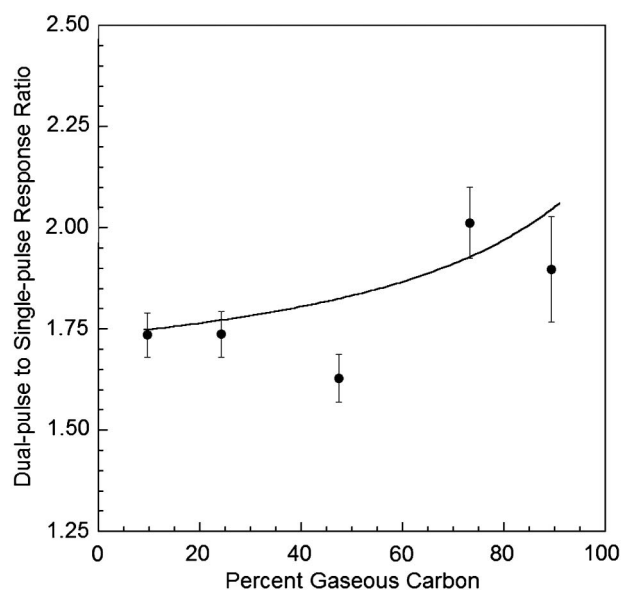


Fig. 8. Ratio of double-pulse to single-pulse LIBS calibration curve slopes as a function of the percentage of gas-phase carbon for the ns-ns configuration. The solid line represents a ratio of the linear trend lines as shown in Fig. 7. The discrete data represent the experimental values at each gas-phase concentration. Error bars are based on the formal propagation of error from Fig. 7 for each respective gas-phase concentration.

the Fig. 7 data. An additional trend is noted, that is, the response of the double-pulse to single-pulse ratio, as measured by the slope of the Fig. 8 curve, is observed to increase as the percentage of gas-phase carbon is increased. This makes sense in view of the overall differences in the response of the gas-phase and solid-phase analytes. As the analyte fraction approaches 100% gas-phase, the addition of a small fraction of solid-phase analyte can appreciably alter the double-to-single pulse ratio response because the solid-phase responds more to the double-pulse approach and the overall response of the solid-phase is greater. However, at the lower overall gas-phase carbon percentages (i.e., nearly all solid-phase analyte), the signal becomes dominated by the solid-phase, resulting in poor overall sensitivity to changes in the gas phase. This behavior can be interpreted as the asymptotic behavior at the lower gas-phase percentages, as observed in Fig. 8.

Measurements made with the fs-ns laser platform again showed a behavior similar to that of the ns-ns laser platform when plotting the  $P/B$  ratios as a function of percent gaseous carbon for a fixed total carbon concentration. The results for the double-pulse and single-pulse approaches are plotted in Fig. 9. As observed for the measurements made with the ns-ns laser platform, the double-pulse fs-ns  $P/B$  ratios are larger than those for the single-pulse case and both decrease with increasing gaseous carbon present. As shown in Fig. 10, a plot of the ratio of the double-pulse to single-pulse  $P/B$  ratios reveals an essentially flat trend (i.e., very small slope) with increasing gaseous carbon present in the sample.



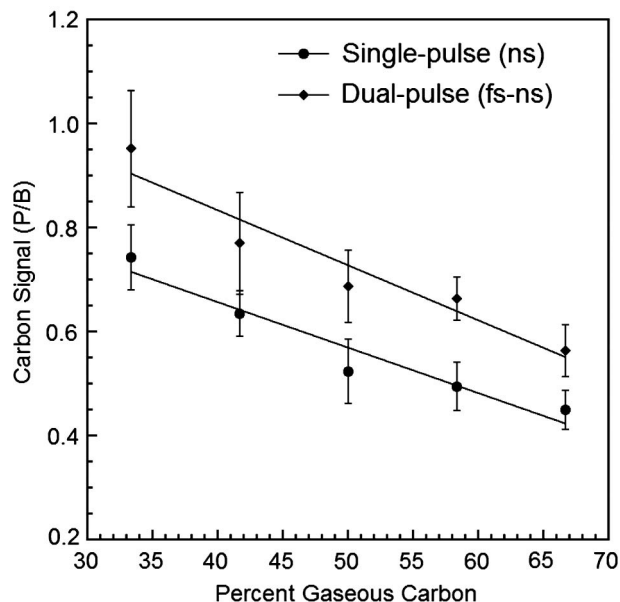


Fig. 9. Peak-to-base ratios for excitation of carbon in gaseous/particle-phase mixtures as a function of the percentage of gaseous carbon present for the fs–ns configuration. The negative slopes are indicative of stronger LIBS signals from the solid-phase carbon. For each mixture, the total mass loading of all carbon present was held to  $1.5\text{ }\mu\text{g/l}$ . Error bars represent one standard deviation.

This is attributed to the relatively low pulse energy of the prepulse fs laser, which produces a much smaller and faster dissipating plasma, notwithstanding the higher field strengths. However, it is also noted that the fs–ns platform data were collected over a smaller range of phase variation, namely, 33%–67% gaseous carbon, as compared with 10%–90% for the ns–ns experiments, while the region of the

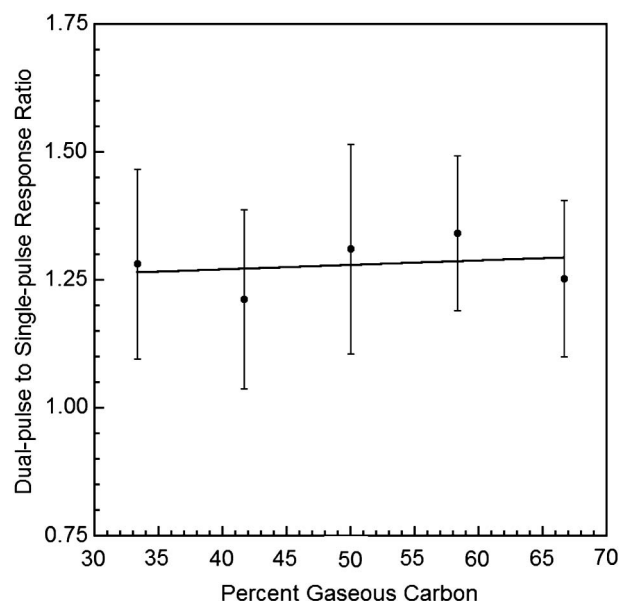


Fig. 10. Ratio of double-pulse to single-pulse  $P/B$  values as a function of the percentage of gas-phase carbon for the fs–ns configuration. Data in the figure were constructed using the data shown in Fig. 9. Error bars represent one standard deviation.

steepest slope of Fig. 8 corresponds to the higher gas percentages (i.e., >67% gas phase).

#### 4. Conclusions

There are clearly some interesting trends that emerge when comparing the LIBS response in the context of the gas-phase and solid-phase analyte fractions in combination with the single-pulse and double-pulse configurations for both the ns–ns and fs–ns laser configurations. Although the measurements presented here were recorded for a single analyte (elemental carbon), the general results should extend to other analytes. As reported in earlier studies [5], the overall signal response for the ns–ns platform is greater for the solid-phase analyte fraction in an aerosol system, which is considered to be rooted in the rarefaction of gas-phase analyte species within the ensuing laser-induced plasma. The same observation for the fs–ns platform may have its origins in both rarefaction and in details of plasma kinetics via pre-ionization by the low-energy fs pulse. In addition, the double-pulse response, as measured by the peak-to-continuum ratio, is greater than that of a single-pulse system (although inherently noisier) for both platforms. More importantly, the enhancement is also related to the phase of the analyte. In aggregate, we have considered the ratio of the double-pulse to single-pulse response as a means to combine the effects of analyte phase on the LIBS response (both double-pulse and single-pulse) with a goal of differentiating between the analyte phases. The present results do show a dependence of the LIBS response on the phase of the analyte as based on the double-pulse to single-pulse response (ns–ns system), although the response curve is not particularly steep at low gas-phase percentages and is characterized overall by scatter in the individual data sets. Importantly, recent research has focused on the dynamics of analyte response in laser-induced plasmas, including the roles of finite rates of dissociation, as well as finite rates of heat and mass transfer [8,10,11,24]. Clearly such results are linked to the original state of the analyte. Therefore, careful optimization of the double-pulse timing and temporal gating could lead to significant improvements in the double-pulse to single-pulse response ratio, as the physics of the relevant processes are exploited to maximize the differences in analyte evaluation and response of the two phases. Ultimately, the use of the double-pulse to single-pulse ratio may hold merit as a new LIBS-based analytical tool for select analyte systems.

The authors thank Thomas Erickson for his assistance in setting up and checking out the fs–ns double-pulse optical system. The authors also thank Bruce Sartwell, Program Manager of the Strategic Environmental Research and Development Program (SERDP WP-1628), for supporting this program. The research was conducted as part of Air Force contract F33615-03-D-2329-0002 with Innovative Scientific Solutions, Inc., Amy Lynch, Air Force Contract

Program Manager. M. Asgill and D. W. Hahn acknowledge the University of Florida Bridge to the Doctorate (DB) program for financial support (M.E.A.).

## References

1. L. J. Radziemski, T. R. Loree, D. A. Cremers, and N. M. Hoffman, "Time-resolved laser-induced breakdown spectrometry of aerosols," *Anal. Chem.* **55**, 1246–1252 (1983).
2. M. Capitelli, A. Casavola, G. Colonna, and A. De Giacomo, "Laser-induced plasma expansion: theoretical and experimental aspects," *Spectrochim. Acta, Part B* **59**, 271–289 (2004).
3. J. Sneddon and Y. Lee, "Novel and recent applications of elemental determination by laser-induced breakdown spectrometry," *Anal. Lett.* **32**, 2143–2162 (1999).
4. D. A. Rusak, B. C. Castle, B. W. Smith, and J. D. Winefordner, "Fundamentals and applications of laser-induced breakdown spectroscopy," *Crit. Rev. Anal. Chem.* **27**, 257–290 (1997).
5. V. Hohreiter and D. W. Hahn, "Calibration effects for laser-induced breakdown spectroscopy of gaseous sample streams: analyte response of gaseous phase species vs. solid phase species," *Anal. Chem.* **77**, 1118–1124 (2005).
6. J. E. Carranza and D. W. Hahn, "Assessment of the upper particle size limit for quantitative analysis of aerosols using laser induced breakdown spectroscopy," *Anal. Chem.* **74**, 5450–5454 (2002).
7. E. Vors and L. Salmon, "Laser-induced breakdown spectroscopy (LIBS) for carbon single shot analysis of micrometer-sized particles," *Anal. Bioanal. Chem.* **385**, 281–286 (2006).
8. P. K. Diwakar, P. B. Jackson, and D. W. Hahn, "Investigation of multi-component aerosol particles and the effect on quantitative laser-induced breakdown spectroscopy: consideration of localized matrix effects," *Spectrochim. Acta, Part B* **62**, 1466–1474 (2007).
9. T. Amodeo, C. Dutouquet, O. Le Bihan, M. Attoui, and E. Frejafon, "On-line determination of nanometric and sub-micrometric particle physicochemical characteristics using spectral imaging-aided laser-induced breakdown spectroscopy coupled with a scanning mobility particle sizer," *Spectrochim. Acta Part B* **64**, 1141–1152 (2008).
10. P. S. Dalyander, I. B. Gornushkin, and D. W. Hahn, "Numerical simulation of laser-induced breakdown spectroscopy: modeling of aerosol analysis with finite diffusion and vaporization effects," *Spectrochim. Acta, Part B* **63**, 293–304 (2008).
11. V. Hohreiter and D. W. Hahn, "Plasma-particle interactions in a laser-induced plasma: implications for laser-induced breakdown spectroscopy," *Anal. Chem.* **78**, 1509–1514 (2006).
12. J. Uebbing, J. Brust, W. Sdorra, F. Leis, and K. Niemax, "Reheating of a laser-produced plasma by a second pulse laser," *Appl. Spectrosc.* **45**, 1419–1423 (1991).
13. F. Colao, V. Lazic, R. Fantoni, and S. Pershin, "A comparison of single and double pulse laser-induced breakdown spectroscopy of aluminum samples," *Spectrochim. Acta, Part B* **57**, 1167–1179 (2002).
14. V. Sturm, L. Peter, and R. Noll, "Steel analysis with laser-induced breakdown spectrometry in the vacuum ultraviolet," *Appl. Spectrosc.* **54**, 1275–1278 (2000).
15. S. Nakamura, Y. Ito, and K. Sone, "Determination of an iron suspension in water by laser-induced breakdown spectroscopy with two sequential laser pulses," *Anal. Chem.* **68**, 2981–2986 (1996).
16. M. Corsi, G. Cristoforetti, M. Guiffrida, M. Hildago, S. Legnaioli, V. Palleschi, A. Salvetti, E. Tognoni, and C. Vallebona, "Three-dimensional analysis of laser-induced plasmas in single and double pulse configuration," *Spectrochim. Acta, Part B* **59**, 723–735 (2004).
17. B. C. Windom, P. K. Diwakar, and D. W. Hahn, "Double-pulse LIBS for analysis of gaseous and aerosol systems: plasma-analyte interactions," *Spectrochim. Acta, Part B* **61**, 788–796 (2006).
18. F. Ferioli and S. G. Buckley, "Measurements of hydrocarbons using laser-induced breakdown spectroscopy," *Combust. Flame* **144**, 435–447 (2006).
19. V. Sturm and R. Noll, "Laser-induced breakdown spectroscopy of gas mixtures of air, CO<sub>2</sub>, N<sub>2</sub>, and C<sub>3</sub>H<sub>8</sub> for simultaneous C, H, O, and N measurement," *Appl. Opt.* **42**, 6221–6225 (2003).
20. P. Gibbon, *Short-Pulse Laser Interactions with Matter*, (Imperial College Press, London, 2007).
21. M. Tran, B. W. Smith, D. W. Hahn, and J. D. Winefordner, "Detection of gaseous and particulate fluorides by laser-induced breakdown spectroscopy," *Appl. Spectrosc.* **55**, 1455–1461 (2001).
22. L. Dudragne, Ph. Adam, and J. Amouroux, "Time-resolved laser-induced breakdown spectroscopy: application for qualitative and quantitative detection of fluorine, chlorine, sulfur, and carbon in air," *Appl. Spectrosc.* **52**, 1321–1327 (1998).
23. D. W. Hahn, J. E. Carranza, G. R. Arsenault, H. A. Johnsen, and K. R. Hencken, "Aerosol generation system for development and calibration of laser-induced breakdown spectroscopy instrumentation," *Rev. Sci. Instrum.* **72**, 3706–3713 (2001).
24. D. W. Hahn, "LIBS analysis of aerosol particles," *Spectroscopy* **24**, 26–33 (2009).

# APPENDIX AE

## Hot electron dominated rapid transverse ionization growth in liquid water

Michael S. Brown,<sup>1,\*</sup> Thomas Erickson,<sup>1</sup> Kyle Frische,<sup>2</sup> and William M. Roquemore<sup>1</sup>

<sup>1</sup>Air Force Research Laboratory, Propulsion Directorate, 1950 Fifth St., Wright-Patterson AFB, Ohio 45433

<sup>2</sup>Innovative Scientific Solutions, Inc, 2766 Indian Ripple Rd., Dayton, Ohio 45440

\*michael.brown@wpafb.af.mil

**Abstract:** Pump/probe optical-transmission measurements are used to monitor in space and time the ionization of a liquid column of water following impact of an 800-nm, 45-fs pump pulse. The pump pulse strikes the 53- $\mu$ m-diameter column normal to its axis with intensities up to  $2 \times 10^{15}$  W/cm<sup>2</sup>. After the initial photoinization and for probe delay times < 500 fs, the neutral water surrounding the beam is rapidly ionized in the transverse direction, presumably by hot electrons with initial velocities of 0.55 times the speed of light (relativistic kinetic energy of  $\sim 100$  keV). Such velocities are unusual for condensed-matter excitation at the stated laser intensities.

©2011 Optical Society of America

**OCIS codes:** (140.3440) Laser-induced breakdown; (190.7110) Ultrafast nonlinear optics; (320.7130) Ultrafast processes in condensed matter; (350.5400) Plasmas.

---

### References and links

1. P. Gibbon, *Short Pulse Laser Interactions with Matter* (Imperial College Press, 2007), Chap. 2.
2. Ch. Reich, P. Gibbon, I. Uschmann I, and E. Forster, "Yield optimization and time structure of femtosecond laser plasma kalpha sources," *Phys. Rev. Lett.* **84**(21), 4846–4849 (2000).
3. N. Zhang, X. Zhu, J. Yang, X. Wang, and M. Wang, "Time-resolved shadowgraphs of material ejection in intense femtosecond laser ablation of aluminum," *Phys. Rev. Lett.* **99**(16), 167602 (2007).
4. C. Schaffer, N. Nishimura, E. Glezer, A. Kim, and E. Mazur, "Dynamics of femtosecond laser-induced breakdown in water from femtoseconds to microseconds," *Opt. Express* **10**(3), 196–203 (2002).
5. S. Minardi, A. Gopal, M. Tatarakis, A. Couairon, G. Tamosauskas, R. Piskarskas, A. Dubietis, and P. Di Trapani, "Time-resolved refractive index and absorption mapping of light-plasma filaments in water," *Opt. Lett.* **33**(1), 86–88 (2008).
6. <http://www.newport.com/The-Effect-of-Dispersion-on-Ultrashort-Pulses/602091/1033/content.aspx>
7. P. W. Barber, and S. C. Hill, *Light Scattering by Particles: Computational Methods* (World Scientific, 1998), Chap. 2.
8. R. del Coso, and J. Solis, "Relation between nonlinear refractive index and third-order susceptibility in absorbing media," *J. Opt. Soc. Am. B* **21**(3), 640–644 (2004).
9. C. Schaffer, Ph.D. thesis, "Interaction of femtosecond laser pulses with transparent materials," Harvard University (2001).
10. J. Noack, and A. Vogel, "Laser-induced plasma formation in water at nanosecond to femtosecond time scales: calculation of thresholds, absorption coefficients, and energy density," *IEEE J. Quantum Electron.* **35**(8), 1156–1167 (1999).
11. I. H. Hutchinson, *Principles of Plasma Diagnostics* (Cambridge University Press, 2002), Chap. 5.
12. See, for example, P. Gibbon, *Short Pulse Laser Interactions with Matter* (Imperial College Press, 2007), p. 174.
13. Y. T. Li, J. Zhang, Z. M. Sheng, H. Teng, T. J. Liang, X. Y. Peng, X. Lu, Y. J. Li, and X. W. Tang, "Spatial distribution of high-energy electron emission from water plasmas produced by femtosecond laser pulses," *Phys. Rev. Lett.* **90**(16), 165002 (2003).
14. V. Sazegari, M. Mirzaie, and B. Shokri, "Ponderomotive acceleration of electrons in the interaction of arbitrarily polarized laser pulse with tenuous plasma," *Phys. Plasmas* **13**, 033102 (2006).
15. The measured transmitted light includes residual 800 nm light and contributions from incident light that was spectrally blue-shifted.
16. C. Elles, A. E. Jilaubekov, R. A. Crowell, and S. E. Bradforth, "Excitation-energy dependence of the mechanism for two-photon ionization of liquid H<sub>2</sub>O and D<sub>2</sub>O from 8.3 to 12.4 eV," *J. Chem. Phys.* **125**, 044515 (2006).
17. W. Theobald, R. Haßner, R. Kingham, R. Sauerbrey, R. Fehr, D. Gericke, M. Schlanges, W.-D. Kraeft, and K. Ishikawa, "Electron densities temperatures and the dielectric function of femtosecond-laser-produced plasmas," *Phys. Rev. E Stat. Phys. Plasmas Fluids Relat. Interdiscip. Topics* **59**(3), 3544–3553 (1999).

18. H. Date, K. L. Sutherland, H. Hasegawa, and M. Shimoizuma, "Ionization and excitation collision processes of electrons in liquid water," *Nucl. Instrum. Methods Phys. Res. B* **265**(2), 515–520 (2007).
  19. R. D. Stewart, W. E. Wilson, J. C. McDonald, and D. J. Strom, "Microdosimetric properties of ionizing electrons in water: a test of the PENELOPE code system," *Phys. Med. Biol.* **47**(1), 79–88 (2002).
  20. H. Gumu, "Simple stopping power formula for low and intermediate energy electrons," *Radiat. Phys. Chem.* **72**(1), 7–12 (2005).
- 

## 1. Introduction

The interaction of short-pulse high-intensity lasers with condensed-phase matter begins with local ionization and acceleration of the free electrons [1]. The subsequent post-pulse dynamics of the hot electrons play a significant role in the radiative properties and the spatiotemporal behavior of the plasma [2]. The dynamics typically occur on time scales on the order of a few ps. At longer times, energy transfer from the electrons to the ions leads to complex material dynamics [3].

In the work reported here, transmission images of the laser-driven plasma in a 53- $\mu\text{m}$ -diameter water column record the spatial and temporal evolution of the ionized region for times  $< 0.5$  ps. Recent experimental work on fs-pulse interaction with bulk water concentrated on the plasma dynamics for times  $> 1$  ps at lower pulse energies (1  $\mu\text{J}$ , 100 fs) [4]. The authors present light-scattering measurements that indicate the rapid short-time growth of the plasma. Assuming an electron density above the critical density for the probe light, they infer a radial plasma expansion of 5  $\mu\text{m}$  in 100 fs, corresponding to a short-time growth rate of  $0.15c$ . ( $c$  denotes the velocity of light in vacuum.) A second study investigated filaments in bulk water over extended distances (hundreds of microns) at low pulse energies (4  $\mu\text{J}$ , 120 fs) [5]. The focused pump-beam intensities used by these researchers is four orders of magnitude lower than that used in the present study and led to observed electron densities that were three orders of magnitude lower than those reported here. Probe-beam shadowgraphy was used to monitor the ionization along the pump-beam axis of propagation after its passage. Increased absorption over time of the probe pulse was postulated to be due to multi-photon absorption by solvated electrons. No significant probe-pulse absorption was observed transverse to the pump-propagation axis.

Here, the sequences of transmission images reveal the growth of the lateral edge of the ionized region as a function of delay with respect to the ionizing pump pulse. Analysis of the opacity of the ionized region as a function of incident pump-pulse energy, combined with energy-conservation considerations, indicates electron densities ranging from  $1.6$  to  $2.3 \times 10^{21} \text{ cm}^{-3}$  and an average electron temperature of  $6 - 20$  eV. Both the electron density and the average temperature increase with the incident pulse energy. The hot electrons with initial energies ranging from 17 to 100 keV account for only  $0.1 - 0.3\%$  of all electrons; however, they carry  $80 - 85\%$  of the total electron kinetic energy.

## 2. Experiment

The target material consisted of a vertical laminar stream of deionized ( $R = 14 \text{ M}\Omega \text{ cm}$ ) water that was directed downward through ambient laboratory air. The 53- $\mu\text{m}$ -diameter column was struck by 45-fs pulses from a 1-kHz Ti:sapphire regenerative amplifier (800 nm) at pulse energies ranging from 0.05 to 0.5 mJ. The propagation axis of the laser beam was oriented normal to the axis of the column, with the electric-field vector being parallel to the column axis. The incident beam was focused with a 40-mm-focal-length singlet, and the column was placed upstream of the focus such that at the center of the water column, the beam had a Gaussian radius of 13  $\mu\text{m}$  that was determined through direct imaging. For pulse energies of 0.51 mJ, the peak focused intensity corresponds to  $1.9 \times 10^{15} \text{ W/cm}^2$ . (For this pulse and focusing lens combination, group velocity dispersion in the lens modifies the pulse width by  $\sim 12\%$  which we include in calculating the focused intensity [6]. No intensity correction is needed for self focusing since this was not observed when the water column was removed from the pump beam path.) Third-order autocorrelation traces of the pulse train indicated a



prepulse leading the main pulse by 8.5 ns with a peak energy that was three orders of magnitude lower. During data collection the transmitted 800-nm light along with the concomitant blue-shifted light was measured as a means of monitoring the amount of incident energy deposited in the target material.

A fraction of the 800-nm light out of the laser was frequency-doubled to yield a 400-nm probe-pulse beam with a pulse energy of  $\sim 1 \mu\text{J}$ . The probe beam was expanded and collimated to  $\sim 1$  cm diameter and was delayed with respect to the excitation (pump) pulse using a stepper-motor-driven optical delay with a temporal resolution of  $\pm 15$  fs. The probe pulse was directed into the target area at right angles to both the water column and the pump-pulse propagation axis. Transmission images were recorded using a lens pair to collect the transmitted probe light and place a magnified image of the pump-irradiated target area onto a ccd (Foculus, 8-bit, b/w, 1/3").

The imaging optics were arranged such that the symmetry plane of the water column normal to the probe beam was in sharp focus. Interference filters were used to reject stray 800-nm light, and neutral-density filters were used to adjust light levels on the CCD. For a range of incident pump-beam energies, transmission images were recorded as a function of pump/probe delay at 30-fs intervals.

Examples of acquired shadowgraph images are shown in Fig. 1. The alternating light and dark bands parallel to the long axis of the water column are light-diffraction manifestations [7]. In the data presented here, time zero corresponds to the passage of the peak of the pump pulse through the longitudinal axis of the water column. Identification of time zero was done in a two-step process using the shadowgraph images. As the pump pulse propagates it weakly ionizes the air via multi-photon processes. This leaves a small perturbation in the images with a leading edge that can be tracked as a function of delay. So, with the water column translated away from its target location, the images as a function of probe delay were examined to find a delay setting that placed the perturbation at the target location (step 1). After translating the water column back to this location a small adjustment was made in the delay to offset the increased transit time of the water column versus air (step 2).

As the pump pulse propagates through the water column, it ionizes the neutral material, leading to absorption of the probe pulse by the free electrons. The neutral deionized water exhibits no linear absorption at either 800 or 400 nm, and the third-order susceptibility for water has no imaginary component. Consequently, no intensity-driven third-order absorption will occur [8]. The darkening of the shadowgraph images after passage of the pump pulse is due entirely to absorption of the probe beam by the free electrons. To avoid the complication of separating diffraction effects, the transmission images are analyzed only along the centerline. The red arrows in Figs. 1b) and 1c) indicate the growth of the plasma in time along the centerline. Based on the first appearance of a change in probe-beam transmission at a delay of 1 ps, the threshold for ionization is  $< 4.5 \times 10^{13} \text{ W/cm}^2$  (an upper limit dictated by the dynamic range of the acquired images). Schaffer et al. [9] found a threshold pulse energy of 0.2  $\mu\text{J}$  for pure water struck by 100-fs pulses. Using their estimated spot size of 1  $\mu\text{m}$ , this corresponds to a threshold intensity of  $6.4 \times 10^{13} \text{ W/cm}^2$ . Both measured values are roughly a factor of three larger than that estimated by Noack and Vogel [10].

### 3. Discussion

Analysis of the pump/probe images proceeded by extracting the measured transmission along the centerline of the water column as a function of time; an example is shown in Fig. 2 for four time delays. The transmission curves are plotted as a function of distance from the beam-propagation axis. Initially, the transmission decreases by 65 - 80% of the pre-pump-pulse value, and over the first  $\sim 200$  fs the transmission further decreases to final values of 10 - 20% of the initial transmission. No strong correlation was found between the minimum transmission and the incident pump pulse energy. The overall shape of the transmission curves is similar for all delay times

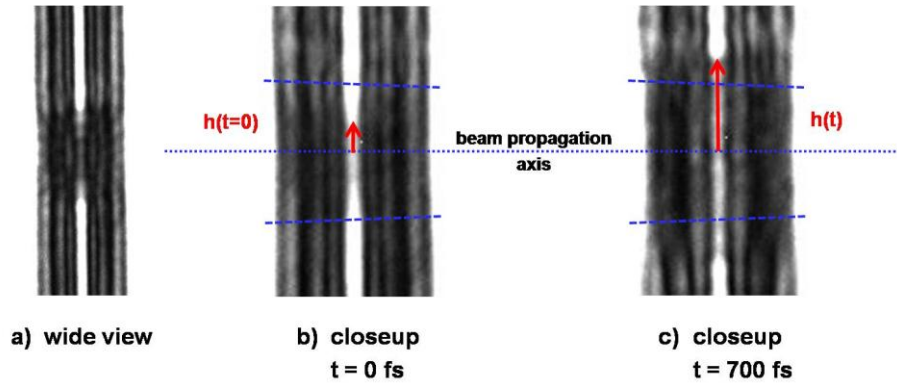


Fig. 1. Transmission images of single-pulse events; pump beam propagates left to right; dashed lines indicate spatial location of Gaussian pump-beam halfwidths. a) Wide view, indicating plasma-formation region in center third of column and unperturbed water above and below. b) Close-up of ionized region at  $t = 0$  fs just as excitation pulse passes center of column. c) Close-up of ionized region 700 fs after arrival of excitation pulse in center of column. Red arrows in b) and c) indicate  $h(t)$  – spatial extent of ionized region along centerline of water column.

and all pump energies. They appear as rounded trapezoids with modulations—presumably due to diffraction—across the transmission minimum. For each curve, an average minimum transmission value was determined across the bottom. Then the width of the full curve was found via curve fitting at half this minimum transmission value. These widths were used to measure the growth of the ionized region as a function of time. Ionized-channel growth for all cases studied was found to be symmetric about the pump-propagation axis.

The growth of the ionized region as a function of delay and pump-beam energy is shown in Fig. 3. The y-axis displays the change in channel width after pump-beam arrival in one direction, as indicated by the red arrow in Fig. 2. For each of the five pump-beam energies studied, ionization-channel growth continues for 300 - 400 fs and then ceases. The ionized region persists until a delay of  $\sim 10$  ps, when large-scale movement of material similar to that reported for solid surfaces begins [3].

By fitting polynomials to the growth-versus-time delay curves and calculating the local derivatives, the speed of the ionization-channel movement as a function of delay was readily determined. Initial values are quite high, ranging from  $0.25c$  to  $0.55c$  for pump energies ranging from 0.05 mJ to 0.5 mJ. It is straightforward to show that for our plasma conditions (see discussion of Table 1 below), the radiant power produced by the associated blackbody radiation or bremsstrahlung is orders of magnitude too weak to produce the observed ionization growth [11]. Consequently, a group of very hot electrons that are initially moving at the speeds indicated above must be responsible for the ionization growth.

The questions that remain are 1) how do electrons achieve such high initial velocities in the transverse direction, and 2) are they present in sufficient numbers to generate the observed ionization-channel growth. Reviews of many previous reports of experimental measurements of hot electron energies [12] suggest that for pump intensities of  $2 \times 10^{15} \text{ W/cm}^2$ , the anticipated hot electron energy should be on the order of 5 keV, corresponding to a velocity of  $0.14c$ , which is much lower than that observed in the experiments. However, using focused intensities that are five times higher than those reported here, Li et al. [13] observed transverse hot-electron jets in liquid water with energies up to 64 keV, corresponding to peak velocities of  $0.46c$ .

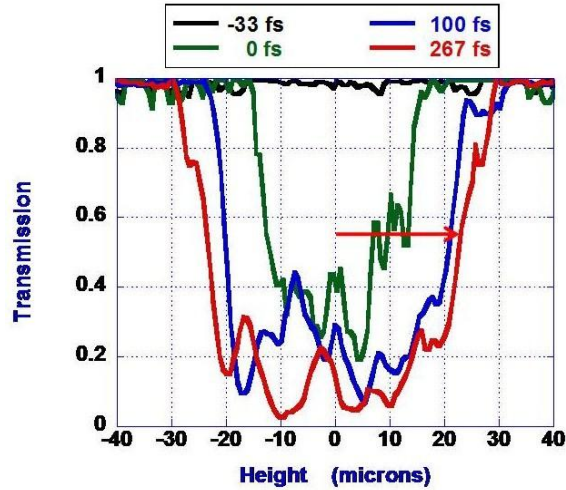


Fig. 2. Relative transmission of 400-nm light along centerline of transmission images for 210- $\mu$ J excitation at four time delays. Red arrow indicates  $h(t = 267 \text{ fs})$ .

For the peak pump-beam intensity used in this study, the quiver velocity and velocity due to the transverse ponderomotive force are estimated to be  $0.02c$ . Similarly, wakefield acceleration leads to estimated velocities of  $10^{-6}c$ . Theoretical work by several groups indicates that longitudinal ponderomotive acceleration can be significant if the electron is accelerated by the leading edge of the incident pulse but not decelerated by the trailing edge. Such acceleration is particularly important for electrons that are generated with a low initial energy just before experiencing the high-intensity portion of the leading edge. For example, using very general arguments, Sazegari et al. [14] estimate that leading-edge longitudinal acceleration is capable of accelerating an electron to velocities on the order of the group velocity of the pulse in the target. The analysis of our data discussed below indicates that during post-ionization, the real part of the index of refraction falls from an initial value of 1.34 to 1.2, leading to an estimated pulse group velocity of  $0.8c$ , which is on par with but greater than the highest velocities observed in our measurements.

To evaluate the possibility of generating a hot subgroup of electrons under the stated conditions, the observed degree of probe-beam transmission along with the measured pump-beam energy deposition was examined. The post-pulse total energy was considered to be equal to the sum of the transmitted pump-beam energy, the reflected pump energy, the energy required to ionize water over the volume indicated by the transmission images, the total kinetic energy of the cool electrons, and the total kinetic energy of the hot electrons. The transmitted pump energy was measured directly [15]; all other contributions to the total energy were calculated. We note that bulk water behaves in the same way as a dielectric with a photoionization threshold of 6.5 eV [16]. This value was used in calculating the ionization contribution to the total-energy budget.

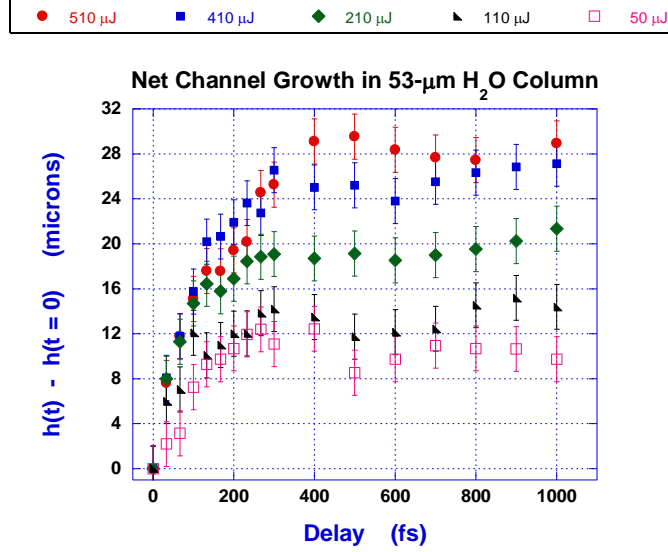


Fig. 3. Net displacement from incident-beam axis of ionized region as function of delay from arrival of excitation pulse for each of five incident pulse energies.

Modeling of the transmission of the probe was conducted following the approach of Theobald et al. [17] who considered the imaginary part of the complex refractive index of water to be due solely to the free electrons. Analysis of the pump-produced plasma proceeded by first estimating the values of the total electron density ( $n_e$ ) and the average electron temperature ( $T_e$ ) and then self-consistently calculating a probe-transmission value ( $T$ ) along with a total energy ( $E$ ) value. This procedure was iterated by adjusting the values for  $n_e$  and  $T_e$  until the calculated probe transmission agreed with the measured transmission and the total energy agreed with the incident pump-beam energy. The calculations were made for the transmission conditions at the arrival of the peak of the pump beam in the center of the water column—probe delay equal to 0 fs. The kinetic energy of the hot electrons was calculated using the initial hot-electron velocities found from the time derivatives of the curves in Fig. 3. The fraction of electrons with these high initial velocities was adjusted such that the initial total kinetic energy of the hot electrons would be sufficient to ionize via binary collisions the volume of water indicated by the growth shown in Fig. 3. The results of these calculations are summarized in Table 1 for four pump-beam energies. Columns 4 and 5 display the degree to which the calculated and observed transmission values agree and how well energy conservation is achieved. As shown, the electron density varies by a factor of approximately two, while the average electron temperature varies by a factor of approximately four for incident pulse energies that are changing by a factor of five. The mean electron density of  $2 \times 10^{21} \text{ cm}^{-3}$  (over all four cases) indicates an ionization fraction of 6%, assuming single ionization of each parent water molecule. The ratio of hot electrons to cold electrons varies by a factor of approximately three and is  $< 0.3\%$  for all cases examined.

Examination of the intermediate values of  $n_e$  and  $T_e$  during the iteration process indicates that the optimal values for these parameters are rather tightly constrained in this model. For example, a  $\pm 20\%$  change in the value of  $n_e$  leads to a calculated optical transmission that deviates by  $\pm 40\%$  from the measured transmission. Interestingly, the ratio of hot to cold electrons is not very sensitive to changes in the total electron density or average electron temperature. This is likely an indirect reflection of the mechanism by which they gain their initial kinetic energy via longitudinal acceleration from the incident pulse. This process would largely be independent of variations in the local plasma environment.

**Table 1. Summary of Plasma Conditions:  $n_e$  (Total Electron Density),  $T_e$  (Avg. Electron Temperature), Ratio of Hot to Cold Electron Density, Ratio of Calculated Transmission to Measured Transmission at 400 nm, and Ratio of Total Post-pulse Energy to Pulse Energy of Incident Light**

E pulse (800 nm)	$n_e$	$T_e$	$n_e$ hot / $n_e$ cold	Calc T / Obs T	E final / E pulse
mJ	$\text{cm}^{-3}$	keV			
0.51	2.3e21	0.020	0.0025	1.04	1.00
0.41	1.9e21	0.020	0.0008	1.01	1.01
0.21	1.4e21	0.007	0.0010	0.98	0.99
0.11	1.6e21	0.006	0.0026	1.03	1.16

The above considerations of energy conservation and probe-beam transmission clearly indicate that the available pump-beam energy was sufficient to produce an ensemble of hot electrons of sufficient density to yield the observed ionization growth—both in spatial extent and growth rate. Since the hot electrons are initially generated with velocities parallel to the pump-beam propagation, collisions must be responsible for redirecting them into trajectories with a significant transverse component. Recently, Date et al. [18] used Monte Carlo simulations to study collisions between energetic electrons (up to 10 keV) and water molecules in liquid water. Their work shows that the hot-electron trajectories rapidly gain significant transverse velocity components via collisions—both ionizing and excitation collisions. These authors also note that the incident hot electrons carry away most of the kinetic energy post-collision. Such electron dynamics would explain the high growth rate of the ionized water volume observed in our measurements. There have been numerous studies of the energy loss range of a free electron in liquid water, both experimental and computational, as a function of incident electron energy (see for example [19,20] and references therein). Such studies do not include a background of positive ions mixed in with the neutral molecules and therefore miss the drag on the particles due to Coulomb forces present in our plasma environment. However, the lateral ionization growth observed in this study is of the same order as that seen in the electron stopping studies – just a little smaller as it should be.

#### 4. Conclusion

In summary, pump/probe-transmission images of a 53- $\mu\text{m}$  water column following the arrival of the 45-fs pump pulse reveal the short-time spatial and temporal growth of the ionized region. Following initial photoionization, the rapid ionization transverse to the pump-propagation axis is driven by hot electrons with unusually high initial velocities (energies) of  $0.55c$  ( $\sim 100$  keV) for a pump intensity of  $1.9 \times 10^{15}$  W/cm<sup>2</sup>. These hot electrons are accelerated by the leading edge of the pump pulse via the longitudinal ponderomotive force and then acquire trajectories with a significant transverse component through ionization and excitation collisions with neutral water. Retaining most of their pre-collision kinetic energy, these hot electrons rapidly ionize the region radially surrounding the pump-pulse propagation axis.

#### Acknowledgments

We acknowledge support from the Air Force Office of Scientific Research, Dr. Tatjana Curic, program manager, and Dr. Arje Nachman.

## LIST OF ABBREVIATIONS, SYMBOLS, AND ACRONYMS

AFOSR	Air Force Office of Scientific Research
AFRL	Air Force Research Laboratory
ANL	Argonne National Laboratory
ASE	amplified spontaneous emission
ATI	above-threshold ionization
BNL	Brookhaven National Laboratory
CCD	charge-coupled device
CPA	chirped-pulse amplification
DARPA	Defense Advanced Research Projects Agency
DoD	Department of Defense
EUV	extreme ultraviolet
FIERO	Frontiers in Extreme Relativistic Optics
FWHM	full width at half maximum
GDD	group delayed dispersion
ISSI	Innovative Scientific Solutions, Inc.
LIBS	laser-induced breakdown spectroscopy
LPI	laser/plasma interactions
MLPC	Mount Laser and Photonics Center, Inc.
MPI	multiphoton ionization
NDE	nondestructive evaluation
NDI	nondestructive inspection
OECD	Organisation for Economic Co-operation and Development
PIC	particle in cell
SAUUL	Science and Applications of Ultrafast, Ultraintense Lasers
TBC	thermal barrier coating
TCC	target-chamber center
UV	ultraviolet
WPAFB	Wright-Patterson Air Force Base
XUV	X-ray ultraviolet